

# UC Berkeley

## UC Berkeley Electronic Theses and Dissertations

### Title

Measuring the fine structure constant with a state-of-the-art atom interferometer

### Permalink

<https://escholarship.org/uc/item/9k91x6th>

### Author

Yu, Chenghui

### Publication Date

2018

Peer reviewed|Thesis/dissertation

**Measuring the fine structure constant with a state-of-the-art atom  
interferometer**

by

Chenghui Yu

A dissertation submitted in partial satisfaction of the

requirements for the degree of

Doctor of Philosophy

in

Physics

in the

Graduate Division

of the

University of California, Berkeley

Committee in charge:

Associate Professor Holger Müller, Chair

Associate Professor Dan Stampurn-Kurn

Professor Eli Yablonovitch

Summer 2018

**Measuring the fine structure constant with a state-of-the-art atom  
interferometer**

Copyright 2018  
by  
Chenghui Yu

## Abstract

Measuring the fine structure constant with a state-of-the-art atom interferometer

by

Chenghui Yu

Doctor of Philosophy in Physics

University of California, Berkeley

Associate Professor Holger Müller, Chair

Measurements of the fine-structure constant  $\alpha$  require methods from across subfields and are thus powerful tests of the consistency of theory and experiment in physics. Using the recoil frequency of Cesium-133 atoms in a matter-wave interferometer, we recorded the most accurate measurement of the fine-structure constant to date:  $\alpha = 1/137.035999046(27)$  at  $2.0 \times 10^{-10}$  accuracy. Using multiphoton interactions (Bragg diffraction and Bloch oscillations), we demonstrate the largest phase (12 million radians) of any Ramsey-Bordé interferometer and control systematic effects at a level of 0.12 part per billion. Comparison with Penning trap measurements of the electron gyromagnetic anomaly  $g_e - 2$  via the Standard Model of particle physics is now limited by the uncertainty in  $g_e - 2$ ; a  $2.5\sigma$  tension rejects dark photons as the reason for the unexplained part of the muon's magnetic moment at a 99% confidence level. Implications for dark-sector candidates and electron substructure may be a sign of physics beyond the Standard Model that warrants further investigation.



To my parents who raised me up with all their love.  
To my brothers and sisters in IGSM who carried me through with unceasing prayers.

# Contents

<b>Contents</b>	<b>ii</b>
<b>List of Figures</b>	<b>iv</b>
<b>List of Tables</b>	<b>x</b>
<b>1 Introduction</b>	<b>1</b>
1.1 The Fine-Structure Constant . . . . .	1
1.2 Test of the Standard Model through Alpha Measurement . . . . .	2
1.3 Measuring $\alpha$ through $h/M$ Measurement . . . . .	3
1.4 Outline of this Thesis . . . . .	5
<b>2 Atom Interferometry</b>	<b>6</b>
2.1 Basics of Atom Interferometry: an Analogy to Light Interferometry . . . . .	6
2.2 Phase Calculation of Atom Interferometry . . . . .	7
2.3 Raman Transition Beam Splitter . . . . .	15
2.4 Bragg Diffraction Beam Splitter . . . . .	19
2.5 Bloch Oscillations . . . . .	31
2.6 Various Atom Interferometer Configurations . . . . .	38
2.7 Diffraction Phase . . . . .	49
2.8 Monte Carlo Simulation . . . . .	54
<b>3 Experiment Setup and Procedure</b>	<b>57</b>
3.1 Overview . . . . .	57
3.2 Frequency Stabilization and Preparation for Reference . . . . .	65
3.3 Laser Cooling . . . . .	67
3.4 Coherent Manipulation . . . . .	84
3.5 Summary . . . . .	105
3.6 Atom Interferometer . . . . .	106
<b>4 Alpha Measurement - Statistical Uncertainty</b>	<b>112</b>
4.1 On the Road to Better Sensitivity . . . . .	112
4.2 Preliminary Measurement . . . . .	118

4.3	The Fine-Structure-Constant Measurement . . . . .	120
<b>5</b>	<b>Alpha Measurement - Systematic Uncertainties</b>	<b>125</b>
5.1	Overview of Systematic Uncertainties . . . . .	125
5.2	Spatially Dependent Potentials . . . . .	126
5.3	Effective Wavenumber Correction . . . . .	130
5.4	Gouy Phase . . . . .	136
5.5	Diffraction Phase Correction . . . . .	141
5.6	Miscellaneous . . . . .	144
<b>6</b>	<b>Conclusion and Future Prospects</b>	<b>153</b>
6.1	Conclusions . . . . .	153
6.2	Implications on Testing New Physics . . . . .	155
6.3	Future Prospects . . . . .	160
	<b>Bibliography</b>	<b>162</b>

# List of Figures

1.1	The normalized contribution to electron magnetic-moment anomaly ( $a_{\text{term}}/a_{\text{total}}$ ) in blue along with relative uncertainty ( $\delta a_{\text{term}}/a_{\text{total}}$ ) in orange is plotted here. Each dash line indicates the relative uncertainty of $\alpha$ measurement from three best measurements to date. . . . .	3
1.2	Results of selected $\alpha$ measurements are plotted in $\delta\alpha/\alpha$ relative scale in parts-per-billion (ppb) [1]. A few accurate measurements are also zoomed in as an inset plot. . . . .	4
2.1	Analogy between the light interferometer and the atom interferometer . . . . .	6
2.2	Mach-Zehnder Atom Interferometer . . . . .	8
2.3	. . . . .	16
2.4	Energy-momentum diagram for a 5th order Bragg diffraction. The initial velocity is taken to be $-5\hbar k$ . . . . .	20
2.5	Atom population distribution in momentums states after a Bragg diffraction at various 2-photon Rabi frequencies . . . . .	24
2.6	Two-photon Rabi frequency of a Bragg $\pi/2$ pulse vs Bragg order n . . . . .	25
2.7	Time evolution solution of a 5th order Bragg $\pi/2$ pulse . . . . .	26
2.8	Bragg beam splitter phase vs two-photon Rabi frequency. Here the phase difference is defined as the phase difference between $ 5\hbar k\rangle$ and $ -5\hbar k\rangle$ after a transition from $ -5\hbar k\rangle$ to $ 5\hbar k\rangle$ . . . . .	27
2.9	Bragg beam splitter phase vs two-photon detuning. Here the phase difference in blue is defined as the phase difference between $ 5\hbar k\rangle$ and $ -5\hbar k\rangle$ after a transition from $ -5\hbar k\rangle$ to $ 5\hbar k\rangle$ ; and that in orange is defined as the phase difference between $ -5\hbar k\rangle$ and $ 5\hbar k\rangle$ after a transition from $ 5\hbar k\rangle$ to $ -5\hbar k\rangle$ . . . . .	28
2.10	Time evolution solution of a 5th order dual-frequency Bragg $\pi/2$ pulse . . . . .	29
2.11	Dual frequency Bragg beam splitter phase vs two-photon Rabi frequency. Here the phase difference in blue is defined as the phase difference between $ -15\hbar k\rangle$ and $ -5\hbar k\rangle$ after a transition from $ -5\hbar k\rangle$ to $ -15\hbar k\rangle$ . . . . .	30

2.12	Dual frequency Bragg beam splitter phase vs two-photon detuning. Here the phase difference in blue is defined as the phase difference between $ -15\hbar k\rangle$ and $ -5\hbar k\rangle$ after a transition from $ -5\hbar k\rangle$ to $ -15\hbar k\rangle$ ; and that in orange is defined as the phase difference between $ 15\hbar k\rangle$ and $ 5\hbar k\rangle$ after a transition from $ 5\hbar k\rangle$ to $ 15\hbar k\rangle$ . . . . .	31
2.13	Energy band structure of an atom in optical lattices with lattice depth $\Omega = \omega_r$ .	35
2.14	Time evolution solution of dual-frequency Bloch Oscillations . . . . .	37
2.15	Bloch oscillations efficiency vs Bloch pulse intensity . . . . .	37
2.16	Classical model of Bloch oscillations for two arms of the interferometer . . . . .	38
2.17	Pulse types in a general atom interferometer configuration . . . . .	40
2.18	Splitting phase in non-closure interferometers . . . . .	41
2.19	Dual Mach-Zehnder Gravity Gradiometer Configuration . . . . .	43
2.20	Ellipse Fitting Technique . . . . .	44
2.21	Ramsey Bordé Atom Interferometer Configuration . . . . .	45
2.22	Simultaneously Conjugated Ramsey Bordé Atom Interferometers Configuration	47
2.23	Simultaneously Conjugated Ramsey Bordé Atom Interferometers Configuration with Bloch Oscillations . . . . .	48
2.24	Ramsey Bordé atom interferometer diffraction phase vs. two-photon detuning at Bragg order $n=5$ , Bloch order $N=0$ . . . . .	51
2.25	Each pulse's contribution to Ramsey Bordé atom interferometer diffraction phase of each pulse vs. two-photon detuning . . . . .	52
2.26	Comparison of diffraction phase dependence on two-photon detuning with and without Bloch oscillations . . . . .	52
2.27	Comparison of diffraction phase dependence on two-photon Rabi frequency with and without Bloch oscillations . . . . .	53
2.28	Each pulse's contribution to Ramsey Bordé atom interferometer diffraction phase vs. two-photon Rabi frequency . . . . .	53
3.1	Simplified optical schematics. Reference frequencies preparation system, laser cooling and trapping system, and coherent manipulation system are labeled red, green and yellow respectively. . . . .	59
3.2	Cesium $D_2$ line energy levels and laser frequencies [42]. See Section ?? for actual detunings. . . . .	60
3.3	Experiment setup overview. Each stage of the experiment is labeled with different colors. . . . .	62
3.4	Experiment timing signal overview. Different parts are shaded by different color. The color code follows Figure 3.3. A same color corresponds to the same stage defined in Figure 3.3. . . . .	64
3.5	Frequency Preparation Optical Schematics . . . . .	65
3.6	Spectroscopy for Reference Lock . . . . .	65
3.7	Working principles of Raman Sideband Cooling in Cesium . . . . .	70
3.8	Laser Cooling Optical Schematics . . . . .	72

3.9	2DMOT, 3DMOT and PGC Setup . . . . .	73
3.10	MOT Stage Timing . . . . .	74
3.11	Launch and PGC Stage Timing . . . . .	75
3.12	RSC and ARP Setup . . . . .	75
3.13	RSC and ARP Stage Timing . . . . .	76
3.14	The first fountain signal compared with the second fountain signal with and without RSC. The first fountain signal is fitted with a Gaussian. . . . .	78
3.15	The second fountain signal with and without RSC. Both of them are fitted with a double Gaussian. . . . .	79
3.16	CCD images of the first fountain and the second fountain with and without RSC	80
3.17	CCD images slices and their 2D Gaussian fit respectively . . . . .	82
3.18	Cesium $D_2$ transition matrix elements relevant for Raman/Bragg processes as multiples of $\langle J' = \frac{3}{2}   er   J = \frac{1}{2} \rangle$ . . . . .	87
3.19	Raman/Bragg beam configuration used in the experiment. . . . .	90
3.20	Coherent Manipulation Optical Schematics . . . . .	93
3.21	Bragg and blow-away beams setup . . . . .	96
3.22	State Preparation Timing . . . . .	97
3.23	Atom Interferometry Timing . . . . .	98
3.24	State Selection signal and its double Gaussian fit . . . . .	99
3.25	State Selection pulse efficiency vs. peak two-photon Rabi frequency given by a Monte Carlo simulation . . . . .	100
3.26	Simulated atom distribution along x axis before and after SS . . . . .	101
3.27	Velocity Selection signal and its Gaussian fit . . . . .	101
3.28	Velocity Selection pulse efficiency vs. peak two-photon Rabi frequency given by a Monte Carlo simulation . . . . .	102
3.29	Simulated atom distribution along x axis before and after VS . . . . .	103
3.30	Simulated atom velocity distribution along z axis before and after VS . . . . .	103
3.31	Bragg diffraction signal and its Gaussian fit . . . . .	104
3.32	Frequency generation diagram . . . . .	105
3.33	Ramsey Bordé Interferometer Scheme with Bloch Oscillations . . . . .	107
3.34	Raw data trace of a Ramsey Bordé interferometer without Bloch oscillations . .	108
3.35	Ellipse data and fit . . . . .	109
3.36	Measured phase difference between conjugated interferometers vs. Bragg 2-photon detuning. Data were taken at Bragg order $n = 5$ , Bloch order $N = 0$ , pulse separation time $T = 10$ ms. . . . .	110
3.37	Measured ellipse contrasts vs. Bragg intensity. Data were taken at Bragg order $n = 5$ , Bloch order $N = 0$ , pulse separation time $T = 10$ ms. . . . .	110
3.38	Measured recoil frequency vs. pulse separation time T . . . . .	111
4.1	Contrast vs. pulse separation time T of a Ramsey Bordé atom interferometer without Bloch oscillations . . . . .	113

4.2	Bloch oscillations efficiency vs. Bloch intensity and Bloch ramp rate at Bragg order $n=4$ and Bloch order $N=50$ . Bloch efficiency here is defined as the ratio between the number of atoms arrived within the Gaussian masks of the four interferometer output ports and the total number of atoms detected in the entire data trace. . . . .	114
4.3	Atom interferometer Y-contrast vs. Bloch intensity and Bloch ramp rate at Bragg order $n=4$ and Bloch order $N=50$ . . . . .	115
4.4	Bloch oscillations efficiency $\times$ atom interferometer Y-contrast vs. Bloch intensity and Bloch ramp rate at Bragg order $n=4$ , Bloch order $N=50$ and pulse separation time $T=80$ ms . . . . .	116
4.5	Ellipses directly from data with and without AC Stark shift compensation at Bragg order $n=5$ , Bloch order $N=25$ . . . . .	116
4.6	Atom interferometer contrast as a function of pulse separation time $T$ with and without AC Stark shift compensation. Data taken with $n=5$ , $N=75$ , $T=80$ ms .	117
4.7	Residual phase vs pulse separation time $T$ under various conditions. Residual phase is defined as the difference of measured phase and the fitted phase based on a constant diffraction phase model. . . . .	118
4.8	Ramsey Bordé atom interferometer contrast vs. pulse separation time $T$ . Mode cleaning techniques have been applied. Other conditions are indicated in the legend.	119
4.9	Moore's law of our atom interferometer performance . . . . .	120
4.10	Data to characterize the system and to measure the fine-structure constant. (A) Detected fluorescence with various Bloch oscillations orders. For visibility, an arbitrary offset is applied for each trace. Data were taken at $T=5$ ms. (B) A sample of interference ellipses used for the measurement. Data were taken at $n=5$ , $N=125$ , $T=5, 20, 40, 80$ ms. (C) Actual $\alpha$ measurement result. Each point shown is the measured value from each dataset. The pink band represents the overall $\pm 1\sigma$ statistical error. These three figures are directly taken from reference [8]. . . . .	121
4.11	Residual phase from $\alpha$ measurement data vs. pulse separation time $T$ . It is adapted from reference [8]. It is used to estimate speckle phase systematic uncertainty in Section 5.2 . . . . .	123
5.1	Dual Mach Zehnder atom interferometer phase vs. pulse separation time $T$ measurement from one dataset. Data were taken at $n = 5$ , $N = 125$ , $T'_1=5$ ms, $T'_2=45$ ms. . . . .	127
5.2	Overall gravity gradient measurements. The red band indicates the mean value and $\pm 1\sigma$ . . . . .	128
5.3	Comb calibration raw data from three measurements and the fitted calibration model . . . . .	132
5.4	Beam profile measured by scanning-slit device. Data were taken at 4 inches out of the fiber port. The Hermite-Gaussian model is obtained by fitting all the data with consistent parameters up to the 2nd order. . . . .	137

5.5	Shift in $\alpha$ as a function of Bloch efficiency. The blue line shows the final reported value of $\alpha$ , assuming no dependence on Bloch intensity. The red lines assumes a linear dependence. Both red and blue band represent $\pm 1\sigma$ error bars. This figure is directly taken from supplementary materials of reference [8]. . . . .	140
5.6	The fine-structure-constant measurement with unapodized beam compared with other measurements. This figure is directly taken from supplementary materials of reference [8]. . . . .	141
5.7	Real optimized pulse shape compared with an ideal Gaussian . . . . .	142
5.8	Residual phase from both a Monte Carlo simulation and the experiment. These two figures are directly taken from reference [108]. . . . .	143
5.9	Atom interferometer configuration with parasitic interferometer plotted in dash lines. This figure is directly taken from reference [108]. . . . .	144
5.10	Fraction of atoms in the parasitic interferometer $ n_p = 1\rangle$ as a function of Bragg pulse duration. Here the pulse duration is defined as $6\sigma$ of Bragg Gaussian pulse. This figure is directly taken from reference [108]. . . . .	145
5.11	Effect of the Earth's rotation on Ramsey Bordé interferometer. The subplot on the left show atom movement in 2D as Bragg beam is rotation along with the earth. The direction of each beam splitter's wave vector is shown by arrows. The subplot on the right is the typical spatial-temporal diagram as a reference to understand the plot on the left. The same color corresponds to the same stage of the inteferometer. . . . .	150
6.1	Some recents precision determination of the fine-structure constant. This figure is directly taken from reference [8] . . . . .	153
6.2	Normalized magnitude of contribution of some theoretical terms to electron magnetic-moment anomaly. $\alpha^4, \alpha^5$ represent 4th and 5th order QED loop correction terms. $\mu, \tau$ represent QED terms related to masses of $\mu$ and $\tau$ . Weak represents correc-tion from weak interaction. Hadron represents correction from hadronic physics. . . . .	154
6.3	Exclusion limits under various statistical methods . . . . .	157
6.4	Dark photon with vector coupling exclusion plot. Constraints from BaBar were based on Bayesian limit/ frequentist profile likelihood statistics at 90% C.L. [120]. Constraints from kaon decay were obtained from BNL E787+E949 experiments at 95% C.L. [121, 122]. Constraints from NA64 2017 were based on $CL_s$ statistics at 90% C.L. [123]. Muon $g_\mu - 2$ data was from CODATA2014 [1]. Its favored region was obtained from its $\pm 2\sigma$ area based on frequentist's statistics. Both electron $g_e - 2$ for LKB and this work were analyzed under frequentists' statistics with 99.5% confidence level [1, 2, 11, 8]. We have also analyzed this work under PCL( $M_{\min} = 16\%$ ) with 90% C.L. Note that NA64 2018 [124] came out after our result was accepted for publication. But for references, here we have also included excluded region from NA64 2018 as shown in dash line. . . . .	158



6.5	Dark photon with axial vector coupling exclusion plot. The plot is given with assumptions $c_A^u = 10^{-3}$ , $c_A^d = 10^{-4}$ , and $c_A^\mu = c_V^l = 0$ . This work is analyzed under frequentist's statistics at 90% C.L. [117]. . . . .	159
-----	---	-----

# List of Tables

2.1	Ingredients for a simple Mach-Zehnder atom interferometer phase calculation . .	14
2.2	The effective two-photon Rabi frequency $\frac{\Omega_1\Omega_2}{2\Delta}$ of a $\frac{\pi}{2}$ Bragg diffraction at various Bragg orders . . . . .	25
2.3	Summary of momentum and phase transfer for different pulse types. For type a-d, they are transferred to the deflected path. For type e-f, momentum is transferred to both paths. $\Delta\phi_{BO}$ is defined as phase difference between two paths added by Bloch oscillations. The sign of the phase difference is defined in the same way as the sign of $\Delta z$ . . . . .	40
2.4	List of Monte Carlo simulations and specific techniques involved . . . . .	55
3.1	List of symbols used in the optical schematics. . . . .	58
3.2	List of terms commonly used for this experiment . . . . .	60
3.3	Fitting parameters for the first and the second fountain . . . . .	82
3.4	Measured atom temperatures . . . . .	84
3.5	Rough estimation of atom number detected by the photodetector with each procedure applied . . . . .	104
3.6	List of frequencies of main lasers and modulators. The components are labeled according to Figure 3.1. . . . .	106
5.1	Error budget of the fine-structure-constant measurement. Related measurements are listed in the second column. And relative systematic corrections and uncertainties in $\alpha$ are listed in the third column. $1 \text{ E} = 10^{-9} \text{ s}^{-2}$ . $u$ is atomic mass unit. . . . .	126
5.2	Systematic shift due to thermal motion of atoms. Certain estimated experimental parameters are listed in the second column with the systematic effect it produces in the third column. . . . .	142

## Acknowledgments

I want to give many thanks to many people in my lives, from my parents to my advisor, from my friends to my coworkers. All that I have received and achieved today would not be possible without their help and support. Looking back over the past six years, I'm very thankful that what I have received is not only a PhD degree or an advancement for academics and career, but also a special opportunity that enriched my understanding of life as well.

In college, I was an independent and competitive student, always striving to outperform my classmates for better advancement of life. In my senior year, I was privileged to be funded by my college to have a short three-month internship in Prof. Jun Ye's lab in Boulder, Colorado. I followed exactly the same study/ research pattern that I had in college, isolating myself to study and work hard to prove myself and be acknowledged. But it did not work well. I still clearly remember how my self-sufficient picture of life was challenged for the first time when I had a car ride with Prof. Jun Ye to a group ski trip. He asked me the motivation behind my research, but I did not even know after a month of hard work. He noticed that I was quiet, doing research alone most of the time. He encouraged me to talk to people and build relationship with other labmates. He said there were many international PhD students like me from China who were smart and competent; however, they did not know how to work and communicate with people because they did not care much about relationships. Very few of them were successful to the end, because many significant breakthrough cannot be achieved by a single person. And he attributed his own success to having such a strong team, in which people can support one another and work for the same purpose. So he encouraged me over and over again to talk to people and build relationship with them.

I did not change overnight. Even to this day, I'm still not quite a relational person. But I'm very thankful for Prof. Jun Ye for challenging me to rethink the trajectory of my life. Following his advice, I noticed something different not only in his lab, but also here in Berkeley. People were not as competitive and ambitious as I thought. They cared a lot about their family and their friends. As I gradually experienced hospitality, help and support from Sara Campbell, Matthew Swallows, Michael Martin, Michael Bishof in Jun's group and Pei-Chen Kuan, Shau-Yu Lan, Paul Hamilton, Geena Kim, Brian Estey, Richard Parker, Weicheng Zhong, Matt Jaffe, Eric Copenhaver, Kayleigh Cassella and many more here in Holger's group.

I want to share a few stories to give thanks to my advisor Holger Müller. I still clearly remember much of his support and advice throughout my graduate school, such as the comments and feedback I received for my qualifying exam presentation, and many lab visits to show me how to do this and that. During my qualifying exam practice talk, he wrote to me two pages filled with feedback and comments that I still keep to this day. I felt especially blessed in the way that though I was poor in writing and speaking in English as an international student, I received extra advice and support from him despite his busy working schedule, having my English grammar corrected almost word by word. He never commanded students with dos and don'ts. After he made some suggestions and advice, he would listen to students of their opinions. I'm thankful for the encouraging lab dynamics

that he promoted, in which I got to learn, grow, and be truly inspired by the beauty and joy of doing scientific research, rather than just following instructions like a slave.

Another thing I was really thankful of was his words of encouragement. Working on a complex experiment like this atomic fountain atom interferometer was not easy at all. Over the past five years, many parts of the experiment were broken at some point. I remember at one time the pump laser Verdi 18, the Titanium doped sapphire laser, the tapered amplifier, and the atomic fountain broke down one after another. Right after we fixed something, something else broke down. It was especially painful to deal with the Verdi failure as it is a highly commercialized laser that we could not do much with until the tech support came. Yet, he never complained to us for our incompetence to deal with the situation. Rather even when all of us in the team were very frustrated, he always had words of encouragement infused with his strong optimistic view about the future. Moreover, he even offered to help and share the burden with us. Even in the midst of a terrible situation, he would always see the positive side of it: at least something was still working and we could still make progress with it. He would encourage us not to lose heart, believing that there would be a way in the future. And that turned out to be the case most of the time. I'm very thankful for his help, support, encouragement infused with his optimism, without which many of us might have already given up many times.

I also want to give thanks to many of my labmates from whom I received a lot of help and got to learn many things. First of all I want to give thanks to my fountain teammates Richard, Weicheng, Brian, and the older generation Pei-Chen and Shau-Yu. Without them I would never be able to achieve all this. When I was on trips in China to visit my family, they were the people keeping the experiment running and making progress. I'm thankful for Richard for a lot of fruitful discussions we had together. I got to learn how to plan and strategize a project when I was stuck and felt lost. I also got to learn how to analyze, interpret and present data. From those discussions I learned that good ideas mostly come from discussing with people rather than thinking hard by myself. I'm thankful for Weicheng for his hard work to babysit the system daily and keep it running at its optimal condition during months of data collection. I'm thankful for Brian for showing me the standard of building electronics, aligning optics, and so on in an excellent fashion. I'm also very thankful for Pei-Chen, who taught me so much during my first semester in the lab. While I was still struggling with my language, he would speak Mandarin to me to teach me and train me so that I could understand better. Because of him, I learned a lot of basic technical skills like fiber coupling.

I would also like to give thanks to many others, to Eric who helped manage the group website and group meetings for years and who offered much help to us in many issues we encountered in the fountain project, to Xuejian who helped us placing orders and getting parts fixed, to Kayleigh who brought donuts generously to encourage us to clean the lab and also to all other group members. It was not an easy and comfortable working environment to have 4 experiments and more than 10 people all working in the same room. There were unavoidable conflicts. But I'm also thankful for them speaking up honestly and giving much understanding and grace for one another.

Definitely there are also many family members and friends I'm grateful for. Without my parents' continuous love and financial support, I would not have been able to come here to pursue a PhD. Studying abroad meant more time away from home. But for my parents, there were nothing that they could not sacrifice for my good. I'm so thankful for the best love they poured out with all that they had. I'm also very thankful for my church Gracepoint and the ministry group International Graduate Student Ministry (IGSM) I'm part of, where I learned so much about life, received my salvation and experienced so much love and support from my fellow brothers and sisters. Especially, I want to give thanks to Chul and Sharon Kim, Jisup and Sara Hong for so much support and many concrete advices about life. This past year has been quite challenging for me. It wasn't easy to deal with research and writing at the same time. There were many moments when I lost my motivation and just wanted to escape. But I'm thankful for many brothers that I live with who would cook for me, do house cleaning for me, keep me accountable and support me in prayers. I'm also very grateful for my fiancée Judy, who prepared care packages for me and encouraged me with many words and prayers. It is through this tough season of life that I understood that I could do nothing without all these people. It's quite true that "one's life does not consist in the abundance of his possessions" (Luke 12:15). Had I followed my old pattern of life, I would have missed so many people in my life and ended up in my own bitter jealousy against anyone more competent than me. But now I'm very thankful above all for God and His grace, in which I believe that Jesus Christ has died on the cross for my sins to be forgiven. Even though I'm still not quite relational, and have many other character flaws to work on, upon such grace, I find my life filled more and more with the true riches and abundance found in the fruits of the Spirit — "love, joy, peace, patience, kindness, goodness, faithfulness, gentleness, self-control" (Galatians 5:22-23).

# Chapter 1

## Introduction

### 1.1 The Fine-Structure Constant

The fine-structure constant is one of the most important fundamental constants in physics. It is a dimensionless constant characterizing the strength of electromagnetic interaction, i.e. how charged particles interact with light. It is the basic building block (the coupling constant) of Quantum Electrodynamics (QED) [1]. Quantitatively,  $\alpha$  is given as the square root of the ratio of Hartree energy to electron rest-mass energy as follows.

$$\alpha = \sqrt{\frac{2hR_\infty}{m_e c}} \quad (1.1)$$

where  $R_\infty, h, c, m_e$  are Rydberg constant, Planck constant, speed of light, electron mass respectively.

Measurement of the fine-structure constant is important in fundamental science. Since the fine-structure constant is very fundamental, its value is an important input parameter in many precision measurements to test existing physics as well as to explore new physics. Even in other areas of science and engineering, the fine-structure constant is widely used in research and technical applications.

The most precise determination of the fine-structure constant ( $\alpha$ ) before this work was through an indirect approach of measuring electron magnetic-moment  $g$  factor [2]. Based on Dirac equation, electron's spin magnetic moment  $g$  factor was predicted to be exactly 2 [3]. But, more precise experiment showed a significant discrepancy between the measured value and Dirac's prediction. It drew a lot of attention of physicists at that time and eventually QED was developed as a new theoretic framework within which this puzzle was successfully resolved. This discrepancy was then called anomalous electron magnetic moment or  $g - 2$  in short. Now after a few decades of development,  $g - 2$  could be calculated and predicted with QED and other branches of Quantum Field Theory altogether. In other words, given an accurate measurement of  $g - 2$ , the fine-structure-constant could be determined reversely through lengthy theoretic calculation involving evaluating thousands of Feynman diagrams

in QED as well as other physics theories of electroweak and strong interactions. It's a very challenging task to do and a few minor theoretical errors have already been reported over the past decades. On the other hand, although these existing established theories, now known as the Standard Model of physics, are very successful in predicting vast majority of phenomena in modern physics, they are still incomplete. There are a handful of observations like dark matter, dark energy, neutrino oscillations beyond the Standard Model. There is no reason that we should fully trust all these theories as well as the value of the fine-structure constant obtained through them. Rather, using a different method to measure  $\alpha$  becomes an important test of the Standard Model, even enabling us to peep into unexplored territory of new physics beyond the Standard Model [4]. In the next section we will go a little further to explain how  $\alpha$  is obtained by  $g - 2$  measurement and how it allows us to test all these theories involved.

## 1.2 Test of the Standard Model through Alpha Measurement

Anomalous electron magnetic moment is mostly contributed by Quantum ElectroDynamics (QED). The reason why there is such anomalous moment is because in Quantum Field Theory vacuum is not empty. It contains fields of virtual particles. When electrons go through scattering process with virtual photons, it would produce correction of electron magnetic-moment. Based on theory of QED, the QED contribution to the electron magnetic-moment anomaly  $a_e$  is

$$a_e(\text{QED}) = A_1 + A_2(m_e/m_\mu) + A_2(m_e/m_\tau) + A_3(m_e/m_\mu, m_e/m_\tau) \quad (1.2)$$

where  $A_1$  is a mass independent term and  $A_2, A_3$  are mass-dependent terms depending on mass ratios among electron, muon and tauon. Each of these terms can be expanded into a power series of  $\alpha$ :

$$A_i = \sum_{n=1}^{\infty} A_i^{(2n)} \left(\frac{\alpha}{\pi}\right)^n \quad (1.3)$$

Each  $i^{\text{th}}$  term of  $\alpha$  here is essentially the sum of all  $i^{\text{th}}$  order Feynman diagram loop corrections. The mass-independent coefficients  $A_1^{(2n)}$  have been precisely calculated up to the 4th order. And a numerical calculation of the 5th order with certain theoretical uncertainty is also available [5, 6, 7]. The mass-dependent coefficients  $A_2$  and  $A_3$  require input of mass ratio measurements from experiments, which results in a small uncertainty in their values.

At current level of electron  $g - 2$  measurement accuracy [2], it's also important to include theories beyond QED (electroweak and strong interaction) into consideration. If we put all these terms together, it is how electron magnetic-moment anomaly is theoretically predicted to our knowledge:

$$a_e(\text{theory}) = a_e(\text{QED}) + a_e(\text{weak}) + a_e(\text{hadron}). \quad (1.4)$$

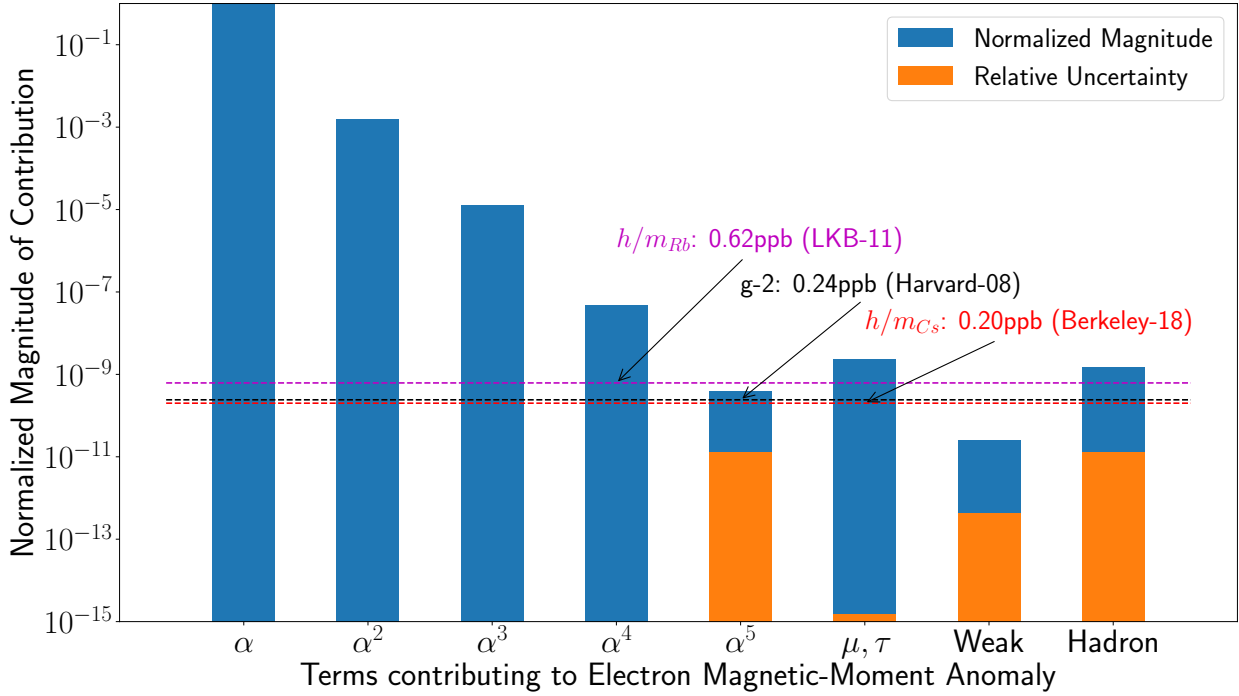


Figure 1.1: The normalized contribution to electron magnetic-moment anomaly ( $a_{\text{term}}/a_{\text{total}}$ ) in blue along with relative uncertainty ( $\delta a_{\text{term}}/a_{\text{total}}$ ) in orange is plotted here. Each dash line indicates the relative uncertainty of  $\alpha$  measurement from three best measurements to date.

Here is a plot showing magnitude of contribution of each term to electron magnetic-moment anomaly in order to visualize what theories we can test at current accuracy of experiments. From the figure we can see that the best  $g - 2$  measurement in Harvard set an uncertainty of  $\alpha$  to 0.24 ppb [2, 1, 5], which means at this stage we can test theories up to 0.24 ppb at best. From our most recent  $\alpha$  measurement, we have achieved an uncertainty of 0.20 ppb [8], which allows us to test the 5th order QED correction for the first time. Beyond that it also allows us to set limit on theories like electron substructure as well as dark photon. More will be discussed in Chapter 6.

### 1.3 Measuring $\alpha$ through $h/M$ Measurement

In the previous section, we have briefly mentioned the indirect way to measure  $\alpha$  through electron  $g - 2$  measurement and theories. Here in order to establish a test of theories, we need to have additional measurements independent of the theory we are testing. Historically various methods like AC Josephson effect [9], Quantum Hall effect [10] as well as atomic  $h/M$  measurements [11, 12, 13] have been employed to measure  $\alpha$ . Here is a plot showing some significant measurements done in recent decades. The fine-structure constant measure-



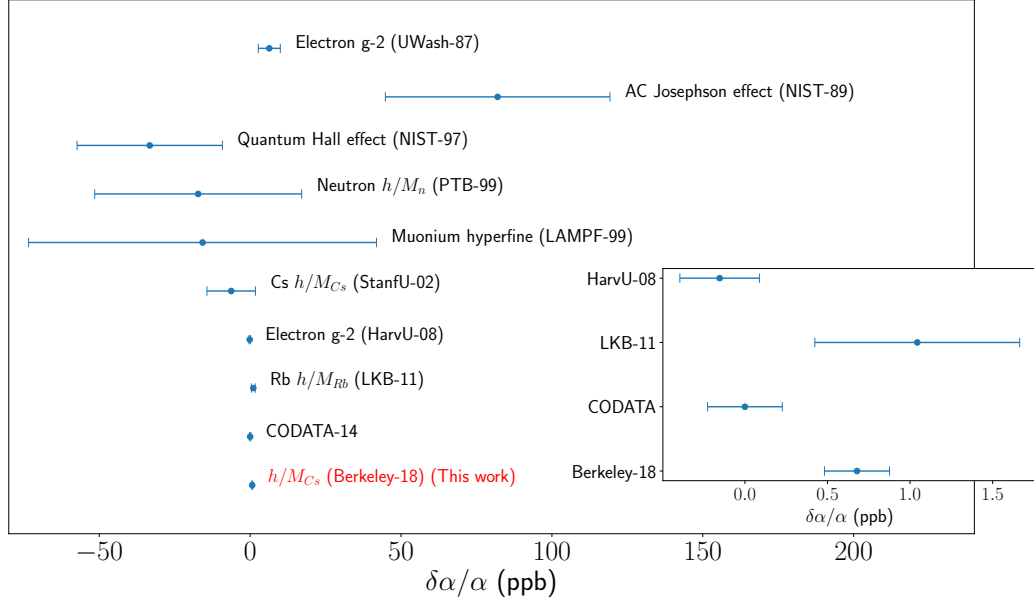


Figure 1.2: Results of selected  $\alpha$  measurements are plotted in  $\delta\alpha/\alpha$  relative scale in parts-per-billion (ppb) [1]. A few accurate measurements are also zoomed in as an inset plot.

ment comes to a point that only two methods (atomic  $h/M$  measurement and electron  $g - 2$  measurement) are able to reach parts-per-billion (ppb) level. It means the weighted average obtained by the Committee on Data for Science and Technology (CODATA) is heavily dominated by few available data entries. It's fairly important to have more measurement done at similar accuracy to avoid human errors. That's another purpose of our  $\alpha$  measurement. Atomic  $h/M$  - the quotient of the Planck constant and mass of atoms have been measured through atom interferometry technologies. Based on the formula of  $\alpha$  below, there are a few constants entering into the determination of  $\alpha$  through this methods.

$$\alpha^2 = \frac{hR_\infty}{m_e c} = \frac{R_\infty}{c} \frac{h}{M} \frac{M}{u} \frac{u}{m_e} \quad (1.5)$$

Here  $R_\infty$  is the Rydberg constant,  $M$  the mass of an atom,  $u$  atomic mass unit,  $h$  the Planck constant,  $m_e$  the mass of electron. In theory it can be any type of atoms. But limited by laser cooling technologies, alkali atoms, especially atoms like Rubidium and Cesium are most commonly used. The Rydberg constant is known to 0.0059 ppb accuracy through Hydrogen spectroscopy [1, 14]; the mass of electron, Rubidium atom as well as Cesium atom are also determined to 0.029 ppb, 0.075 ppb, 0.065 ppb accuracy in atomic mass unit  $u$  through Penning trap techniques [1, 15, 16, 17, 18]. The last remaining piece here is  $h/M$ . It is noted that the measurement of the Planck constant (12 ppb) and atomic mass in SI unit

(>10 ppb) are not as accurate as  $h/M$  measurement [1]. The best way to measure this piece is to measure it altogether in atom interferometry. Two groups in the world have demonstrated ppb level measurement of the fine-structure constant with this method. One is a group in Laboratoire Kastler Brossel (LKB), France lead by François Biraben and Saïda Guellati-Khélifa where  $\alpha$  was determined through Rubidium atom  $h/M$  measurement to 0.62 ppb accuracy [11]. The other is the predecessor of our group led by Dr. Chu in Stanford University and where a preliminary measurement of  $\alpha$  through Cesium atom  $h/M$  to 8.0 ppb accuracy was reported [12]. Recently in 2017 we have finished a new measurement of  $\alpha$  to 0.20 ppb accuracy [8].

In our experiment, what we directly measure is called recoil frequency of Cesium atom. It is defined as the frequency associated with the recoil energy of an atom when it absorbs a photon. i.e. quantitatively it is defined as

$$\hbar\omega_r = \frac{p^2}{2M} = \frac{\hbar^2 k^2}{2M} \quad (1.6)$$

where  $p = \hbar k$  is the momentum of photon, and  $M$  the mass of atom. The recoil frequency can be read out from phase measurement of atom interferometers. The wave number of laser  $k$  could be accurately measured by a frequency comb.  $h/M$  could thus be determined. The details of our measurement would be topics of the rest of the thesis.

## 1.4 Outline of this Thesis

Here is the outline of the rest of this thesis. The basic theory of atom interferometry technique in the context of our  $\alpha$  measurement will be introduced in chapter 2. Experiment setup and implementation can be found in chapter 3. The result of our recent  $\alpha$  measurement will be discussed in chapter 4 and 5. In chapter 4 we will mostly focus on sensitivity and statistical uncertainty of our measurement. And chapter 5 will be devoted to the systematic uncertainty analysis of our measurement. The conclusion and implication of this measurement compared with  $g - 2$  measurement would be discussed in chapter 6.

# Chapter 2

## Atom Interferometry

### 2.1 Basics of Atom Interferometry: an Analogy to Light Interferometry

Atom interferometer is a powerful tool for precision measurement. Since its invention, it has been used as an important tool for precision measurement of gravity [19, 20], gravity gradient [21, 22, 23, 24], inertial force [25, 26], photon recoil [11, 12, 8, 27], Newtonian gravitational constant [28, 29], microscopic mass [30]. It has also been used to test Einstein equivalence principle [31], local Lorentz invariance [32], general relativity [33, 34], dark energy [35, 36] and dark matter theories [8]. Its basic working principles are founded on wave-matter duality of quantum mechanics. Interference is one of the basic properties of wave. Both light and matter have interference phenomena. In this sense, matter wave interferometer is quite similar to its counterpart in light. Here we mostly focus on the most basic two-armed interferometer. Mach-Zehnder light interferometer is one of the typical examples,

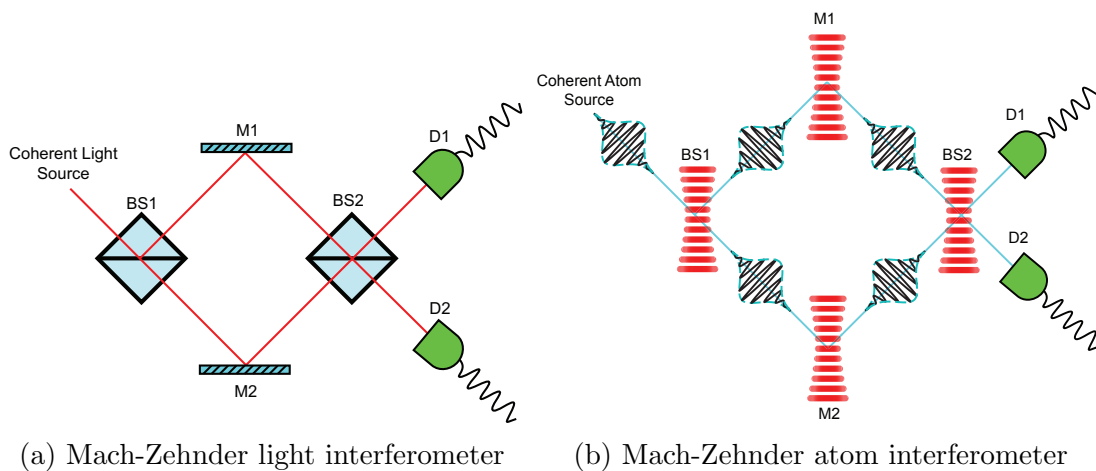


Figure 2.1: Analogy between the light interferometer and the atom interferometer

as shown in Figure 2.1 (a). It has a coherent light source, a beam splitter, two mirrors, a beam recombiner, detectors. (A beam recombiner is identical to a beam splitter as beam recombining is merely the reverse of beam splitting by the same device.) Coherent light from the source is spitted into two path by the first beam splitter. And then they are deflected by mirrors so they can intersect with each other again at the second beam splitter, where they recombine and mix with each other. Normally there are two output ports after the second beam splitter. We can set two detectors to detect the intensity of light (or count the number of photons) at two output ports. If we vary the length of either interferometer arm, variance of intensity at the output ports will be observed. And the intensity variation can be described by  $\cos^2(\Phi_d)$  where  $\Phi_d$  is the phase difference accumulated between two arms as light passing through. Here if we change the light source to atomic source, light beam-splitters to atomic beam-splitters, light mirrors to atom mirrors, light detectors to atom detectors, it's essentially an atom interferometer. Atom interferometry is based on the basic postulate of quantum mechanics: wave-particle duality. It asserts that all particles behave not only like particles but also like wave. There is no way to fully describe it in the classical concepts of particle and wave. We can send atom into the interferometer one by one. And they can be counted by the detector one by one. In the classical picture, a single atom can only go through either path 1 or 2. The count ratio at the detectors should only be dependent on the nature of the splitters. And a small change in one path locally shouldn't affect the other path. But experiments showed that the atom counts at detectors vary based on the phase difference between the two paths in a very similar way to the light interferometer. It shows the wave nature of atoms. In the picture of quantum mechanics, when an atom enters into the interferometer, it doesn't just go through a single path. It's like wave going through both paths at the same time though atom itself cannot be split into halves. If somehow by any means we can know which way the atom goes, quantum interference would be completely gone. The intrigue nature of quantum mechanics is that all quantum phenomena are based on the protection of "quantum-which-way information" from being leaked out. It is the essential key principle we will apply in Section 4.1 to discuss decoherence mechanism and ways to improve quantum coherence [37].

## 2.2 Phase Calculation of Atom Interferometry

In the last section, we described the nature of interference qualitatively. We mentioned that interference is related to phase difference between two arms. In this section, we will try to use a Mach-Zehnder atom interferometer shown in Figure 2.2 as an example to describe atom interferometry quantitatively. Assuming there is no decoherence, we can use wave functions to calculate the states throughout the entire interferometer. Suppose the initial state right before the beam splitter is  $|\psi_i\rangle$ . The beam splitter or mirror is essentially a unitary operator to rotate the state to a different orientation in Hilbert space. We denote the operator for beam splitters and mirrors are  $\hat{U}_{BS}$  and  $\hat{U}_M$  respectively. Detectors are defined as Hermitian operators  $\hat{O}_1$  and  $\hat{O}_2$  through which we can measure the expectation

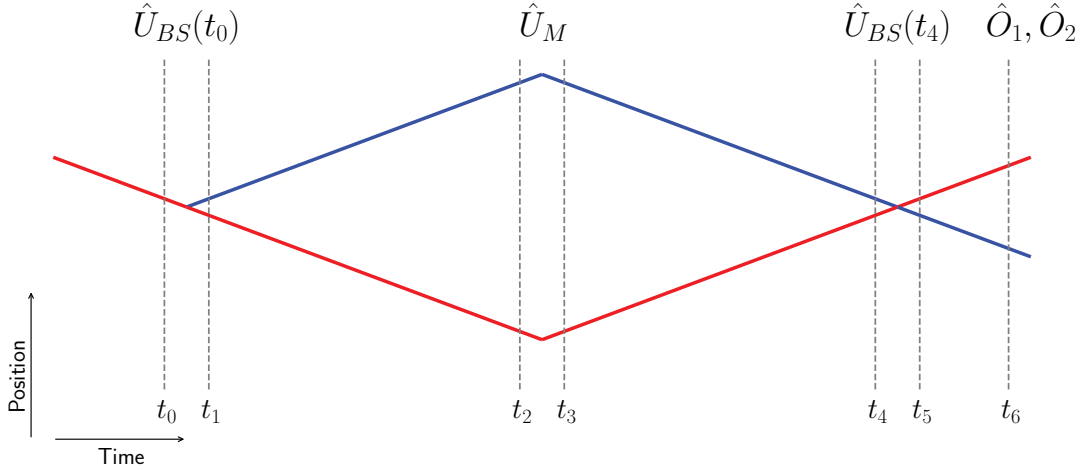


Figure 2.2: Mach-Zehnder Atom Interferometer

value of observables (counts at detector 1 and 2). And we can choose path 1 (colored red) and path 2 (colored blue) as basis of the system  $|1\rangle, |2\rangle$ . So the system can be simplified into such a basic quantum two-level system. At time  $t = t_0$ , the atom is at path 1. We can assume its wave function  $|\psi_i\rangle = |1\rangle$ . After passing through the first beam splitter, the overall wave function at time  $t = t_1$  becomes

$$|\Psi(t_1)\rangle = \hat{U}_{BS}(t_0) |1\rangle = \langle 1 | \hat{U}_{BS}(t_0) |1\rangle |1\rangle + \langle 2 | \hat{U}_{BS}(t_0) |1\rangle |2\rangle \quad (2.1)$$

From time  $t_1$  to time  $t_2$  the atom goes through free evolution  $\hat{U}_f^{12}$ .

$$|\Psi(t_2)\rangle = \hat{U}_f^{12} |\Psi(t_1)\rangle = \langle 1 | \hat{U}_f^{12} |1\rangle \langle 1 | \hat{U}_{BS}(t_0) |1\rangle |1\rangle + \langle 2 | \hat{U}_f^{12} |2\rangle \langle 2 | \hat{U}_{BS}(t_0) |1\rangle |2\rangle \quad (2.2)$$

Following this procedure, after going through mirror ( $\hat{U}_M$ ) and free evolution from  $t_3$  to  $t_4$  ( $\hat{U}_f^{34}$ ), we can get the wave function right before the second beam splitter as

$$|\Psi(t_4)\rangle = \langle 1 | \hat{U} |1\rangle \langle 1 | \hat{U}_{BS}(t_0) |1\rangle |1\rangle + \langle 2 | \hat{U} |2\rangle \langle 2 | \hat{U}_{BS}(t_0) |1\rangle |2\rangle \quad (2.3)$$

where  $\hat{U} = \hat{U}_f^{34} \hat{U}_M \hat{U}_f^{12}$  is the product of three operators along the path from the first beam splitter to the second beam splitter. At the second beam splitter two states would be mixed by this beam splitter operator,

$$\begin{pmatrix} \langle 1 | \Psi(t_5) \rangle \\ \langle 2 | \Psi(t_5) \rangle \end{pmatrix} = \begin{pmatrix} \langle 1 | \hat{U}_{BS}(t_4) |1\rangle & \langle 1 | \hat{U}_{BS}(t_4) |2\rangle \\ \langle 2 | \hat{U}_{BS}(t_4) |1\rangle & \langle 2 | \hat{U}_{BS}(t_4) |2\rangle \end{pmatrix} \begin{pmatrix} \langle 1 | \hat{U} |1\rangle \langle 1 | \hat{U}_{BS}(t_0) |1\rangle \\ \langle 2 | \hat{U} |2\rangle \langle 2 | \hat{U}_{BS}(t_0) |1\rangle \end{pmatrix} \quad (2.4)$$

i.e.

$$\langle 1|\Psi(t_5)\rangle = \langle 1|\hat{U}_{BS}(t_4)|1\rangle \langle 1|\hat{U}|1\rangle \langle 1|\hat{U}_{BS}(t_0)|1\rangle + \langle 1|\hat{U}_{BS}(t_4)|2\rangle \langle 2|\hat{U}|2\rangle \langle 2|\hat{U}_{BS}(t_0)|1\rangle \quad (2.5)$$

and

$$\langle 2|\Psi(t_5)\rangle = \langle 2|\hat{U}_{BS}(t_4)|1\rangle \langle 1|\hat{U}|1\rangle \langle 1|\hat{U}_{BS}(t_0)|1\rangle + \langle 2|\hat{U}_{BS}(t_4)|2\rangle \langle 2|\hat{U}|2\rangle \langle 2|\hat{U}_{BS}(t_0)|1\rangle \quad (2.6)$$

After that, there is no more mixing between the two states. The detector 1 only detects state  $|1\rangle$  and detector 2 detect state  $|2\rangle$ . So from  $t_5$  to  $t_6$  it only adds an common phase to both states that won't change the phase difference. If we ignore that free evolution phase, the observable detected at the detector 1 is

$$\langle \hat{O}_1 \rangle = \langle \Psi(t_5) | \hat{O}_1 | \Psi(t_5) \rangle = |\langle 1 | \Psi(t_5) \rangle|^2 \quad (2.7)$$

$$\begin{aligned} \langle \hat{O}_1 \rangle = & |\langle 1 | \hat{U}_{BS}(t_4) | 1 \rangle \langle 1 | \hat{U} | 1 \rangle \langle 1 | \hat{U}_{BS}(t_0) | 1 \rangle|^2 \\ & + |\langle 1 | \hat{U}_{BS}(t_4) | 2 \rangle \langle 2 | \hat{U} | 2 \rangle \langle 2 | \hat{U}_{BS}(t_0) | 1 \rangle|^2 \\ & + 2Re\left(\langle 1 | \hat{U}_{BS}(t_4) | 1 \rangle \langle 1 | \hat{U} | 1 \rangle \langle 1 | \hat{U}_{BS}(t_0) | 1 \rangle^* \langle 1 | \hat{U}_{BS}(t_4) | 2 \rangle \langle 2 | \hat{U} | 2 \rangle \langle 2 | \hat{U}_{BS}(t_0) | 1 \rangle\right) \end{aligned} \quad (2.8)$$

The first two terms contribute to a constant offset independent of phase variation. All the interference phenomena comes in through the third term. It depends on the phase difference between  $\langle 1 | \hat{U}_{BS}(t_4) | 1 \rangle \langle 1 | \hat{U} | 1 \rangle \langle 1 | \hat{U}_{BS}(t_0) | 1 \rangle$  and  $\langle 1 | \hat{U}_{BS}(t_4) | 2 \rangle \langle 2 | \hat{U} | 2 \rangle \langle 2 | \hat{U}_{BS}(t_0) | 1 \rangle$ . Likewise, the observable detected at the detector 2 can be calculated. This is the basic framework of atom interferometer phase calculation. More substances regarding how to calculate each operator will be filled in under specific contexts in subsequent sections.

## Beam Splitters and Atom Mirrors

In theory, beam splitters and atom mirrors could be essentially any special unitary operators in  $SU(2)$ . This is a group of all 2-dimensional unitary matrices with determinant  $+1$  to preserve chirality of the coordinates. It can be generated by identity matrix and three Pauli matrices. In analogy to rotation in real space where its quantum unitary transformation can be generally written as [38]

$$\hat{U}_{\hat{n}}(\theta) = e^{\frac{i}{\hbar} \hat{J}_{\hat{n}} \theta} = e^{i \frac{\theta}{2} (\hat{n} \cdot \vec{\sigma})} = I \cos\left(\frac{\theta}{2}\right) + i(\hat{n} \cdot \vec{\sigma}) \sin\left(\frac{\theta}{2}\right) \quad (2.9)$$

where  $\hat{n}$  is the unit vector of the axis along which rotation of angle  $\theta$  is performed.  $\hat{J}_{\hat{n}}$  is the 2-dimensional (spin- $\frac{1}{2}$ ) angular momentum operator

$$\hat{J}_{\hat{n}} = \frac{\hbar}{2} (\hat{n} \cdot \vec{\sigma}) \quad (2.10)$$

And the Pauli matrices  $\vec{\sigma}$  is given by

$$\sigma_x = \begin{pmatrix} 0 & 1 \\ 1 & 0 \end{pmatrix}, \quad \sigma_y = \begin{pmatrix} 0 & -i \\ i & 0 \end{pmatrix}, \quad \sigma_z = \begin{pmatrix} 1 & 0 \\ 0 & -1 \end{pmatrix} \quad (2.11)$$

So rotation along a general axis  $\vec{n} = (\sin \psi \cos \phi, \sin \psi \sin \phi, \cos \psi)$  by  $\theta$  can be described by the unitary transformation matrix

$$\hat{U}_{\vec{n}}(\theta) = \begin{pmatrix} \cos \theta + i \sin \theta \cos \psi & i \sin \theta \sin \psi e^{-i\phi} \\ i \sin \theta \sin \psi e^{i\phi} & \cos \theta - i \sin \theta \cos \psi \end{pmatrix} \quad (2.12)$$

Similarly a beam splitter is a rotation operator in the Hilbert space spanned by two paths of an interferometer. The general form of a beam splitter can be written in this way. In the context of atom interferometry, many types of beam splitters have been invented and implemented [39]. Among all these techniques, beam splitters by interacting with laser light is one of the most common and robust types. It is a pretty straightforward technique in atomic physics to use laser to drive atom transition in a two-level system. Considering a two-level atomic system in the electromagnetic fields  $\mathbf{E} = \mathbf{E}_0 \cos(\omega t - kz)$ , its Hamiltonian can be roughly written as [38, 40]

$$\hat{H} = \frac{\hat{\mathbf{P}}_{\text{COM}}^2}{2M} + \sum_i \left( \frac{(\hat{\mathbf{p}}_i - e\hat{\mathbf{A}})^2}{2m_e} + \hat{V}_i + \dots \right) \quad (2.13)$$

where  $P_{\text{COM}}$  is the center-of-mass momentum,  $M$  atomic mass,  $p_i$   $i$ th electron momentum,  $e$  electron charge,  $m_e$  electron mass,  $\mathbf{A}$  vector potential,  $V_i$  Coulomb potential of  $i$ th electron. The first term describes the center-of-mass motion of the atom, which determines external degrees of freedom for the atom. The second term describes electron dynamics inside the atom, which determines internal degrees of freedom of the atom. In the presence of electromagnetic wave, the momentum of charged particles like electron would be substitute by its canonical momentum. Under dipole approximation we can drop higher order terms of  $\hat{\mathbf{A}}$ , and approximate the  $\hat{\mathbf{A}} \cdot \hat{\mathbf{p}}_i$  term into  $\hat{\mathbf{x}}_i \cdot \hat{\mathbf{E}}$  [40]. After reducing the internal Hilbert space into a simplified two-level system of a ground state  $|g\rangle$  and an excited state  $|e\rangle$ , the Hamiltonian can be written as

$$H = \frac{\hat{\mathbf{P}}_{\text{COM}}^2}{2M} + \frac{\hbar}{2} \begin{pmatrix} -\omega_0 & \Omega_0 \cos(\omega t - kz) \\ \Omega_0 \cos(\omega t - kz) & \omega_0 \end{pmatrix} \quad (2.14)$$

where  $\hbar\omega_0$  is the internal energy level separation, and  $\Omega_0$  the Rabi frequency defined as

$$\Omega_0 = \sum_i \frac{-e\mathbf{x}_i \cdot \mathbf{E}_0}{\hbar}. \quad (2.15)$$

In fact, the atom external degree of freedom is coupled to the internal degree of freedom in this case. When the atom absorbs a photon, due to conservation of momentum, it has to

gain  $\hbar k$  momentum and change its external momentum state accordingly. So we can absorb the first term into the second term. Suppose the atom is initially at rest, after it absorb a photon, it would gain kinetic energy exactly by the amount of recoil energy  $\frac{\hbar^2 k^2}{2M}$ . So the external degrees of freedom can be couple to internal degree of freedom in the Hamiltonian,

$$H = \frac{\hbar}{2} \begin{pmatrix} -\omega_0 - \omega_r & \Omega_0 \cos(\omega t - kz) \\ \Omega_0 \cos(\omega t - kz) & \omega_0 + \omega_r \end{pmatrix} \quad (2.16)$$

where  $\omega_r$  is the recoil frequency defined as

$$\hbar\omega_r = \frac{\hbar^2 k^2}{2M} \quad (2.17)$$

In order to simplify calculation, we can apply a unitary transformation  $U$  to rotate the state  $|\Psi\rangle$  to the laser rotating frame.

$$|\tilde{\Psi}\rangle = U |\Psi\rangle = e^{-i\frac{\sigma_z}{2}(\omega t - kz)} |\Psi\rangle \quad (2.18)$$

Thus the Schrödinger equation

$$i\hbar \frac{\partial |\Psi\rangle}{\partial t} = H |\Psi\rangle \quad (2.19)$$

could be rewritten into the form

$$i\hbar(U^\dagger \frac{\partial |\tilde{\Psi}\rangle}{\partial t} - \frac{i\omega}{2}\sigma_z U^\dagger |\tilde{\Psi}\rangle) = H U^\dagger |\tilde{\Psi}\rangle \quad (2.20)$$

i.e.

$$i\hbar \frac{\partial |\tilde{\Psi}\rangle}{\partial t} = (U H U^\dagger - \frac{\hbar\omega}{2}\sigma_z) |\tilde{\Psi}\rangle \quad (2.21)$$

Under the new basis, the effective Hamiltonian becomes

$$\tilde{H} = \begin{pmatrix} \frac{1}{2}\hbar\delta & \hbar\Omega_0 \cos(\omega t - kz) e^{i(\omega t - kz)} \\ \hbar\Omega_0 \cos(\omega t - kz) e^{-i(\omega t - kz)} & -\frac{1}{2}\hbar\delta \end{pmatrix} \quad (2.22)$$

where the angular frequency difference between the laser and the internal energy splitting  $\delta = \omega - \omega_0 - \omega_r$  is called detuning. The cross terms could be further simplified as

$$\begin{aligned} \cos(\omega t - kz) e^{i(\omega t - kz)} &= \frac{1}{2}(1 + e^{i2(\omega t - kz)}) \\ \cos(\omega t - kz) e^{-i(\omega t - kz)} &= \frac{1}{2}(1 + e^{-i2(\omega t - kz)}) \end{aligned} \quad (2.23)$$

Since the laser frequency is way faster than the dynamics of this atomic transition, the  $e^{\pm i2\omega t}$  terms would be averaged to 0 at the time scale of atom dynamics. This approach is called



Rotating Wave Approximation (RWA) in atomic physics. After this step, we get a simplified Hamiltonian very much similar to a nuclear magnetic resonance (NMR) system [41].

$$\tilde{H} = \frac{\hbar}{2} \begin{pmatrix} \delta & \Omega_0 \\ \Omega_0 & -\delta \end{pmatrix} \quad (2.24)$$

It is exactly the case of a spin- $\frac{1}{2}$  system under the magnetic field along the direction  $\hat{n} = (\sin \psi, 0, \cos \psi)$  and  $\psi = \arctan(\Omega_0/\delta)$ . i.e.

$$\tilde{H} = \frac{\hbar}{2} (\hat{n} \cdot \vec{\sigma}) \sqrt{\delta^2 + \Omega_0^2} = \Omega_{\text{eff}} \hat{n} \cdot \hat{\mathbf{J}} (s = \frac{1}{2}) \quad (2.25)$$

where the effective Rabi frequency is defined as  $\sqrt{\delta^2 + \Omega_0^2}$ . The solution of this Hamiltonian is exactly the solution of Larmor precession. In this context, this phenomena is called Rabi flopping. We can get an evolution matrix similar to that of Larmor precession.

$$\tilde{U}_{\text{evo}} = e^{-\frac{i}{\hbar} H t} = e^{-i \frac{\hat{n} \cdot \hat{\mathbf{J}}}{\hbar} \Omega_{\text{eff}} t} = \begin{pmatrix} \cos(\frac{\Omega_{\text{eff}} t}{2}) - i \frac{\delta}{\Omega_{\text{eff}}} \sin(\frac{\Omega_{\text{eff}} t}{2}) & -i \frac{\Omega_0}{\Omega_{\text{eff}}} \sin(\frac{\Omega_{\text{eff}} t}{2}) \\ -i \frac{\Omega_0}{\Omega_{\text{eff}}} \sin(\frac{\Omega_{\text{eff}} t}{2}) & \cos(\frac{\Omega_{\text{eff}} t}{2}) + i \frac{\delta}{\Omega_{\text{eff}}} \sin(\frac{\Omega_{\text{eff}} t}{2}) \end{pmatrix} \quad (2.26)$$

Keep in mind that this evolution operator is under the new basis. In order to apply it to beam splitters and atom mirrors, we need to reverse the unitary transformation we did before. The new evolution matrix under the original basis would be

$$\begin{aligned} U_{\text{evo}} &= e^{-i \frac{\sigma_z}{2} (kz - \omega t)} \tilde{U}_{\text{evo}} e^{i \frac{\sigma_z}{2} (kz - \omega t)} \\ &= \begin{pmatrix} \cos(\frac{\Omega_{\text{eff}} \tau}{2}) - i \frac{\delta}{\Omega_{\text{eff}}} \sin(\frac{\Omega_{\text{eff}} \tau}{2}) & -i \frac{\Omega_0}{\Omega_{\text{eff}}} \sin(\frac{\Omega_{\text{eff}} \tau}{2}) e^{-i(kz - \omega t)} \\ -i \frac{\Omega_0}{\Omega_{\text{eff}}} \sin(\frac{\Omega_{\text{eff}} \tau}{2}) e^{i(kz - \omega t)} & \cos(\frac{\Omega_{\text{eff}} \tau}{2}) + i \frac{\delta}{\Omega_{\text{eff}}} \sin(\frac{\Omega_{\text{eff}} \tau}{2}) \end{pmatrix} \end{aligned} \quad (2.27)$$

where  $\tau$  is used here as the pulse duration to distinguish the absolute time  $t$  of the pulse in the transformation matrix. Note that all the model discussed above assumed a square pulse with duration  $\tau$ . For arbitrary pulses, under the adiabatic condition, we can use the integral of Rabi frequency over time to substitute the factor  $\Omega_{\text{eff}}$  instead.

The most common 50-50 beam splitter can be generated in the case when detuning  $\delta = 0$  and  $\Omega_0 \tau = \frac{\pi}{2}$  (called  $\frac{\pi}{2}$  pulse). In that case, the beam splitter operator would be simplified to

$$\hat{U}_{BS} = \begin{pmatrix} \frac{\sqrt{2}}{2} & -i \frac{\sqrt{2}}{2} e^{-i(kz - \omega t)} \\ -i \frac{\sqrt{2}}{2} e^{i(kz - \omega t)} & \frac{\sqrt{2}}{2} \end{pmatrix} \quad (2.28)$$

Similarly for an ideal atom mirror with 100% efficiency, the operator would be the case when  $\delta = 0$  and  $\Omega_0 \tau = \pi$

$$\hat{U}_M = \begin{pmatrix} 0 & -i e^{-i(kz - \omega t)} \\ -i e^{i(kz - \omega t)} & 0 \end{pmatrix} \quad (2.29)$$

It is to be noted that the basis we are using here is  $(|g\rangle, |e\rangle)$ , different from the basis we were using in the beginning of this section  $(|\text{path1}\rangle, |\text{path2}\rangle)$ . So when we apply it to the real case, we need to adjust the operator accordingly to match the state of each path.

## Free Evolution

During free evolution, the quantum state evolves under free particle Hamiltonian with the presence of gravity, i.e.

$$\hat{H} = \frac{\hat{P}^2}{2M} + mg\hat{z} \quad (2.30)$$

In the presence of gravity, the direct treatment through free particle quantum mechanics is not quite trivial. The free particle state is not an eigenstate of the Hamiltonian. It takes quite a bit efforts to calculate the free evolution phase in this way. In this context, another approach called Feynman's path integral works better. It's an equivalent but quite intuitive formulation of quantum mechanics. In order to evaluate the evolution from initial state  $|z_i, t_i\rangle$  to final state  $|z_f, t_f\rangle$ , the basic idea here is to slice the entire time period from  $t_i$  to  $t_f$  to multiple time slices and calculate the evolution during each slice and integrate them all together. Suppose the entire time is sliced into  $N$  slices equally, then

$$\begin{aligned} \langle z_f, t_f | U_f | z_i, t_i \rangle &= \int_{z_1=-\infty}^{\infty} dz_1 \int_{z_2=-\infty}^{\infty} dz_2 \dots \int_{z_{N-1}=-\infty}^{\infty} dz_{N-1} \langle z_f, t_f | e^{-i\frac{H\delta t}{\hbar}} | z_{N-1}, t_{N-1} \rangle \\ &\dots \langle z_2, t_2 | e^{-i\frac{H\delta t}{\hbar}} | z_1, t_1 \rangle \langle z_1, t_1 | e^{-i\frac{H\delta t}{\hbar}} | z_i, t_i \rangle \end{aligned} \quad (2.31)$$

where  $\delta t = (t_f - t_i)/N$  [38]. Feynman showed that when  $N \rightarrow \infty$  it is equivalent to the functional integral of all the path over the phase factor of the action.

$$\langle z_f, t_f | U_f | z_0, t_0 \rangle = \int_{z_0=z_i}^{z_N=z_f} \mathcal{D}z \exp \left[ \frac{i}{\hbar} S(z, \dot{z}) \right] \quad (2.32)$$

where the action  $S$  is defined as integral of Lagrangian over time,

$$S(z, \dot{z}) = \int dt L(z, \dot{z}) = \int dt (p\dot{z} - H) = \int dt \left( \frac{1}{2} m \dot{z}^2 - mgz \right) \quad (2.33)$$

If we integrate the path integral along its classical path where Euler-Lagrangian equation ( $\frac{d}{dt}(\frac{\partial L}{\partial \dot{z}}) - \frac{\partial L}{\partial z} = 0$ ) is satisfied, then the phase contribution from path deviated from the classical path would cause higher order oscillation, which only contributes to an amplitude factor, i.e.

$$\int_{z_0=z_i}^{z_N=z_f} \mathcal{D}z \exp \left[ \frac{i}{\hbar} S(z, \dot{z}) \right] = A \exp \left[ \frac{i}{\hbar} S_{cl}(z, \dot{z}) \right] \quad (2.34)$$

For most atom interferometer applications calculating the action along its classical paths is sufficient.

$$\hat{U}_f = \begin{pmatrix} e^{\frac{i}{\hbar} \int_{path1} dt (\frac{1}{2} m \dot{z}^2 - mgz)} & 0 \\ 0 & e^{\frac{i}{\hbar} \int_{path2} dt (\frac{1}{2} m \dot{z}^2 - mgz)} \end{pmatrix} \quad (2.35)$$

Ingredient	Matrix form in the current case under ideal conditions
$\hat{U}_{BS}(t_0)$	$\begin{pmatrix} \frac{\sqrt{2}}{2} & -i\frac{\sqrt{2}}{2}e^{-i(kz_0-\omega t_0)} \\ -i\frac{\sqrt{2}}{2}e^{i(kz_0-\omega t_0)} & \frac{\sqrt{2}}{2} \end{pmatrix}$
$\hat{U}_f$	$\begin{pmatrix} e^{\frac{i}{\hbar} \int_{path1} dt(\frac{1}{2}m\dot{z}^2 - mgz)} & 0 \\ 0 & e^{\frac{i}{\hbar} \int_{path2} dt(\frac{1}{2}m\dot{z}^2 - mgz)} \end{pmatrix}$
$\hat{U}_M(t_2)$	$\begin{pmatrix} -ie^{i(kz_2-\omega t_2)} & 0 \\ 0 & -ie^{-i(kz_2-\omega t_2)} \end{pmatrix}$
$\hat{U}_{BS}(t_4)$	$\begin{pmatrix} \frac{\sqrt{2}}{2} & -i\frac{\sqrt{2}}{2}e^{i(kz_4-\omega t_4)} \\ -i\frac{\sqrt{2}}{2}e^{-i(kz_4-\omega t_4)} & \frac{\sqrt{2}}{2} \end{pmatrix}$

Table 2.1: Ingredients for a simple Mach-Zehnder atom interferometer phase calculation

## A Simple Mach-Zehnder Atom Interferometer

Now we have the recipe ready to calculate the phase of the simple Mach-Zehnder (MZ) atom interferometer we started in the beginning of the section. Before starting, we need to add state labels in the original scheme to adjust the transformation matrix accordingly. The ground state is plotted with solid line and the excited state dash line. Here is a table to summarize all the ingredients we have. After applying all these formulas to this specific case, and categorizing phases into free evolution phase  $\phi_f$  accumulated through free evolution and laser phase  $\phi_\gamma$  accumulated at each laser pulse, we can get the final states

$$\langle 1|\Psi(t_5)\rangle = \frac{1}{2}(e^{i(\phi_{f1}+\phi_{\gamma 0}^{11}+\phi_{\gamma 2}^{11}+\phi_{\gamma 4}^{11})} + e^{i(\phi_{f2}+\phi_{\gamma 0}^{21}+\phi_{\gamma 2}^{22}+\phi_{\gamma 4}^{12})}) \quad (2.36)$$

$$\langle 2|\Psi(t_5)\rangle = \frac{1}{2}(e^{i(\phi_{f1}+\phi_{\gamma 0}^{11}+\phi_{\gamma 2}^{11}+\phi_{\gamma 4}^{21})} + e^{i(\phi_{f2}+\phi_{\gamma 0}^{22}+\phi_{\gamma 2}^{22}+\phi_{\gamma 4}^{22})}) \quad (2.37)$$

$$(2.38)$$

where  $\phi_i$  is the free evolution phase through path  $i$ ;  $\phi_{\gamma i}^{kj}$  is the laser phase induced by a pulse (either a beam splitter or a mirror) at time  $t_i$  under which atom transition from path  $j$  to path  $k$ . So the detected signal at both detectors would be

$$\langle \hat{O}_1 \rangle = \frac{1}{2}(1 + \cos(\phi_{f1} + \phi_{\gamma 0}^{11} + \phi_{\gamma 2}^{11} + \phi_{\gamma 4}^{11} - \phi_{f2} - \phi_{\gamma 0}^{21} - \phi_{\gamma 2}^{22} - \phi_{\gamma 4}^{12})) = \frac{1}{2}(1 + \cos(\Delta\phi_1))$$

$$\langle \hat{O}_2 \rangle = \frac{1}{2}(1 + \cos(\phi_{f1} + \phi_{\gamma 0}^{11} + \phi_{\gamma 2}^{11} + \phi_{\gamma 4}^{21} - \phi_{f2} - \phi_{\gamma 0}^{22} - \phi_{\gamma 2}^{22} - \phi_{\gamma 4}^{22})) = \frac{1}{2}(1 + \cos(\Delta\phi_2))$$

In the end the most interesting information is in the phase difference  $\Delta\phi$ . Following this algebra and plug in specific parameter for the simple Mach-Zehnder atom interferometer shown in Figure 2.2, the phase difference could be calculated as

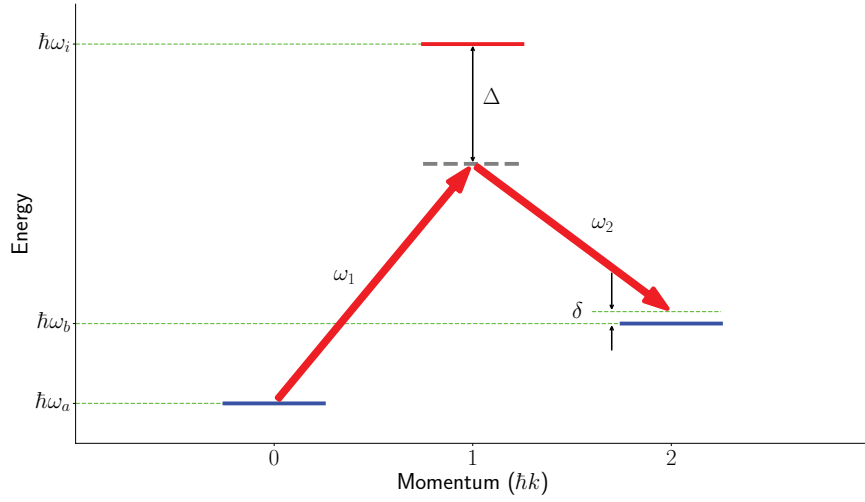
$$\Delta\phi_1 = \pi + kgT^2 \text{ and } \Delta\phi_2 = kgT^2 \quad (2.39)$$

We see that Mach Zehnder atom interferometer is very useful to measure gravity precisely, as will be used in this experiment to measure gravity gradient in Section 2.6 and 5.2.

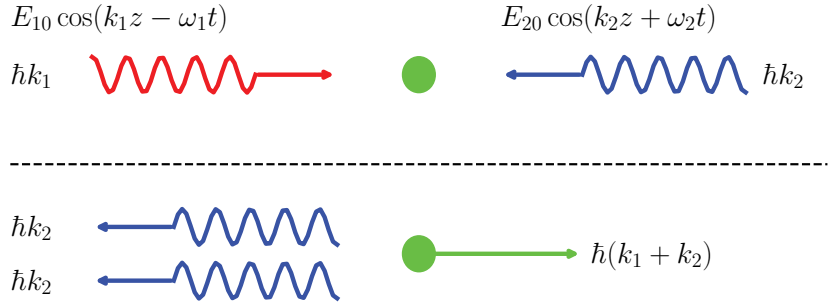
## 2.3 Raman Transition Beam Splitter

In the previous section, we discussed the simple Mach-Zehnder atom interferometry under ideal condition where a single photon transition is used as a beam splitter to achieve the ideal 50-50 beam-splitting and 100% efficiency atom mirror. But this kind of scenario doesn't really exist in most of the experiments. In the real case of atoms, it is limited by very short excited state lifetime. Take Cesium for example, the lifetime of its D2 transition ( $6^2S_{1/2} \rightarrow 6^2P_{3/2}$ ) is only about 30 ns [42], which means we have to close the atom interferometer before spontaneous emission happens. Otherwise when spontaneous emission happens, atom itself gives away its quantum information so there would be no interference. In order to extend coherence time, we have to choose an excited state with long lifetime. For conventional alkali atoms, a good option would be to use a different hyperfine state as the excited state. But it's impossible to drive a single photon transition from a hyperfine state to another one since it's dipole forbidden. That's also the reason why it has long lifetime. But a technique called Raman transition allows it to happen with a two-photon process. It couples one hyperfine state through some dipole allowed excited states (virtual states) as bridges to another hyperfine state as illustrated in Figure 2.3 (a). However, it doesn't mean it's impossible to operate single-photon transition atom interferometer. Recent development in Strontium cooling and trapping and optical atomic clock technologies makes it possible to do single-photo-transition atom interferometry with its super-narrow-linewidth clock transition. It has promising applications for space-based atom interferometer [43]. But it's beyond the scope of the thesis. For most of the thesis we will be only focusing on Raman transition and Bragg diffraction as will be introduced later as tools for beam splitting. In this section particular, we will be discussing the dynamics of atom in two counter-propagating laser beams with specially chosen frequencies as shown in Figure 2.3 (b), as well as how it can be used as a beam splitter for atom interferometer. Consider two counter-propagating laser fields  $\mathbf{E}_1 = \mathbf{E}_{10} \cos(k_1z - \omega_1t)$  and  $\mathbf{E}_2 = \mathbf{E}_{20} \cos(k_2z + \omega_2t)$  to drive Raman transition between the first hyperfine ground state  $|g_a\rangle$  and the second hyperfine ground state  $|g_b\rangle$  via the intermediate excited state  $|i\rangle$ . The frequencies are chosen to be very far-detuned from resonate with any excited state. Following the similar procedure of two-level system, we start with the Hamiltonian with light-atom interaction terms [44, 45]:

$$\hat{H}_{\text{Raman}} = \frac{\hat{\mathbf{P}}_{\text{COM}}^2}{2M} + \begin{pmatrix} \hbar\omega_a & 0 & -\mathbf{d} \cdot (\mathbf{E}_1 + \mathbf{E}_2) \\ 0 & \hbar\omega_b & -\mathbf{d} \cdot (\mathbf{E}_1 + \mathbf{E}_2) \\ -\mathbf{d} \cdot (\mathbf{E}_1 + \mathbf{E}_2) & -\mathbf{d} \cdot (\mathbf{E}_1 + \mathbf{E}_2) & \hbar\omega_i \end{pmatrix} \quad (2.40)$$



(a) Raman transition energy-momentum diagram



(b) Effects of Raman transition on atomic motion

Figure 2.3

where  $\hbar\omega_a$ ,  $\hbar\omega_b$  and  $\hbar\omega_i$  are internal energy levels of the three states and the basis of the system chosen to be  $\{|a\rangle, |b\rangle, |i\rangle\}$ . Similarly we can define Rabi frequencies as

$$\hbar\Omega_{1a} = \langle i | -\mathbf{d} \cdot \mathbf{E}_{10} | g_a \rangle \quad (2.41)$$

$$\hbar\Omega_{2a} = \langle i | -\mathbf{d} \cdot \mathbf{E}_{20} | g_a \rangle \quad (2.42)$$

$$\hbar\Omega_{1b} = \langle i | -\mathbf{d} \cdot \mathbf{E}_{10} | g_b \rangle \quad (2.43)$$

$$\hbar\Omega_{2b} = \langle i | -\mathbf{d} \cdot \mathbf{E}_{20} | g_b \rangle \quad (2.44)$$

Under this Hamiltonian, we can write down Schrödinger equations as

$$i\hbar \frac{\partial \langle i | \psi \rangle}{\partial t} = \frac{\hat{\mathbf{P}}_{\text{COM}}^2}{2M} + \hbar\omega_i \langle i | \psi \rangle + (\hbar\Omega_{1a} \cos(k_1 z - \omega_1 t) + \hbar\Omega_{2a} \cos(k_2 z + \omega_2 t)) \langle g_a | \psi \rangle + (\hbar\Omega_{1b} \cos(k_1 z - \omega_1 t) + \hbar\Omega_{2b} \cos(k_2 z + \omega_2 t)) \langle g_b | \psi \rangle \quad (2.45)$$

$$i\hbar \frac{\partial \langle g_a | \psi \rangle}{\partial t} = \frac{\hat{\mathbf{P}}_{\text{COM}}^2}{2M} + \hbar\omega_a \langle g_a | \psi \rangle + (\hbar\Omega_{1a} \cos(k_1 z - \omega_1 t) + \hbar\Omega_{2a} \cos(k_2 z + \omega_2 t)) \langle i | \psi \rangle \quad (2.46)$$

$$i\hbar \frac{\partial \langle g_b | \psi \rangle}{\partial t} = \frac{\hat{\mathbf{P}}_{\text{COM}}^2}{2M} + \hbar\omega_b \langle g_b | \psi \rangle + (\hbar\Omega_{1b} \cos(k_1 z - \omega_1 t) + \hbar\Omega_{2b} \cos(k_2 z + \omega_2 t)) \langle i | \psi \rangle \quad (2.47)$$

For simplicity, we can shift the overall energy by  $-\hbar\omega_i - \hbar(\omega_1 - \omega_i + \omega_a)$  and apply the similar unitary transformation to rotate the basis to its "laser rotating frame"

$$(|\tilde{g}_a\rangle, |\tilde{g}_b\rangle, |i\rangle) = (|g_a\rangle, |g_b\rangle, |i\rangle) \begin{pmatrix} e^{i\omega_1 t} & 0 & 0 \\ 0 & e^{i\omega_2 t} & 0 \\ 0 & 0 & 1 \end{pmatrix} \quad (2.48)$$

There would be terms associated with fast oscillation at frequency  $2\omega_1$ ,  $2\omega_2$  and  $\omega_1 + \omega_2$ . Based on rotating wave approximation (RWA), these fast dynamics will be averaged to zero at a slower time scale. So the Schrödinger equations can be simplified in the new basis as

$$i\hbar \frac{\partial \langle i | \psi \rangle}{\partial t} = \frac{\hat{\mathbf{P}}_{\text{COM}}^2}{2M} - \hbar\Delta_{1ai} \langle i | \psi \rangle + \frac{\hbar\Omega_{1a}}{2} e^{ik_1 z} \langle \tilde{g}_a | \psi \rangle + \frac{\hbar\Omega_{2b}}{2} e^{-ik_2 z} \langle \tilde{g}_b | \psi \rangle \quad (2.49)$$

$$i\hbar \frac{\partial \langle \tilde{g}_a | \psi \rangle}{\partial t} = \frac{\hat{\mathbf{P}}_{\text{COM}}^2}{2M} + \frac{\hbar\Omega_{1a}}{2} e^{-ik_1 z} \langle i | \psi \rangle \quad (2.50)$$

$$i\hbar \frac{\partial \langle \tilde{g}_b | \psi \rangle}{\partial t} = \frac{\hat{\mathbf{P}}_{\text{COM}}^2}{2M} + \hbar(\Delta_{2bi} - \Delta_{1ai}) \langle g_b | \psi \rangle + \frac{\hbar\Omega_{2b}}{2} e^{ik_2 z} \langle i | \psi \rangle \quad (2.51)$$

where we define the detuning  $\Delta_{1ai} = \omega_1 - (\omega_i - \omega_a)$  and  $\Delta_{2bi} = \omega_2 - (\omega_i - \omega_b)$ .

Since the laser is far-detuned from resonating with the excited state, mathematically it means the detuning  $\Delta_{1ai} \gg$  Rabi frequencies  $\Omega_{1a}, \Omega_{2b}$  and the recoil frequency  $\omega_r$ . Consider the dynamics of the excited state under the equation (2.49). From the basic picture of the two-level system, we know the excited state will be undergoing a very fast "Larmor precession" and a much slower population exchange with ground states. So what the ground states see at the slower dynamics is only the average value of  $\langle i | \psi \rangle$ . It means if we solve the problem only for the slower dynamics, we can approximately consider the excited state as "stationary". i.e.

$$0 = i\hbar \frac{\partial \langle i | \psi \rangle}{\partial t} = -\hbar\Delta_{1ai} \langle i | \psi \rangle + \frac{\hbar\Omega_{1a}}{2} e^{ik_1 z} \langle \tilde{g}_a | \psi \rangle + \frac{\hbar\Omega_{2b}}{2} e^{-ik_2 z} \langle \tilde{g}_b | \psi \rangle \quad (2.52)$$

This process is called adiabatic elimination through which faster and irrelevant dynamics can be adiabatically eliminated. Based on the previous equation, the average value of  $\langle i | \psi \rangle$  could be solved and substituted into original equations.

$$\langle i | \psi \rangle_{\text{ave}} = \frac{\frac{\hbar\Omega_{1a}}{2} e^{ik_1 z} \langle \tilde{g}_a | \psi \rangle + \frac{\hbar\Omega_{2b}}{2} e^{-ik_2 z} \langle \tilde{g}_b | \psi \rangle}{\hbar\Delta_{1ai}} \quad (2.53)$$

Then the effective Hamiltonian could be written as

$$\begin{aligned} H_{\text{eff}} = & \frac{\hat{\mathbf{P}}_{\text{COM}}^2}{2M} + \hbar\omega_{ACa} |\tilde{g}_a\rangle \langle \tilde{g}_a| + \hbar(\Delta_{2bi} - \Delta_{1ai} + \omega_{ACb}) |\tilde{g}_b\rangle \langle \tilde{g}_b| \\ & + \frac{\Omega_0}{2} e^{-i(k_1+k_2)z} |\tilde{g}_a\rangle \langle \tilde{g}_b| + \frac{\Omega_0}{2} e^{i(k_1+k_2)z} |\tilde{g}_b\rangle \langle \tilde{g}_a| \end{aligned} \quad (2.54)$$

where the effective two-photon Rabi frequency  $\Omega_0$  is defined as

$$\Omega_0 = \frac{\Omega_{1a}\Omega_{2b}}{\Delta_{1ai}} \quad (2.55)$$

and the two-photon AC Stark shift as

$$\omega_{ACa} = \frac{\Omega_{1a}^2}{4\Delta_{1ai}} \quad (2.56)$$

$$\omega_{ACb} = \frac{\Omega_{2b}^2}{4\Delta_{1ai}} \quad (2.57)$$

Essentially it becomes a two-level system again. An atom in the state  $|g_a\rangle$  could absorb a photon from laser field  $\mathbf{E}_1$  and simultaneously stimulated emit another photon into laser field  $\mathbf{E}_2$ . As a result, the atom would be transferred into the state  $|g_b\rangle$  and gain a momentum of  $\hbar(k_1 + k_2)$  due to conservation of momentum. In the same way, an atom in the state  $|g_b\rangle$  could transition into  $|g_a\rangle$  and lose a momentum of  $\hbar(k_1 + k_2)$ . The external momentum states are thus coupled to the internal states. So we can label the two states as  $|g_a, P_{\text{COM}}\rangle$  and  $|g_b, P_{\text{COM}} + 2\hbar k\rangle$  where  $k$  is defined as  $k = (k_1 + k_2)/2$ . So we can evaluate the external kinetic energy term and get the final Hamiltonian after proper shifting of global energy level,

$$\tilde{H}_{\text{eff}} = -\frac{1}{2}\hbar\delta |\tilde{g}_a, P_{\text{COM}}\rangle \langle \tilde{g}_a, P_{\text{COM}}| + \frac{1}{2}\hbar\delta |\tilde{g}_b, P_{\text{COM}} + 2\hbar k\rangle \langle \tilde{g}_b, P_{\text{COM}} + 2\hbar k| \quad (2.58)$$

$$+ \frac{\Omega_0}{2} e^{-i2kz} |\tilde{g}_a, P_{\text{COM}}\rangle \langle \tilde{g}_b, P_{\text{COM}} + 2\hbar k| + \frac{\Omega_0}{2} e^{i2kz} |\tilde{g}_b, P_{\text{COM}} + 2\hbar k\rangle \langle \tilde{g}_a, P_{\text{COM}}| \quad (2.59)$$

where the two-photon detuning  $\delta$  is defined as

$$\delta = \Delta_{2bi} - \Delta_{1ai} + \omega_{ACb} - \omega_{ACa} + \frac{(P_{\text{COM}} + 2\hbar k)^2}{2M\hbar} - \frac{P_{\text{COM}}^2}{2M\hbar} \quad (2.60)$$

The Hamiltonian then in its original basis can be written as

$$\hat{H}_{\text{Raman, eff}} = \frac{\hbar}{2} \begin{pmatrix} -\delta & \Omega_0 e^{-i(2kz - (\omega_1 - \omega_2)t)} \\ \Omega_0 e^{i(2kz - (\omega_1 - \omega_2)t)} & \delta \end{pmatrix} \quad (2.61)$$

So the general evolution matrix under Raman transition would follow the form as in the two-level system,

$$U_{\text{evo}}(\tau) = \begin{pmatrix} \cos(\frac{\Omega_{\text{eff}}\tau}{2}) + i\frac{\delta}{\Omega_{\text{eff}}}\sin(\frac{\Omega_{\text{eff}}\tau}{2}) & -i\frac{\Omega_0}{\Omega_{\text{eff}}}\sin(\frac{\Omega_{\text{eff}}\tau}{2})e^{-i(2kz - (\omega_1 - \omega_2)t)} \\ -i\frac{\Omega_0}{\Omega_{\text{eff}}}\sin(\frac{\Omega_{\text{eff}}\tau}{2})e^{i(2kz - (\omega_1 - \omega_2)t)} & \cos(\frac{\Omega_{\text{eff}}\tau}{2}) - i\frac{\delta}{\Omega_{\text{eff}}}\sin(\frac{\Omega_{\text{eff}}\tau}{2}) \end{pmatrix} \quad (2.62)$$

where  $\tau$  is the pulse duration and  $\Omega_{\text{eff}}$  is defined as  $\Omega_{\text{eff}} = \sqrt{\Omega_0^2 + \delta^2}$ . The most simple 50-50 beam splitter would be modified to

$$\hat{U}_{BS} = \begin{pmatrix} \frac{\sqrt{2}}{2} & -i\frac{\sqrt{2}}{2}e^{-i(2kz - (\omega_1 - \omega_2)t)} \\ -i\frac{\sqrt{2}}{2}e^{i(2kz - (\omega_1 - \omega_2)t)} & \frac{\sqrt{2}}{2} \end{pmatrix} \quad (2.63)$$

With this type of beam splitter, the phase difference read out by a Mach-Zehnder interferometer would be modified accordingly to

$$\Delta\phi_{MZ} = 2kgT^2 \quad (2.64)$$

## 2.4 Bragg Diffraction Beam Splitter

Raman transition has been very successfully applied and becomes one of the most popular beam splitting techniques in atom interferometry. But as the demands for the precision and accuracy is higher and higher, Raman transition starts to fall short in many ways. First of all, Raman transition always deals with two different electronic states which normally contributes to AC Stark shift differently. So in the real atom interferometry measurement, differential AC Stark shift would be a significant source of systematic uncertainty. And it depends on laser power and detuning, so it's quite hard to monitor and control it to a very precise level. Secondly, Raman transition is only a two-photon transition so the total phase is only gained by a factor of 2 compared with the single-photon atom interferometer. But is there a way to boost momentum transfer at each beam splitter so the overall sensitivity would be improved significantly? The answer is yes. Back in 2000s, the group led by Dr. Chu who first implemented Raman transition into atom interferometry [20] again pioneered the quest into large momentum transfer atom interferometry techniques [46, 47]. The technique they started investigating is called Bragg diffraction. The term Bragg diffraction was originally used to describe constructive interference of x-ray diffraction on a periodic lattice structure. But the idea could be extended to constructive interference of any wave scattered by a periodic structure. Compared with Raman transition, it drives the transition from one momentum state to another within the same electronic state of atoms. And it enables momentum transfer to exceed  $2\hbar k$  set by Raman transition. The scenario is quite similar to Raman transition. Consider two counter-propagating laser fields  $\mathbf{E}_1 = \mathbf{E}_{10} \cos(k_1 z - \omega_1 t)$  and  $\mathbf{E}_2 = \mathbf{E}_{20} \cos(k_2 z + \omega_2 t)$  to form optical lattices to drive Bragg diffraction as shown in Figure 2.4. The frequencies here are chosen to be very far-detuned from any resonance as well. But the two-photon detuning is quite different from that in Raman transition. Assume the atom wave function is defined as

$$|\psi\rangle = g(z, t) |g\rangle + e(z, t) |e\rangle \quad (2.65)$$

Following the similar procedure, we can start with the Hamiltonian [46]

$$\hat{H}_{\text{Bragg}} = \frac{\hat{\mathbf{P}}_{\text{COM}}^2}{2M} + \begin{pmatrix} 0 & \hbar\Omega_1 \cos(k_1 z - \omega_1 t) + \hbar\Omega_2 \cos(k_2 z + \omega_2 t) \\ \hbar\Omega_1 \cos(k_1 z - \omega_1 t) + \hbar\Omega_2 \cos(k_2 z + \omega_2 t) & \hbar\omega_0 \end{pmatrix} \quad (2.66)$$

under the similar definitions of Rabi frequencies

$$\hbar\Omega_1 = \langle e | -\mathbf{d} \cdot \mathbf{E}_{10} | g \rangle \quad (2.67)$$

$$\hbar\Omega_2 = \langle e | -\mathbf{d} \cdot \mathbf{E}_{20} | g \rangle \quad (2.68)$$

After rotating the original state to its "laser rotating frame" by the unitary transformation below and applying appropriate Rotating Wave Approximation (RWA), the Hamiltonian will be simplified to

$$\tilde{H}_{\text{Bragg}} = \frac{\hat{\mathbf{P}}_{\text{COM}}^2}{2M} + \frac{\hbar}{2} \begin{pmatrix} 0 & \Omega_1 e^{i(-\frac{\delta}{2}t + k_1 z)} + \Omega_2 e^{i(\frac{\delta}{2}t - k_2 z)} \\ \Omega_1 e^{i(\frac{\delta}{2}t - k_1 z)} + \Omega_2 e^{i(-\frac{\delta}{2}t + k_2 z)} & -2\Delta \end{pmatrix} \quad (2.69)$$



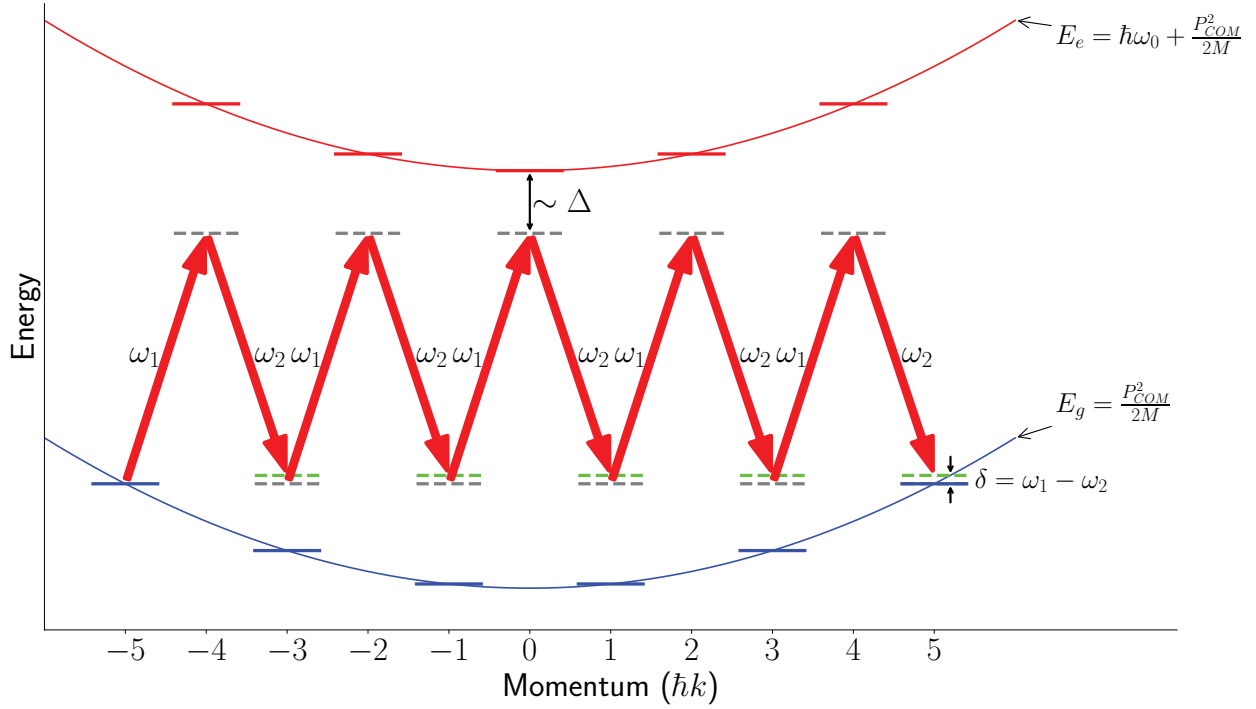


Figure 2.4: Energy-momentum diagram for a 5th order Bragg diffraction. The initial velocity is taken to be  $-5\hbar k$ .

where the new basis is chosen to be

$$(|\tilde{g}\rangle, |\tilde{e}\rangle) = (|g\rangle, |e\rangle) \begin{pmatrix} e^{-i\frac{(\omega_1+\omega_2)t}{2}} & 0 \\ 0 & e^{i\frac{(\omega_1+\omega_2)t}{2}} \end{pmatrix} \quad (2.70)$$

The two-photon detuning  $\delta$  here is defined as  $\delta = \omega_1 - \omega_2$  and the single photon detuning  $\Delta = (\omega_1 + \omega_2)/2 - \omega_0$ . The Schrödinger equations for the wave function of each state are given as

$$i\hbar \frac{\partial}{\partial t} e(z, t) = -\frac{\hbar^2}{2M} \frac{\partial^2}{\partial z^2} e(z, t) + \frac{\hbar}{2} (\Omega_1 e^{i(\frac{\delta}{2}t - k_1 z)} + \Omega_2 e^{i(-\frac{\delta}{2}t + k_2 z)}) g(z, t) - \hbar \Delta e(z, t) \quad (2.71)$$

$$i\hbar \frac{\partial}{\partial t} g(z, t) = -\frac{\hbar^2}{2M} \frac{\partial^2}{\partial z^2} g(z, t) + \frac{\hbar}{2} (\Omega_1 e^{i(-\frac{\delta}{2}t + k_1 z)} + \Omega_2 e^{i(\frac{\delta}{2}t - k_2 z)}) e(z, t) \quad (2.72)$$

In the regime of large single-photon detuning  $\Delta \gg \Omega \gg \omega_r$ , adiabatic elimination could be applied in the same way, i.e.  $(\partial/\partial t)e(z, t) = 0$ . The average value of  $e(z, t)$  at a slower time scale would be

$$e(z, t)_{\text{ave}} = \frac{\Omega_1 e^{i(\frac{\delta}{2}t - k_1 z)} + \Omega_2 e^{i(-\frac{\delta}{2}t + k_2 z)}}{2\Delta} g(z, t) \quad (2.73)$$

It simplified the question to a single Schrödinger equation

$$i\frac{\partial}{\partial t}g(z, t) = -\frac{\hbar}{2M}\frac{\partial^2}{\partial z^2}g(z, t) + \frac{\Omega_1^2 + \Omega_2^2 + 2\Omega_1\Omega_2 \cos(\delta t - (k_1 + k_2)z)}{4\Delta}g(z, t). \quad (2.74)$$

According to Bloch's theorem, the energy eigenfunction of Hamiltonian in a periodic potential can be written as a Bloch wave, which is the product of a periodic function and a plane wave, namely

$$\psi_n(\mathbf{r}) = e^{i\mathbf{k}_q \cdot \mathbf{r}} u_{n, \mathbf{k}_q}(\mathbf{r}) \quad (2.75)$$

The ground state wave function could thus be expanded as a sum of Fourier series

$$g(z, t) = e^{ik_q z} \sum_{m=-\infty}^{\infty} g_m(t) e^{2imkz} \quad (2.76)$$

where  $k_q$  is the quasi-wave number and  $k = (k_1 + k_2)$  is the effective wave number. It could be written as a series of coupled differential equations for each  $g_m$  component.

$$i\dot{g}_m(t) = \frac{\hbar(k_q + 2mk)^2}{2M}g_m(t) + \omega_{AC}g_m(t) + \frac{\Omega}{2}(e^{-i\delta t}g_{m-1}(t) + e^{i\delta t}g_{m+1}(t)) \quad (2.77)$$

where the quasi-wave vector  $k_q$  is restricted in the first Brillouin zone  $[-k, k]$ . Each Fourier component  $g_m(t)$  represents a momentum state with momentum  $\hbar(k_q + 2mk)$ . Equations (2.77) is essentially a series of infinite Schrödinger equations of each momentum state with potential energy given by a common AC Stark shift  $\omega_{AC}$  and hopping interaction by the two-photon Rabi frequency  $\Omega$ . The hopping can only happen between nearest momentum states separated by  $2\hbar k$ . Here  $\omega_{AC}$  and  $\Omega$  are defined as [46]

$$\omega_{AC} = \frac{\Omega_1^2 + \Omega_2^2}{4\Delta}. \quad (2.78)$$

$$\Omega = \frac{\Omega_1\Omega_2}{2\Delta}. \quad (2.79)$$

## Analytic Solution

In order to obtain an analytical solution, certain approximations are required. There are two commonly used approximations in this context.

### Raman-Nath Regime

When the pulse length is quite short such that its frequency spread is larger than recoil frequency scale, i.e.  $1/\tau \gg \omega_r$ , the kinetic energy difference between different momentum state would be unimportant. Under that condition, we can just simplify the equation to be

$$i\dot{g}_m(t) = \frac{\Omega}{2}(g_{m-1}(t) + g_{m+1}(t)) \quad (2.80)$$

There is known solution to this differential equations [46].

$$g_m = (-i)^m J_m(\Omega t) \quad (2.81)$$

The initial condition is defined as  $g_0 = 1$  and  $g_{m \neq 0} = 0$  at  $t = 0$ . So after the pulse, the population in all momentum states would be symmetrically distributed based on the value of each order of Bessel function. This is not the regime commonly used for most large-momentum-transfer atom interferometers.

### Bragg Regime

Another approximation happens in Bragg regime in which the pulse is so long that its frequency spread would be very narrow. Unless conservation of momentum and energy are both strictly satisfied, no Bragg diffraction could happen. In this regime,  $\Omega$  would be typically small to keep  $\Omega\tau$  roughly the same. Mathematically it means  $\Omega \sim 1/\tau \ll m^2\omega_r$ . So we can apply the same technique of adiabatic elimination to eliminate far-detuned intermediate states. Consider the same situation as shown in Figure 2.3, where the state initially at  $|-n\hbar k\rangle$  is undergoing a  $n^{\text{th}}$  order Bragg diffraction to the final state  $|n\hbar k\rangle$ . It is resonant when  $\omega_1 = \omega_2$ . Note that the order  $n$  here is different from the subscription  $m$  in  $g_m$ . Depending on whether  $n$  is odd or even,  $k_q$  should be chosen as 0 or  $k$  to match resonance condition. For simplicity we will consider a new way to define the states as  $\tilde{g}_n$  where  $n$  means real momentum index. So in this new definition the Schrödinger equation reads

$$i\dot{\tilde{g}}_n(t) = n^2\omega_r\tilde{g}_n(t) + \frac{\Omega}{2}(\tilde{g}_{n-2}(t) + \tilde{g}_{n+2}(t)) \quad (2.82)$$

A hand waving way to solve this would be to break it into  $n$  "Raman transitions" and adiabatically eliminate each state successively. Suppose initially  $\tilde{g}_{-n} = 1$  and  $\tilde{g}_{k \neq -n} = 0$ . For each intermediate state  $k \neq \pm n$  we can assume  $\dot{\tilde{g}}_k(t) = 0$  and eliminate it one by one following the direction of the population transfer. Thus we have simplified equations (the overall energy shifted by  $-n^2\hbar\omega_r$ )

$$i\dot{\tilde{g}}_{-n}(t) = \frac{\Omega}{2}(\tilde{g}_{-n+2}(t)) \quad (2.83)$$

$$i\dot{\tilde{g}}_{-n+2}(t) = (4 - 4n)\omega_r\tilde{g}_{-n+2}(t) + \frac{\Omega}{2}(\tilde{g}_{-n}(t)) = 0 \quad (2.84)$$

...

$$i\dot{\tilde{g}}_{n-2}(t) = (4 - 4n)\omega_r\tilde{g}_{n-2}(t) + \frac{\Omega}{2}(\tilde{g}_{n-4}(t)) = 0 \quad (2.85)$$

$$i\dot{\tilde{g}}_n(t) = \frac{\Omega}{2}(\tilde{g}_{n-2}(t)) \quad (2.86)$$

$$(2.87)$$

This problem could be simplified to a simple two-level system again with the Schrödinger equation

$$i\hbar\dot{\tilde{g}}_{-n}(t) = \frac{1}{2}\hbar\Omega_{\text{eff}}\tilde{g}_n \quad (2.88)$$

$$i\hbar\dot{\tilde{g}}_n(t) = \frac{1}{2}\hbar\Omega_{\text{eff}}\tilde{g}_{-n} \quad (2.89)$$

and effective Rabi frequency [46]

$$\Omega_{\text{eff}} = \frac{\Omega^n}{(8\omega_r)^{n-1} [(n-1)!]^2}. \quad (2.90)$$

So after including the Fourier phase factor, the general matrix form for nth order Bragg beam splitter in Bragg regime could be written as

$$\hat{U}_{BS} = \begin{pmatrix} \cos(\frac{1}{2}\Omega_{\text{eff}}\tau) & -i\sin(\frac{1}{2}\Omega_{\text{eff}}\tau)e^{-i2nkz} \\ -i\sin(\frac{1}{2}\Omega_{\text{eff}}\tau)e^{i2nkz} & \cos(\frac{1}{2}\Omega_{\text{eff}}\tau) \end{pmatrix} \quad (2.91)$$

One can perform Lorentz transformation to shift it to a general reference frame.

## Numerical Solution

Realistically speaking, neither of the approximations above really describes the real beam splitter we are using in the experiment. Firstly, the real Bragg pulse is between the Raman-Nath regime and the Bragg regime. The approximation isn't sufficient at the precision required by the experiment. Secondly, a square Bragg pulse doesn't quite work in the experiment. The Fourier spectrum of a square pulse is a sinc function, which produces significant sideband that drives unwanted transitions unless the pulse length is unrealistically long. In the experiment we use a Gaussian pulse to generate Bragg diffraction, which gives a clean Gaussian spectrum in the frequency domain. It's more convenient to use numerical method to study Bragg diffraction under realistic experimental conditions. In the experiment we use truncated Gaussian from  $-3\sigma$  to  $3\sigma$  to drive Bragg diffraction. The real pulse shape is obtained through intensity servo so there is certain amount distortion. By adjusting the lockbox settings, we can achieve the optimal pulse shape as shown in Figure 5.7. In theory we can put arbitrary pulse shape into the program to generate the beam splitter matrix. But in this section only the ideal truncated Gaussian waveform would be used in the calculation and discussion. For the real pulse form, it would be discussed under the chapter for systematic uncertainties. For simplicity, numerical calculation is generally done through a dimensionless form of the equation. After rescaling the time in the unit of  $\omega_r^{-1}$ , the equation becomes

$$i\frac{\partial g_m(\tau)}{\partial \tau} = (m_0 + 2m)^2 g_m(\tau) + \alpha g_m(\tau) + \beta(e^{-i\delta'\tau} g_{m-1}(\tau) + e^{i\delta'\tau} g_{m+1}(\tau)) \quad (2.92)$$

where  $k_q = m_0 k$ ,  $t = \omega_r^{-1}\tau$ ,  $\alpha\omega_r = \omega_{AC}$ ,  $\beta\omega_r = \frac{\Omega}{2}$ ,  $\delta' = \delta\omega_r^{-1} = (\omega_1 - \omega_2)\omega_r^{-1}$ . Note that it is the general form of equation with non-zero laser detuning taken into account. Normally

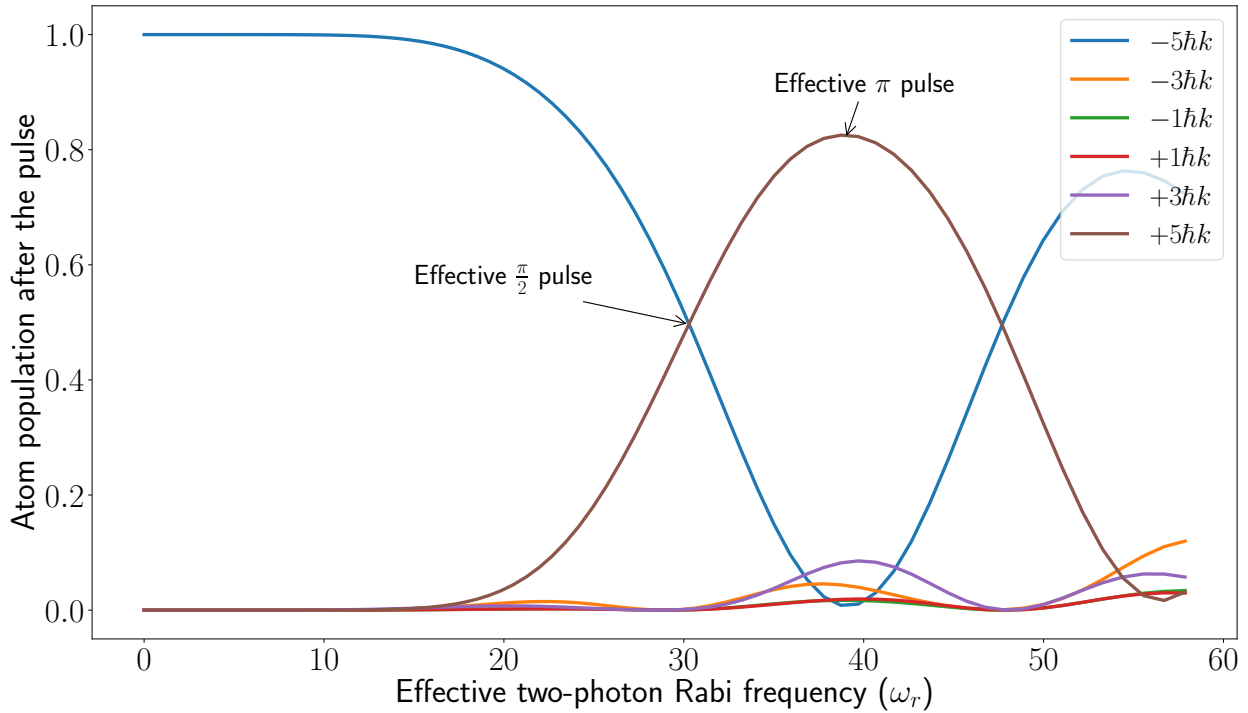


Figure 2.5: Atom population distribution in momentums states after a Bragg diffraction at various 2-photon Rabi frequencies

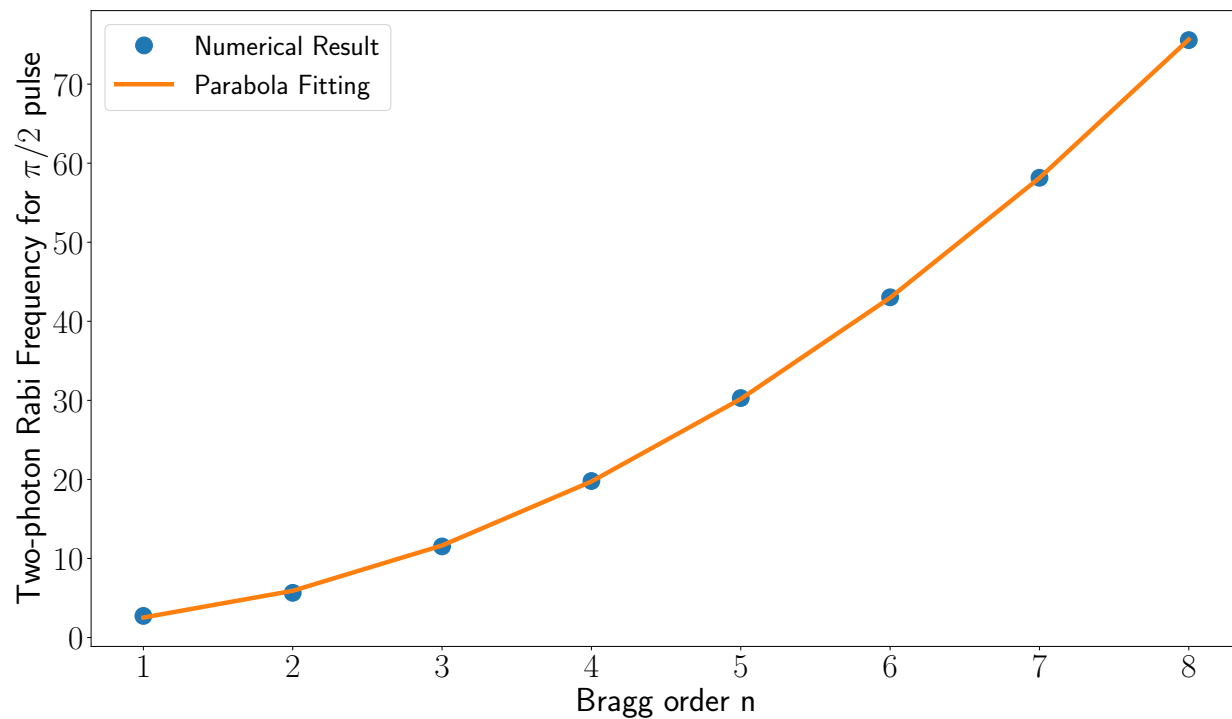
we can set  $\alpha$  to be 0 as it produces no differential AC Stark shift unless we consider the beam profile (see Section 5.6 for details). Sometimes it's easier to use interaction picture to eliminate the first term by the unitary transformation,

$$g_m(t) = g_m^I(t) e^{-i(m_0+2m)^2 \omega_r t} \quad (2.93)$$

The Schrödinger equation would be modified in that picture to

$$i \frac{\partial g_m^I(\tau)}{\partial \tau} = \beta (e^{-i\delta'\tau} e^{i4(m_0+2m-1)\tau} g_{m-1}^I(\tau) + e^{i\delta'\tau} e^{-i4(m_0+2m+1)\tau} g_{m+1}^I(\tau)) \quad (2.94)$$

For the best performance, a code in C was written to implement Runge-Kutta algorithm to solve these ordinary differential equations (ODEs) [48]. Here we take 5th order Bragg diffraction as an example to show specific effects of Bragg diffraction beam splitters. And we choose  $T_{\text{pulse}} = 109 \mu\text{s} = 1.41532\omega_r^{-1}$  as our the pulse duration, which is obtained to minimize parasitic interferometer (see Section 5.5 for details). Under this condition, it's closer to Bragg regime. In order to obtain the effective 2-photon Rabi frequency  $\Omega$  for  $\pi/2$  transition for a beam splitter, we scan the Rabi frequency to see how atom population transfer among different momentum states as a function of 2-photon Rabi frequency. The result is shown in Figure 2.5. A distinctive feature is that it's not an ideal two-level system.

Figure 2.6: Two-photon Rabi frequency of a Bragg  $\pi/2$  pulse vs Bragg order n

Bragg order n	Rabi frequency $\Omega (\omega_r)$	Bragg order n	Rabi frequency $\Omega (\omega_r)$
1	2.735	5	30.291
2	5.656	6	43.035
3	11.524	7	58.155
4	19.798	8	75.566

Table 2.2: The effective two-photon Rabi frequency  $\frac{\Omega_1 \Omega_2}{2\Delta}$  of a  $\frac{\pi}{2}$  Bragg diffraction at various Bragg orders

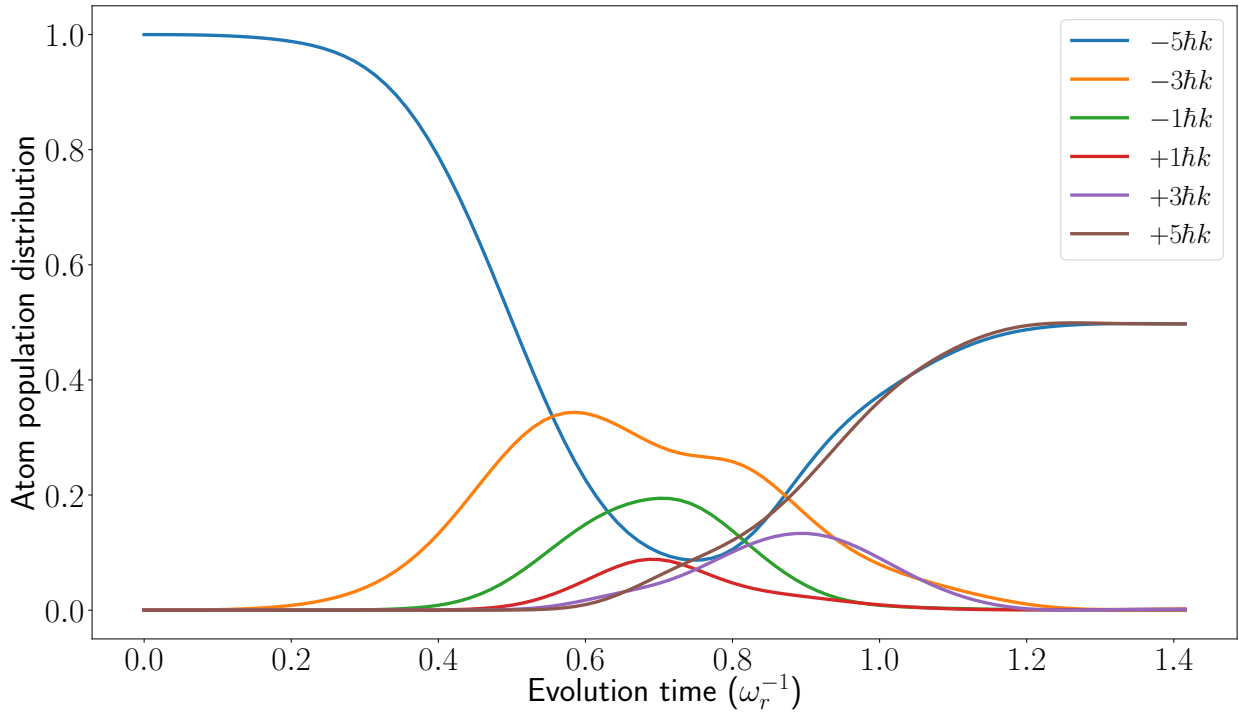


Figure 2.7: Time evolution solution of a 5th order Bragg  $\pi/2$  pulse

The population at intermediate momentum states are non-zero. This is especially obvious if we want to drive a  $\pi$  pulse. The maximum transfer efficiency is only about 80% in this case. The point of  $\pi/2$  and  $\pi$  transitions are indicated in the figure based on the definition that a  $\pi/2$  pulse reaches equal population between the initial and the final state and a  $\pi$  pulse delivers the maximum transfer into the final state. The effective two-photon Rabi frequency for  $\pi/2$  pulse for different Bragg orders are also listed and plotted below, which is quite useful for experiment. The two-photon Rabi-frequencies can be well fitted by a parabola as shown in the Figure 2.6.

In the experiment, we usually use 5th order Bragg diffraction as beam splitters for its best performance in sensitivity and contrast. So here we will be only focusing on 5th order Bragg  $\pi/2$  pulse. Its time evolution solution is also shown here in Figure 2.7.

It shows that under this condition the Bragg  $\pi/2$  pulse is very close to Bragg regime where intermediate states can be well adiabatically eliminated, which makes it a good beam splitter. But it's not an ideal two-level system as we can see from the phase plots shown in Figure 2.8 and Figure 2.9. An ideal  $\pi/2$  pulse gives exactly  $-\pi/2$  phase in a two-level system. But it here varies a lot depending on the detuning and Rabi frequency of the laser input into the system. In the real experiment, we are dealing a large ensemble of atoms in the atom cloud. And the laser beam forms Gaussian beam instead of an ideal plane wave. And atom also has non-zero velocity distribution. A large number of atoms would be addressed

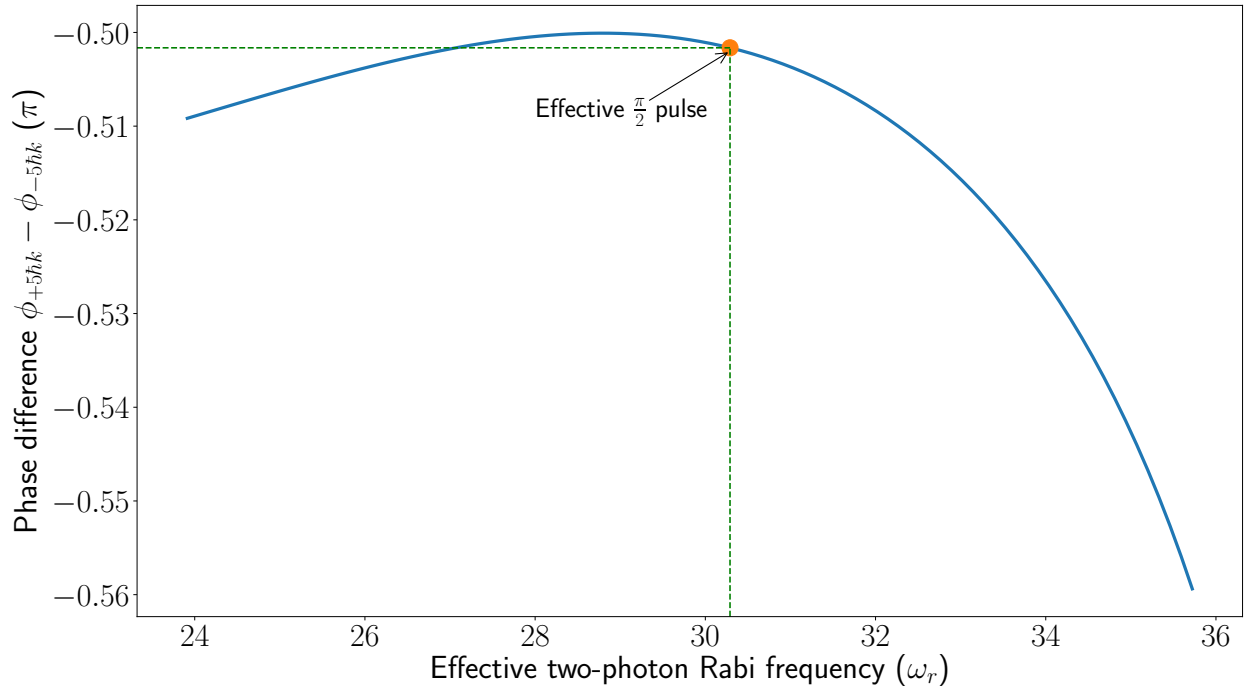


Figure 2.8: Bragg beam splitter phase vs two-photon Rabi frequency. Here the phase difference is defined as the phase difference between  $|5\hbar k\rangle$  and  $|-5\hbar k\rangle$  after a transition from  $|-5\hbar k\rangle$  to  $|5\hbar k\rangle$ .

by Bragg diffraction in non-resonant condition, which is equivalent to atom with the same initial velocity addressed by Bragg diffraction with certain detuning after shifting the frames of reference. Realistically to model the real Bragg diffraction we need to take into account effective power and detuning each atom sees. It becomes a quite complicated simulation work. We will talk about this briefly in Section 2.7 and 2.8. In the subsequent section, we will introduce a more complex type of Bragg diffraction where two atom clouds with different velocity could be driven to different final states simultaneously. This is another very useful beam splitter in doing simultaneously conjugated interferometers we will discuss in Section 2.6.

## Simultaneous Bragg Diffraction Beam Splitter

In the case of what we called simultaneous conjugated interferometer we will introduce in Section 2.6, we need a kind of Bragg diffraction to simultaneously drive transitions from  $|-5\hbar k\rangle$  to  $|-15\hbar k\rangle$  and from  $|5\hbar k\rangle$  to  $|15\hbar k\rangle$ . Here we use a dual frequency laser beam  $\mathbf{E}_2 = \mathbf{E}_{20+} \cos((k_2 + k_m)z + (\omega_2 + \omega_m)t) + \mathbf{E}_{20-} \cos((k_2 - k_m)z + (\omega_2 - \omega_m)t)$  to replace the original  $\mathbf{E}_2$  and keep  $\mathbf{E}_1$  the same. The pair with  $\omega_1$  and  $\omega_2 + \omega_m$  would drive  $|-5\hbar k\rangle$  to  $|-15\hbar k\rangle$  and the pair with  $\omega_1$  and  $\omega_2 - \omega_m$  will drive another transition. It is configured in



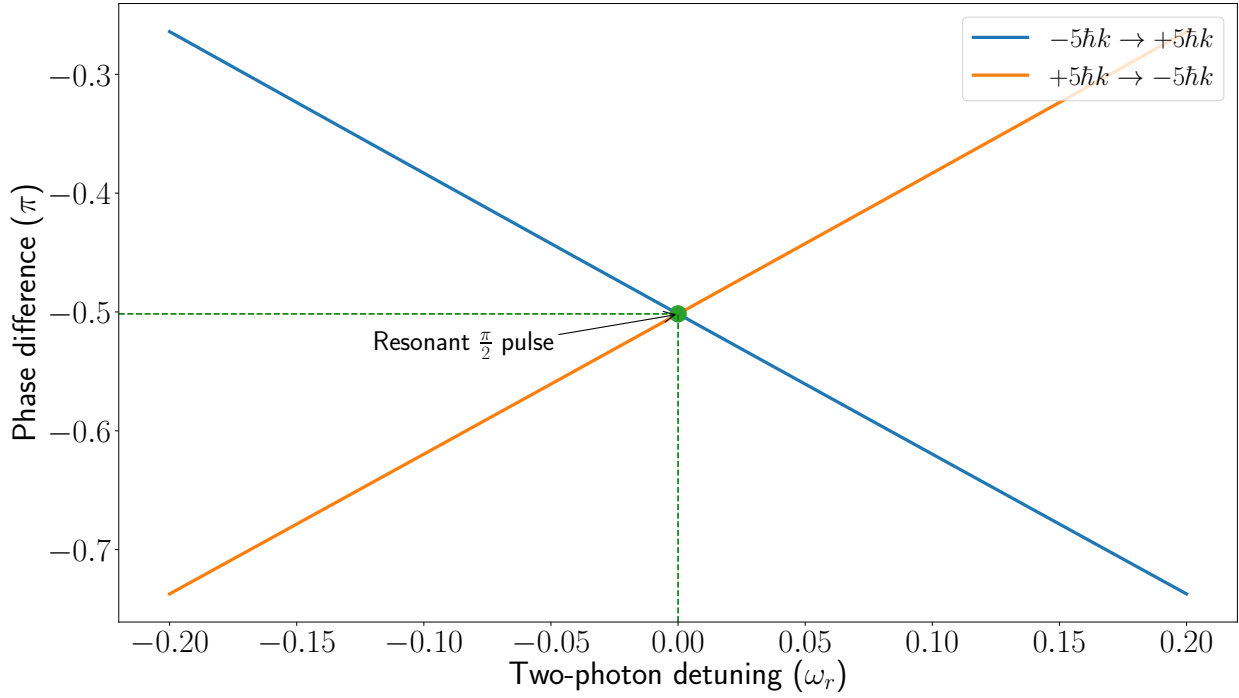


Figure 2.9: Bragg beam splitter phase vs two-photon detuning. Here the phase difference in blue is defined as the phase difference between  $|5\hbar k\rangle$  and  $|-5\hbar k\rangle$  after a transition from  $|-5\hbar k\rangle$  to  $|5\hbar k\rangle$ ; and that in orange is defined as the phase difference between  $|-5\hbar k\rangle$  and  $|5\hbar k\rangle$  after a transition from  $|5\hbar k\rangle$  to  $|-5\hbar k\rangle$

this way in order to match our experiment conventions. Based on conservation of momentum and energy, the modulation frequency  $\omega_m$  is chosen to be

$$\omega_m = 8n\omega_r \quad (2.95)$$

Following the same procedure of approximations, and adiabatic elimination, we can write the Schrödinger equation for the ground states,

$$i\frac{\partial}{\partial t}g(z,t) = -\frac{\hbar}{2M}\frac{\partial^2}{\partial z^2}g(z,t) + \frac{\Omega_1^2 + \Omega_{2+}^2 + \Omega_{2-}^2 + 2\Omega_{2+}\Omega_{2-}\cos(2k_m z + 2\omega_m t)}{4\Delta}g(z,t) + \frac{\Omega_1\Omega_{2+}\cos(2kz + k_m z + \omega_m t - \delta t) + \Omega_1\Omega_{2-}\cos(2kz - k_m z - \omega_m t - \delta t)}{2\Delta}g(z,t) \quad (2.96)$$

where Rabi frequency  $\Omega_{2\pm}$  are defined in a very similar way. Consider the real situation where the size of atom wave packet is as small as the thermal de Broglie wavelength at 0.2 recoil temperature

$$\lambda_{\text{thermal}} = \frac{h}{\sqrt{3mk_B T}} = 1.58 \mu m \quad (2.97)$$

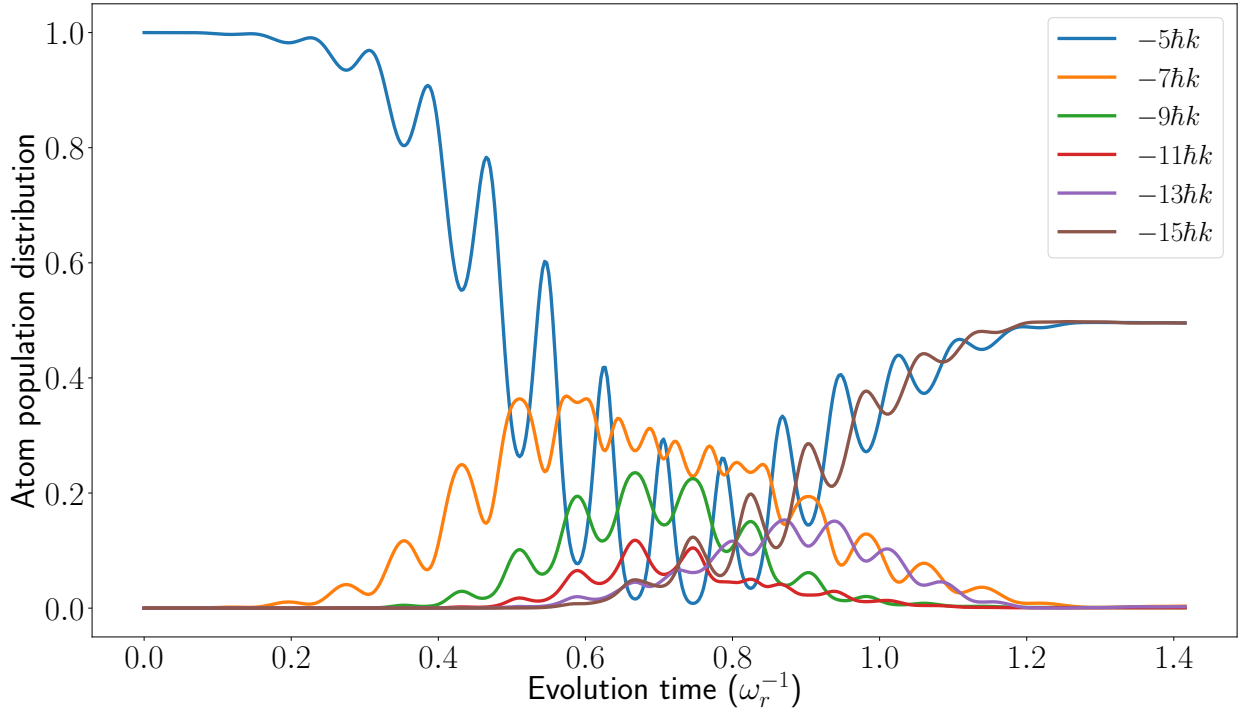


Figure 2.10: Time evolution solution of a 5th order dual-frequency Bragg  $\pi/2$  pulse

In this regime, we find that  $k_m \lambda_{\text{thermal}} \ll kz$  and  $k_m \lambda_{\text{thermal}} \ll \omega_m \tau$  where  $\tau$  is the length of the pulse. So the contribution from  $k_m$  is insignificant and thus could be neglected. And assuming  $\Omega_{2+} = \Omega_{2-} = \Omega_2$  for simplicity in the scheme we perform dual frequencies, we can simplify the equation as

$$i \frac{\partial}{\partial t} g(z, t) = -\frac{\hbar}{2M} \frac{\partial^2}{\partial z^2} g(z, t) + \frac{2\Omega_1^2 + \Omega_2^2 + 2\Omega_2^2 \cos(2\omega_m t)}{4\Delta} + \frac{\Omega_1 \Omega_2 \cos(2kz - \delta t) \cos(\omega_m t)}{\Delta} g(z, t) \quad (2.98)$$

Since the potential still has  $\lambda = \pi/k$  translational invariance symmetry, we can apply Bloch's theorem again to expand the wavefunction in Fourier series. And each Fourier component of the Bloch wave satisfies the equation

$$i \dot{g}_m(t) = \frac{\hbar(k_q + 2mk)^2}{2M} g_m(t) + \frac{2\Omega_2^2(1 + \cos(2\omega_m t)) + \Omega_1^2}{4\Delta} g_m(t) + \frac{\Omega_1 \Omega_2 \cos(\omega_m t)}{2\Delta} (e^{-i\delta t} g_{m-1}(t) + e^{i\delta t} g_{m+1}(t)) \quad (2.99)$$

For the convenience of numerical simulation, it can be rewritten as

$$i \dot{g}_m(\tau) = (\lambda_0 + 2m)^2 g_m(\tau) + (\alpha + \gamma \cos(2\omega_m \tau)) g_m(\tau) + 2\beta \cos(\omega_m \tau) (e^{-i\delta' \tau} g_{m-1}(\tau) + e^{i\delta' \tau} g_{m+1}(\tau)), \quad (2.100)$$

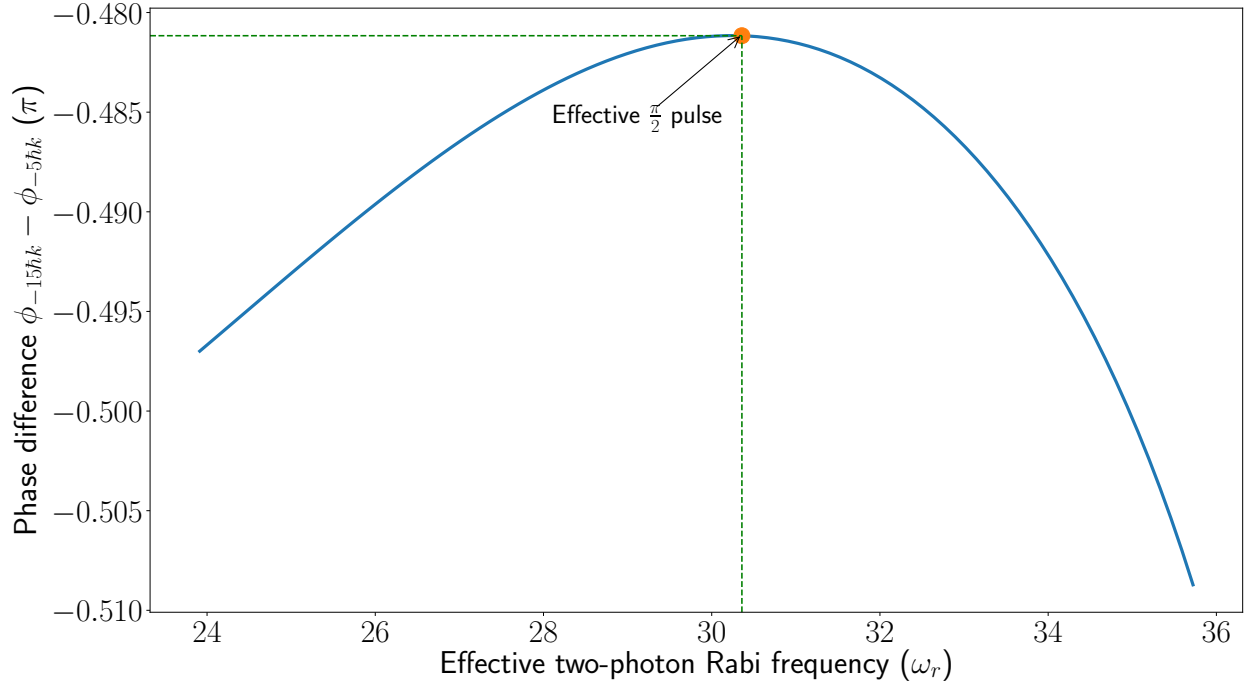


Figure 2.11: Dual frequency Bragg beam splitter phase vs two-photon Rabi frequency. Here the phase difference in blue is defined as the phase difference between  $|-15\hbar k\rangle$  and  $|-5\hbar k\rangle$  after a transition from  $|-5\hbar k\rangle$  to  $|-15\hbar k\rangle$ .

or in the interaction picture as

$$i \frac{\partial g_m^I(\tau)}{\partial \tau} = 2\beta \cos(\omega_m t) (e^{-i\delta'\tau} e^{i4(m_0+2m-1)\tau} g_{m-1}^I(\tau) + e^{i\delta'\tau} e^{-i4(m_0+2m+1)\tau} g_{m+1}^I(\tau)) \quad (2.101)$$

where  $\alpha = \frac{2\Omega_2^2 + \Omega_1^2}{4\Delta}$ ,  $\gamma = \frac{\Omega_2^2}{2\Delta}$ ,  $\beta = \frac{\Omega_1\Omega_2}{2}$ , and  $\delta' = \delta\omega_r^{-1}$ . Normally we can assume  $\alpha = \gamma = 0$  for the same reason as discussed earlier. Based on the simulation result, the population evolution during the pulse is oscillating a lot but it reaches a stable distribution similar to the single frequency Bragg pulse as shown in Figure 2.10. The effective two-photon Rabi frequency at  $\pi/2$  pulse is about  $\Omega = 30.359$ , a little larger than single Bragg result. But the population distribution as we scan the Bragg power is about the same as in Figure 2.5. The relative phase dependence on power and detuning is a little bit different in this case. They are shown in Figure 2.11 and Figure 2.12. The conclusion here is that simultaneous Bragg diffraction serves well as a beam splitter. But it has different phase dependence on experiment parameters, which may introduce additional phase into the system that won't be canceled throughout the entire interferometer.

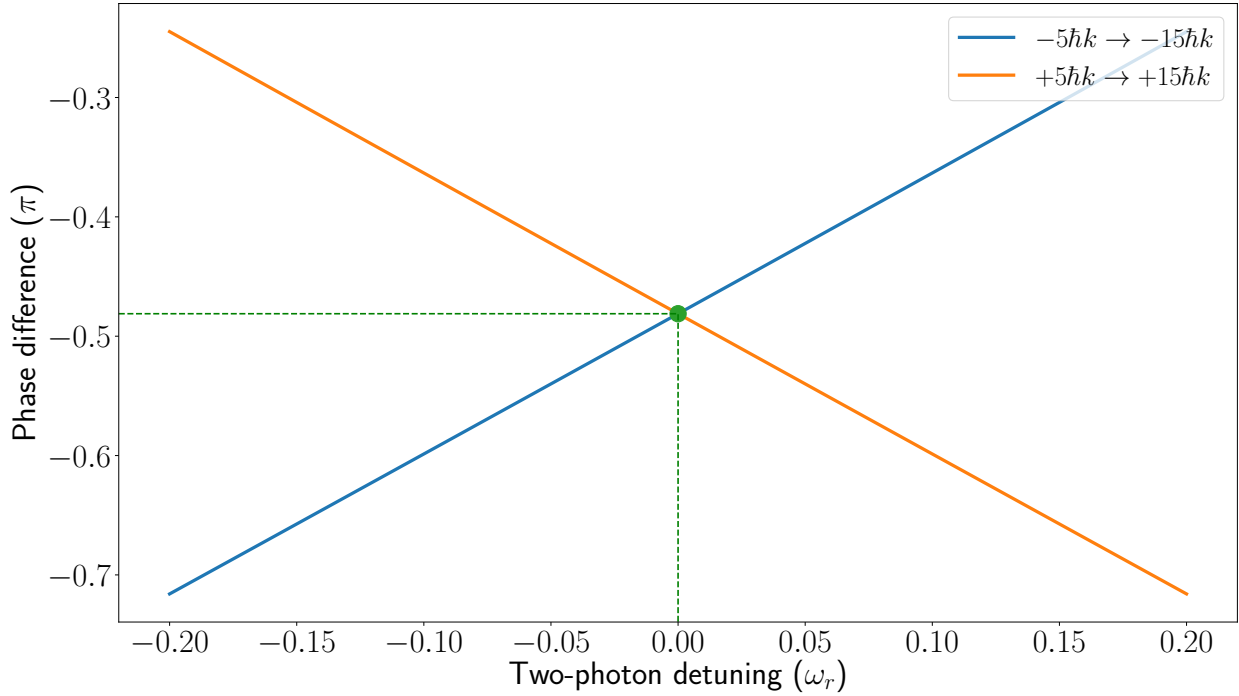


Figure 2.12: Dual frequency Bragg beam splitter phase vs two-photon detuning. Here the phase difference in blue is defined as the phase difference between  $|-15\hbar k\rangle$  and  $|-5\hbar k\rangle$  after a transition from  $|-5\hbar k\rangle$  to  $|-15\hbar k\rangle$ ; and that in orange is defined as the phase difference between  $|15\hbar k\rangle$  and  $|5\hbar k\rangle$  after a transition from  $|5\hbar k\rangle$  to  $|15\hbar k\rangle$ .

## 2.5 Bloch Oscillations

Ideally, Bragg diffraction should be able to improve the sensitivity of atom interferometry by orders of magnitude. But in reality, when large order Bragg diffraction is applied, significant decoherence is observed at moderate pulse separation time. In order to recover coherence, the pulse separation time has to be shortened significantly. So there is a trade-off between the Bragg order  $n$  and the pulse separation time  $T$  we can use. We found that 5th order Bragg diffraction gives the best overall sensitivity in our application. But that's still not enough to reach the sub-ppb level of the fine-structure constant measurement. That's where a new technique called Bloch oscillations were brought in. Again Bloch oscillation is a concept first introduced in solid-state physics. It describes the dynamics of the electron placed in a periodic lattice potential with a constant force on. It was predicted by the theory first that instead of constant acceleration like a free electron, the electron bounded in the lattices would undergo certain kind of oscillation. But it's quite challenging to observe it in normal solids as the relaxation time of solids is way smaller than the period of Bloch oscillations. But in the cold atomic system, it's quite a lot easier observe it in optical lattices as decoherence happens way slower than Bloch oscillations [49, 50]. Due to this reason, Bloch

oscillations have been a very useful tool in atom optics to transfer more than hundreds of photon momentum. In this section, we will look into some details and application specifically in atom interferometry [51].

Consider a standing optical lattice formed by strongly detuned counter-propagating laser beams  $\mathbf{E}_1 = \mathbf{E}_0 \cos(kz - \omega t)$  and  $\mathbf{E}_2 = \mathbf{E}_0 \cos(kz + \omega t)$ . Following the same tricks of approximation in the section of Bragg diffraction, we can simplified the Hamiltonian for the ground state wavefunction  $g(z, t)$  as

$$H_0 = \frac{\hat{\mathbf{P}}_{\text{COM}}^2}{2M} + \hbar\omega_{AC} + \hbar\Omega \cos(2kz) \quad (2.102)$$

The AC Stark shift and effective 2-photon Rabi frequency  $\omega_{AC}$  and  $\Omega$  are defined in the same way as in Section 2.4. We know that the solution of this Hamiltonian can be written as Bloch waves,

$$g_{n,k_q}(z) = e^{ik_q z} u_{n,k_q}(z) \quad (2.103)$$

where  $n$  is the band index and  $k_q$  is the quasi-wave number taken from the first Brillouin zone  $[-\frac{\pi}{d}, \frac{\pi}{d})$ . Here  $d$  is the distance between the nearest lattice sites. In this case of optical lattices, it's given by

$$d = \lambda_{\text{optical lattice}} = \frac{\pi}{k} \quad (2.104)$$

Now in the problem of Bloch oscillations, an additional term  $-Fz$  is added for an uniform force field. In total, the Hamiltonian becomes

$$\hat{H}_{\text{BO}} = \frac{\hat{\mathbf{P}}_{\text{COM}}^2}{2M} + \hbar\Omega \cos(2kz) - Fz \quad (2.105)$$

Note that the AC Stark shift term is omitted as it doesn't change the dynamics of physics here. The physics is quite rich and complicated here. In the weak field regime, where the field potential term can be treated as a small perturbation. The solution is mostly constructed based on the eigenstate of the force-free Hamiltonian, i.e. Bloch states. That solution is called Houston functions [52]. Whereas in the strong field regime when the field potential difference between the nearest sites becomes larger than the lattice potential, Bloch wave would be localized to each site. In this regime it starts with localized Wannier state and treat the lattice as perturbation and the solution is the so-called Wannier-Stark lattice [53]. In the application of atom interferometry, we stay in the weak field regime to preserve atom's coherence.

## Weak Field Approximation

When there is no lattice, the particle will follow the force to increase its momentum constantly. However with the lattice potential, momentum is not a good quantum number. But quasi-momentum is conserved based on the discrete translational invariance. So intuitively speaking, we may guess that in this situation, instead of momentum, quasi-momentum would

constantly accelerate. Following this idea, Houston proposed a attempted wave function as [52]

$$\psi(z, t) = e^{ik_q(t)z} u_{n, k_q(t)}(z) e^{-\frac{i}{\hbar} \int^t E_{k_q(\tau)} d\tau} \quad (2.106)$$

where  $E_{k_q(t)}$  is the eigen energy of Bloch wave with a quasi-wave number  $k_q(t)$  and  $k_q(t)$  follows the constant acceleration

$$k_q(t) = k_q(t=0) + \frac{Ft}{\hbar} \quad (2.107)$$

It shows that this solution would be a good approximation as long as

$$\left| F \frac{\partial u_{n, k_q}}{\partial k_q} \right| \ll 1 \quad (2.108)$$

What the force does is to make a transition from Bloch wave  $g_{n, k_q}$  to  $g_{n, k_q + F\Delta t/\hbar}$ . This condition means the process is not fast enough to make a transition that the atom cannot follow. It is essentially the quantitative definition of adiabatic condition in this context. Since quasi-momentum is not real momentum, it follows a periodic boundary condition  $g_{n, k_q + \frac{2\pi}{d}}(z) = g_{n, k_q}(z)$ . So in real space, atom is undergoing Bloch oscillations with oscillation period  $T_B$  given by

$$\frac{FT_B}{\hbar} = \frac{2\pi}{d} \quad (2.109)$$

## Landau-Zener Tunnelling

So far all the discussion above is based on an assumption that there is no interband transition, which is not true in the real case. This kind of interband transition is called Landau-Zener tunneling. When the atom cannot follow the force field adiabatically, Landau-Zener tunnelling happens. Using Houston's formulations above, we can write the real wave function as a superposition of multiple bands,

$$\psi(z, t) = \sum_n c_n(t) e^{-\frac{i}{\hbar} \int^t d\tau E_{n, k_q(\tau)}} e^{ik_q(t)z} u_{n, k_q(t)}(z) \quad (2.110)$$

Putting it into Schrödinger equation we have [54]

$$\langle n, k_q(t) | i\hbar \frac{\partial}{\partial t} | \psi \rangle = \langle n, k_q(t) | (H_0 - Fz) | \psi \rangle \quad (2.111)$$

$$\dot{c}_n(t) = - \int dz \sum_m c_m(t) \frac{F}{\hbar} u_{n, k_q(t)}^*(z) \frac{\partial}{\partial k_q} u_{m, k_q(t)}(z) e^{-\frac{i}{\hbar} \int^t d\tau (E_{m, k_q(\tau)} - E_{n, k_q(\tau)})} \quad (2.112)$$

The famous Landau-Zener tunneling formula is based on a toy model where a quantum state is swept through an avoided crossing of two energy levels. The tunneling rate depends on the coupling between two states as well as how fast the quantum system is sweeping through

a varying parameter. In the case of Bloch oscillations, the interband transition probability can be written as [55]

$$P \approx \exp\left(-\frac{\pi\Delta_{n,m}^2}{8\hbar(|\epsilon_m| + |\epsilon_n|)F}\right) \quad (2.113)$$

where  $\Delta_{n,m}$  is the energy gap between the band  $n$  and  $m$ ;  $\epsilon_m$  is the slope of the bands at the avoided crossing in the no-band-gap limit. It built upon the assumption of weak lattices, which may not be true in real cases. In the following section we will try to simulate Bloch oscillations of cold atoms in optical lattices with numerical methods.

## Numerical Simulation

Coming back to our original optical lattices model where the potential is  $\hbar\Omega \cos(2kz)$ , the solution with zero-force field can be written as Bloch waves

$$g_{n,k_q}(z) = e^{ik_q z} u_{n,k_q}(z) \quad (2.114)$$

Since  $u_{n,k_q}(z+d) = u_{n,k_q}(z)$ , we can expand it into Fourier series as

$$g_{n,k_q}(z, t) = e^{ik_q z} \sum_m c_{n,m}(t) e^{i2mkz} \quad (2.115)$$

Plugging it to the Schrödinger equation with force-free Hamiltonian  $H_0$  we have the central equations

$$\frac{\hbar^2(k_q + 2mk)^2}{2M} c_m + \frac{\hbar\Omega}{2}(c_{m-1} + c_{m+1}) = E_{n,k_q} c_m \quad (2.116)$$

Eigenvalues of these equations give the band structure and eigenvectors give Bloch state of each band. For example in the system with  $\Omega = \omega_r$ , band structure can be given as shown in Figure 2.13. Bloch oscillations sweep through the first band over and over again. But at the edge of the first Brillouin zone, the atom goes through the avoided crossing between the first band and the second band where Landau-Zener tunneling is the strongest. For each Bloch order, when the atom runs through the Brillouin zone once, it gains  $2\hbar k$  momentum kick at the edge so that the real momentum of the atom is oscillating in the lattice rest frame.

In optical lattices the way to control the constant force field is through ramping the lattice frequency. Based on Doppler shift, we know that optical lattices with ramping frequency is moving with a constant acceleration in the lab frame. So in the rest frame of the lattices atoms would experience a inertial force  $F = -ma$  which drives the Bloch oscillations. If we go back to the lab frame, Bloch oscillations essentially accelerate atoms coherently and transfer large momentum  $2N\hbar$  depending on the Bloch order  $N$ . Suppose the frequency is ramping such that

$$\frac{d}{dt}(\omega_1 - \omega_2) = r \quad (2.117)$$

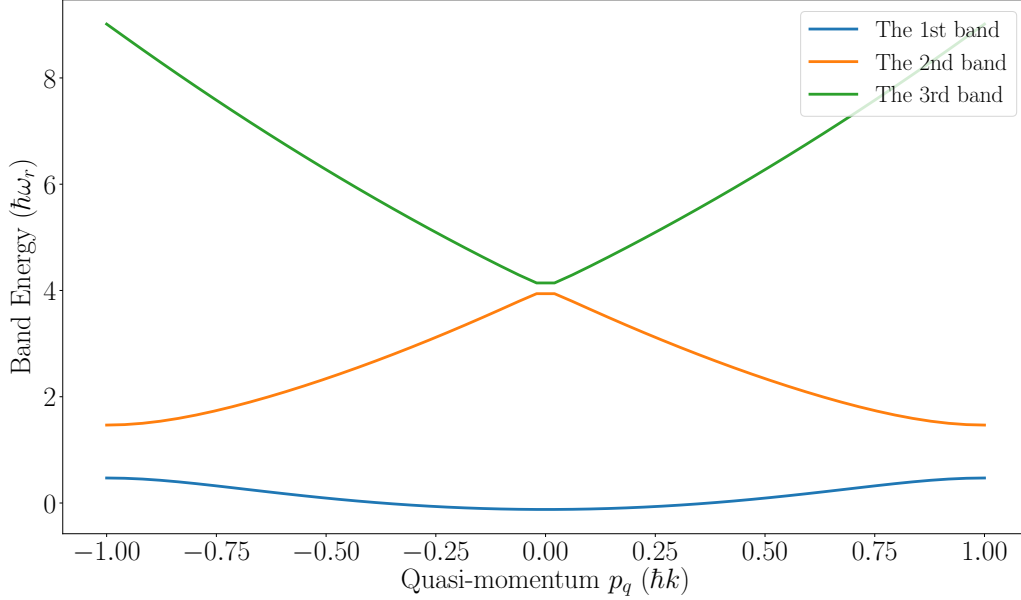


Figure 2.13: Energy band structure of an atom in optical lattices with lattice depth  $\Omega = \omega_r$

where  $r$  is the ramp rate. Then based on Doppler shift, the lattices rest-frame velocity is related to the frequency difference as

$$\omega_1 - \omega_2 = 2kv \quad (2.118)$$

So the inertial force with frequency ramp is

$$F = -Ma = -\frac{rM}{2k} \quad (2.119)$$

The Bloch period can thus be determined as

$$T_B = \frac{2\hbar k}{|F|} = \frac{4\hbar k^2}{rM} \quad (2.120)$$

In our experiment, we use the same system as the dual-frequency Bragg diffraction beam splitter to drive simultaneous Bloch oscillations for those two simultaneously conjugated interferometers in opposite directions. The only difference is that in Bloch oscillations, the modulation frequency  $\omega_m$  is a ramp and the pulse shape is a square pulse with adiabatic ramp on and off. But simply using the simulation for Bragg diffraction with frequency ramp added wouldn't work as the Bloch wave basis used in Bragg diffraction is not a complete basis for Bloch oscillation. The good basis to use here is Houston functions

$$g_{n,k_q(t)}(z, t) = e^{-\frac{i}{\hbar} \int^t E_{n,k_q(\tau)} d\tau} e^{ik_q(t)z} u_{n,k_q(t)}(z) = e^{ik_q(t)z} \tilde{u}_{n,k_q(t)}(z, t) \quad (2.121)$$



Since all these periodic functions  $\tilde{u}_{n,k_q}(z, t)$  could be expanded as Fourier series  $\sum_m g_m e^{i2mkz}$ , we can express all the bands together as a sum of the Fourier series. So the general solution for Bloch oscillations could be written as

$$g_{n,k_q(t)}(z, t) = e^{ik_q(t)z} \sum_m g_m(t) e^{i2mkz} \quad (2.122)$$

Substitute this solution to Schrödinger equation of Bloch oscillations, we can get the the following differential equations in Schrödinger picture for simulation,

$$\begin{aligned} i\dot{g}_m(\tau) = & (\lambda(\tau) + 2m)^2 g_m(\tau) + (\alpha + \gamma \cos(2\omega_{m0} + r'\tau^2)) g_m(\tau) + \beta(e^{i(\omega_m\tau+r'\tau^2)} + e^{-i\omega_m\tau}) g_{m-1}(\tau) \\ & + \beta(e^{-i(\omega_m\tau+r'\tau^2)} + e^{i\omega_m\tau}) g_{m+1}(\tau) \end{aligned} \quad (2.123)$$

where  $\lambda(\tau) = k_q(\tau)/k$  and ramp rate in the recoil unit  $r' = r\omega_r^{-1}$ . The modulation frequency is ramped up with a constant rate. i.e.  $\omega_m = \omega_{m0} + r\tau$ . All the other parameters are defined in the same way as in the previous sections. The force doesn't have to be constant force. This method applies to any slow varying force that satisfies the adiabatic condition. In this case for simplicity, we apply a constant force such that

$$\lambda(\tau) = \frac{1}{k}(k_{q0} + \int^\tau d\tilde{\tau} \frac{F(\tilde{\tau})}{\hbar}) = \lambda_0 + \frac{1}{4}r'\tau \quad (2.124)$$

For Bloch oscillations, the effective two-photon Rabi frequency and ramp rate are the most important two parameters to optimize its performance. Generally the larger the effective two-photon Rabi frequency and the slower the ramp, the more efficient Bloch oscillations would be. But there is a trade-off in the real interferometer where larger intensity and longer pulse tend to cause decoherence of atoms. More details would be discussed in Section 4.1. With a set of parameters used in the real experiment where the two-photon Rabi frequency  $\Omega_{BO} = 0.2\Omega_{\text{Bragg}} \pi/2$  and the ramp rate  $r = 11r_g$  where gravity ramp rate  $r_g = 23$  MHz/s, a simulation of 125th order Bloch oscillations is performed under simultaneous Bloch oscillations configuration as shown in Figure 2.14. The calculation is performed in the atom rest frame where 0 and  $\pm 2\hbar k$  are momentum states in this frame of reference. We can see Bloch efficiency drop caused by Landau-Zener tunneling as we increase the Bloch oscillations order.

In the experiment, Bloch oscillations are used to boost the interferometer phase. So it's important to know how much phase atom would receive from the pulse. Intuitively speaking, besides the general phase due to AC Stark shift when the light is on, the atom gain phase when it's kicked at the wall of the Brillouin zone through absorption of a photon from one beam and stimulated emission of a photon to another beam, which means for this specific "kick" the atom gains phase by

$$\Delta\phi = k_1 z - \omega_1 t - (-k_2 z - \omega_2 t) = 2k_{\text{eff}} z - \Delta\omega t \quad (2.125)$$

In the specific case of our atom interferometer geometry, atoms in both arms are moving with the same velocity during Bloch oscillations. Consider the classical model of Bloch oscillations

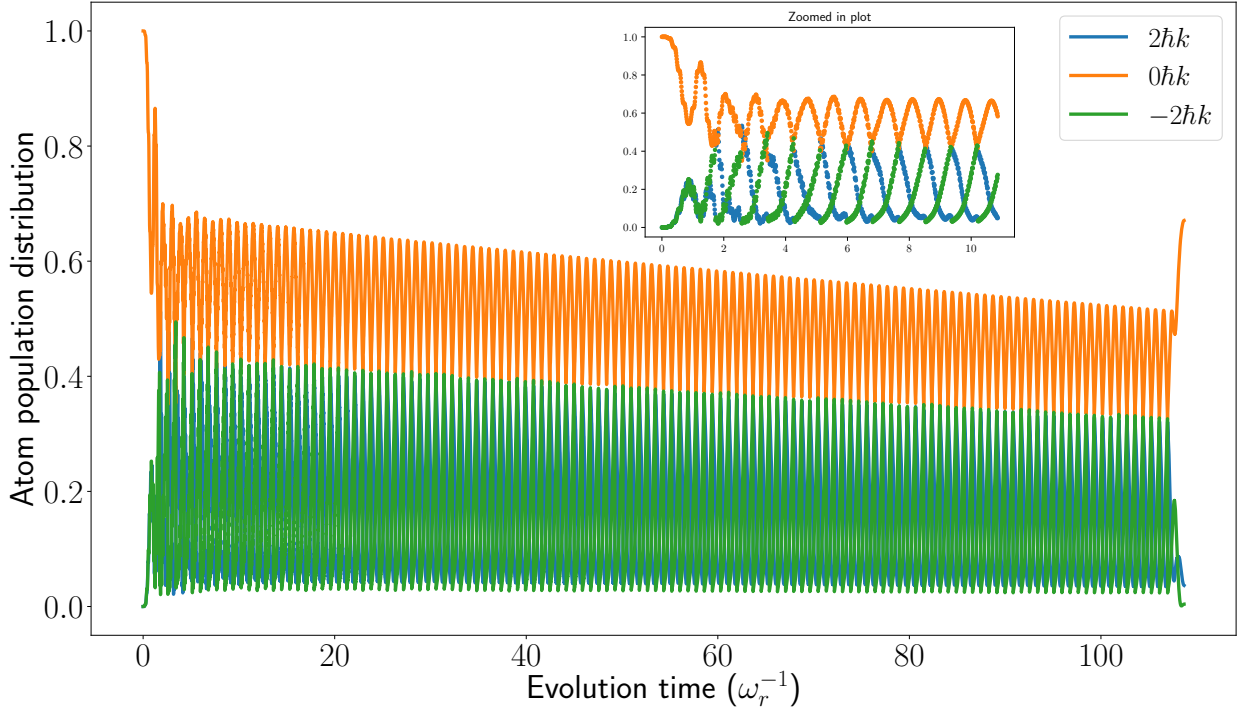


Figure 2.14: Time evolution solution of dual-frequency Bloch Oscillations

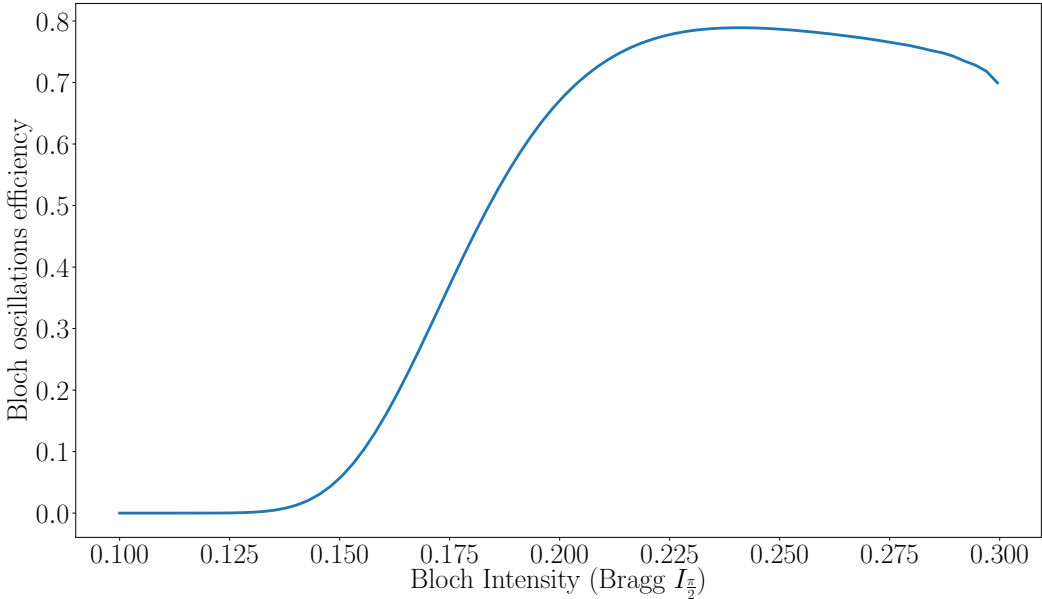


Figure 2.15: Bloch oscillations efficiency vs Bloch pulse intensity

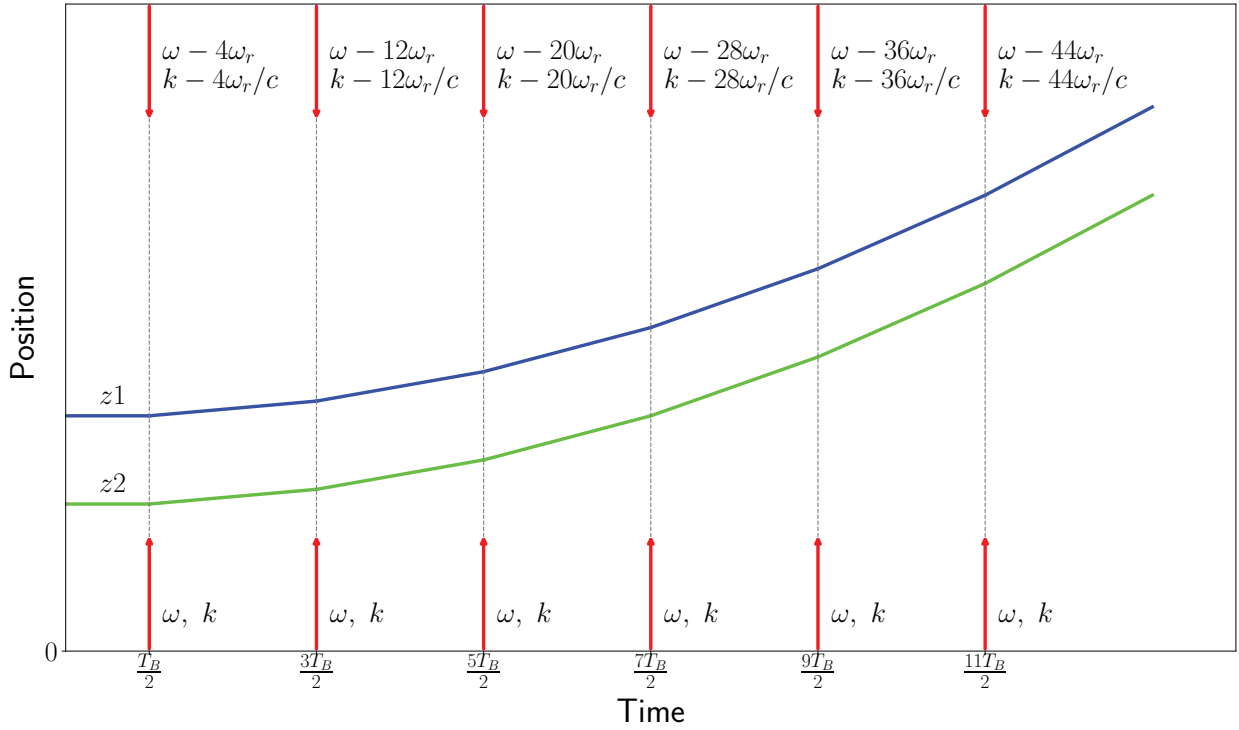


Figure 2.16: Classical model of Bloch oscillations for two arms of the interferometer

as shown in Figure 2.16. Atom 1 and 2 are kicked by  $2\hbar k$  simultaneously at  $t_m = (m - \frac{1}{2})T_B$  where  $T_B$  is the Bloch oscillations period. So the total phase difference is added up to be

$$\Delta\Phi_{BO} = \Delta\phi_1 - \Delta\phi_2 = \sum_m 2k_{\text{eff}}(t_m)(z_1(t_m) - z_2(t_m)) \quad (2.126)$$

Note that as we ramp the frequency, effective  $k$  would no longer be the same. Suppose initially  $\omega_1 = \omega_2 = \omega = kc$  and we know that the position difference of both atoms under gravity remains the same as the initial position difference, so we have

$$\Delta\Phi_{BO} = \sum_{m=1}^N (2k + 4\frac{\omega_r}{c} - 8\frac{m\omega_r}{c})\Delta z_0 = (2Nk - \frac{4N^2\omega_r}{c})\Delta z_0 \quad (2.127)$$

In the next section, we will apply this formula to calculate the full phase formula of the atom interferometers commonly used in our experiments.

## 2.6 Various Atom Interferometer Configurations

Now we have prepared all the ingredients ready for this section to calculate the phase of several atom interferometer configurations used in this experiment. The phase calculation

for the real experiment could be very complicated as many experiment parameters could potentially change the phase. But based on the precision of the experiment, we don't have to know phase terms below the experiment precision. So we can adopt perturbation methods to calculate the phase in general. We can calculate the phase based on the toy model where laser beam is treated as plane wave and atom trajectory is taken to be simple quadratic form under constant gravitational acceleration. And all other influences will be taken as a small perturbation added as phase corrections (e.g. gravity gradient, Guoy phase and so on) [56]. This methods allows us to evaluate the phase accurately at the precision we want.

Two typical of perturbations are common in our atom interferometer systems. One is perturbation added to the free particle Lagrangian. The other is perturbation added to pulse. In this section we will only be focusing on the first type and the second type will be discussed in Chapter 5.

The Lagrangian of a free atom with gravity gradient could be written as

$$L = \frac{1}{2}m\dot{z}^2 - mgz + \frac{1}{2}m\gamma z^2 \quad (2.128)$$

where gravity gradient  $\gamma$  is defined as

$$\gamma = -\frac{dg}{dz} \quad (2.129)$$

Before going into specific configurations, here we will present a brief summary of basic procedures to calculate the phase of an atom interferometer.

## Basic Procedure

In this section we will summarize basic ingredients we have from previous sections as well as discuss the basic procedure to calculate atom interferometer phase. Atom interferometer phase consists of free evolution phase, light atom interaction phase as well as splitting phase in general. The first two types are already discussed in the previous sections. The third type comes from atom interferometers in which the path doesn't close at the last pulse. This type will be discussed in detail here.

### Free Evolution Phase

Free evolution phase is simply the matter wave phase from Feynman integral. Based on the perturbation theory, we can use the classical path without perturbation to calculate free evolution phase

$$\phi_f = \frac{1}{\hbar} \int_{\text{unperturbed path}} \left( \frac{1}{2}m\dot{z}^2 - mgz + \frac{1}{2}m\gamma z^2 \right) dt \quad (2.130)$$

### Light-Atom Interaction Phase

We have also carefully studied the phase from light atom interaction during at beam splitters and atom mirrors. The phases were obtained by solving Schrödinger Equation with

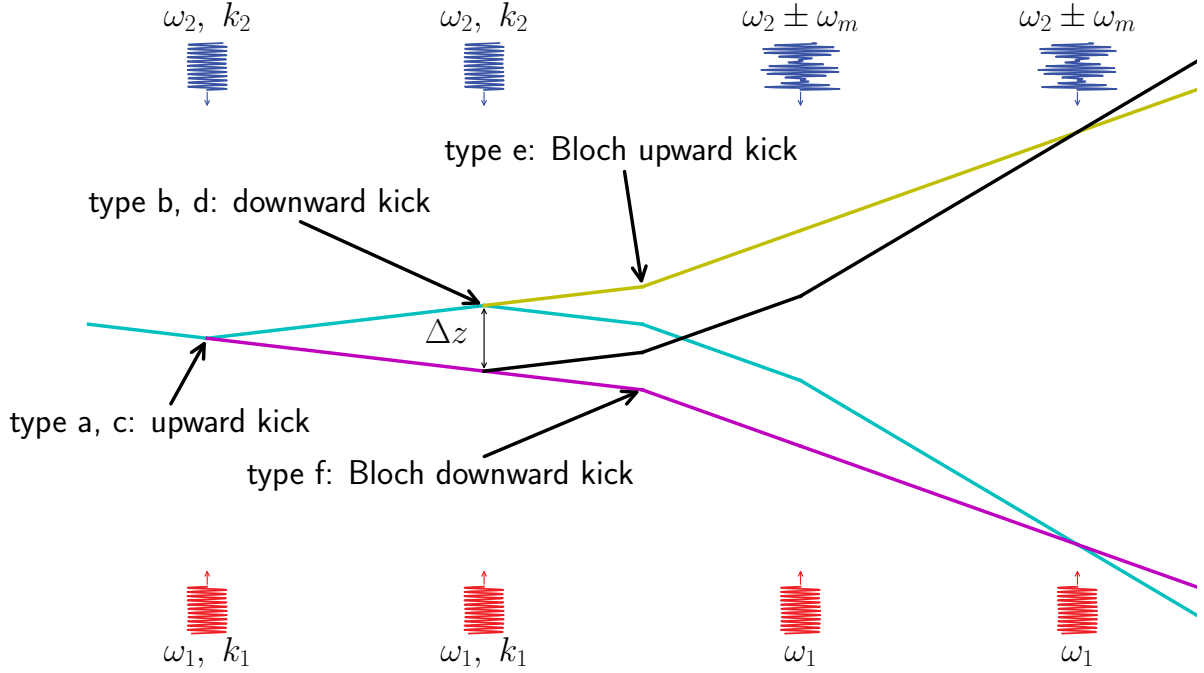


Figure 2.17: Pulse types in a general atom interferometer configuration

Type	Momentum Transfer	Light Atom Interaction Phase
a) Raman upward kick	$\hbar(k_1 + k_2)$	$k_1 z + k_2 z - (\omega_1 - \omega_2)t + \phi_{BS}$
b) Raman downward kick	$-\hbar(k_1 + k_2)$	$-k_1 z - k_2 z + (\omega_1 - \omega_2)t + \phi_{BS}$
c) Bragg upward kick	$n\hbar(k_1 + k_2)$	$nk_1 z + nk_2 z - n(\omega_1 - \omega_2)t + \phi_{BS}$
d) Bragg downward kick	$n\hbar(k_1 + k_2)$	$-nk_1 z - nk_2 z + n(\omega_1 - \omega_2)t + \phi_{BS}$
e) Bloch upward kick	$N\hbar(k_1 + k_2)$	$\Delta\phi_{BO} = (2Nk - \frac{4N^2\omega_r}{c})\Delta z$
f) Bloch downward kick	$-N\hbar(k_1 + k_2)$	$\Delta\phi_{BO} = (2Nk - \frac{4N^2\omega_r}{c})\Delta z$

Table 2.3: Summary of momentum and phase transfer for different pulse types. For type a-d, they are transferred to the deflected path. For type e-f, momentum is transferred to both paths.  $\Delta\phi_{BO}$  is defined as phase difference between two paths added by Bloch oscillations. The sign of the phase difference is defined in the same way as the sign of  $\Delta z$ .

the presence light atom interaction. Integrating Schrödinger Equation for general atom interferometer phase calculation could be cumbersome. Here are some simplified rules that could be generalized from solving Schrödinger Equations as we did before. They are summarized here in Table 2.3 and shown in Figure 2.17

During a pulse, if a photon is absorbed, atom will gain exactly the same phase the absorbed photon is carrying. Likewise, if a photon is emitted, atom will lose exactly the same

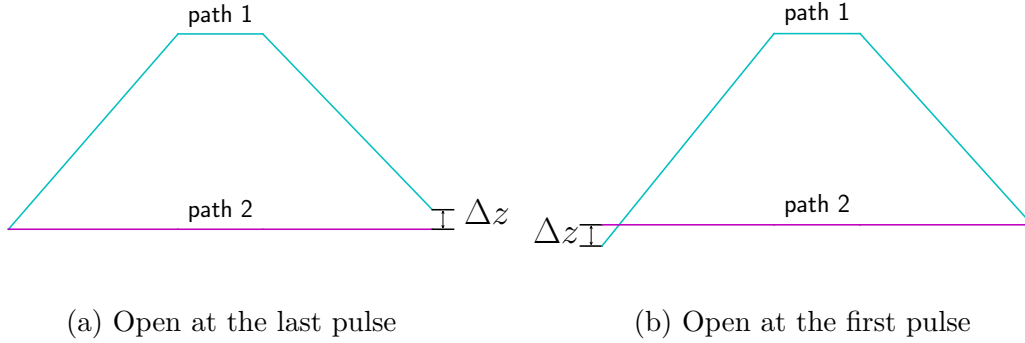


Figure 2.18: Splitting phase in non-closure interferometers

phase the the emitted photon is carrying. The photon phase could be obtained by the phase of the laser fields (only in the case of stimulated emission for the emitted photon). For Raman and Bragg beam splitter, the process could be simplified as absorbing and spontaneous emitting photon pairs, except that there is an additional diffraction phase given by the transition matrix elements. We have also analyzed Bloch oscillations momentum and phase transfer and presented here.

### Splitting Phase

Splitting phase is a special type of phase introduced in interferometers where two paths don't exactly close. Theoretically when two paths don't close, we may be able to distinguish which-way the atom went through so there would be no interference. But in reality, atom is not an infinitesimal point particle. It is a wave packet with certain coherent length. As long as the separation between two paths at the last (or the first) pulse is smaller than the coherent length ( 100nm given atom temperature in our experiments) [57], we could still observe interference. But the offset in space will introduce another phase term from the matter wave itself as there is a phase difference between different parts of the matter wave. That is the so-called splitting phase. Practically this can be calculated in either case (a) or case (b) as shown in the figure, considering the open end at the first pulse or the past pulse. The splitting phase is equal to the matter wave phase difference between two paths. If we label paths according to the figure, then the total phase difference of the whole interferometer for both cases would be

$$\Delta\Phi = \begin{cases} \phi_1 - \phi_2 + \frac{p_{\text{last}}}{\hbar}(z_{1, \text{last}} - z_{2, \text{last}}) & \text{case a} \\ \phi_1 - \phi_2 + \frac{p_{\text{first}}}{\hbar}(z_{1, \text{first}} - z_{2, \text{first}}) & \text{case b,} \end{cases} \quad (2.131)$$

where  $p_{\text{first}}$  and  $p_{\text{last}}$  are the momentum of atom at the first or the last pulse,  $z_{i, \text{first}}$  and  $z_{i, \text{last}}$  the location of path  $i$  at the first or the last pulse.

Note that this phase term is not Lorentz invariant. It depends on the reference frame we are choosing. But it doesn't bring crisis to the phase calculation. It can be proved that the

phase difference of a non-closure atom interferometer is reference frame dependent. Adding the splitting phase exactly cancels this dependence so the system is Lorentz invariant as expected. It has also to be noted that both cases are not equivalent when atom trajectories under consideration are influenced by gravity gradient. But based on the perturbation theory, using non-perturbed trajectories is sufficient for us [56]. Therefore both cases shown in Figure 2.18 give equivalent result in our calculation.

## Mach-Zehnder Atom Interferometer

Mach-Zehnder is the most basic atom interferometer geometry we have introduced in the previous section. With gravity gradient included, we can get the following formula for the phase difference [45].

$$\Delta\Phi = 2nkT^2(g + \gamma(\frac{7}{12}gT^2 - z_0 - (v_0 + \frac{n\hbar k}{m})T)) \quad (2.132)$$

where  $n$  is the Bragg order,  $k$  laser wavenumber,  $T$  pulse separation time,  $z_0/v_0$  initial location/velocity. In our experiment, we don't run single Mach-Zehnder atom interferometer simply because there is no vibration isolation built in our system. Any vibration will be coupled to gravity acceleration so when pulse separation  $T$  is large, vibration phase noise will wash out visible fringes.

## Dual Mach-Zehnder Gravity Gradiometer

But vibration noise won't be a problem for dual Mach-Zehnder configuration. Dual Mach-Zehnder interferometer is simply two Mach-Zehnder interferometers running at the same time. So phase noise from laser or vibration would be common for both and the phase difference between two interferometer would be vibrational noise independent. This configuration is commonly used by us to measure gravity gradient  $\gamma$ . In our experiment, such a gravity gradiometer is configured as shown in the Figure 2.19. We use a single Bragg beam splitter to split the initial wave packet into two different velocity classes. After delaying for  $T_1$  we apply dual Bloch lattices which simultaneously accelerate two wave packets in opposite directions so as to further split them. After delaying for  $T_2$ , two wave packets are spatially separated by roughly  $\frac{2\hbar k}{m}(nT_1 + NT_2)$  where  $n$  and  $N$  are Bragg and Bloch orders. Due to different initial velocities of two interferometers, simultaneous Bragg beam splitters are required to address both interferometers at the same time. In order for Bragg diffractions to be resonant, we shift the lower beam frequency by  $4\omega_r$  (recoil frequency  $\omega_r = \frac{\hbar k^2}{2m}$ ) and run the upper beam in dual frequency mode ( $\omega_2 \pm \omega_m$  where  $\omega_m = 4\omega_r(2N + n)$ ). The last three simultaneous Bragg diffractions consist the dual Mach-Zehnder atom interferometer. After all pulses, we can detect all four output port to extract the phase. If we define the phase of the upper and the lower interferometers as  $\Delta\Phi_u$  and  $\Delta\Phi_l$  respectively, the population of all

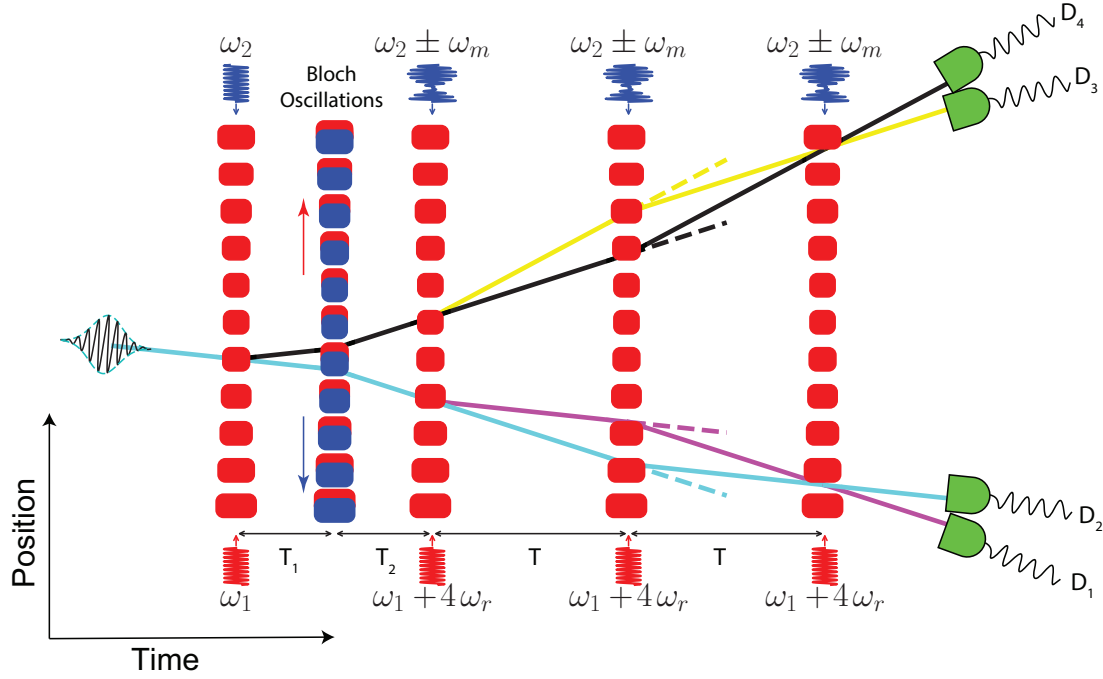


Figure 2.19: Dual Mach-Zehnder Gravity Gradiometer Configuration

four output ports could be written as

$$\langle D_1 \rangle = \frac{a_l}{2}(1 + \cos(\Delta\Phi_l)) + b_1 \quad (2.133)$$

$$\langle D_2 \rangle = \frac{a_l}{2}(1 - \cos(\Delta\Phi_l)) + b_2 \quad (2.134)$$

$$\langle D_3 \rangle = \frac{a_u}{2}(1 + \cos(\Delta\Phi_u)) + b_3 \quad (2.135)$$

$$\langle D_4 \rangle = \frac{a_u}{2}(1 - \cos(\Delta\Phi_u)) + b_4 \quad (2.136)$$

We can define

$$X = \frac{\langle D_1 \rangle - \langle D_2 \rangle}{\langle D_1 \rangle + \langle D_2 \rangle} = \frac{a_l}{a_l + b_1 + b_2} \cos(\Delta\Phi_l) + \frac{b_1 - b_2}{a_l + b_1 + b_2} = C_l \cos(\Delta\Phi_l) + O_l \quad (2.137)$$

$$Y = \frac{\langle D_3 \rangle - \langle D_4 \rangle}{\langle D_3 \rangle + \langle D_4 \rangle} = \frac{a_u}{a_u + b_3 + b_4} \cos(\Delta\Phi_u) + \frac{b_3 - b_4}{a_u + b_3 + b_4} = C_u \cos(\Delta\Phi_u) + O_u \quad (2.138)$$

Thus we have defined the contrasts  $C_l$ ,  $C_u$  and offsets  $O_l$ ,  $O_u$  of the interferometers accordingly. Meanwhile, the upper and lower phase can be written as a combo of common mode phase and differential mode phase. i.e.

$$\Delta\Phi_l = \Phi_c + \frac{\Phi_d}{2} \quad (2.139)$$

$$\Delta\Phi_u = \Phi_c - \frac{\Phi_d}{2} \quad (2.140)$$



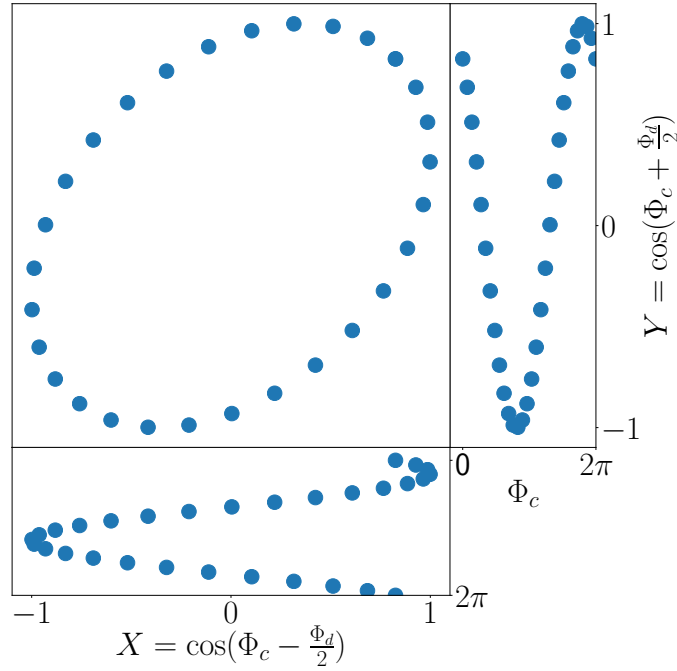


Figure 2.20: Ellipse Fitting Technique

In the experiment, the differential phase is generally extracted through ellipse fitting [58]. As we plot the quantities  $X$  and  $Y$  in a cartesian coordinate while we scan the common mode phase, we can obtain an ellipse as shown in Figure 2.20. And the differential phase could be obtained by the orientation of the ellipse. In the experiment, the common mode phase is automatically scanned by vibration noise so we don't need to add one artificially. More details about the ellipse fitting techniques can be found in the literatures [58, 59, 60, 61, 62]

The ellipse fitting technique we are using gives minimum systematic error when the differential phase is close to  $\pi/2$ . For this purpose we add a ramp  $r_m$  to the modulation frequency  $\omega_m$  to give an artificial phase. In general the differential phase due to gravity gradient tends to be small ( $\sim 100$  mrad). So we add  $\pm\pi/2$  through the ramp and take the average value to cancel the ramp. With the ramp added, the differential phase is given as [62]

$$\Phi_d = -2nT^2r_m + \frac{8gn(n+2N)T^2\omega_r}{c} + 8nT^2\gamma\omega_r(n(T+T'_1+T'_2) + N(2T-NT_B+2T'_2)) \quad (2.141)$$

where pulse separation time  $T$ ,  $T'_1$ ,  $T'_2$  is defined as shown in the figure.  $T_B$  is Bloch oscillations pulse duration. We have used this Dual Mach-Zehnder interferometer to successfully determine the local gravity gradient  $\gamma$  below 1% accuracy as required by the fine-structure constant measurement. More analysis will be discussed in Section 5.2.

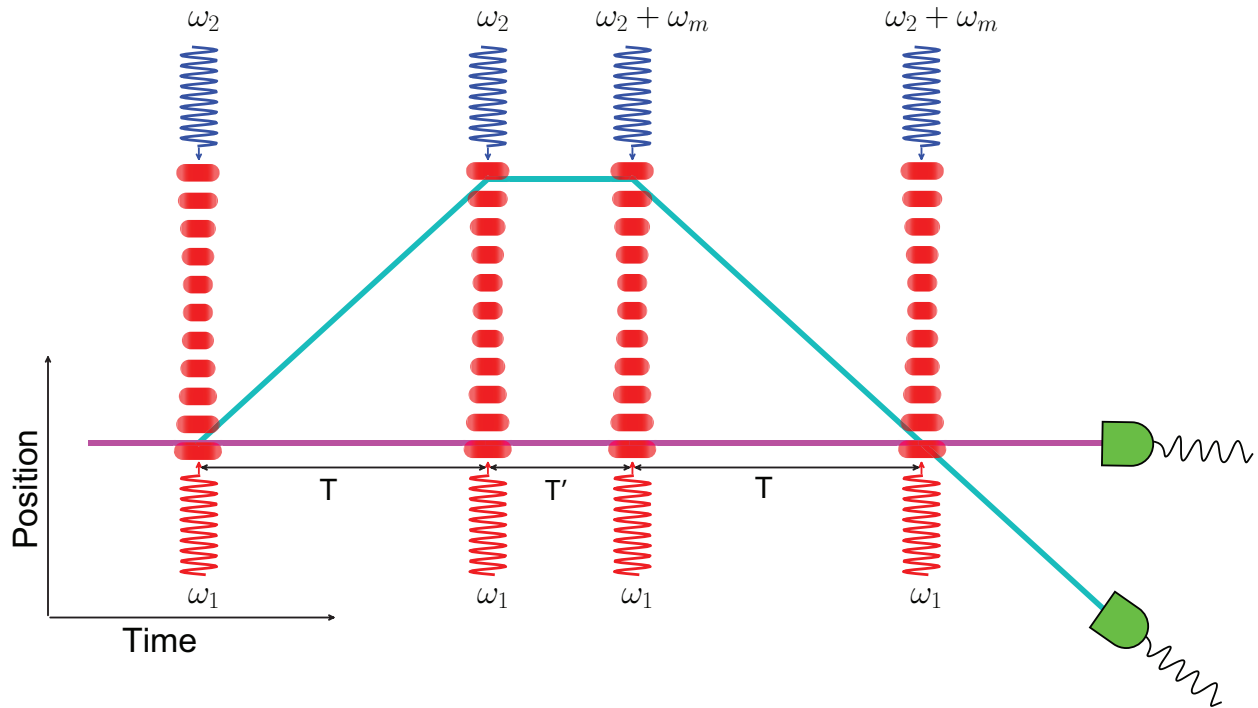


Figure 2.21: Ramsey Bordé Atom Interferometer Configuration

## Ramsey-Bordé Atom Interferometer

Ramsey-Bordé is the main configuration we use to measure the fine-structure constant. As we mentioned earlier that what we are measuring directly with atom interferometer is recoil frequency  $\omega_r$ . Through the recoil frequency measurement we can determine the quotient  $h/M$  and thus the fine-structure constant with the input of the Rydberg constant and electron mass and Cesium mass. In a symmetric configuration like Mach-Zehnder atom interferometer, major phase terms depending on the recoil frequency would be canceled in the phase difference. So asymmetric geometry is essential to probe the recoil frequency in Ramsey-Bordé interferometer. It consists of four  $\pi/2$  pulses for beam splitting and recombining as shown in Figure 2.21. With Bragg diffraction beam splitters, if we keep the frequency of upward going Bragg beam constant, we need to add a frequency shift  $\omega_m$  to the downward going beam for the 3rd and the 4th beam in order to keep them resonant. The final phase difference of this type of interferometer is [44, 61, 62]

$$\begin{aligned}
\Delta\Phi = & -nT\omega_m\left(1 + \frac{v_0}{c}\right) + \frac{gn\omega_m}{2c}(3T^2 + 2TT') \\
& + 8n^2T\omega_r\left(1 + \frac{\gamma}{12}(2T^2 + 3TT' + 3T'^2)\right) \\
& + 2gknT(T + T')\left(1 + \frac{\gamma}{12}(7T^2 + 7TT' + 2T'^2)\right) \\
& + knT\gamma(T + T')((2T + T')v_0 + 2z_0) + 4n^2\omega_rT\frac{\omega_m}{\omega}
\end{aligned} \tag{2.142}$$

The higher order terms have been discarded here. Note that gravitational acceleration has a major contribution to the phase difference. In order to determine the recoil frequency accurately, we also need to determine the local gravitational acceleration accurately. And this gravity dependence also means vibration noise will be coupled to the system as well. So we need a good vibration isolation system to do this measurement well. Given these thoughts, a new technique of simultaneously conjugated Ramsey Bordé configuration was proposed and realized by Holger Müller *et al.* [63]. It uses the same four Bragg pulses to drive two Ramsey Bordé atom interferometers at the same time as shown in Figure 2.22. In order to drive the conjugated interferometer, we add another frequency component  $\omega_2 - \omega_m$  to the downward going beam at the 3rd and 4th pulses so it's running at dual frequency mode. Under this configuration, the junk atoms we used to discard after the 2nd pulse are used for this conjugated interferometer. We can define interferometer fringe parameters for the four output port signals as

$$X = \frac{\langle D_1 \rangle - \langle D_2 \rangle}{\langle D_1 \rangle + \langle D_2 \rangle} = C_l \cos(\Delta\Phi_l) + O_l \tag{2.143}$$

$$Y = \frac{\langle D_3 \rangle - \langle D_4 \rangle}{\langle D_3 \rangle + \langle D_4 \rangle} = C_u \cos(\Delta\Phi_u) + O_u \tag{2.144}$$

And the phase difference of the upper interferometer ( $\Delta\Phi_l$ ) and the lower interferometer ( $\Delta\Phi_u$ ) could also be decomposed to the common mode phase  $\Phi_c$  and the differential mode phase  $\Phi_d$  in the same way as we did in the previous section. It turns out that the differential mode phase cancels the major contribution from gravitational acceleration, giving

$$\begin{aligned}
\Phi_d = & -2nT\omega_m\left(1 + \frac{v_0}{c}\right) + \frac{3gn\omega_m}{c}(3T^2 + 2TT') \\
& + 16n^2\omega_rT\left(1 + \frac{\gamma}{12}(2T^2 + 3TT' + 3T'^2)\right) \\
& - 4n^2\omega_rT\frac{\omega_m}{\omega}
\end{aligned} \tag{2.145}$$

So while we are scanning the common mode phase, the differential mode phase can be extracted by ellipse fitting. As the common mode phase is canceled, so also the vibration and laser noise that enter through the common mode phase would be canceled. So in this configuration, even though each interferometer is very noisy, we can still obtain very good signal to noise ratio in the differential mode phase extraction. The other important ingredients like gravity gradient or initial velocity will be discussed in detail in Chapter 5. We have

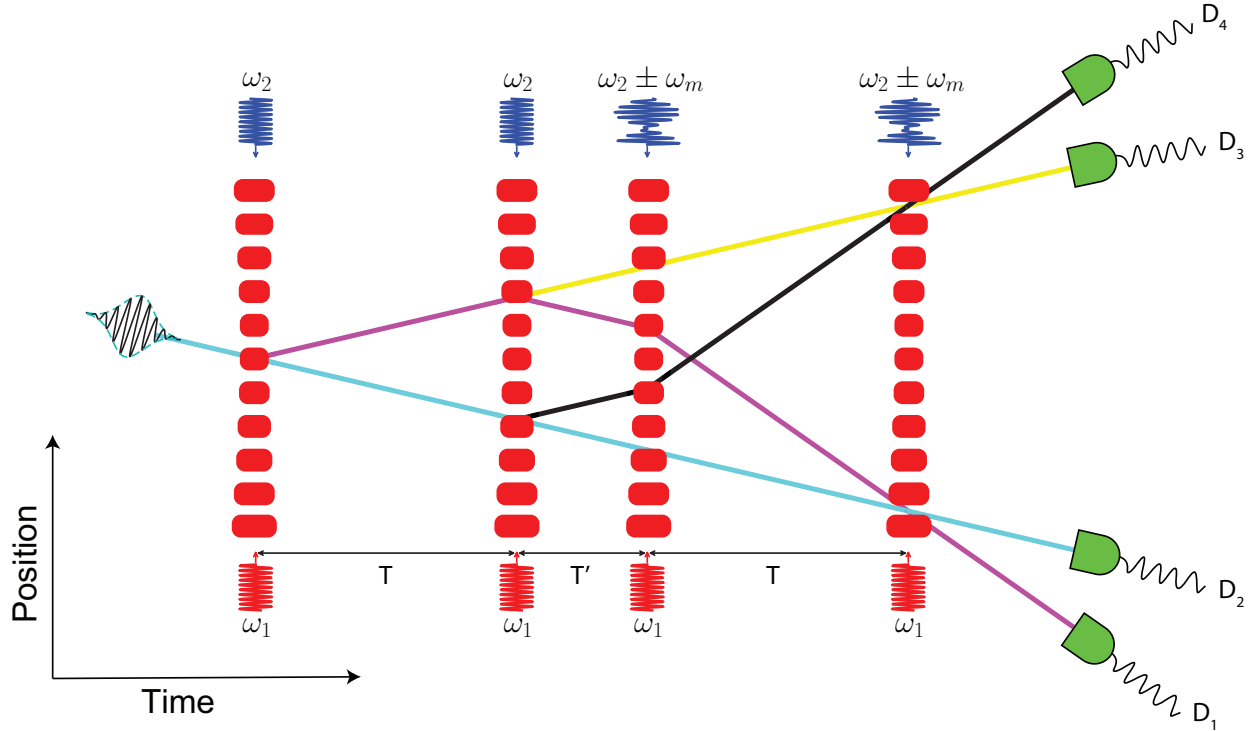


Figure 2.22: Simultaneously Conjugated Ramsey Bordé Atom Interferometers Configuration

demonstrated the recoil measurement down to parts per billion (ppb) precision with this configuration. But in order to push sub-ppb precision, we need even more sensitive configuration to do the measurement. That's the reason why we introduced Bloch oscillations between the second and third pulse so as to add common mode acceleration to each interferometer as shown in Figure 2.23. With Bloch oscillations inserted, an additional major term linearly dependent on Bloch order  $N$  is added. In our experiment, a large Bloch order ( $N > 100$ ) can be implemented compared to the small Bragg order ( $n=5$ ) so we gain sensitivity quite a bit through Bloch oscillations. Further analysis of sensitivity would be discussed in Chapter 4. Here with Bloch oscillations the differential mode phase is given as

$$\begin{aligned} \Phi_d = & -2nT\omega_m\left(1 + \frac{v_0}{c}\right) + \frac{gnT(3T + 2T'_1 + 2T'_2)\omega_m}{c} - 4n^2\omega_r T \frac{\omega_m}{\omega_L} \\ & + 16n(n + N)\omega_r T \left[ 1 + \frac{\gamma}{12} \left[ \frac{n}{n + N} \left( 2T^2 + 3TT'_2 + 3(T'_1 + T'_2)^2 \right) \right. \right. \\ & \left. \left. \frac{2N}{n + N} \left( T^2 + 3T(T'_2 - \frac{NT_B}{2}) + 3T'_2(T'_2 - NT_B) + (N^2 - \frac{1}{4})T_B^2 \right) \right] \right] \end{aligned} \quad (2.146)$$

where  $T_B$  is the period of one Bloch oscillation defined in Equation 2.120 and  $v_0$  the initial velocity at the first pulse. This is the main phase formula we will be using to extract recoil

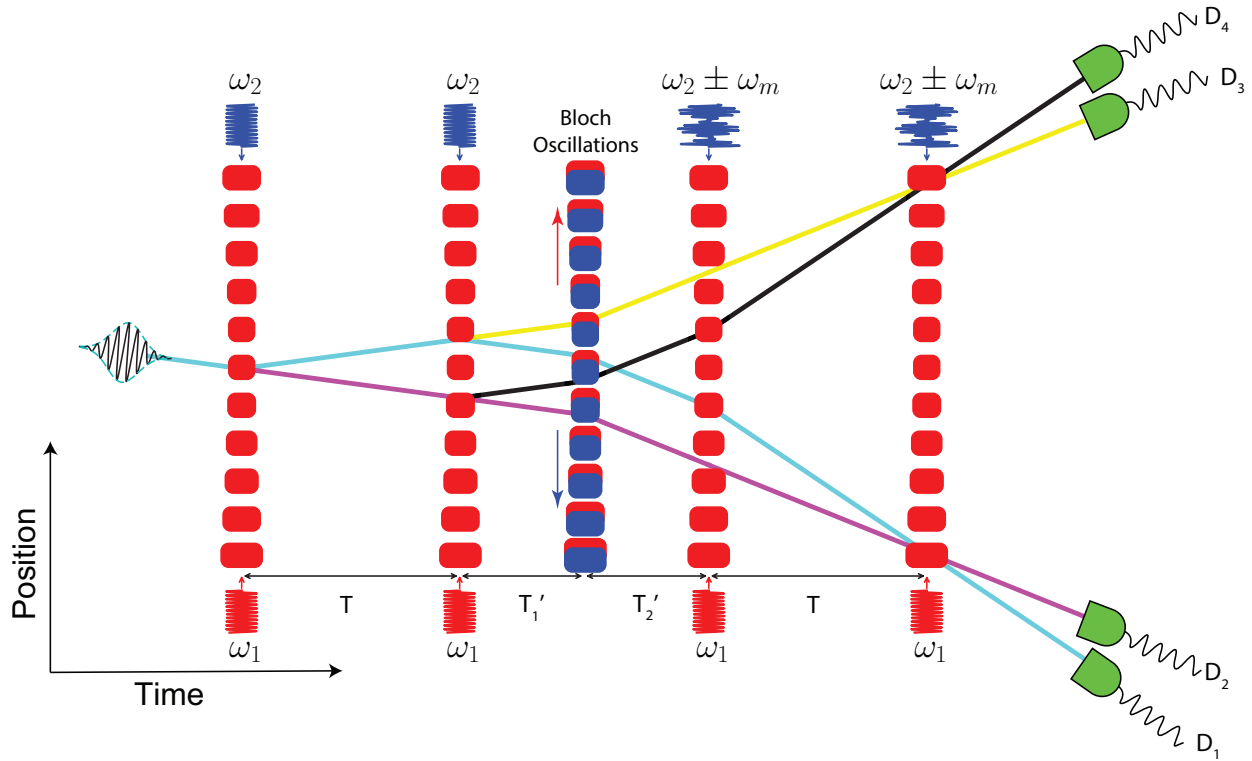


Figure 2.23: Simultaneously Conjugated Ramsey Bordé Atom Interferometers Configuration with Bloch Oscillations

frequency for the fine-structure-constant measurement. Given such a complex phase formula, it's also important to know the physical meaning of each major phase term.

### Recoil Phase Term

$$16n(n + N)\omega_r T \tag{2.147}$$

This is the main phase of Ramsey Bordé atom interferometers we are measuring. Through measuring this phase term we can determine the recoil frequency.

### Modulation frequency Phase Term

$$-2nT\omega_m \tag{2.148}$$

This is the phase added due to the modulation frequency  $\omega_m$  during the last two dual frequencies Bragg pulses. This is the phase term to counterbalance the main phase term. In the experiment, we try to tune  $\omega_m$  so that the overall phase is measured to be zero. Under this condition,  $\omega_m = 8(n + N)\omega_r + \text{small corrections}$ .

### Gravity Gradient Phase Term

$$\frac{4}{3}\gamma n(n+N)\omega_r T \left[ \frac{n}{n+N} \left( 2T^2 + 3TT'_2 + 3(T'_1 + T'_2)^2 \right) \right. \\ \left. \frac{2N}{n+N} \left( T^2 + 3T(T'_2 - \frac{NT_B}{2}) + 3T'_2(T'_2 - NT_B) + (N^2 - \frac{1}{4})T_B^2 \right) \right] \quad (2.149)$$

This is the important phase term to determine the systematic effect due to gravity gradient. Gravity gradient is one of the major systematic uncertainties we need to take into account in this system. It will be discussed in details in Section 5.2.

### Splitting/Doppler Phase Term

$$-2nT\omega_m \frac{v_0}{c} + \frac{gnT(3T + 2T'_1 + 2T'_2)\omega_m}{c} - 4n^2\omega_r T \frac{\omega_m}{\omega_L} \quad (2.150)$$

This is a new term we verified recently [8]. It's very unique to our interferometer geometry where each Ramsey Bordé interferometer does not close at the last pulse. It's because the last two pulses transfer a momentum  $\pm\hbar\omega_m/kc$  different from the momentum transferred by the first two pulses. It's unavoidable in the way we operate the dual frequency splitters. We can view this from different reference frames. When we turn to the lab frame, atoms are moving with a quite large velocity relative to the lab frame ( $\sim v_0$ ). It contributes to a large splitting phase. This splitting phase term plus correction from open atom interferometer gives this phase term. We can also view it from the atom rest frame. In that frame the splitting phase is small. But there is an additional phase due to Doppler shift of the modulation frequency  $\omega_m$  when we transform the reference frame from the lab frame by the velocities of atoms at last two pulses. One can show that the two pictures under different frames of reference are equivalent.

## 2.7 Diffraction Phase

In this section, we will apply Bragg diffraction phase we modeled earlier to Ramsey Bordé atom interferometer specifically in order to explain some experimental phenomena. In a Ramsey Bordé interferometer, we can define  $\Delta\phi_i^j$  (where  $j = u$  or  $l$ ) as diffraction phase difference the upper(u) or the lower(l) atom interferometer received at the  $i^{\text{th}}$  beam splitter. So for simultaneously conjugated interferometers, these phase relation can be explicitly given

as (the atom interferometer configuration under consideration could be found in Figure 2.23.)

$$\Delta\phi_1^l = \phi_{|-5\hbar k\rangle \rightarrow |-5\hbar k\rangle} - \phi_{|-5\hbar k\rangle \rightarrow |5\hbar k\rangle} \quad (2.151)$$

$$\Delta\phi_2^l = \phi_{|-5\hbar k\rangle \rightarrow |-5\hbar k\rangle} - \phi_{|5\hbar k\rangle \rightarrow |-5\hbar k\rangle} \quad (2.152)$$

$$\Delta\phi_2^u = \phi_{|-5\hbar k\rangle \rightarrow |5\hbar k\rangle} - \phi_{|5\hbar k\rangle \rightarrow |5\hbar k\rangle} \quad (2.153)$$

$$\Delta\phi_3^l = \phi_{|-5\hbar k\rangle \rightarrow |-5\hbar k\rangle} - \phi_{|-5\hbar k\rangle \rightarrow |-15\hbar k\rangle} \quad (2.154)$$

$$\Delta\phi_3^u = \phi_{|5\hbar k\rangle \rightarrow |15\hbar k\rangle} - \phi_{|5\hbar k\rangle \rightarrow |5\hbar k\rangle} \quad (2.155)$$

The phase difference for the last pulse is a bit tricky to define. If we define the phase of the states  $|-15\hbar k\rangle$ ,  $|-5\hbar k\rangle$ ,  $|5\hbar k\rangle$ ,  $|15\hbar k\rangle$  right before the last pulse as  $\phi_1$ ,  $\phi_2$ ,  $\phi_3$ ,  $\phi_4$  respectively. The last pulse diffraction phase can be defined as

$$\Delta\phi_{41}^l = \phi_{|-5\hbar k\rangle \rightarrow |-15\hbar k\rangle} - \phi_{|-15\hbar k\rangle \rightarrow |-15\hbar k\rangle} \quad (2.156)$$

$$\Delta\phi_{42}^l = \phi_{|-5\hbar k\rangle \rightarrow |-5\hbar k\rangle} - \phi_{|-15\hbar k\rangle \rightarrow |-5\hbar k\rangle} \quad (2.157)$$

$$\Delta\phi_{43}^u = \phi_{|15\hbar k\rangle \rightarrow |5\hbar k\rangle} - \phi_{|5\hbar k\rangle \rightarrow |5\hbar k\rangle} \quad (2.158)$$

$$\Delta\phi_{44}^u = \phi_{|15\hbar k\rangle \rightarrow |15\hbar k\rangle} - \phi_{|5\hbar k\rangle \rightarrow |15\hbar k\rangle} \quad (2.159)$$

such that the wavefunction of each output port after the last pulse can be written as

$$|-15\hbar k\rangle = C_1 e^{i\phi_1} + C_2 e^{i\phi_2 + \Delta\phi_{41}^l} \quad (2.160)$$

$$|-5\hbar k\rangle = C_1 e^{i\phi_1} + C_2 e^{i\phi_2 + \Delta\phi_{42}^l} \quad (2.161)$$

$$|5\hbar k\rangle = C_3 e^{i\phi_3} + C_4 e^{i\phi_4 + \Delta\phi_{43}^u} \quad (2.162)$$

$$|15\hbar k\rangle = C_3 e^{i\phi_3} + C_4 e^{i\phi_4 + \Delta\phi_{44}^u} \quad (2.163)$$

So the interference signal  $X$  and  $Y$  are,

$$X = \frac{|\langle -15\hbar k | \Phi \rangle|^2 - |\langle -5\hbar k | \Phi \rangle|^2}{|\langle -15\hbar k | \Phi \rangle|^2 + |\langle -5\hbar k | \Phi \rangle|^2} \approx \frac{\pm C_1 C_2 \sin(\phi_2 - \phi_1 + \frac{\Delta\phi_{41}^l + \phi_{42}^l}{2})}{|C_1|^2 + |C_2|^2} \quad (2.164)$$

$$Y = \frac{|\langle 5\hbar k | \Phi \rangle|^2 - |\langle 15\hbar k | \Phi \rangle|^2}{|\langle 5\hbar k | \Phi \rangle|^2 + |\langle 15\hbar k | \Phi \rangle|^2} \approx \frac{\pm C_3 C_4 \sin(\phi_4 - \phi_3 + \frac{\Delta\phi_{43}^u + \phi_{44}^u}{2})}{|C_3|^2 + |C_4|^2} \quad (2.165)$$

where we have applied approximation based on the facts that  $\Delta\phi_{41}^l - \Delta\phi_{42}^l \approx \pm\pi$  and  $\Delta\phi_{43}^u - \Delta\phi_{44}^u \approx \pm\pi$ . And the sign in the formula for  $X$  and  $Y$  are determined by the sign in these two approximation conditions. Based on the definition above, the diffraction phase contribution for each interferometer can be calculated as

$$\Delta\phi_{\text{diffraction}}^l = \Delta\phi_1^l + \Delta\phi_2^l + \Delta\phi_3^l + \frac{1}{2}(\Delta\phi_{41}^l + \Delta\phi_{42}^l) \mp \frac{\pi}{2} \quad (2.166)$$

$$\Delta\phi_{\text{diffraction}}^u = \Delta\phi_1^u + \Delta\phi_2^u + \Delta\phi_3^u + \frac{1}{2}(\Delta\phi_{43}^u + \Delta\phi_{44}^u) \mp \frac{\pi}{2} \quad (2.167)$$

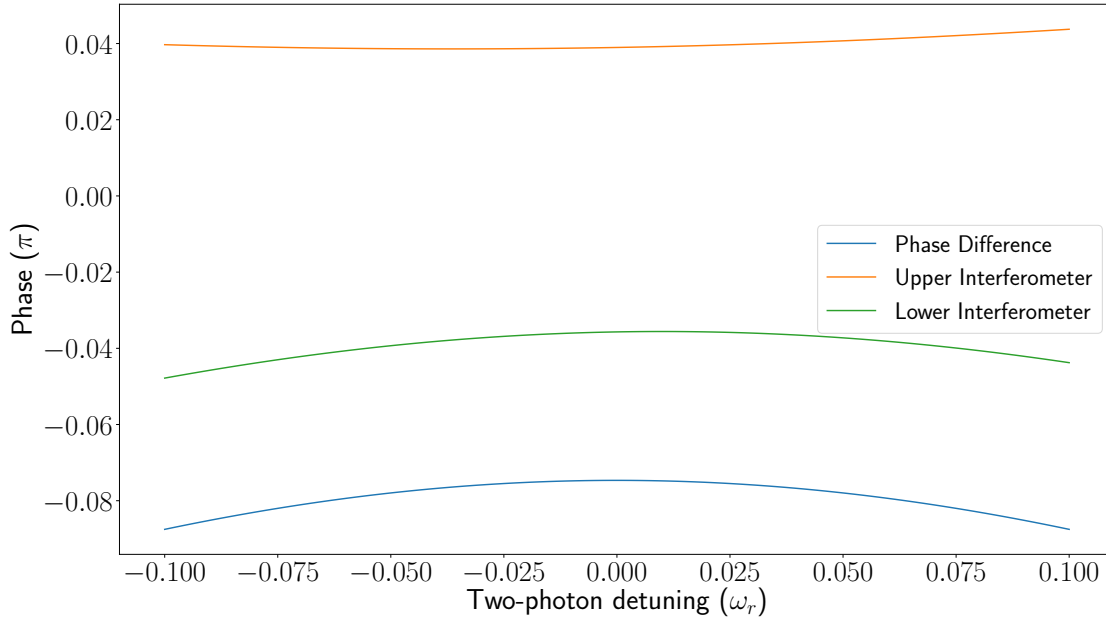


Figure 2.24: Ramsey Bordé atom interferometer diffraction phase vs. two-photon detuning at Bragg order  $n=5$ , Bloch order  $N=0$

where the minus sign in this formula corresponds to the plus sign in the formula above for  $X$  and  $Y$ . Taking the difference between the lower interferometer phase and the upper interferometer phase, we can get the equation of diffraction phase contribution to the overall phase difference,

$$\Phi_{d, \text{diffraction}} = (\Delta\phi_2^l - \Delta\phi_2^u) + (\Delta\phi_3^l - \Delta\phi_3^u) + \frac{1}{2}(\Delta\phi_{41}^l + \Delta\phi_{42}^l - \Delta\phi_{43}^u - \Delta\phi_{44}^u) \quad (2.168)$$

It shows that diffraction phase from the first pulse does not contribute to the overall conjugated interferometer phase difference. So we don't have to consider that in the analysis below. With these equations, we can scan Bragg two-photon detuning (equivalent to scanning atom velocity) and two-photon Rabi frequency to get Ramsey Bordé simultaneously conjugated interferometers overall diffraction phase dependence on Bragg two-photon detuning and intensity [62].

Take Bragg order  $n=5$ , Bloch order  $N=0$  (without Bloch oscillations), we can plot the total diffraction phase of the upper interferometer and the lower interferometer individually as well as their difference as shown in Figure 2.24. We can see that besides the parabola shape, there is an additional phase shift even at zero detuning. If we plot each pulse's contribution to the diffraction phase as a function of two-photon detuning as shown in Figure 2.25, we could notice that the parabola shape is the nature of Bragg diffraction but that additional phase shift mostly comes from the last two pulses. This additional phase shift could be suppressed when we operate it with large Bloch oscillations as shown



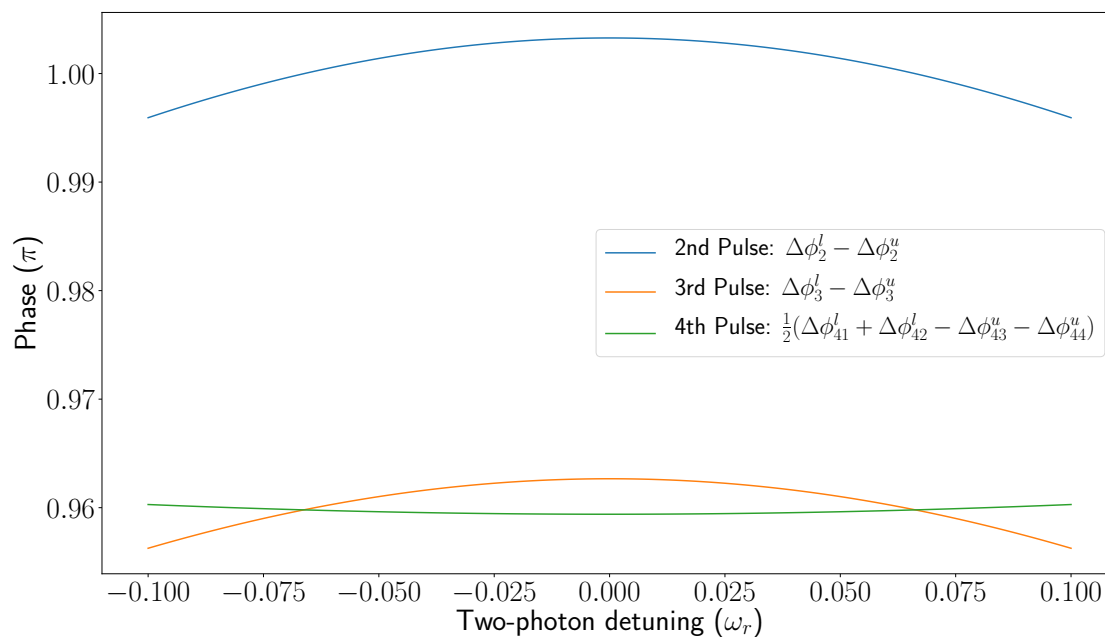


Figure 2.25: Each pulse’s contribution to Ramsey Bordé atom interferometer diffraction phase of each pulse vs. two-photon detuning

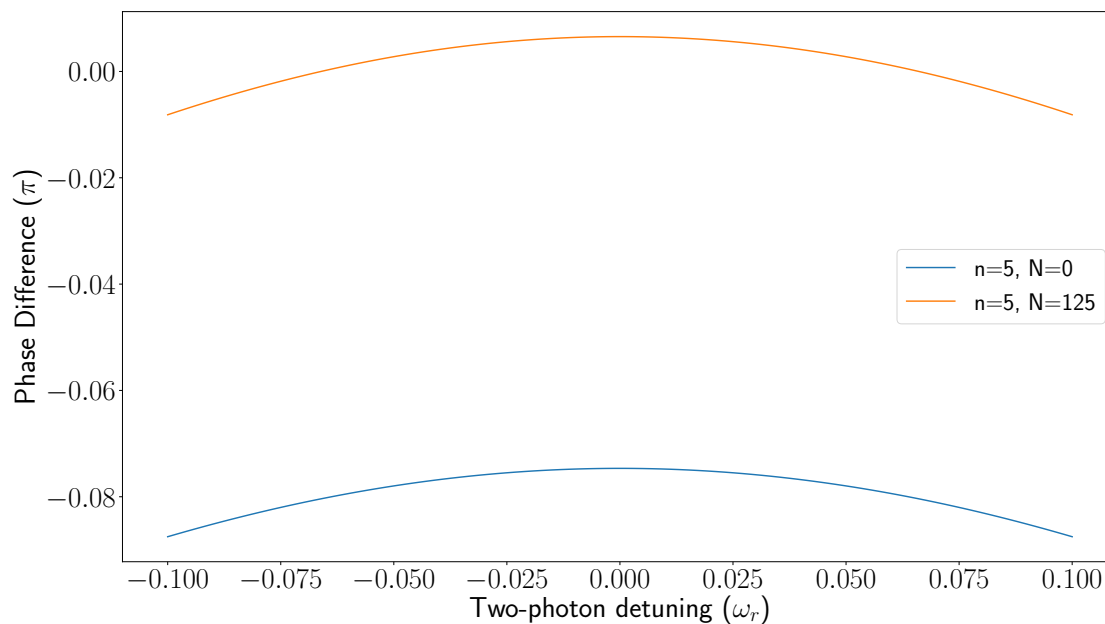


Figure 2.26: Comparison of diffraction phase dependence on two-photon detuning with and without Bloch oscillations

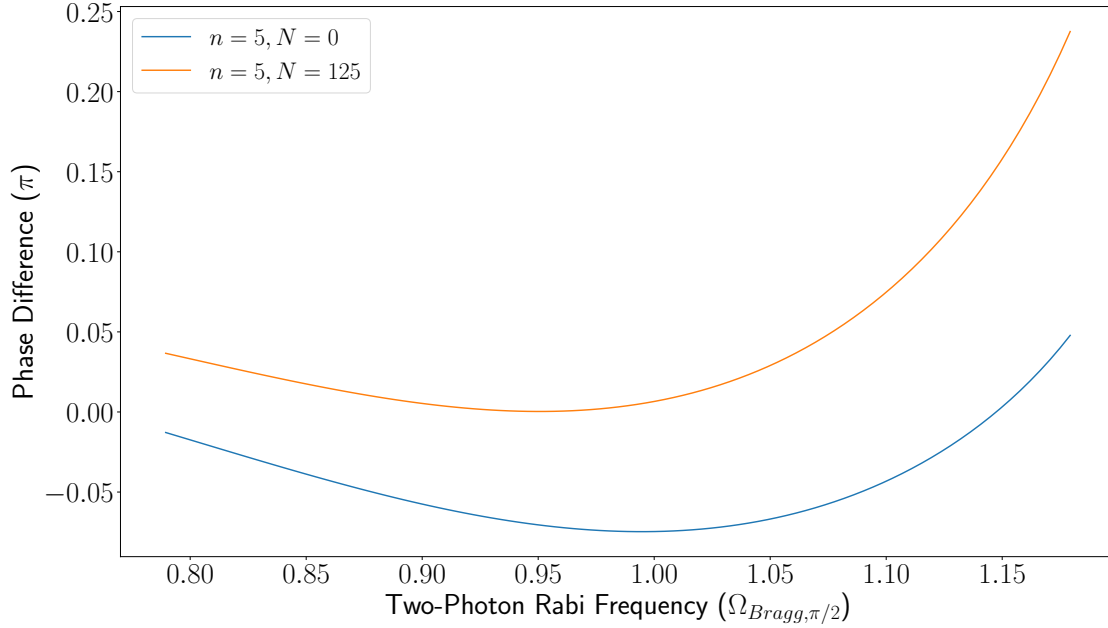
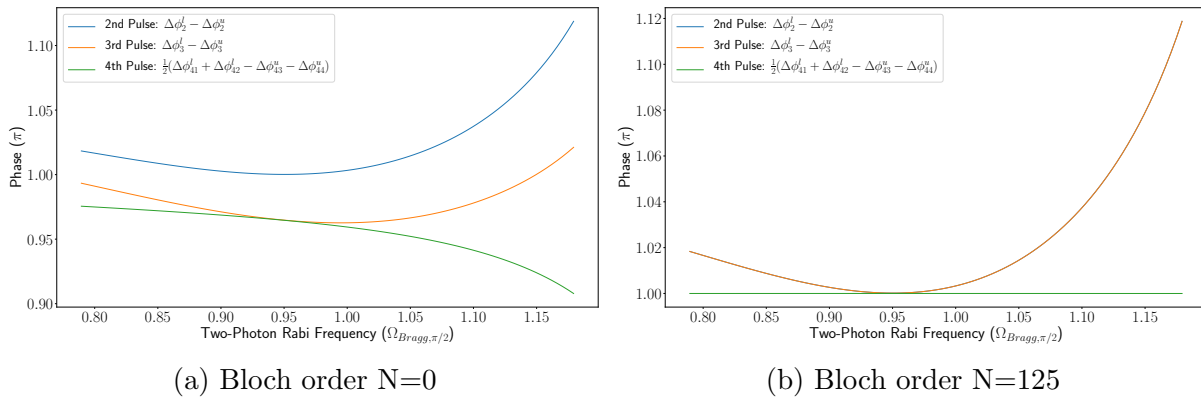


Figure 2.27: Comparison of diffraction phase dependence on two-photon Rabi frequency with and without Bloch oscillations



(a) Bloch order N=0

(b) Bloch order N=125

Figure 2.28: Each pulse's contribution to Ramsey Bordé atom interferometer diffraction phase vs. two-photon Rabi frequency

in Figure 2.26. That is because Bloch oscillations further increase the velocity difference between two interferometers so that cross-talk between dual-frequency Bragg diffraction would be highly suppressed. In this case, the third pulse contribution would coincide with the second pulse contribution, which results in a very small overall phase shift as shown in Figure 2.26. Diffraction phase dependence on two-photon detuning will be very useful for us to find the optimal Bragg frequency as shown in Section 3.6 Figure 3.36. We could also study the diffraction phase dependence on Bragg intensity as shown in Figure 2.27. Again, adding Bloch oscillations would shift the zero detuning diffraction phase closer to 0 as shown in Figure 2.27. Another interesting thing we found is that applying large order Bloch oscillations would significantly remove 4th pulse diffraction phase dependence on beam intensity as shown in Figure 2.28 In practice, Bragg beam intensity could vary according to absolute time  $T$  of the pulse or absolute location of atoms at that moment. But since intensity doesn't matter for the 4th pulse, we can align the 2nd and the 3rd pulses such that they would happen at the same absolute time for all pulse separation time  $T_s$ . In this way even though there is still a large diffraction phase caused by the 2nd and the 3rd pulse, it will be the same for all  $T_s$ . So it won't add additional higher order diffraction phase linear to  $T$ .

## 2.8 Monte Carlo Simulation

All the theories mentioned above is based on the ideal picture of a single atom addressed by plane waves. That's not how experiment is realized in the lab. When we prepare a sample, it's always an atom cloud with Gaussian-like spatial and velocity distribution. And the beam we use for Raman, Bragg and Bloch processes are close to Gaussian beam. It means atoms at different location relative to the beam center and move with different longitudinal velocity would experience different detuning and Rabi frequency. It's hard to use any single atom theory to quantitatively characterize the behavior of the interferometer. So it's important to have a Monte Carlo simulation system not only to understand some collective behavior of the interferometer, but also to help calculate certain systematic uncertainties for precision measurement.

Monte Carlo simulation is a quite broad term in this project. Depending on the needs, we could add in different factors into consideration. But three basic necessary building blocks are atom state distribution, beam characterization and amplitude-phase function for a certain process. Most of the time we only apply 2D Monte Carlo simulation where atom position and velocity distribution along the  $z$ -axis is ignored. It is sufficient when the distribution on the third dimension is irrelevant or the spreads is too narrow to make a difference. Only in one case when we study the influence of atom thermal motion on diffraction phase do we apply 3D Monte Carlo simulation. In general we can use Gaussian distribution to set initial position and velocity of each individual atom. Most programming languages have such built-in library that supports normal distribution sampling. But in case we need precision for the simulation result, we can use an arbitrary distribution obtained from experiment

Simulation Type	Atom Distribution	Beam	Required Processes
SS Efficiency	2D, Gaussian from CCD data	Gaussian from beam profile	Raman
VS Efficiency	3D, Distribution from SS simulation	Gaussian from beam profile	Raman
Atom Interferometer Contrast	2D, Distribution from VS simulation	CCD measurement	Bragg, Bloch
Thermal Effects on Diffraction Phase	3D, Gaussian from CCD data	Gaussian from beam profile	Bragg
Guoy Phase	2D, Distribution from SS simulation	CCD measurement	Bragg, Bloch

Table 2.4: List of Monte Carlo simulations and specific techniques involved

data or another simulation. This can be done by calculating inverse cumulative distribution function, which establishes a relation between cumulative probability and the value of a random variable. For example, since there is rotational symmetry with respect to the z-axis for atom distribution, we can calculate the inverse cumulative distribution function as a function of the polar radius  $r$ . And we can use computer to generate a random number from 0 to 1 to find the corresponding  $r$ . The polar angle can be separately generated by a random number from 0 to  $2\pi$ . Thus we can generate arbitrary atom distribution with rotational symmetry.

For beam characterization, in general, a pure Gaussian beam is sufficient for most simulations. The parameters of the Gaussian beam model can be determined by a beam profile measurement. But for simulation of atom interferometer contrast or Gouy phase, the local structure of beam is critical. So we directly use CCD beam measurement as input to simulate the beam. The local intensity determines the local Rabi frequency so as to determine the amplitude and phase of a certain pulse. For Raman process, this functional form could be obtained analytically as in Section 2.3. But for Bragg and Bloch processes, we relies on the numerical simulation as in Section 2.4 and 2.5 to establish such a function with methods of interpolation, which helps speed up the simulation as well.

The implementation of the Monte Carlo simulation is fairly simple. We precompute the atom distribution function, beam intensity function from measurement. And we also generate amplitude-phase responses for Raman, Bragg and Bloch processes either from analytical function or from an interpolated numerical function. And we use random function generator to generate atom position and velocity based on given distributions. And we let atoms evolve following Newtonian mechanics for exact the same time length until detection according to the experiment. At certain times in the simulation, we also apply certain pulses to exactly follow what we do in the experiment. The Rabi frequency of the pulse is determined by the position of the atom at that specific time relative to the pulse. The detuning could also be determined by atom longitudinal velocity and input frequency of laser beams at that moment. Based on the Rabi frequency and detuning, we multiply an appropriate amplitude and phase factor onto the atom wave function and apply proper momentum transfer to their motional state. After the evolution time, if the atom falls into the detection region at the detection time, it would be read out and added to certain simulated output ports. So we repeat this process millions of times for millions of atoms for one shot of the experiment. In this way we can get the simulated output for each shot. If we are simulating the whole

interferometer process, we will use the same ellipse fitting technique to distract the phase after several shots of data. We use Matlab, Mathematica, Python and C to carry out the simulation depending on the work load. The fastest speed could be realized with C where a full atom interferometer shot with 1 million atoms could be simulated within 1s. But for general purpose, simulations with Matlab or Python are sufficient in speed and are also easy to write and maintain. The details of each type of simulation is summarized in Table 2.4. The results of different types of simulations would be intersperse in Chapter 3-5.

# Chapter 3

## Experiment Setup and Procedure

### 3.1 Overview

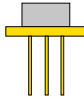
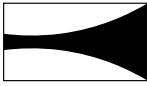
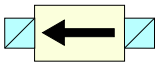
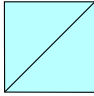
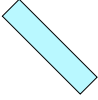
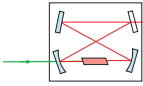


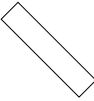
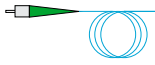

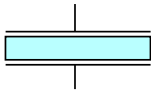
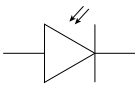
From this chapter, we will be focusing on the experiment side of this project. In this chapter, we will cover basic setup and operating principles of the experiment. Interference of light has been observed experimentally through Young double-slit experiment in early 1800s [64]. It has also been applied as Michelson-Morley interferometer in early 1900s which laid the foundation of special relativity [65]. But it has been truly a challenge for decades to realize matter wave interferometers experimentally after postulation of matter wave as proposed in early days of quantum mechanics [39]. The major challenges revolve around the question how to maintain matter wave coherence as it evolves and splits.

Light and matter wave are very different by nature. Photon has linear dispersion relation so that vacuum is non-dispersive for photons. But atom has quadratic dispersion relation so its wave packet spreads as it propagates. It fundamentally limits the total coherence time of matter wave. The rate the wave packet spreads is related to the momentum distribution of atoms, i.e. its temperature. One way to improve its coherent time is to cool down atoms to lower temperature, which was made possible through the invention of laser cooling and trapping techniques for atoms [66, 67, 68].

Low temperature is also the key to maintain coherence during beam splitters. For atom interferometers, if we are using well-controlled optical lattice as our beam splitters (Bragg or Raman), momentum transfer is on the order of magnitude of  $\hbar k$ . In order to resolve different momentum states especially for Bragg beam splitters, atom momentum spread along the direction of momentum transfer should be way less than the order of  $\hbar k$ . Laser cooling is sufficient to cool down specific atom species below the temperature required. We will revisit laser cooling and trapping in Section 3.3.

For convenience of laser cooling and trapping, atom species like Rubidium or Cesium in the alkali group are the most favored. We chose Cesium in our experiment for the same purpose. Among all alkali atoms, though a smaller recoil frequency may seem to be a disadvantage, Cesium has the smallest recoil temperature as well as the smallest thermal

---

				
Diode Laser	Tapered Amplifier	Isolator	Polarizing Beam Splitter	Mirror
				
Ti-sapphire laser	$\lambda/2$ Waveplate	$\lambda/4$ Waveplate	Beam Splitter	Optical Fiber
				
Acoustic Optical Modulator (AOM)	Electric Optical Modulator (EOM)	Photodetector		

---

Table 3.1: List of symbols used in the optical schematics.

expansion at the same temperature due to its heavy mass. So with only standard laser cooling and without evaporative cooling, Cesium gives the best performance in extending the total coherence time [44]. Though evaporative cooling is able to further cool down atoms, it also makes the experiment cycle a lot slower and may introduce additional systematic errors [69, 62]. So for our specific experiment of the fine-structure constant measurement, Cesium seems to be one of the best choices.

In order to make a Cesium atom interferometer sensitive enough to measure the fine structure constant, we need a vacuum system producing ultra high vacuum required by laser cooling techniques, a optics system delivering all required laser frequencies with enough power for cooling and beam splitting, and an electronics system to generate right control signals at the right time. Among these systems, the most complex is the optics system, which we will be focusing on for most of this chapter.

The optics system can naturally be divided into three subsystems in our experiment: frequencies preparation system, laser cooling system, and coherent manipulation system. They are shown in the system optical schematics below and labelled in red, green and yellow respectively. It is to be noted that this is a simplified optical scheme. All lenses, additional Ti-sapphire components, additional mirrors, additional PBS for polarization purifications are neglected. And the scheme does not show how optics are exactly arranged on the table, and some PBS splitting direction may be inverted for simplicity of drawing. But it shows the essential parts of the experiment and how it works. For details about the entire setup, one can refer to literatures like [62, 61]. All symbols used in the scheme are listed in Table 3.1.

Most of the laser frequencies relevant to our experiment are around Cesium  $D_2$  line as shown in Figure 3.2. Cesium  $D_2$  line is the transition from its ground state  $6^2S_{1/2}$  to one

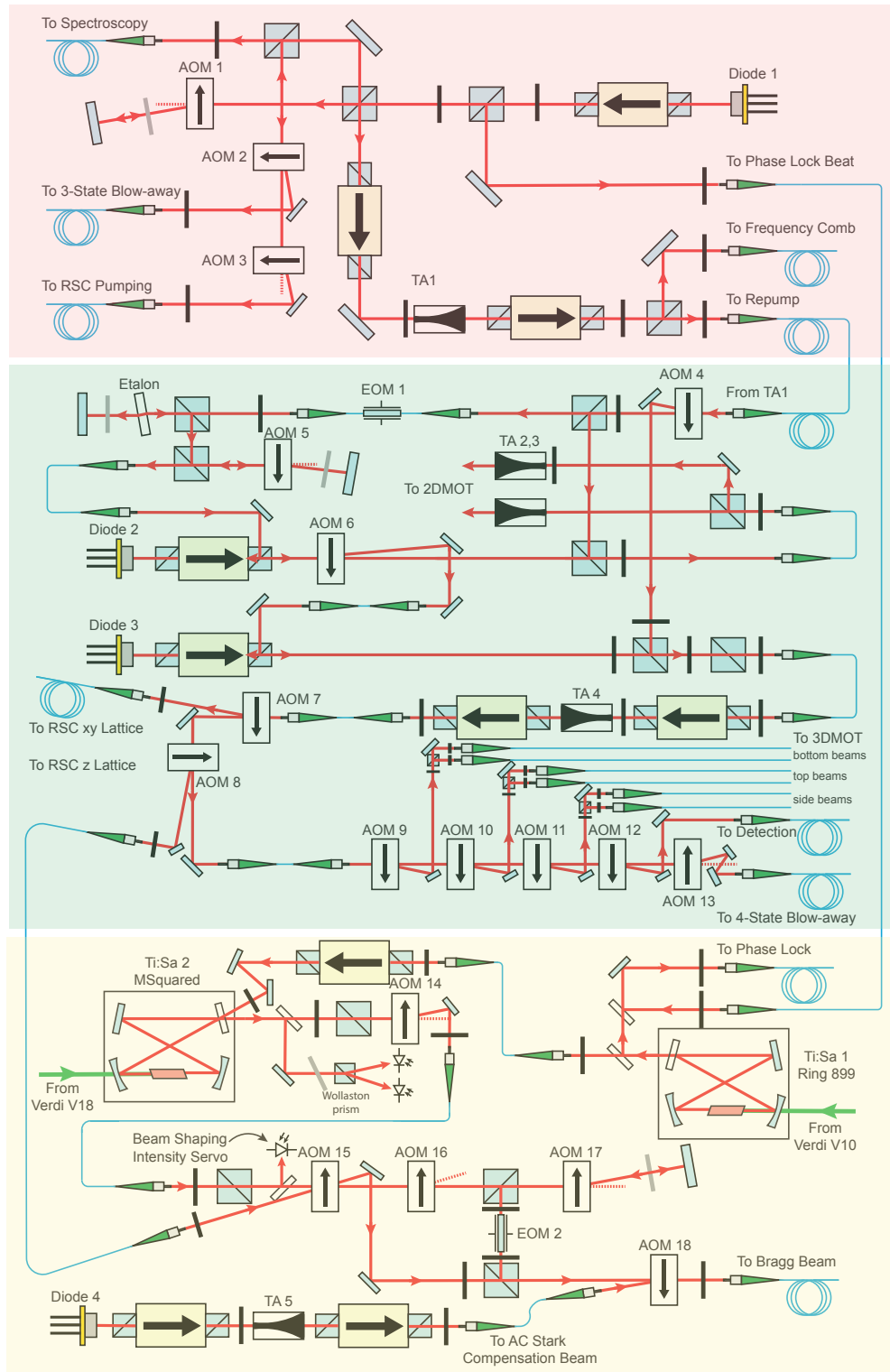
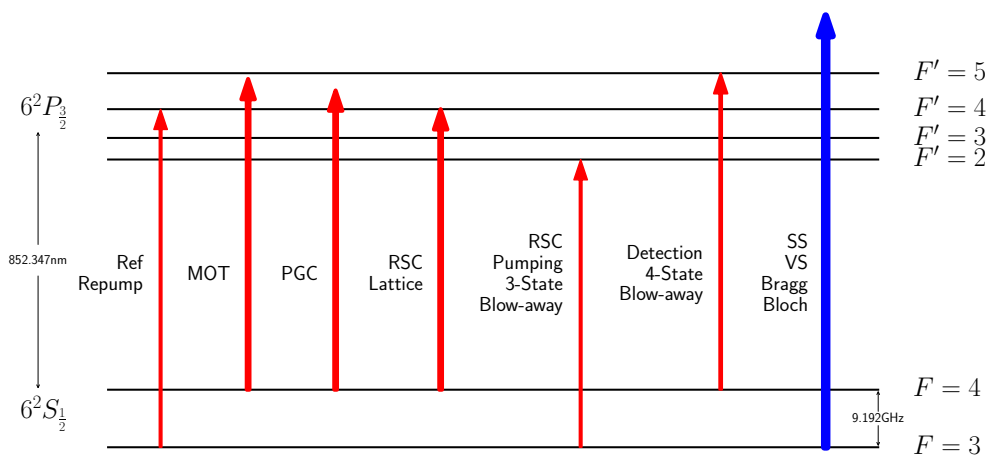


Figure 3.1: Simplified optical schematics. Reference frequencies preparation system, laser cooling and trapping system, and coherent manipulation system are labeled red, green and yellow respectively.



MOT	Magneto-Optical Trap
RSC	Raman Sideband Cooling
PGC	Polarization Gradient Cooling
ARP	Adiabatic Rapid Passage
SS	State Selection
VS	Velocity Selection
ECDL	External Cavity Diode Laser
TA	Tapered Amplifier
Ti:Sa	Titanium doped Sapphire Laser
AOM	Acoustic Optical Modulator
EOM	Electric Optical Modulator
3-state blow-away	laser beam that is resonate with atoms in $F=3$ state and blows them away
4-state blow-away	laser beam that is resonate with atoms in $F=4$ state and blows them away

Table 3.2: List of terms commonly used for this experiment

Figure 3.2: Cesium  $D_2$  line energy levels and laser frequencies [42]. See Section ?? for actual detunings.

excited state  $6^2P_{3/2}$ . The transition frequency corresponds to 852 nm in wavelength. It is accessible by semiconductor lasers as well as Ti-sapphire lasers. These are two basic types we are using in our experiment. These two states further split to 6 hyperfine states. The two hyperfine ground states are separated by the clock frequency about 9.19 GHz. And four hyperfine excited states are separated by hundreds of MHz [42]. We start from an External Cavity Diode Laser (ECDL) locked to transition ( $F = 3 \rightarrow F' = 4$ ) as reference for other frequencies. This is also exactly the frequency needed for repump, an essential ingredient of laser cooling. And we use an electric optical modulator (EOM) to generate sidebands 9.2 GHz away from the reference laser and use one of the shifted sidebands to injection lock the diode laser (close to  $F = 4 \rightarrow F' = 5$ ) for cooling. And we further use acoustic optical modulator (AOM) with various shift frequencies to reach different desired frequencies within hundreds of MHz. And part of the reference laser is sent to phase lock the Ti-sapphire laser at a variable detuning within  $\pm 15$  GHz. And the second Ti-sapphire laser which injection locked to the first one would be used to generate state preparation and interferometer beam splitting pulses with various pulse shapes and frequencies. More details will be in subsequent sections.

Once all frequencies are prepared, we send them to different parts of the experiment at different time through optical fibers. The experiment setup is shown in Figure 3.3. In order to avoid systematic effect as much as we want, we choose to perform the atom interferometer in free space. It means the atom would drop under gravity. In order to extend usable time for interferometry, we build the atom interferometer with atomic fountain and extend the vertical dimension as much as we can. So we have a vacuum structure about 3 meters tall. There are two main chambers and two secondary chambers. One main chamber is for laser cooling and trapping at 3D Magneto-Optical Trap (MOT) stage; the other one is for Raman Sideband Cooling (RSC) when atoms are moving upward and for detection when atoms are falling back after interferometer sequence. The main science of atom interferometry happens inside the tube above the RSC/detection chamber. We intentionally add Mu Metal to shields this tube from magnetic fields outside the vacuum to avoid additional systematic error. And we put a small solenoid inside to create a small magnetic fields to define the quantization axis so that the polarization of State Selection (SS), Velocity Selection (VS) and Bragg diffraction are well defined. We send the coherent manipulation beam (SS, VS, Bragg) from the bottom chamber. And we put a retro-reflection mirror and a quarter wave plate in the top chamber to generate the retro-reflect beam, which forms a lattice with the original upgoing beam to address atoms in the tube. We use ion pump to maintain the vacuum at the order of magnitude of  $10^{-10}$  torr for both laser cooling and maintaining atom coherence by reducing the scattering from background atoms. More details about the vacuum design will be covered in these references [61, 62].

The experiment sequence is running repetitively. Each cycle takes about 2.1 seconds. The science part (atom interferometry) only takes no longer than 350ms in general so the duty cycle is less than 17%. The whole process can be divided into 5 stages. The first stage is MOT stage. Cesium atoms are stored in the bellows near the 2DMOT glass cell. Cesium atoms are slowly evaporating into the background for the whole time. During the

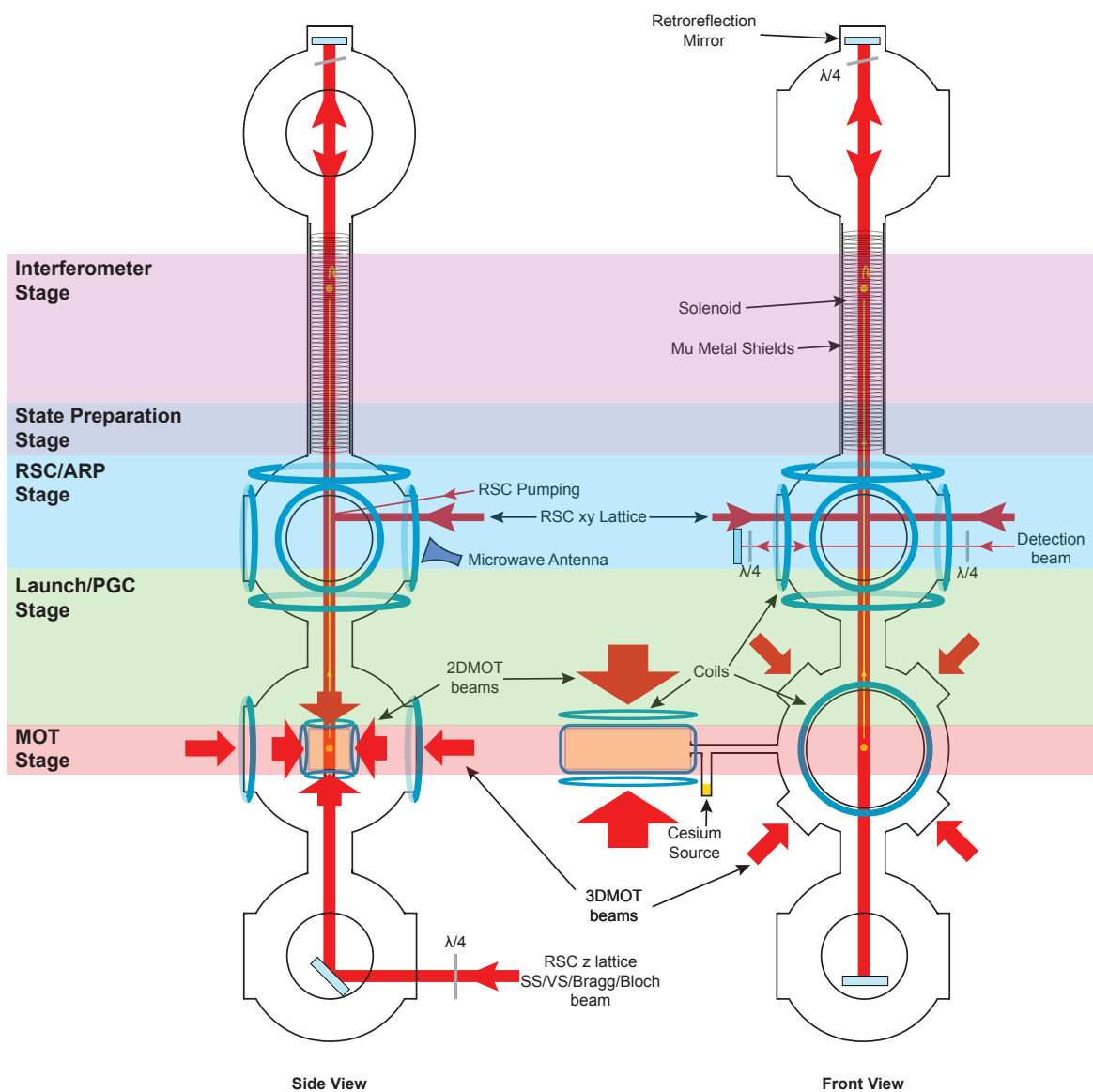


Figure 3.3: Experiment setup overview. Each stage of the experiment is labeled with different colors.

first stage, we turn on 2DMOT beams to perform basic Doppler cooling to cool and capture the background atoms transversely in the 2DMOT glass cell. It generates a high atomic flux and thus high loading rate for 3DMOT. At the same time we turn on 3DMOT beams and MOT coils to cool and trap atoms at the center of the 3DMOT chamber. After 1s of cooling, we turn off MOT coils and start the next stage: Launch and Polarization Gradient Cooling (PGC) stage. During this stage we turn on the extra detuning for the top and bottom 3DMOT beam so atoms are launched at the velocity about 4 m/s based on the detuning set. Right after the launch, we shift the laser to far detune to start polarization gradient cooling below Doppler limit. After atoms reach the RSC/detection chamber, we enter Raman Sideband Cooling (RSC)/ Adiabatic Rapid Passage (ARP) stage. Atoms are further cooled below recoil limit in the RSC lattice and we transfer atom from  $m_F \neq 0$  Zeeman state to  $m_F = 0$  state with microwave through ARP techniques. Afterwards, we started state preparation stage with State Selection (SS) and Velocity Selection (VS). The purpose of SS is to select  $m_F = 0$  Zeeman state only so that it would be insensitive to the first-order Zeeman effect. And we use VS to further narrow the longitudinal momentum distribution so that it would be well below recoil limit to increase Bragg diffraction efficiency for interferometry. After state preparation, we start atom interferometer sequences based on our need mostly during the rising part of the fountain. After all interferometer pulses, atoms fall down to the RSC/detection chamber again. At that point we use a detection beam to excite atoms and collect fluorescence signals.

The whole sequence of the experiment is controlled by a series of digital and analog control signals as shown in Figure 3.4. Different channels are used at different time to control different stages of the experiment shaded in the same color as shown in the experiment setup figure. Not all control signals are shown there. Some channels are consolidated for simplicity. We use National Instrument high-speed digital pattern I/O board NI-PCI-6534 and NI-PCI-6533-DIO-32HS to generate the digital control signals [70]. They are programmed with home built Labview programs. The two board could have been running in sync. But for historical reasons, we run NI6534 as the master board and use one of its channel to generate pattern to trigger the slave board NI6533. It has been working reliably enough in this way to provide digital control signals for more than 40 digital channels. This gives us the basic framework of the timing system. On top of this, we have analog control signals as well as accurate pulse timing signals triggered by the basic digital timing system. Two analog control signals are shown here. One is MOT TA intensity controlled by NI-PCIe-6321 board [71]. The other one is double pass gravity ramp used to compensate the Doppler shift change during free fall. This is generated with AD9954 Direct Digital Synthesizer (DDS) [72]. We have referenced the time base of the timing system to a Rubidium atom clock SRS FS725 in short term and GPS in long term [73]. But the resolution of NI digital boards are only about  $1\mu s$ . For more precise timing related to beam splitter pulses, we use SRS DG535 and DG645 delay generator to control pulse timing [74]. More details about the timing will be covered in the following sections.

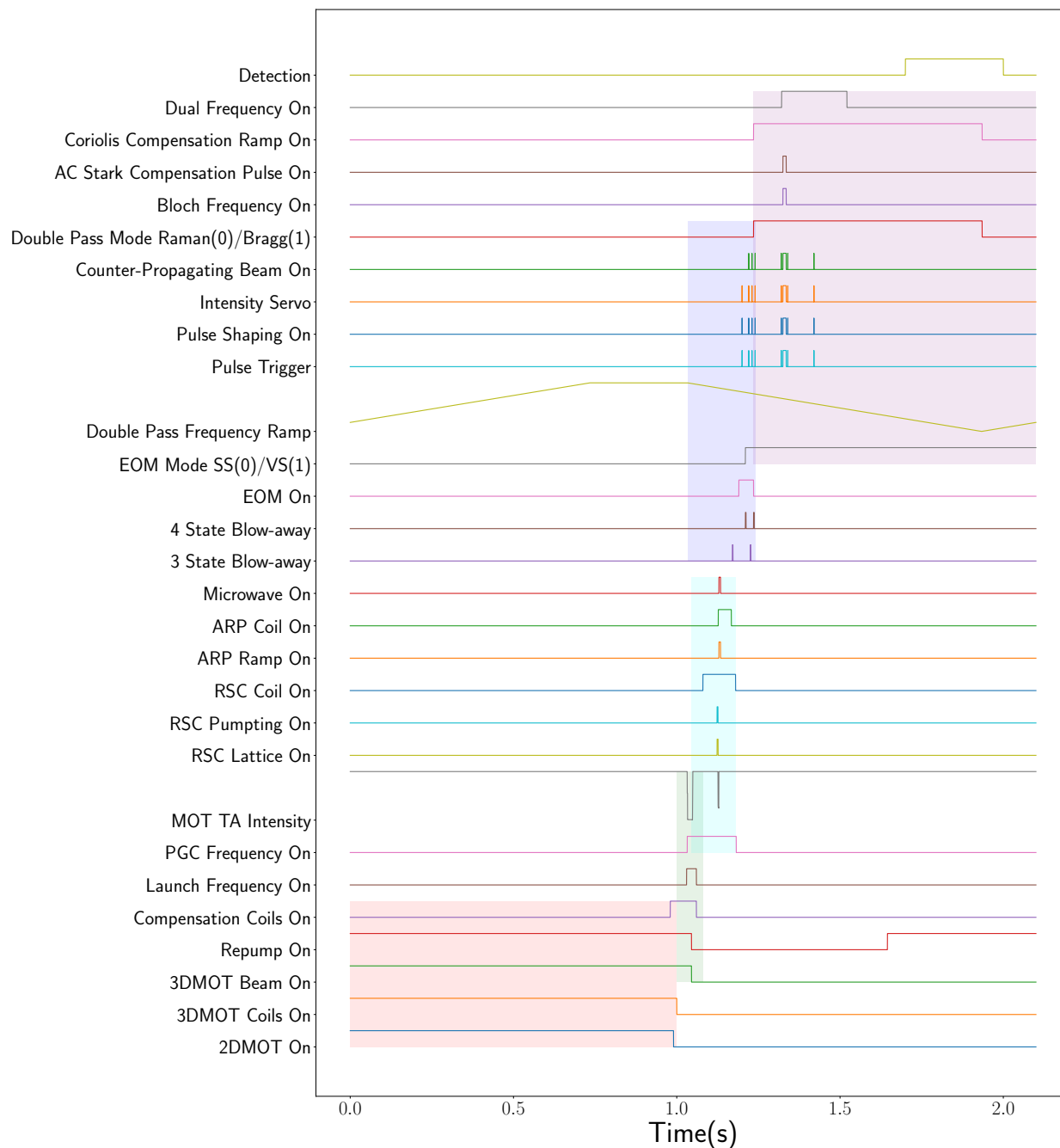


Figure 3.4: Experiment timing signal overview. Different parts are shaded by different color. The color code follows Figure 3.3. A same color corresponds to the same stage defined in Figure 3.3.

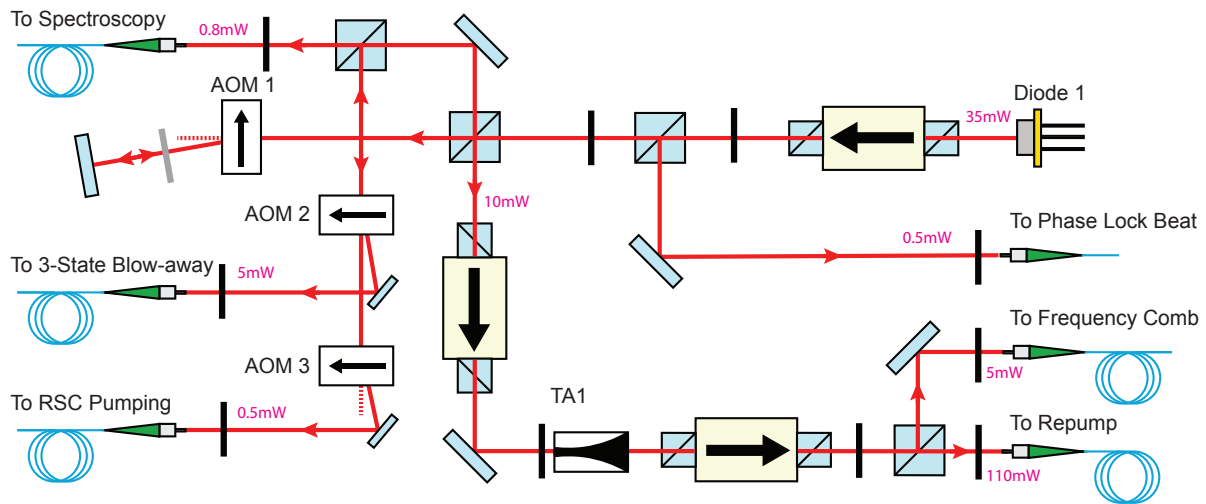


Figure 3.5: Frequency Preparation Optical Schematics

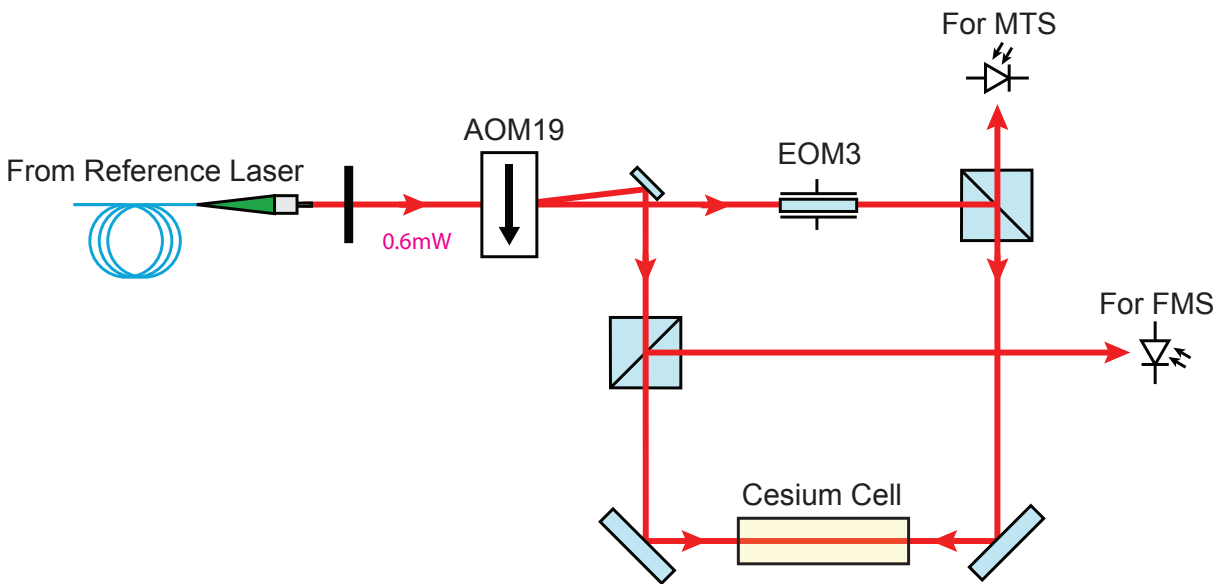


Figure 3.6: Spectroscopy for Reference Lock

## 3.2 Frequency Stabilization and Preparation for Reference

In this section we will go over frequency generation scheme in details. A reliable system starts with a reliable reference frequency source. And it serves as reference source for cooling and Bragg lasers.

As shown in Figure 3.5, we use Newfocus TLB-6917 Vortex II External Cavity Diode Laser as our reference laser labeled Diode 1 [75]. Our goal is to lock it to the repump frequency (Cesium  $D_2$  line  $F = 3 \rightarrow F' = 4$  transition). But for the purpose of better Signal to Noise Ratio (SNR) in the spectroscopy signal, we shift reference laser with AOMs to Cesium  $D_2$  line  $F = 3 \rightarrow F' = 2$  transition. To be more precise, we send part of the reference laser to AOM1 to shift its frequency lower with a double pass scheme and fiber coupled for spectroscopy.

And then we use saturation spectroscopy to lock it as shown in Figure 3.6. We send the spectroscopy beam to AOM19 and take -1 and 0 order as the pump and probe beams respectively. Each beam is expanded with a set of telescope (not shown in the figure) and enter the Cesium cell in a pump-probe counter-propagating configuration. The probe is also modulated by EOM3 with modulation frequency  $\omega_m$ . The pump and probe beam each individually shows a Doppler broadened absorption line. But when both beams are resonate with the same velocity class of atoms, there would be a nonlinear effect showing a Doppler free peak. The width of the peak is dominated by the transition natural linewidth. In this way we could lock the laser to a Doppler-free frequency reference [76, 77].

We can use the resonance condition to calculate the actual reference laser frequency. If we define the reference laser frequency as  $f_L$ , AOM1 frequency as  $f_{\text{AOM1}}$ , AOM19 frequency as  $f_{\text{AOM19}}$ , the transition frequency as  $f_{3 \rightarrow 2'}$ , the wavelength of the laser  $\lambda$ , the velocity of atoms that resonate with both pump and probe is  $v$ , then we have the resonance condition,

$$f_L - 2f_{\text{AOM1}} + \frac{v}{\lambda} = f_{3 \rightarrow 2'} = f_L - 2f_{\text{AOM1}} - f_{\text{AOM19}} - \frac{v}{\lambda}. \quad (3.1)$$

Thus the reference laser would be locked to

$$f_L = f_{3 \rightarrow 2'} + 2f_{\text{AOM1}} + \frac{1}{2}f_{\text{AOM19}} \approx f_{3 \rightarrow 4'}. \quad (3.2)$$

We send 141 MHz RF to both AOM1 and AOM19, which makes the reference laser very close to the repump frequency we want. Two methods are used here to extract the error signal from saturation spectroscopy. One is called Frequency Modulation Spectroscopy (FMS) [76, 77], and the other is called Modulation Transfer Spectroscopy (MTS) [78, 79]. For FMS we detect the signal of the probe beam after the Cesium cell. The probe beam mostly consists of the carrier and two sidebands. Each component has slightly different response on Cesium atoms. Part of the response is modulated by the frequency of EOM3  $\omega_m$ . After demodulation with proper phase added, the signal would be turned into the absorption difference between the two sidebands, yielding a sharp error signal for locking. MTS looks similar but the operating principle is quite different. For MTS we detect the unmodulated pump beam. Due to nonlinear effects cross resonance, modulation in the probe beam could be transferred to the pump. Similarly after proper demodulation, we can get error signal for locking. The reason that we use both techniques in our experiments is that each one has advantages and disadvantages. FMS error signal is sharper but subject to saturation absorption line background shift due to long-term environment change like temperature drift. It's good for

short-term locking but not as reliable for the long term. MTS is good for the long-term performance because its error signal is background free. We AC-couple the FMS signal and DC-couple the MTS signal to utilize the advantages of each. We have thus reached drift below 10 kHz for both short-term and long-term performance [79].

Once the reference laser is locked, it serves as the absolute frequency reference for the rest of the experiment. Part of the reference laser is used to phase lock the Ti sapphire laser; part of it seeds the Tapered Amplifier (TA) for repump; part of the double pass shifted reference beam is further shifted by AOM2 and AOM3 to a frequency close to Cesium  $F = 3 \rightarrow F' = 2$  transition for 3-state blow-away and Raman Sideband Cooling (RSC) Pumping. We also sample the output of TA1 for monitoring frequency with a frequency comb. It is necessary for our precision measurement as we need to keep it controlled within 0.1ppb accuracy.

### 3.3 Laser Cooling

#### Basic Theory

As we mentioned before, low temperature is the key to do atom interferometry based on laser pulses as beam splitters. There have been a lot of cooling techniques in atomic physics to cool dilute atomic gas to the order of magnitude of nK and even reach the quantum degeneracy regime. Here is a brief survey of what typical techniques are available. Typically atoms are at room temperature or even higher in a oven. And the first step is to slow down [80] and cool atom transversely [81] to provide a large atom flux with small velocity spreads so that they could be efficiently loaded into a 3D Magneto-Optical Trap for Doppler cooling and trapping [67]. After Doppler cooling, atoms are cooled to above the Doppler temperature about hundreds of  $\mu K$ . And then MOT coils would be typically turned off and atoms are further cooled by some sub-Doppler cooling techniques to cool it down to above the recoil temperature limit about several hundreds of nK [68]. Below the recoil temperature limit, there are a few fast sub-recoil cooling methods. Evaporative cooling is one of them widely used among cold atom community to reach the degeneracy temperature [69]. But it has some disadvantages for us as we mentioned earlier. Instead, we use Raman sideband cooling [82] to cool atoms closer to the recoil temperature and use Raman velocity selective [83] process to further reduce the longitudinal (the direction of beam splitter beams) velocity spreads of atoms way below the recoil limit so that it is well resolved during Bragg beam splitters as well as detection.

#### Doppler Cooling and MOT

Doppler Cooling is the basic step of laser cooling. We essentially need a two level system with proper natural linewidth. And we use laser beams close to resonance to this transition for laser cooling. As the atom absorbs a photon and reemit it spontaneously, due to conservation of momentum, atom receives a force by the laser beam. The force equals to the



product of the momentum transferred by a single photon and the scattering rate [41]:

$$F(v) = -\hbar k \Gamma \frac{\Omega^2/4}{(\omega + kv - \omega_0)^2 + (\Gamma^2/4) + (\Omega^2/2)} \quad (3.3)$$

where  $k$  is the laser wave number;  $\omega$  laser angular frequency;  $\omega_0$  transition frequency;  $\Omega$  single photon transition Rabi frequency;  $\Gamma$  the natural linewidth;  $v$  atom velocity. This formula is given in the situation where atom is moving with velocity  $v$  on the opposite direction of the laser beam. Due to the special dependence of velocity through the Doppler effect, when we use a counter-propagating beam in  $\sigma^+ - \sigma^-$  configuration, it generates a net frictional force as [41]

$$F = -\alpha v = -\hbar k^2 \frac{s}{(1+s)^2} \frac{(-\Delta)\Gamma}{\Delta^2 + (\Gamma^2/4)} \quad (3.4)$$

where  $s = (\Omega^2/2)/(\Delta^2 + \Gamma^2/4)$  is the saturation parameter;  $\Delta = \omega - \omega_0$  the single photon detuning. Doppler cooling only provides a damping force to slow down atoms. But there is no trapping at specific location. Atoms are just slowing down in the area called optical molasses where cooling lights overlap [66]. With a pair of anti-Helmholtz coils set up and 3 pairs of circularly polarization light specially chosen, we can achieve cooling and trapping simultaneously in the so-called Magneto-Optical Trap [67]. The anti-Helmholtz coil will produce a quadrupole trap with magnetic field  $B = (b'x, b'y, -2b'z)$  near the center. The magnetic field will create Zeeman-state dependent potential for the excited state. When we drive the transition  $F = F_g \rightarrow F' = F_g + 1$  with red detuned light, it's more likely to absorb one particular  $\sigma$  polarization light than the other one depending on the location. Thus it produces a location dependent force, namely trapping force. So the full force term in 1D is

$$F_z = -\alpha v_z - \kappa z \quad (3.5)$$

where  $\kappa = 2k\mu b's \frac{-\Delta\Gamma}{\Delta^2 + (\Gamma^2/4)}$  and  $\mu$  is the magnetic moment of the excited state and  $s$  the saturation parameter.

Based on the design of MOT and the force formula, we need to find a closed two level transition  $F = F_g \rightarrow F' = F_g + 1$  to form a cycling transition where no atom would be lost into other states. For Cesium this cycling transition is  $D_2 F = 4 \rightarrow F' = 5$ . We use cooling frequency about  $\Gamma/2 \approx 2\pi \times 2.6$  MHz red detuned from that transition with power close to saturation intensity (where  $s = 1$ ). In the experiment, these parameters are subject to optimization based on real experimental parameters. But it's the good place to start. However, it's not so ideal yet. It's still possible to have  $F = 4 \rightarrow F' = 4$  transition so some atoms on  $F' = 4$  would end up in the dark state  $F = 3$  ground state. So we use a weak laser resonant to transition  $F = 3 \rightarrow F' = 4$  to drive those lost atoms back to the cycling transition. This weak laser is called repump laser.

MOT doesn't have infinite capture range to capture all atoms in the vacuum background. So we need a step to pre-cool atom within the capture range to significantly improve the loading rate of MOT. 2DMOT is one of the easy ways to do this step [81, 84, 85]. The principle is quite similar to MOT. Instead of using one pair of anti-Helmholtz coil in  $z$ -direction, it

uses two pairs of anti-Helmholtz coils to form a two-dimensional magnetic quadrupole trap  $B = (b'x, -b'y, 0)$ . It is essentially a MOT without cooling and trapping along the third dimension. It effectively cool atoms down transversely so that atoms are collimated to inject into 3DMOT with large atom flux. Though it doesn't have cooling on the third dimension, it effectively select colder atoms along z direction in the way that hot atoms will pass through the 2DMOT chamber quickly without effective transverse cooling, so most of the fast atoms would be filtered by an aperture at the exit of the 2DMOT chamber. After 2DMOT, atom velocity width would be significantly reduced to the order of magnitude of 10 m/s, so most atoms would be captured by 3DMOT. The laser requirement for 2DMOT is quite similar to 3DMOT.

### Polarization Gradient Cooling

The cooling limit of MOT is the Doppler temperature  $T_D = \frac{\hbar\Gamma}{k_B}$ , which is originated momentum recoil from random spontaneous emission [86]. In Cesium the Doppler temperature of  $D_2$  line is about 125  $\mu\text{K}$ . It is possible to cool atoms below this limit with sub-Doppler cooling techniques. Polarization Gradient Cooling (PGC) is the common one for Alkali atoms [87]. The basic idea is to make the spontaneous emission more regular with certain polarization pattern instead of being completely random. For systems with transition  $F = 1/2 \rightarrow F' = 3/2$ , it is the famous Sisyphus cooling mechanism with lin $\perp$ lin counter-propagating beams. But in systems with  $F \geq 1$ , the mechanism tends to be more complex. We use  $\sigma^+ - \sigma^-$  counter-propagating beams to achieve PGC in such systems. For Doppler cooling, the force is generated by Doppler shift difference in counter-propagating beams due to atom velocity. But this force won't be effective when the heating rate dominated by random spontaneous emission is faster than the cooling rate. In this regime, we need a more efficient driving force for cooling. Atom polarization gradient could drive such a force. If we consider all Zeeman sublevels of the ground state  $F = F_g$ , different state has different probability to absorb  $\sigma^+$  and  $\sigma^-$  photons. This probability is determined by Clebsch-Gordan coefficients. For example, state  $|F = F_g, m_F = F_g\rangle$  is more likely to absorb a  $\sigma^+$  photon than a  $\sigma^-$  photon. So if we can encode velocity into atom polarization gradient, it's another mechanism to generate damping force. It turns out that atom motion would induce such polarization gradient and generate a damping force under  $\sigma^+$  and  $\sigma^-$  configuration. The damping force is a few times larger but the cooling temperature is about 1-2 orders of magnitude smaller. That's because the spontaneously emission has specific polarization pattern in PGC. The cooling temperature at equilibrium is about the order of magnitude of  $\hbar\Omega^2/|\Delta|$  [87]. It means experimentally we need to further shift the cooling laser detuning and lower its intensity. It's not that so hard to do on top of existing MOT system.

### Raman Sideband Cooling

The quantum limit of sub-Doppler cooling is the recoil temperature ( $T_r = \hbar k/k_B$ ) associated with incoherent momentum transfer of a single photon absorption or emission [88].

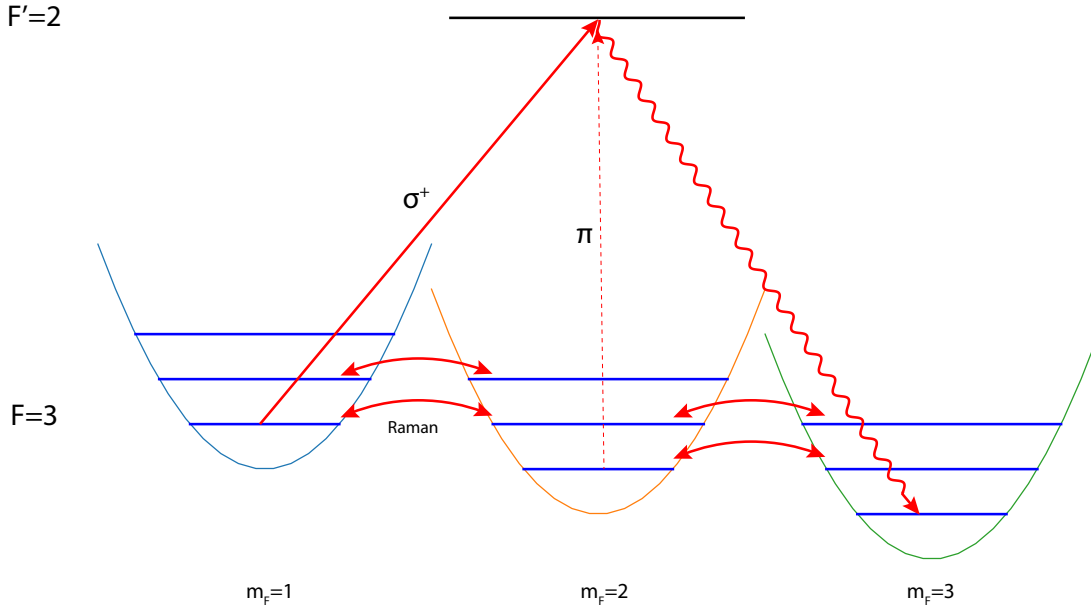


Figure 3.7: Working principles of Raman Sideband Cooling in Cesium

In order to achieve sub-recoil cooling, we need to prevent atom with sub-recoil velocity from absorbing another photon from laser or spontaneous emission. That is the idea to introduce a velocity-selective dark state. Raman Sideband Cooling (RSC) is one of the universal way for sub-recoil cooling [82, 89]. It sets up an optical lattice to confine atoms on each lattice site. Each lattice site is approximately a harmonic trap. In Quantum Mechanics, the motion of particles in the harmonic trap could be quantized into equally separated vibrational states. Here we need a mechanism to make the harmonic trap ground state a dark state. Raman Sideband Cooling (RSC) is such technique. After Polarization Gradient Cooling, atoms are distributed in all Zeeman sublevels of the ground state. For degenerate Raman Sideband Cooling, a magnetic field is specially tuned to match the energy level separation between nearest vibrational states with the energy difference between nearest Zeeman states as shown in Figure 3.7. And we use the same lattice beams as Raman beam to drive degenerate Raman transition among different Zeeman states. So through this Raman process, if we lower the Zeeman state by 1 unit, we simultaneously lower the vibrational state by 1 unit. But Raman process is bi-directional. It does cooling and heating at the same time. So on top of this, a pumping beam could utilize the selection rules to drive transition in one direction. In Cesium, we chose  $F = 3 \rightarrow F' = 2$  for RSC in order to play with the selection rules to make a dark state. We use  $\sigma^+$  mixed with weak  $\pi$  for the pumping beam. Under this configuration, the vibrational ground state of  $|m_F = 3, \nu = 0\rangle$  is the dark state. Neither Raman transition nor optical pumping is coupled to this state. ( $\nu$  is the vibrational quantum number to label its state.) Atom from  $|F = 3, m_F = 1, \nu = 0\rangle$  could absorb a  $\sigma^+$

photon to  $|F' = 2, m_{F'} = 2, \nu = 0\rangle$  and re-emit it spontaneously into the dark state. Atom from  $|F = 3, m_F = 2, \nu = 0\rangle$  could also enter the same excited state by absorbing a  $\pi$  photon. That's why  $\pi$  polarization is important to make RSC more efficient.

The idea of Raman Sideband Cooling is quite straightforward. But in order to make it experimentally feasible and efficient, a lot of experimental parameters need to be well adjusted. Polarization and orientation of each lattice beam (i.e. Raman beam) needs to be optimized to maximize Raman coupling based on Clebsch-Gordan coefficients. The ratio between  $\sigma^+$  and  $\pi$  in the pumping beam also needs to be optimized to achieve efficient pumping. And the depth of the lattice also needs to be large enough to suppress non-degenerated Raman transition to protect the dark state. RSC can be implemented in 1D, 2D and 3D cases. In our experiment we use 3D Raman Sideband Cooling to cool all 3 dimensions. We implement this step after Polarization Gradient Cooling in which atoms end up in  $F = 4$  state. So we need a beam to depump atom to  $F = 3$  state. The easy choice for us is to use laser resonant to  $F = 4 \rightarrow F' = 4$  transition to both depump and serve as the far-detuned Raman sideband lattice. On top of that we add  $F = 3 \rightarrow F' = 2$  laser beam for pumping. Both frequencies are enough to do RSC. More details on experiment setup will be discussed later.

## Setup and Timing

In this section, we will mostly focus on the experiment side how to implement cooling based on the ideas discussed above. One important part is to prepare all required frequencies with enough power in laser beams. It all starts from repump frequency (Cesium  $D_2$   $F = 3 \rightarrow F' = 4$ ) we generated from the reference laser and amplified through TA1 as mentioned earlier. The cooling frequency (Cesium  $D_2$   $F = 4 \rightarrow F' = 5$ ) is about 9 GHz detuned from the repump frequency. We need a separate laser source to generate the cooling frequency and reference to the repump frequency.

One way is to lock this new laser with offset to the reference frequency using frequency lock or phase lock. It's straightforward but also requires a good laser system and a good design for servo feedback. For us we chose injection locking as an easier and cheaper yet reliable option instead. The main challenge is how to shift the repump frequency to cooling frequency. It starts with fiber coupled repump laser beam from TA1 as shown in Figure 3.8. Part of the repump power was taken from the zeroth order after AOM4 and sent through the fiber Electric Optical Modulator 1 (EOM1). EOM1 is modulated at about 9.2 GHz. The RF source is generated from frequency tripling of a function generator output running at 3.07 GHz with amplifiers and bandpass filters. After EOM1, most laser power goes to one carrier and two  $\pm 9$  GHz sidebands in the beam. In order to get only the -9 GHz sideband for the cooling frequency, we properly align the beam through a temperature controlled etalon with linewidth below 9 GHz. This selectivity could be tuned by beam alignment and temperature of the etalon. We used a double pass configuration to further improve the selectivity of the etalon to suppress other frequency components by more than 20 dB. In theory, that's enough to injection lock a slave laser and get the cooling frequency. But considering the need

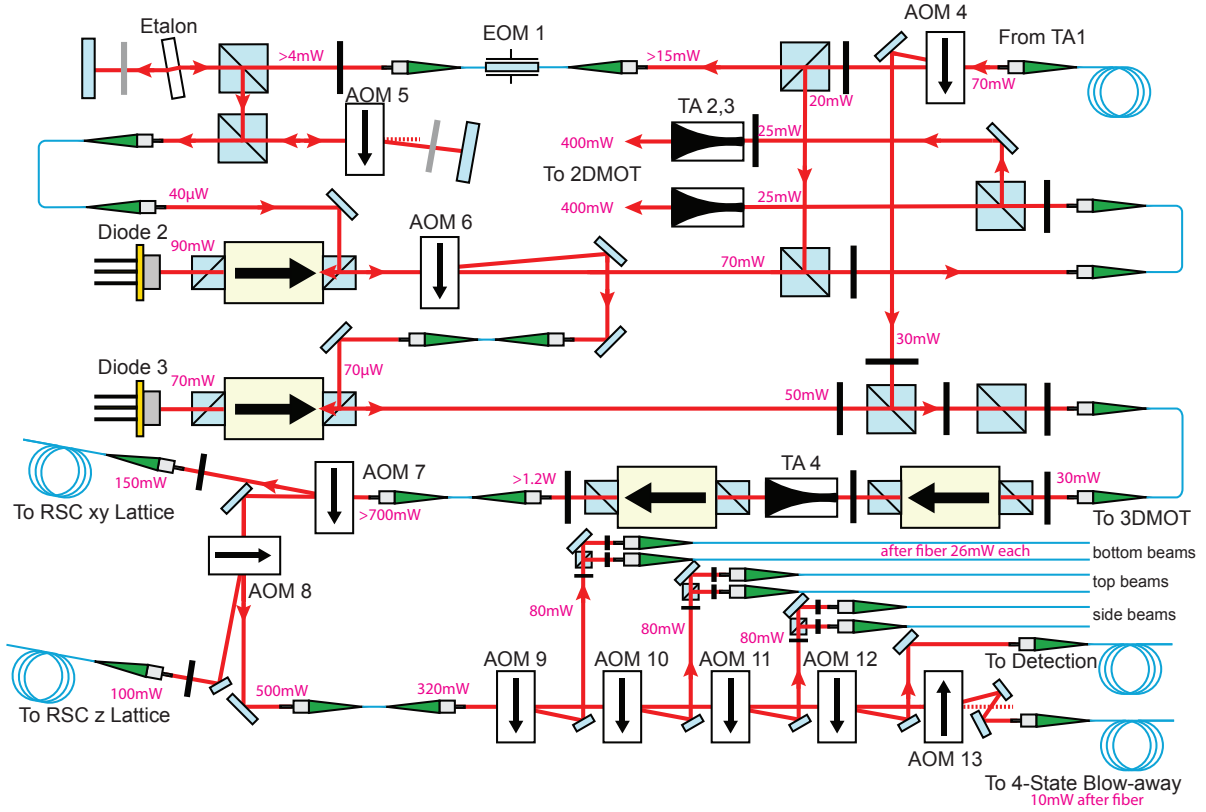


Figure 3.8: Laser Cooling Optical Schematics

to further shift detuning for PGC and RSC, we add a double pass scheme through AOM5 to conveniently switch detuning between Doppler cooling and PGC/RSC. The frequency source of AOM5 comes from octupling a function generator frequency by a Phase Locked Loop (PLL). We send 16.3 MHz from the function generator to get the cooling frequency for Doppler cooling at about  $f_{F=4 \rightarrow F'=5} - 15$  MHz and we shift it to 14.5 MHz by Frequency Shift Key (FSK) to get the cooling frequency for PGC at about  $f_{F=4 \rightarrow F'=5} - 44$  MHz. After these steps, the injection beam is sent into Qphotonics QLD-850-150S/SB laser diode (Diode 2) through an isolator for injection lock. This diode laser (Diode 2) is used as a slave diode laser to provide cooling frequency for 2 Dimensional Magneto-Optical Trap (2DMOT). Most of its power is combined with repump from TA1 to seed TA2 and TA3 for 2DMOT. 2DMOT cooling beam is operating at about 7.5 MHz red detuned from  $f_{F=4 \rightarrow F'=5}$ . And a small part of the power from Diode 2 is shifted down by AOM6 by about 88 MHz to injection lock the same kind of slave diode laser (Diode 3). Diode 3 provides the cooling frequency for 3DMOT. It is combined with repump-80 MHz from -1 order of AOM4 to seed TA4 for 3DMOT, Raman Sideband Cooling (RSC), Detection and 4-state blow-away. The reason why it is further shifted down by 80 MHz is because we would use 80 MHz AOM (AOM9-11) as switches to shift it back up to the right frequency. Along its path, we also use AOM7-8 to

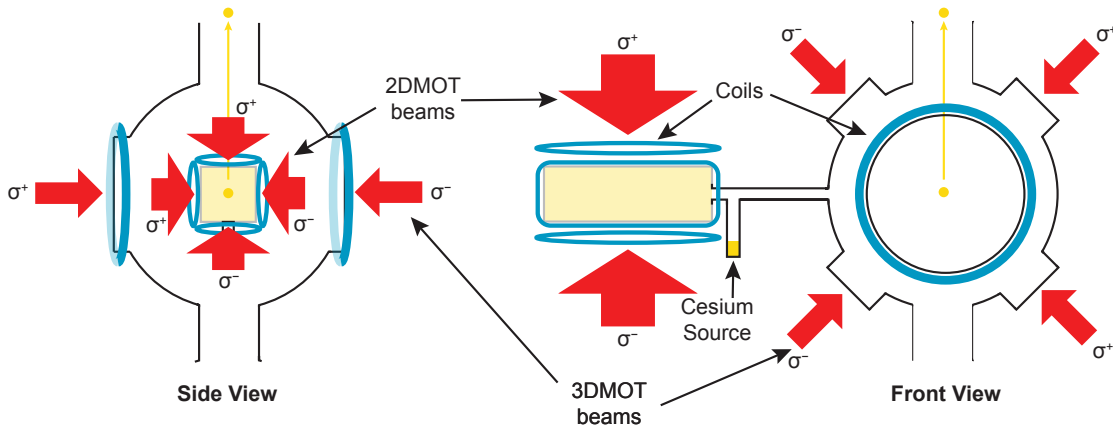


Figure 3.9: 2DMOT, 3DMOT and PGC Setup

generate RSC  $xy$  and  $z$  lattice frequencies (close to  $f_{F=4 \rightarrow F'=4}$ ) respectively. We also generate detection and 4-state blow-away beams (close to  $f_{F=4 \rightarrow F'=5}$ ) with the same laser source by AOM12-13.

## MOT

2DMOT is the first step of the experiment. It is set up in the way very similar to traditional MOT (3DMOT) we mentioned earlier as shown in Figure 3.9. Instead of using 1 pair of anti-Helmholtz coils, it uses two pairs anti-Helmholtz coils to form a 2D magnetic quadrupole trap ( $B = (b'x, -b'y, 0)$ ). And we send the same  $\sigma^+ - \sigma^-$  counter-propagating laser beams with polarization properly chosen to match the direction of the magnetic field gradient such that it forms cooling and trapping potential in those two dimensions and the third dimension remains free of control.

The timing sequence of MOT Stage is also shown here in Figure 3.10. At the beginning of the cycle, we turn on both 2DMOT and 3DMOT, which include cooling, repump lasers as well as magnetic coils for each one. We use mechanical shutters to control 2DMOT beams, AOM9-11 to control 3 pairs of 3DMOT beams, and AOM4 to control whether or not to mix repump frequency into TA4. 2DMOT repump laser and coils are constantly on as they won't interfere with the experiment.

Cesium ampoule is loaded into a bellow. After the vacuum system was pumped and baked, we broke the ampoule and let Cesium vapor fill the entire chamber. The vapor pressure of Cesium at room temperature is way larger than the background vacuum pressure so the natural evaporation of Cesium supplies more than enough Cesium atoms for cooling. When 2DMOT is on, we turn on large cigar shape 2DMOT cooling/repump beam. Cesium vapor starts to get cooled transversely. Though there is no cooling mechanism in the third dimension, the aperture at the exit of the 2DMOT chamber serves as a filter to filter out atoms with large transverse velocity. Atoms with large longitudinal velocity pass through

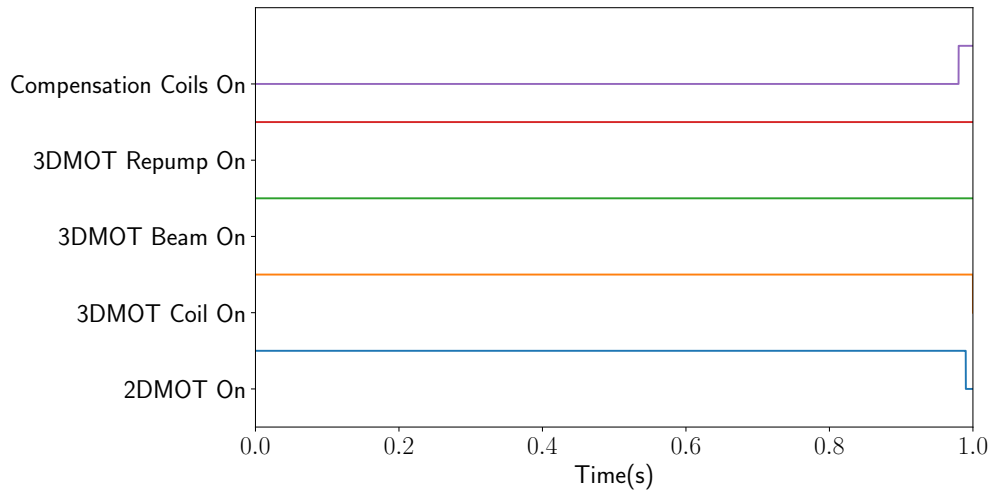


Figure 3.10: MOT Stage Timing

the 2DMOT chamber too fast to be effectively cooled transversely. So most of these atoms will be filtered by the aperture. Effectively 2DMOT provides a good source of collimated atom flux with longitudinal velocity spreads about 20 m/s.

3DMOT is also turned on simultaneously when 2DMOT is on. Most atoms from 2DMOT flux fall into the capture range of the 3DMOT and get cooled and trapped. So with the help of 2DMOT, the number of atoms trapped in 3DMOT could increase by more than 2 orders of magnitude. Before we turn off 3DMOT, we turn on 3 pairs of compensation coils. These are coils to compensate earth magnetic fields as well as any asymmetric quadrupole fields generated by MOT coils. Effectively it shifts the location of the magnetic zero point of the quadrupole trap to match the center of MOT beams. At  $t=1$  s, we turn off 3DMOT coils and keep 3DMOT beams on to allow subsequent cooling stages. But turning off such coils with high inductance generates Eddy currents, which lasts about 30ms. So we set a 30ms pause before we start the next stage.

### Launch and PGC

At  $t = 1.03$  s as shown in Figure 3.11, we start the launching stage. It is the key step to make atomic fountain happen. In our experiment, we use moving molasses to launch atoms [84, 90]. During MOT stage, the top and bottom MOT beams have the same frequency so they cool atoms toward zero velocity relative to the lab frame. But during launch stage, we turn on the launch frequency, which shifts the bottom MOT frequency by +4 MHz and the top MOT frequency by -4 MHz. This is done by mixing the launch frequency 4 MHz with the MOT switch frequency (80 MHz). And we use special RF splitter with phase delays to make both sidebands asymmetric. So we can preferably select one of them and lock it with a tracking VCO. Thus we generate bottom and top launch frequencies separately and feed them to AOM 9 and AOM 10 respectively. The new molasses beams are moving up at about

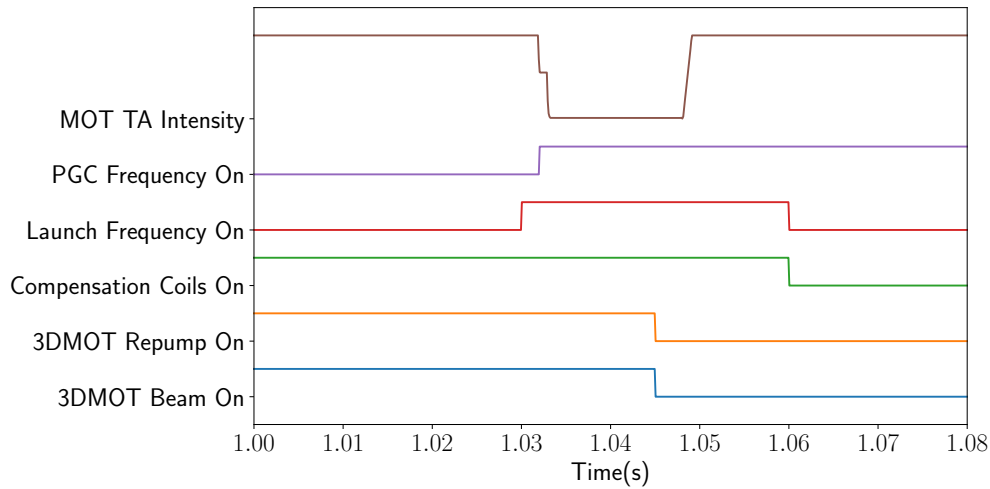


Figure 3.11: Launch and PGC Stage Timing

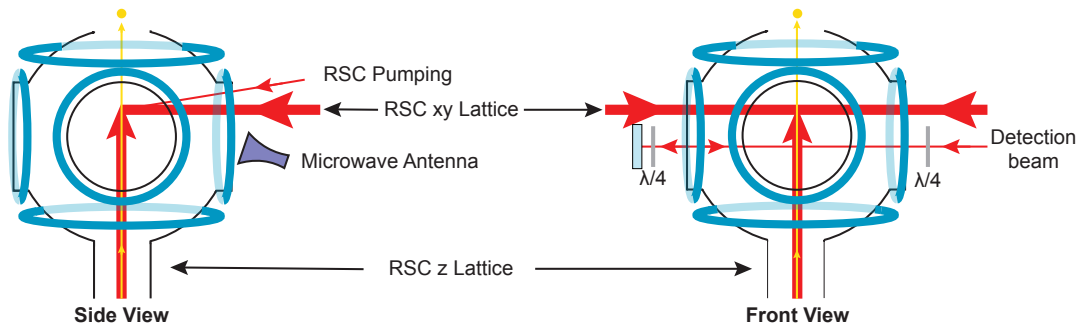


Figure 3.12: RSC and ARP Setup

4 m/s. In its "rest" frame, most of Doppler cooled atoms are moving downward at about -4 m/s and thus within the capture range of the new molasses. During this stage, atoms are adiabatically cooled to the new moving molasses and start moving up. At  $t = 1.033$  s, we start Polarization Gradient Cooling, during which we essentially increase the detuning of the cooling laser and turn down its power. The detuning switch is done by frequency shift key of the function generator that controls the frequency of the double pass AOM5. At the same time we use the analog timing control board NI-PCIe-6321 to generate the waveform to feedback to TA4 current to reduce its power accordingly. We also add a slow ramp down at the end to adiabatically turn down the laser power to 0 to avoid additional heating. After launch and PGC we turn off 3DMOT beams and repump AOM4. It is to be noted that we keep PGC frequency on for the next stage as well.



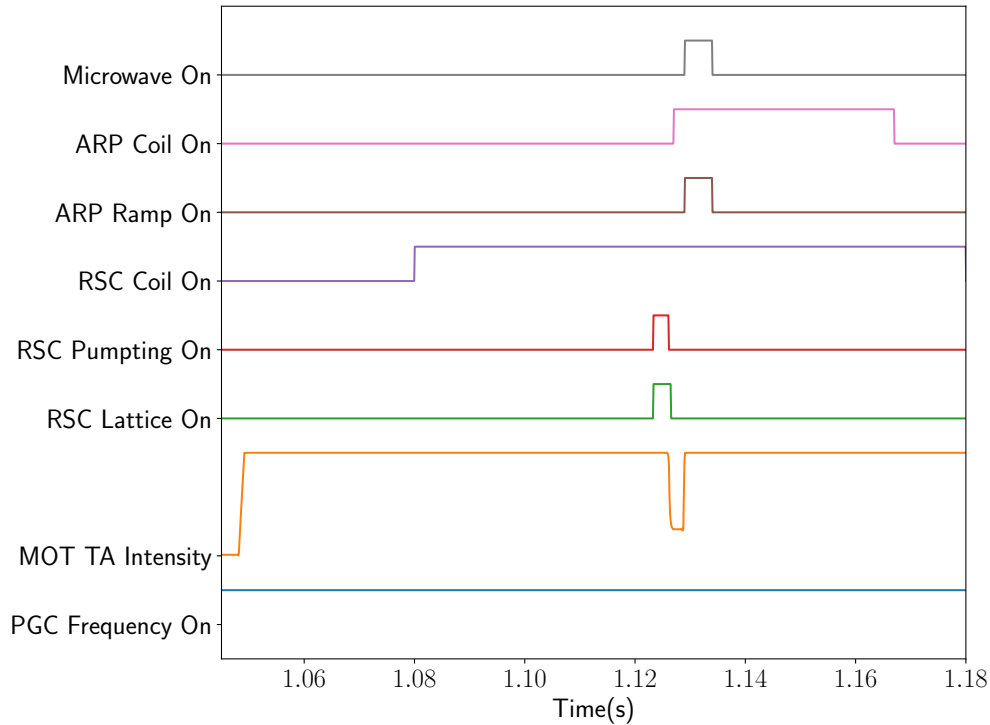


Figure 3.13: RSC and ARP Stage Timing

### RSC and ARP

When atoms are passing through the upper chamber, we start the stage for Raman Sideband Cooling (RSC). It happens at about  $t = 1.12$  s. Before atoms reach this point, we turn on RSC coils beforehand to prepare the magnetic fields to cancel earth magnetic fields as well as to provide Zeeman splitting to satisfy degenerate RSC condition. The beam configuration is shown in Figure 3.12. We switch on AOM7 running at about 120 MHz for RSC xy-lattice and AOM8 running at about 116 MHz for RSC z-lattice. RSC z-lattice is coupled to the vacuum chamber through the same fiber we use for Bragg beam splitter. This generates a lattice close to  $F = 4 \rightarrow F' = 4$  transition frequency, which is used to depump atoms from  $|F = 4\rangle$  to  $|F = 3\rangle$  and served as the far-detuned lattice for RSC as well. The z-lattice (vertical) is slightly detuned from xy-lattice (horizontal) such that it's co-moving at the same velocity as atoms in order to effectively trap them. This 3D lattices are constructed with 4 beams, one vertically going up as z-lattice, one pair counter-propagating along x-axis, one along y-axis. The magnetic field is prepared along y axis as well. At the same time the pumping beam is also turned on by AOM3. Its frequency is close to  $F = 3 \rightarrow F' = 2$  transition. The pumping beam is oriented at a small angle to the direction of the magnetic field in order to mix weak  $\pi$  polarization into its  $\sigma^+$  polarization. The whole RSC lasts about 3 ms. We turn off the pumping beam at 2.8 ms and start to ramp down lattices intensity by TA current adiabatically for another 0.4 ms to avoid additional heating.

After RSC, most atoms are in  $|F = 3, m_F = 3\rangle$  state, which is not the zero  $m_F$  state we want to use for the interferometer. So we add another sequence to adiabatically transfer atom population from  $|F = 3, m_F = 3\rangle$  to  $|F = 4, m_F = 3\rangle$ . This process is called Adiabatic Rapid Passage (ARP), in which we use microwave antenna to drive transition between  $F = 3$  and  $F = 4$  while sweeping frequency from 9193.5 MHz to 9192.5 MHz. In order to make this process more efficient, we also further increase the magnetic field along y direction to increase the Zeeman splitting between nearest  $m_F$  states. Since Landé  $g_F$ -factor are opposite in sign for  $F = 3$  and  $F = 4$  states, as we sweep the frequency, we can cover transitions from  $|F = 3, m_F = 3\rangle \rightarrow |F = 4, m_F = 3\rangle$  all the way to  $|F = 3, m_F = 0\rangle \rightarrow |F = 4, m_F = 0\rangle$  one by one. The microwave frequency is generated from a Dielectric Resonator Oscillator (DRO) locked to the 51th comb line of 180 MHz plus an RF offset ramping from 13.5 MHz to 12.5 MHz in 5 ms. This microwave frequency is then fed into a 10 W Hughes 1177H03F000 Traveling Wave Tube Amplifier and sent to the antenna. Experimentally the overall efficiency of ARP could reach 30%-50%. After ARP, atoms keep moving up into the region where magnetic field generated by solenoid inside the vacuum chamber is along z axis. Atoms adiabatically follow the change in magnetic field direction into  $|F = 4, m_F = 0\rangle$  state defined by z axis as the quantization axis. From this moment, we enter the next stage for state preparation and atom interferometry that will be discussed in the next section.

## Detection

Detection is an important step for us to read out atom population at different output port or characterize fountain performance. In our experiment, we use an apertured detection beam to detect atoms that are going through the detection region as shown in Figure 3.12. There are two windows to detect atom signal: one when atoms are moving up, the other when atoms are falling back. But we can not use both simultaneously as our detection scheme is destructive. We use laser beam resonant to  $F = 4 \rightarrow F' = 5$  cycling transition to detect atoms by collecting fluorescence. We also mix repump into detection beam to prevent atoms from falling into the dark state. The reason to use this cycling transition instead of  $F = 3 \rightarrow F' = 2$  is to boost the scattering rate in order to have a high signal to noise ratio, even though we use  $F = 3$  atoms for interferometer.

The detection beam comes from the same source as 3DMOT. We use AOM12 to switch it on and shift it to be resonant with the cycling transition. After it get coupled to the detection region, we first aperture it horizontally with a pinhole and vertically with an optical slit. After these, the beam becomes roughly 1.5 mm wide, 0.5 mm high rectangularly shaped. We then send it to a PBS to purify its polarization. We use  $\sigma^+ - \sigma^-$  optical molasses configuration for detection in order to increase the scattering rate as well as avoid atom from being pushed away by either side. This polarization scheme could be done with two quarter wave plates as well as a retro-reflect mirror as shown in Figure 3.12. If we define the direction of detection beam as x-axis to be consistent with the definition in RSC, we put our detector along y axis facing the chamber. In order to be as sensitive as possible, we use large 100 mm diameter, 100 mm focal length lenses to collect fluorescence light to a

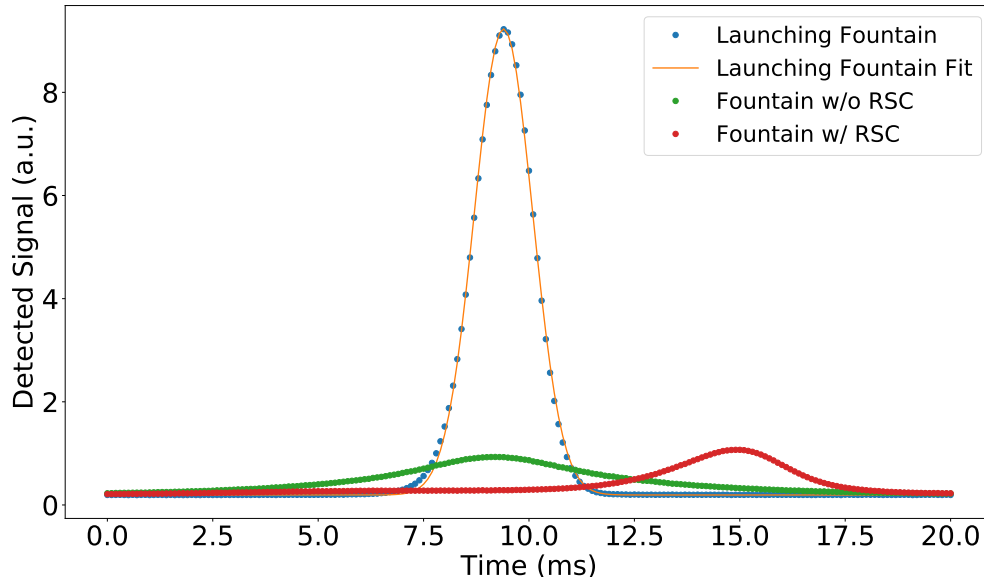


Figure 3.14: The first fountain signal compared with the second fountain signal with and without RSC. The first fountain signal is fitted with a Gaussian.

photodiode (Thorlabs FDS100). Previously we have been using a photomultiplier. But for the application here, photodiode with large trans-impedance gain would be a cheap, easy and low-noise choice. We also put a "daylight filter" to block visible light in front of the sensor. In our setup, signal to noise in detection is mostly limited by strayed detection light inside the chamber. It can be improved by better coating of the vacuum chamber windows.

When atoms are passing through (normally at 4 m/s), we turn on the detection beam and start to collect fluorescence. Normally it only takes at most 10 ms (depending on the size of atom cloud) for an atom cloud to pass through. That's also the reason why we choose photodetector instead of CMOS/CCD camera. Camera definitely has advantages for its spatial resolution, but at a cost of losing temporal resolution as well as signal to noise ratio. Since the exposure time is quite short, signal to noise ratio is relatively poor at each pixel level. For our application, different interferometer output ports are spatially separated in vertical direction and have to be read out at different time, so temporal resolution is more important for us. That's why we prefer photodiode to read out signals. At the same time, we do have another camera collecting part of the fluorescence from another direction at the same time when we detect atoms. We can read out any signal before state preparation. It gives us important information about atom cloud size, temperature, and fountain alignment.

## Performance

In the experiment, we use 1-2  $I_{\text{sat}}$  intensity as well as about 10G/cm magnetic field gradient for 2DMOT. It supplies more than  $10^9$  atoms/s flux for 3DMOT. And we use

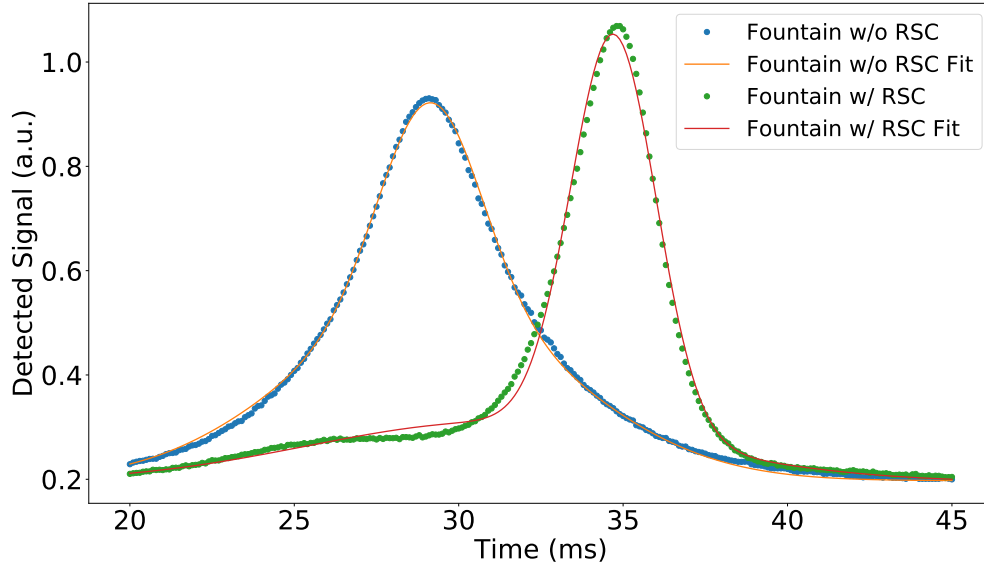


Figure 3.15: The second fountain signal with and without RSC. Both of them are fitted with a double Gaussian.

roughly  $3-5I_{\text{sat}}$  and about  $8.6\text{G}/\text{cm}$  for 3DMOT to trap about  $10^9 - 10^{10}$  atoms. The exact number of atoms has never been carefully calibrated but it's enough for our purpose. Here  $I_{\text{sat}}$  is defined as [42]

$$I_{\text{sat}} = \frac{c\epsilon_0\Gamma^2\hbar^2}{4|\hat{\epsilon} \cdot \mathbf{d}|^2} \quad (3.6)$$

such that the saturation parameter  $s$  in Equation 3.4 is equal to  $I/I_{\text{sat}}$  when the detuning  $\Delta = 0$ .

Here are some data we collect with our detection scheme to characterize the performance of atom cooling. We take detection trace and CCD images when fountain is passing through the detection region during launching and falling separately. We call its first passing (during launching) the first fountain and its second passing (during falling) the second fountain. The second fountain could be either with Raman Sideband Cooling (RSC) or without. We can plot these three signal traces in the same scale as shown in Figure 3.14. During atoms' first passing, the majority of atoms fall into the range of the detection beam. But after about 800 ms during its second passing, only few are still within the range. Typically the ratio between the launching and falling fountain is about 12 for a well aligned fountain. It can also be visually shown in the camera pictures below. The shape of the signal is cigar-like because of the shape of the detection beam. In order to quantitatively analyze the performance of laser cooling, we have also fit all these data traces shown in Figure 3.14 and 3.15 to Gaussian (the first fountain) and double Gaussian (the second fountain). The second fountain signals (either with or without RSC) only fits well with double Gaussian model. It suggests that a group of hot atoms that are not effectively cooled are also mixed in the signal. However

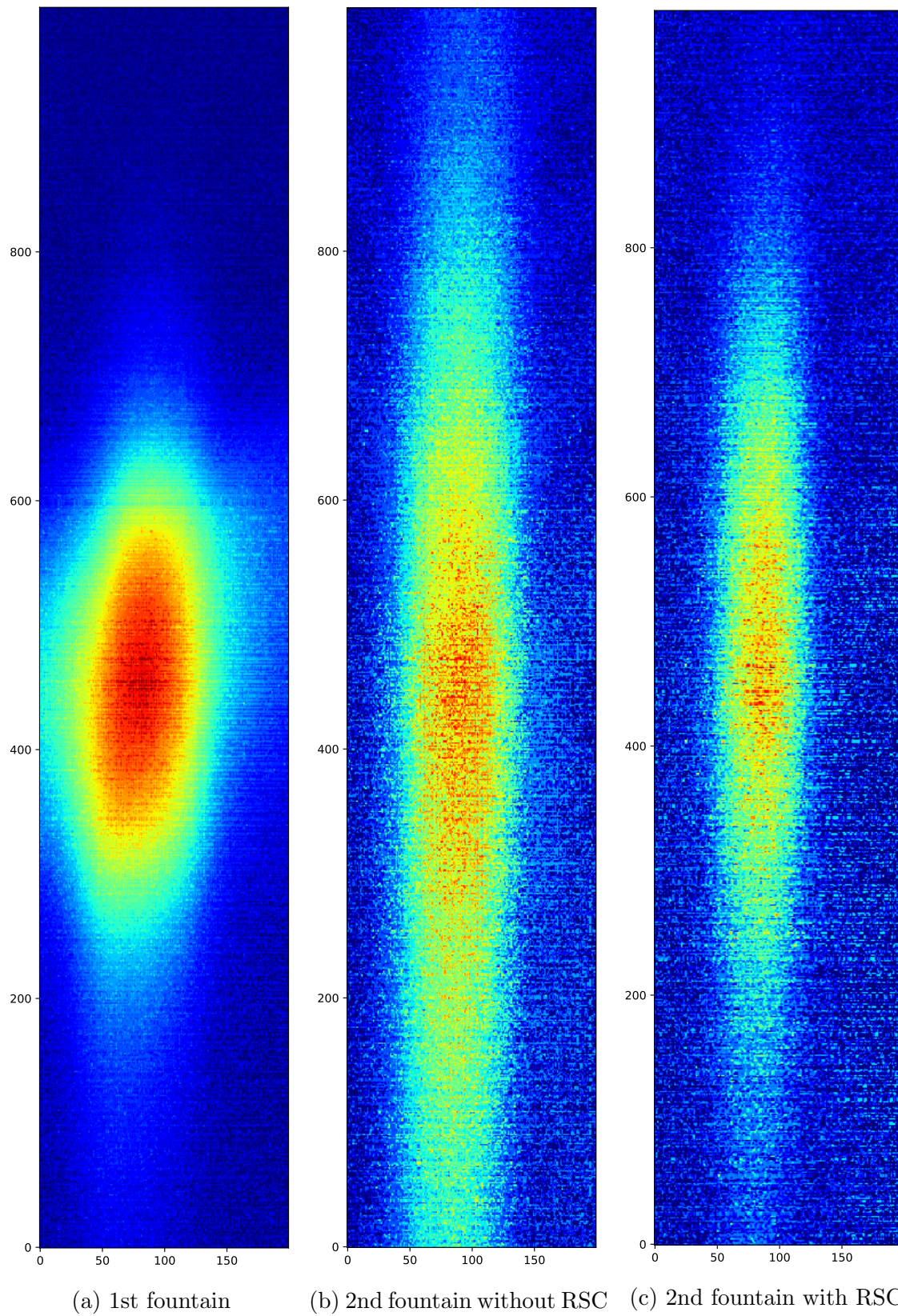
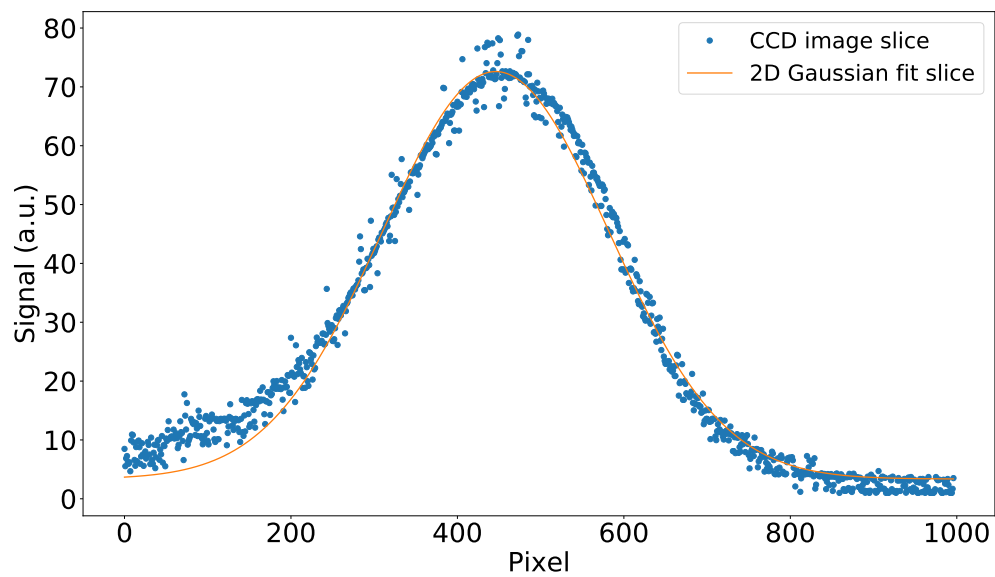
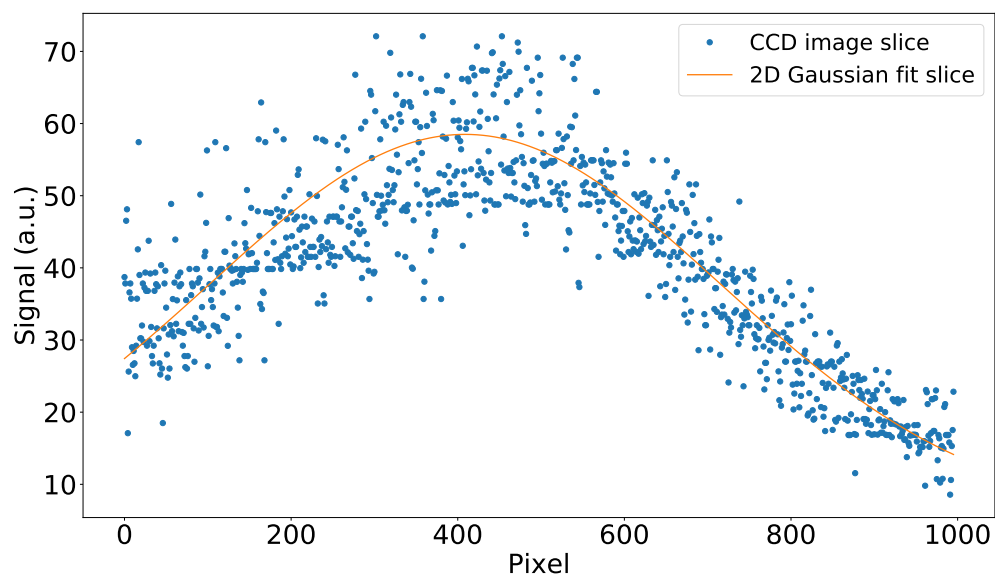


Figure 3.16: CCD images of the first fountain and the second fountain with and without RSC

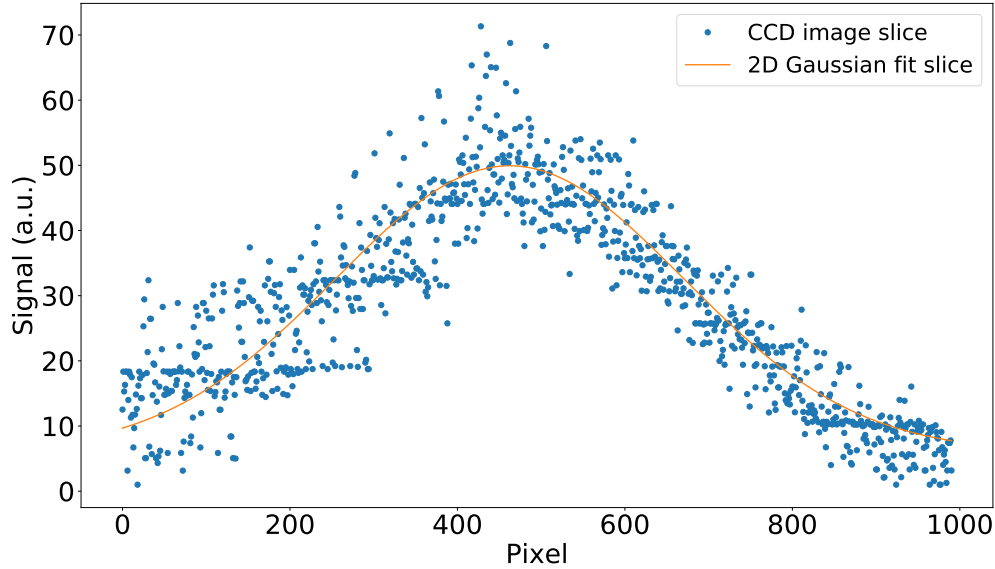




(a) 1st Fountain



(b) 2nd fountain without RSC



(c) 2nd fountain with RSC

Figure 3.17: CCD images slices and their 2D Gaussian fit respectively

Signal Name	Fit Model	$\sigma_z$ (mm)	$\sigma_x$ (mm)	$\sigma_y$ (mm)
1st Fountain	$Ne^{-\left(\frac{x^2}{2\sigma_x^2} + \frac{y^2}{2\sigma_y^2} + \frac{z^2}{2\sigma_z^2}\right)}$	3.91	3.86	1.44
2nd Fountain without RSC	$Ne^{-\left(\frac{x^2}{2\sigma_x^2} + \frac{y^2}{2\sigma_y^2} + \frac{z^2}{2\sigma_z^2}\right)} + \text{hot atoms Gaussian}$	8.76	8.70	1.02
3rd Fountain with RSC	$Ne^{-\left(\frac{x^2}{2\sigma_x^2} + \frac{y^2}{2\sigma_y^2} + \frac{z^2}{2\sigma_z^2}\right)} + \text{hot atoms Gaussian}$	7.34	5.87	0.74

Table 3.3: Fitting parameters for the first and the second fountain

these data traces from photodetectors only tell us information along vertical direction. But we can get good estimate for atom distribution in the transverse directions through CCD images. Since the Signal/Noise is not relatively poor for CCD images, we cannot distinguish the difference between a double Gaussian or a single Gaussian so we have only applied a single 2D Gaussian to fit them. All the fitting results are summarized in Table 3.3. It's to be noted that the unit of  $\sigma_z$  has already been converted to length unit with the measured atom velocity about 4 m/s.

Based on these data, we can estimate the number of atoms and the cooling temperature of the fountain. Since the launching fountain are mostly within the detection region, we can use the CCD data to estimate the number of atoms launched. We use weak 852 nm laser beam with known power to calibrate the camera's photon conversion rate  $\eta$  to be about 400 photons/count. The f-stop of the lens is 0.95 and its focal length is 50 mm. And the distance from the atom to the lens is about 250 mm. So only about  $r = 0.3\%$  of fluorescent photons

are collected by the lens. The single photon scattering rate for on resonance detection beam is given as

$$R = \frac{\Gamma}{2} \frac{s}{1+s} \quad (3.7)$$

where the saturation number is about 1. Each atom is flying through the 0.5 mm thin detection beam with a velocity about 4 m/s, which means that the effective exposure time  $t$  is about 0.125 ms. The total count  $C$  of the CCD signal subtract the background noise is about  $2.8 \times 10^6$ . So taking all these factors into account, the number of atoms detected during launching is about

$$N = \frac{\text{the total number of photons emitted}}{\text{the number of photons emitted by one atom}} \quad (3.8)$$

$$= \frac{C\eta/r}{Rt} \quad (3.8)$$

$$= 3.6 \times 10^8 \quad (3.9)$$

It's not the total number of atoms launched since only atoms within the detection range are detected. If we suppose that the original shape of atom cloud is symmetric, we can roughly multiply a shape factor  $\sigma_x/\sigma_y$ , yielding  $9.8 \times 10^8$ . It is to be noted that it's not an accurate estimation of the atom number since some parameters list above are not accurately measured. It could be a small numeric factor off. But it serves as a good order-of-magnitude estimation not only for the first fountain, but also for interferometer. We can use the relative signal ratio from photodetectors to estimate the number of atoms detected for the second fountain with RSC or without or after state preparation.

For atom temperature, we can use Time-of-Flight (ToF) method to estimate [91]. It's a very straightforward method given Maxwell distribution of atoms. Take 1D for example, the atom follows the initial distribution after MOT

$$n = N e^{-\frac{x^2}{2\sigma_x^2}} e^{-\frac{v^2}{2\sigma_v^2}} \quad (3.10)$$

where  $N$  is the normalization factor. After time  $t$  of thermal expansion, the distribution becomes  $N \exp(-(x - vt)^2/(2\sigma_x^2)) \exp(-v^2/(2\sigma_v^2))$ . If we integrate over all velocity, the real space distribution follows a new Gaussian distribution with a new  $\sigma'_x = \sigma_x + \sigma_v t$ . So if we have measurement of atom real space Gaussian distribution at two different time, we can solve it to get atom temperature  $T = \frac{m\sigma_v^2}{k_B}$  according to Maxwell distribution. This methods can be extended to all three dimensions. In our experiment, the longitudinal temperature would be the most accurate because of high signal/noise in the photodetector signal. We can also estimate the transverse temperature along the direction of the detection beam. But it would be less accurate. We won't be able to estimate the temperature along the direction limited by the size of the detection beam. Following the procedure above, given the time separation between the first and the second fountain to be 0.81s, we can obtain the results listed in Table 3.4. It is to be noted that the actual RSC happens after atom



Cooling Type	$T_z$ (nK)	$T_x$ (nK)
MOT and PGC	573	571
MOT and PGC and RSC	287	93

Table 3.4: Measured atom temperatures

passing through the detection region. In theory we won't be able to determine the effective atom distribution at its first passing of the detection beam. The result here relies on the assumption that atoms selected by RSC follows the same distribution at the first passing. This assumption might not hold for estimation of transverse velocity since the size of RSC lattice filters atom distribution horizontally. That's why the transverse temperature of RSC is surprisingly small.

## 3.4 Coherent Manipulation

### Basic Theory

As is briefly mentioned earlier, coherent manipulation includes all the pulses for state preparation and atom interferometry. The physics processes behind, Raman transition, Bragg diffraction and Bloch oscillations have been extensively discussed in the previous chapter. Here we are more focused on how to implement them in the context of our experiment. After Raman Sideband Cooling (RSC) and Adiabatic Rapid Passage (ARP), we need to only select atoms in  $|m_F = 0\rangle$  state with significantly narrow velocity spread to participate atom interferometry in order to eliminate systematic effects from first-order Zeeman effect and improve Bragg diffraction efficiency.

After ARP, most atoms are transferred to  $|F = 4, m_F = 0\rangle$  state while some remains in wrong states. We use Raman transition to selection atoms in the right state while blow away atoms in wrong states. We use the so-called blow-away beam to blow away atoms. We tune a laser beam to  $F = 3 \rightarrow F' = 2$  transition frequency plus detuning required to compensate Doppler shift to blow away atoms in  $F = 3$  states, which is called 3-state blow-away. By selection rules, this transition is a closed transition as  $F' = 2$  atoms can only decay to  $F = 3$  by spontaneous emission. After one cycle, an atom would absorb a photon from the blow-away beam and emit another photon spontaneously, receiving momentum transfer by two-photon recoil kicks. Since photons emitted by spontaneous emission is randomly oriented, atoms would experience a force along the direction of the blow-away beam in average. As a result, it pushes atoms away. We normally turn on the blow-away pulse for 2 ms, which will transfer more than a few meters-per-second velocity on resonant atoms to blow them away from the rest of selected atoms. We do the same kind of blow-away for  $F = 4$  state as well called 4-state blow-away, with laser beam tuned to another closed transition  $F = 4 \rightarrow F' = 5$ . However, it's not 100% ideal, since there is non-zero probability to excite atoms to wrong states and later decay to the dark state. Based on the energy level

structure, it's more likely to happen for 3-state blow-away due to smaller detuning so it's less ideal in the experiment.

We use Raman transitions with appropriate blow-away pulses in-between to realize state preparation. Since there would be a small magnetic field generated by solenoid along z axis inside the chamber, there would be non-zero Zeeman splitting among all Zeeman sublevels. A Raman transition with specially chosen polarization and frequency could drive atoms between  $|F = 3, m_F = 0\rangle$  and  $|F = 4, m_F = 0\rangle$  back and forth and leave the rest atoms in the original Zeeman states. Thus by driving such Raman transition and blow away the rest, we could effectively select atoms in  $|m_F = 0\rangle$  states. We normally perform State Selection (SS) with Doppler insensitive co-propagating Raman beams. But if we choose the counter-propagating configuration, it would be Doppler sensitive, i.e. velocity selective [83]. Thus only a small fraction of velocity class of atoms that resonant with the Raman transition would be selected. Once state preparation is done, we finally enter the stage of atom interferometry. We use Bragg diffraction as beam splitters and Bloch oscillations to further increase common mode acceleration as discussed in the previous chapter. We will be focusing on some theoretical considerations on polarization and frequency requirement to achieve these experimentally.

### Polarization Requirement

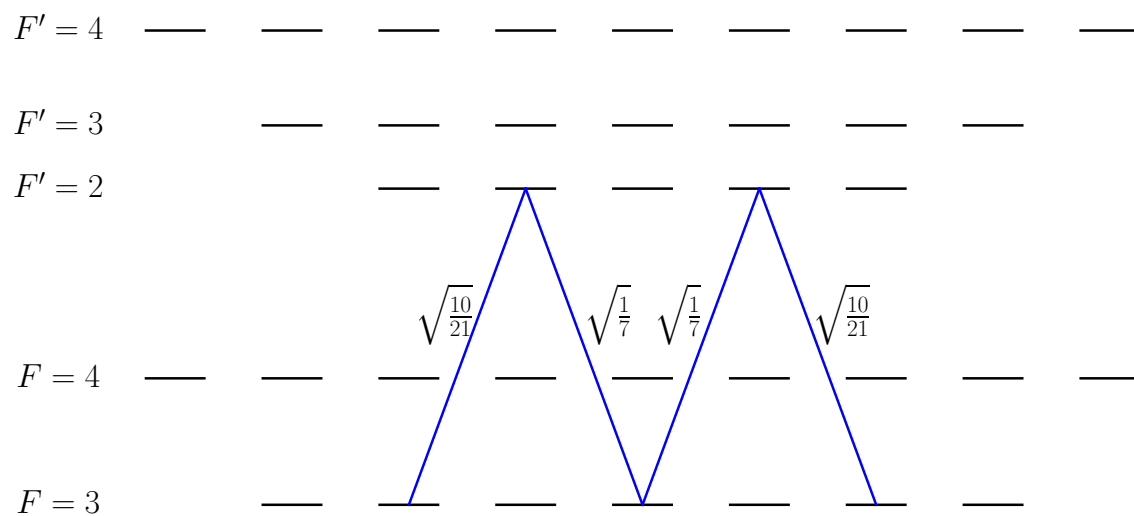
Let's first review the selection rule for the Raman process in Cesium. It starts from the selection rule for electric dipole transition of atoms with hyperfine interaction. For electric dipole transition, one photon is directly involved. Because the photon carries an angular momentum  $1\hbar$ , it imposes that  $\Delta L = \pm 1, \Delta F = 0, \pm 1$ . And for circularly polarized light ( $\sigma^\pm$ ),  $\Delta m_F = \pm 1$ ; for linearly polarized light ( $\pi$ ),  $\Delta m_F = 0$  [42]. Raman transition could be view as connecting two electric dipole transitions via virtual excited states. For Cesium, if we start from  $F = 3$  ground hyperfine state to  $F = 4$  ground hyperfine state via a Raman transition, the most probable intermediate virtual states would be  $F' = 3$  and  $F' = 4$  excited hyperfine states based on selection rules. As mentioned earlier, we want to keep selected atoms in  $|m_F = 0\rangle$  throughout the state selection and atom interferometry stage, no matter it's Raman transition, Bragg diffraction or Bloch oscillations. So this put us under restrains on polarization to maximize the transition Rabi frequency that keeps atoms staying at  $m_F = 0$  and to minimize the transition Rabi frequency that makes atoms leak to other  $m_F$  states. Based on this criteria, we can test those common polarization configurations such as  $\sigma^\pm - \sigma^\pm$ ,  $\sigma^\pm - \sigma^\mp$ ,  $\text{lin}||\text{lin}$ ,  $\text{lin}\perp\text{lin}$  for both Raman and Bragg processes to decide what type of configuration to use in our experiment.

The matrix element of single photon electric dipole transition from the ground state to the excited state is

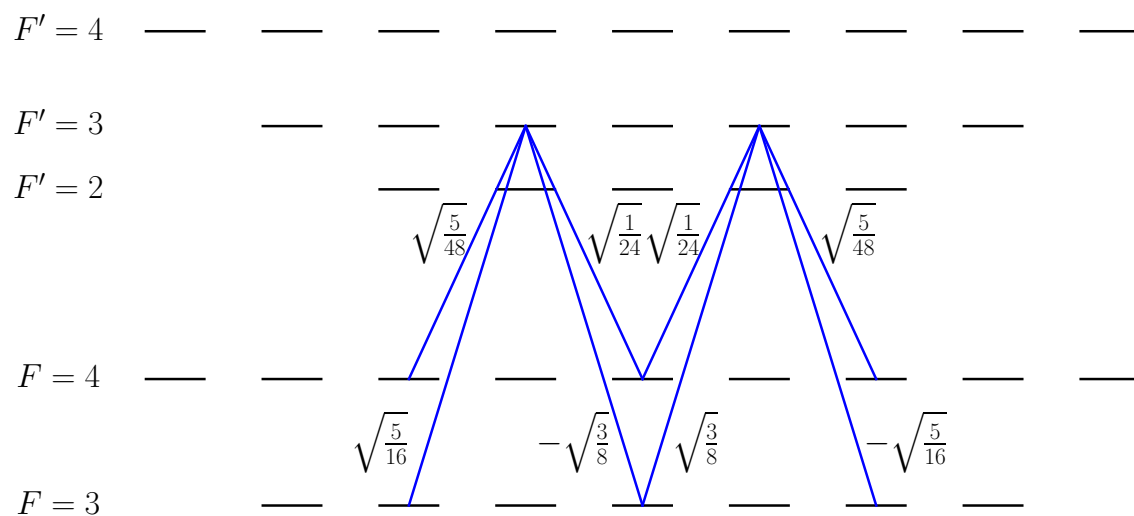
$$H = \langle e | \mathbf{d} \cdot \mathbf{E}_0 | g \rangle = d_{eg} E_0 = \hbar \Omega \quad (3.11)$$

where the matrix element of the dipole moment

$$d_{eg} = -e \langle e | \hat{\mathbf{e}} \cdot \mathbf{r} | g \rangle. \quad (3.12)$$



(a)



(b)

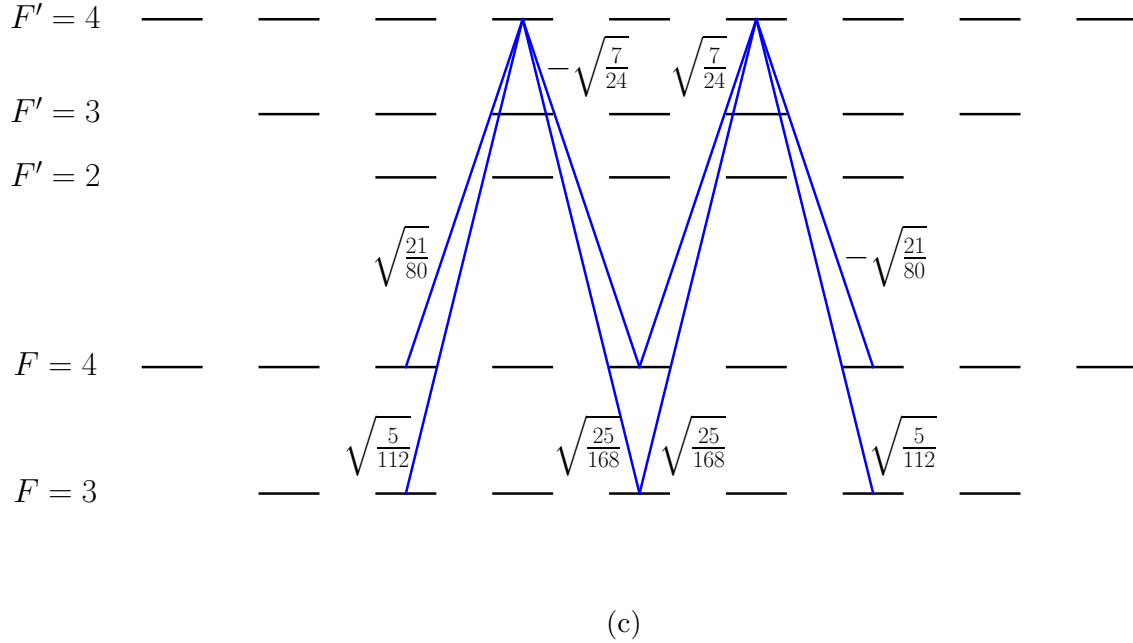


Figure 3.18: Cesium  $D_2$  transition matrix elements relevant for Raman/Bragg processes as multiples of  $\langle J' = \frac{3}{2} || er || J = \frac{1}{2} \rangle$

The unit vector  $\hat{\epsilon}$  represents the polarization of the light. Here we choose the spherical units [92, 93],

$$\hat{\epsilon}_{\pm 1} = \mp \frac{1}{\sqrt{2}}(\hat{\epsilon}_x \pm i\hat{\epsilon}_y) \quad (3.13)$$

$$\hat{\epsilon}_0 = \hat{\epsilon}_z \quad (3.14)$$

such that

$$\hat{\epsilon} \cdot \mathbf{r} = \hat{\epsilon}_q \cdot \mathbf{r} = \sqrt{\frac{4\pi}{3}} r Y_1^q(\theta, \phi). \quad (3.15)$$

where  $Y_l^m(\theta, \phi)$  is spherical harmonics in quantum mechanics definition. If we write specifically the ground state and the excited state as  $|g\rangle = |F, m_F\rangle$  and  $|e\rangle = |F', m'_F\rangle$ . Then the matrix element can be calculated according to Wigner-Eckart theorem [42].

$$d_{eg} = e \langle F', m'_F | \hat{\epsilon}_q \cdot \mathbf{r} | F, m_F \rangle = \langle F' || er || F \rangle (-1)^{F-1+m'_F} \sqrt{2F'+1} \begin{pmatrix} F & 1 & F' \\ m_F & q & -m'_F \end{pmatrix} \quad (3.16)$$

$$= \langle J' || er || J \rangle (-1)^{J'+I+m'_F} \sqrt{(2F'+1)(2F+1)(2J'+1)} \begin{Bmatrix} J' & J & 1 \\ F & F' & I \end{Bmatrix} \begin{pmatrix} F & 1 & F' \\ m_F & q & -m'_F \end{pmatrix} \quad (3.17)$$

All the relevant matrix elements are calculated and shown in Figure 3.18. For Raman transition from  $F = 3, m_F = 0$  to  $F = 4, m_F = 0$  or the other way around, it is obvious that

$\sigma^\pm - \sigma^\pm$  would work according to the selection rule. It requires a little bit calculations for the case of  $\text{lin}||\text{lin}$  and  $\text{lin}\perp\text{lin}$ . Based on definitions above, the linear polarization in  $\hat{\epsilon}_x$  and  $\hat{\epsilon}_y$  could be decomposed as

$$\hat{\epsilon}_x = \frac{1}{\sqrt{2}}(-\hat{\epsilon}_{+1} + \hat{\epsilon}_{-1}) \quad (3.18)$$

$$\hat{\epsilon}_y = \frac{i}{\sqrt{2}}(\hat{\epsilon}_{+1} + \hat{\epsilon}_{-1}) \quad (3.19)$$

For example, if we drive from the ground state  $|F = 3, m_F = 0\rangle$  to an intermediate virtual state  $|F', m'_F\rangle$  with the electric field  $E_{10}\hat{\epsilon}_x$  and drive from the intermediate state to the other ground state  $|F = 4, m_F = 0\rangle$  with another electric field  $E_{20}\hat{\epsilon}_x$ , then the combined 2-photon Rabi frequency via this pathway is

$$\Omega_{F', m'_F}^{(2)} = \frac{\Omega_{3,0 \rightarrow F', m'_F} \Omega_{F', m'_F \rightarrow 4,0}}{2\Delta_{F', m'_F}} \quad (3.20)$$

where single photon Rabi frequencies could be calculated based on the formula above with circular polarized light, e.g

$$\begin{aligned} \Omega_{3,0 \rightarrow F', m'_F} &= \frac{d_{eg} E_{10}}{\hbar} \\ &= -\frac{e E_{10}}{\sqrt{2}\hbar} (-\langle F', m'_F | \hat{\epsilon}_{+1} | 3, 0 \rangle + \langle F', m'_F | \hat{\epsilon}_{-1} | 3, 0 \rangle) \end{aligned} \quad (3.21)$$

So if we add all possible pathways based on selection rules ( $F' = 3, 4, m'_F = \pm 1$ ), we can get the 2-photon Rabi frequency for Raman processes under  $\text{lin}||\text{lin}$  configuration as

$$\Omega_{3,0 \rightarrow 4,0, \text{lin}||\text{lin}}^{(2)} = 0 \quad (3.22)$$

This Raman process is destructively interfering among all pathways under  $\text{lin}||\text{lin}$  configuration. In the same way, we can switch the polarization of  $E_{20}$  to  $\hat{\epsilon}_y$  so we have

$$\Omega_{3,0 \rightarrow 4,0, \text{lin}\perp\text{lin}}^{(2)} = \left( \frac{e \langle J' = \frac{3}{2} || e\mathbf{r} || J = \frac{1}{2} \rangle}{\hbar} \right)^2 E_{10} E_{20} \left( \frac{1}{8\Delta_{F'=3}} + \frac{5}{24\Delta_{F'=4}} \right) \quad (3.23)$$

If it's sufficiently far detuned, then the detuning for different intermediate  $F'$  state would be about the same. In that case this can be reduced to

$$\Omega_{3,0 \rightarrow 4,0, \text{lin}\perp\text{lin}}^{(2)} = \left( \frac{e \langle J' = \frac{3}{2} || e\mathbf{r} || J = \frac{1}{2} \rangle}{\hbar} \right)^2 \frac{E_{10} E_{20}}{3\Delta} \quad (3.24)$$

It is exactly the same as the Rabi frequency generated by  $\sigma^\pm - \sigma^\pm$  beams.

As for the leakage into other Zeeman states under  $\text{lin}\perp\text{lin}$  configuration. Based on selection rules, the only other possible states are  $|F = 4, m_F = \pm 2\rangle$ . We can calculate the Rabi frequency in the same way to get

$$\Omega_{3,0\rightarrow 4,\pm 2, \text{lin}\perp\text{lin}}^{(2)} = \left(\frac{e\langle J' = \frac{3}{2} || e\mathbf{r} || J = \frac{1}{2} \rangle}{\hbar}\right)^2 \frac{E_{10}E_{20}}{16} \sqrt{\frac{5}{2}} \left(-\frac{1}{\Delta_{F'=3}} + \frac{1}{\Delta_{F'=4}}\right) \quad (3.25)$$

This result is almost 0 if the detuning is sufficiently large. Same conclusions could be reached for the Raman process from  $F = 4 \rightarrow F = 3$ . In conclusion,  $\text{lin}\perp\text{lin}$  is a good configuration to drive Raman transition between  $F = 3$  and  $F = 4$  while retaining  $m_F = 0$  under sufficiently large detuning but  $\text{lin}||\text{lin}$  does not work for this purpose.

Likewise, we can also calculate the Rabi frequency for Bragg diffraction and Bloch oscillations. These are different from Raman in the way that the final state is in the same electronic state. The  $\sigma^\pm - \sigma^\pm$  configuration works for the obvious reason too. But we get the opposite conclusion for the linearly polarized light. The Rabi frequencies are calculated as follows:

$$\begin{aligned} \Omega_{3,0\rightarrow 3,0, \text{lin}||\text{lin}}^{(2)} &= \left(\frac{e\langle J' = \frac{3}{2} || e\mathbf{r} || J = \frac{1}{2} \rangle}{\hbar}\right)^2 E_{10}E_{20} \left(\frac{1}{7\Delta_{F'=2}} + \frac{3}{8\Delta_{F'=3}} + \frac{25}{168\Delta_{F'=4}}\right) \\ &\approx \left(\frac{e\langle J' = \frac{3}{2} || e\mathbf{r} || J = \frac{1}{2} \rangle}{\hbar}\right)^2 \frac{2E_{10}E_{20}}{3\Delta} \end{aligned} \quad (3.26)$$

$$\begin{aligned} \Omega_{3,0\rightarrow 3,\pm 2, \text{lin}||\text{lin}}^{(2)} &= \left(\frac{e\langle J' = \frac{3}{2} || e\mathbf{r} || J = \frac{1}{2} \rangle}{\hbar}\right)^2 \frac{E_{10}E_{20}}{16} \sqrt{\frac{5}{6}} \left(\frac{1}{7\Delta_{F'=2}} - \frac{3}{16\Delta_{F'=3}} + \frac{5}{112\Delta_{F'=4}}\right) \\ &\approx 0 \end{aligned} \quad (3.27)$$

$$\Omega_{3,0\rightarrow 3,0, \text{lin}\perp\text{lin}}^{(2)} = 0 \quad (3.28)$$

It concludes that  $\text{lin}||\text{lin}$  configuration works well with Bragg diffraction and Bloch oscillations for our purpose under sufficiently large detuning but  $\text{lin}\perp\text{lin}$  doesn't.

### Frequency Requirement

Based on the discussion above, the best polarization configuration works for both Raman transition and Bragg diffraction is  $\sigma^\pm - \sigma^\pm$  configuration. As shown in Figure 3.19, we send one beam with orthogonal circular polarization vertically up into the vacuum chamber. Each polarization carries independently prepared frequency. In this section we want to figure out how to play tricks on frequency to realize resonance conditions (essentially energy-momentum conservation) for all Raman, Bragg and Bloch processes.

There are two different types of Raman transition configurations used in the experiment. The first type is Doppler insensitive co-propagating Raman transition. Suppose the angular frequencies and wave numbers for both co-propagating beams are  $\omega_1, k_1$  and  $\omega_2, k_2$  respectively, and we are going to drive Raman transition from  $|F = 3, m_F = 0\rangle$  to  $|F = 4, m_F = 0\rangle$

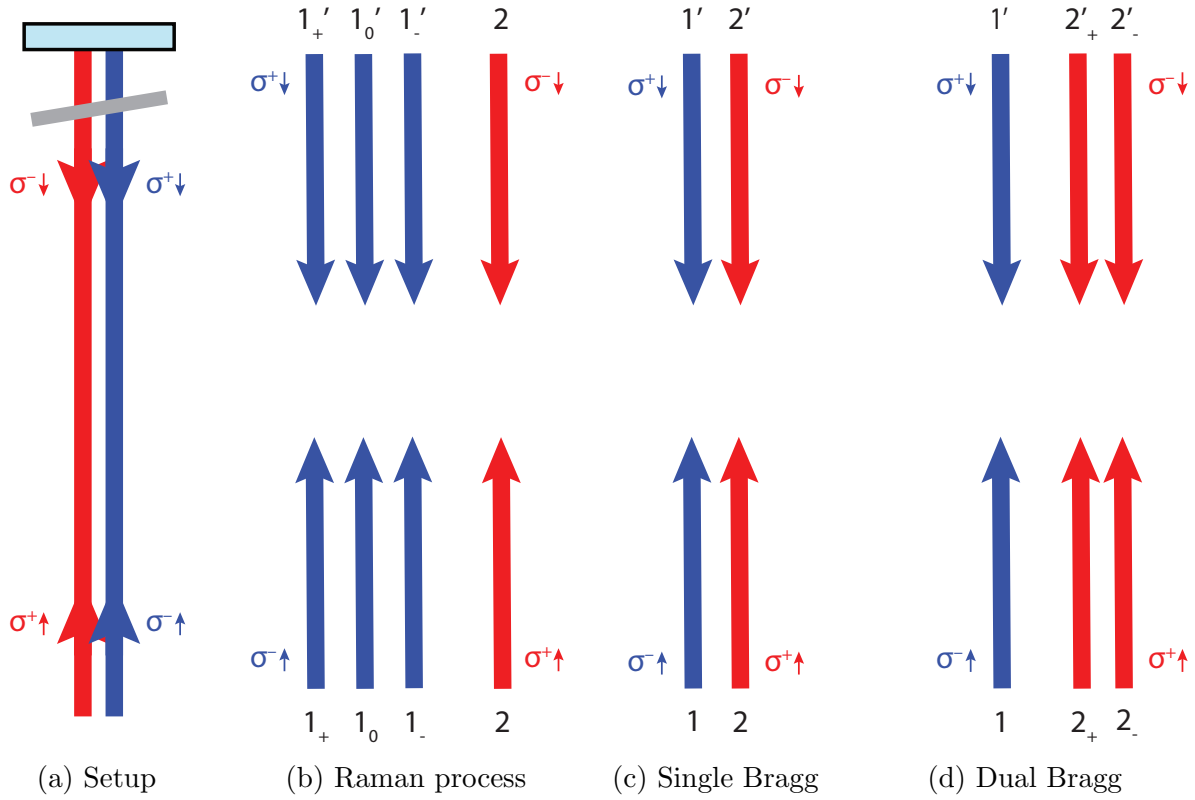


Figure 3.19: Raman/Bragg beam configuration used in the experiment.

with these two beams. If an atom is moving with velocity  $v$  up vertically, then the conservation of energy-momentum for the Raman process (absorbing  $\hbar\omega_1$  photon and emitting  $\hbar\omega_2$  photon) would imply

$$E_{|F=3, m_F=0\rangle} + \frac{1}{2}Mv^2 + \hbar\omega_1 - \hbar\omega_2 = E_{|F=4, m_F=0\rangle} + \frac{1}{2}M\left(v + \frac{\hbar k_1}{M} - \frac{\hbar k_2}{M}\right)^2 \quad (3.29)$$

Since  $k_1 - k_2 \ll (k_1 + k_2)/2$ , taking only the leading order terms, it yields

$$\omega_1 - \omega_2 = \frac{1}{\hbar}(E_{|F=4, m_F=0\rangle} - E_{|F=3, m_F=0\rangle}) \quad (3.30)$$

So this process is Doppler shift insensitive (or velocity insensitive) at the leading order. We just need to tune the frequency difference between these two beams to the hyperfine splitting between  $F = 3$  and  $F = 4$  plus small AC Stark shift ( $\sim 9.192$  GHz). We use this type for State Selection (SS).

The other type is Doppler sensitive counter-propagating Raman transition. Using the same scenario with the direction of  $\omega_2, k_2$  inverted, we have the following resonance equation,

$$E_{|F=3, m_F=0\rangle} + \frac{1}{2}Mv^2 + \hbar\omega_1 - \hbar\omega_2 = E_{|F=4, m_F=0\rangle} + \frac{1}{2}M\left(v + \frac{\hbar k_1}{M} + \frac{\hbar k_2}{M}\right)^2, \quad (3.31)$$

which gives

$$\omega_1 - \omega_2 = \frac{1}{\hbar}(E_{|F=4, m_F=0\rangle} - E_{|F=3, m_F=0\rangle}) + 2kv + 8\omega_r \quad (3.32)$$

where  $k = (k_1 + k_2)/2$  and the recoil frequency  $\omega_r = \hbar k^2/2M$ . This is clearly Doppler sensitive. We use it for Velocity Selection (VS). Since atom velocity keeps changing due to gravity, it would be convenient to add a frequency ramp in  $\omega_1 - \omega_2$  so that the same resonance condition can be satisfied everywhere along the atom trajectory.

Based on the need for both co-propagating and counter-propagating Raman transition, we prepare one beam to pass through an Electric-Optical Modulator (EOM) running close to 9.19 GHz to get one carrier and two sidebands labelled  $1_-$ ,  $1_0$  and  $1_+$  in Figure 3.19. At the same time, we add a frequency ramp through Acoustic-Optical Modulator (AOM) double pass scheme. In this way, when we are doing SS under the co-propagating configuration, we tune EOM frequency resonate with the hyperfine splitting plus AC Stark shift to drive SS with any pair from  $1_+ - 1_0$ ,  $1_- - 1_0$ ,  $1'_+ - 1'_0$ ,  $1'_+ - 1'_0$ . We noted that though any matching pair could drive Raman transition, the Raman processes with beams going up and with beams going down are interfering with each other. That's what we noticed in the experiment as spatial modulation of 2-photon Rabi frequency.

And when we run Velocity Selection (VS) under the counter-propagating configuration, we detune EOM frequency significantly from resonating with the hyperfine splitting in order to suppress co-propagating Raman processes. The absolute frequency of beam 1 is deliberately tuned through the double pass frequency ramp so that the beam pair  $1_- - 2'$  would be resonant for counter-propagating Raman transition. We use square pulses for Raman processes. It's not only easy to generate experimentally, but also necessary for VS. Though Gaussian waveform offers cleaner Fourier spectrum, any variation in intensity would vary AC Stark shift. AC Stark shift is very important for VS process as it determines what velocity class of atoms would be selected. So in practice, Gaussian Raman pulse would broaden the selected velocity width. For square Raman pulse, its velocity selectivity could be calculated quite straightforward as follows.

Based on the solution of Raman square pulse in Section 2.3, if we drive an atom from  $|F = 3, m_F = 0\rangle$  (labeled  $|1\rangle$ ) to  $|F = 4, m_F = 0\rangle$  (labeled  $|2\rangle$ ) with a Raman square  $\pi$  pulse of length  $\tau$ , the final state would be

$$|\Phi(\tau)\rangle = \cos\left(\frac{\Omega_{\text{eff}}\tau}{2}\right) + i\frac{\delta}{\Omega_{\text{eff}}}\sin\left(\frac{\Omega_{\text{eff}}\tau}{2}\right)|1\rangle - i\frac{\Omega_0}{\Omega_{\text{eff}}}\sin\left(\frac{\Omega_{\text{eff}}\tau}{2}\right)e^{i(2kz - \Delta\omega t)}|2\rangle \quad (3.33)$$

where  $\Omega_0$  is the 2-photon Rabi frequency in the absence of detuning;  $\delta$  is the detuning; the effective 2-photon Rabi frequency is  $\Omega_{\text{eff}} = \sqrt{\Omega_0^2 + \delta^2}$ ;  $\Delta\omega$  is the frequency difference of two laser beams. If the Raman process is on resonance, then the detuning is simply determined by atom velocity spreads, so

$$\Omega_0\tau = \pi \quad (\pi \text{ pulse definition}) \quad (3.34)$$

$$\delta = 2kv \quad (\text{detuning definition for non-resonant atoms}) \quad (3.35)$$



Here we can define velocity selectivity by the full velocity width at half Raman transition probability into state  $|2\rangle$ . i.e. we need to find velocity width  $\Delta v$  satisfying  $\langle 2|\Phi(\tau)\rangle \geq \frac{1}{2}$ . By solving

$$\left(\frac{\Omega_0}{\Omega_{\text{eff}}}\right)^2 \sin^2\left(\frac{\Omega_{\text{eff}}\tau}{2}\right) = \frac{1}{2} \quad (3.36)$$

we can get the simple numerical relation of the velocity selectivity as a function of Raman  $\pi$  pulse length  $\tau$ .

$$\frac{\Delta v}{v_r} = \frac{1.2546}{\omega_r \tau} \quad (3.37)$$

where recoil velocity  $v_r = \hbar k/M$ .

The resonance condition for Bragg diffraction is quite similar. The difference is that the initial and final states are now in the same electronic state so there is no internal energy difference as well as differential AC Stark shift. And now instead of a two-photon process, the  $n^{\text{th}}$  order Bragg diffraction is a  $2n$ -photon process.

$$\frac{1}{2}Mv^2 + n\hbar\omega_1 - n\hbar\omega_2 = \frac{1}{2}M\left(v + \frac{n\hbar k_1}{M} + \frac{n\hbar k_2}{M}\right)^2 \quad (3.38)$$

which yields

$$\omega_1 - \omega_2 = 2kv + 8n\omega_r. \quad (3.39)$$

where  $k = (k_1 + k_2)/2$ .

For Bloch oscillations, the resonance condition is set by optical lattices such that it's co-moving with atoms, which means atoms always see the lattice roughly at rest. Based on the Doppler shift atoms see for each lattice beam, the resonance condition simply implies

$$\omega_1 - \omega_2 = 2kv. \quad (3.40)$$

Based on the Simultaneously Conjugated Ramsey Bordé atom interferometer with Bloch oscillations configuration we discussed in the previous chapter, we need two kinds of Bragg pulses for single Bragg diffraction and dual Bragg diffraction, which were also shown in Figure 3.19. Unlike the Raman process, we don't need to turn on EOM for sidebands. Instead, we shift the absolute frequency of the gravity ramp for beam 1 so that the beam pair  $1 - 2'$  could be resonant for single Bragg diffraction. For dual Bragg mode, we want to drive the transition from  $nv_r$  to  $3nv_r$  for upper interferometer and  $-nv_r$  to  $-3nv_r$  for the lower interferometer in the reference frame symmetric for both upper and lower interferometers. Based on the resonance condition, we need  $\omega_1 - \omega_2 = (\omega_1 - \omega_2)_{\text{single Bragg}} - 8(n + N)\omega_r$  for the upper interferometer and  $\omega_1 - \omega_2 = (\omega_1 - \omega_2)_{\text{single Bragg}} + 8(n + N)\omega_r$  for the lower one. ( $n$  is the order of Bragg diffraction and  $N$  the order of Bloch oscillations.) We achieve this by running the beam 2 in dual frequency mode with frequency separation by  $2\omega_m$ . So the beam pair  $1 - 2'_-$  and  $1 - 2'_+$  would be resonant for the upper and lower interferometers respectively.  $\omega_m$  is set very close but not exactly to  $8(n + N)\omega_r$  so that  $\omega_m$  would be a tunable parameter entering the phase of the atom interferometer. Essentially the atom interferometer is a

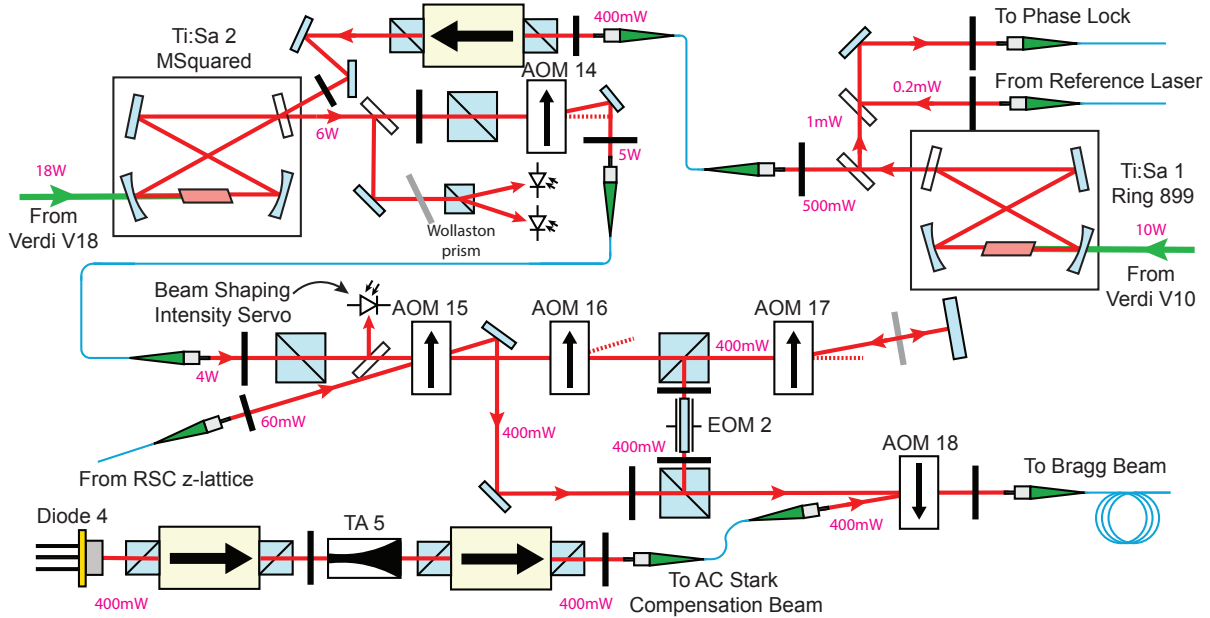


Figure 3.20: Coherent Manipulation Optical Schematics

phase lock system to lock recoil frequency in a complex way to the modulation frequency  $\omega_m$  through measuring zero phase in the interferometer.

Given this setup, Bloch oscillations could be realized with the same configuration as the dual Bragg with modification of the value of  $\omega_m$ . Instead of a single value  $\omega_m$  close to  $8(n + N)\omega_r$ , we use ramp  $\omega_m$  from  $4n\omega_r$  to  $4n\omega_r + 8N\omega_r$  in order to accelerate the upper interferometer from  $nv_r$  to  $(n + 2N)v_r$  and the lower one from  $-nv_r$  to  $-(n + 2N)v_r$  in the reference frame symmetric to both interferometers.

## Setup and Timing

The setup starts with a laser source with high power and clean mode because of the demands of Bragg diffraction. So we use Ti-sapphire lasers as such a source at 852 nm. In our experiment as shown in Figure 3.20, we use two Ti-sapphire lasers to generate 852 nm laser beam for this purpose. The first one (Ti:Sa1) is the old Coherent 899 Ring Ti-sapphire laser pumped by 10 W Coherent V10 pump laser to phase lock to the reference frequency and to provide an accurate and stable frequency source. The second one (Ti:Sa2) is a special one customized based on M Squared SolsTiS [94]. Compared with its base model, frequency filtering components like birefringence filter, etalon as well as optical diode are removed to ensure highest possible output power. This customized Ti-sapphire laser is pumped by 18 W Coherent V18 pump laser and is able to output more than 8 W in free running mode and more than 6 W at 852 nm. Ti:Sa2 is locked to Ti:Sa1 with injection locking scheme

[95]. To be more specific, the whole locking scheme is done as follows. We send a sampled beam from Ti:Sa1 and beat with the beam from the reference laser. The beating signal is mixed with a local oscillator generated by a microwave function generator. The RF after mixing at the intermediate frequency port ( $<100$  MHz) is phase locked to the gravity ramp frequency generated by a Direct Digital Synthesizer (DDS). The feedback is applied at a reference cavity to which Ti:Sa1 is locked. So the frequency of the Ti:Sa is

$$f_{\text{Ti:Sa}} = f_{3 \rightarrow 4'} + f_{\delta} - f_{\text{DDS}} \quad (3.41)$$

The microwave function generator is used to set the single photon detuning of the Raman/Bragg/Bloch beam. Limited by the phase lock detector as well as actual Ti:Sa power available for Bragg diffraction, we normally set it either red or blue detuned from 4.5 GHz to 15 GHz. The DDS is used to add a frequency ramp into the system to cancel Doppler frequency shift due to gravity as we mentioned earlier. We define this frequency ramp (gravity ramp) as  $f_{g,\text{ramp}} = 2f_{\text{DDS}}$ . The reason to lock Ti:Sa1 to the gravity ramp is to make beam 1 ramp with  $f_{g,\text{ramp}}/2$  and beam 2 ramp with  $-f_{g,\text{ramp}}/2$  so that the average wave number  $k = (k_1 + k_2)/2$  would be ramp independent. It eliminates the dependence of ramp in the measured phase. Ti:Sa1 then is directly fed into Ti:Sa2 ring cavity as shown in Figure 3.20 for injection lock. This is different from diode laser injection lock. Since the ring cavity in Ti:Sa2 is longer and has higher finesse, if the cavity is off resonance, the injection beam will mostly be rejected. So we use polarization spectroscopy to lock the cavity to be resonant with the injection beam. This method is called Hänsch-Couillaud technique [96]. When we inject a beam into the ring cavity through the output coupler, part of the beam will enter the ring cavity, while the rest got reflected based on the inject beam orientation, polarization as well as the coating of the output coupler. The ring cavity itself is polarization selective. Only the light with the correct linear polarization would pass through and be built up inside the cavity due to some polarization selective elements inside. The orthogonal polarization would be fully reflected. At the output we combine both reflected and injected polarization and send to device made by a quarter wave plate and a Wollaston prism to detect if the cavity is on resonance or not. When it is on resonance (giving a phase delay of either  $\pi$  or  $2\pi$ ), the cavity output combined with the reflected injection beam with orthogonal polarization would result in a linear polarized beam as the total output. The quarter wave plate is properly aligned such that when the output beam is linearly polarized, it would be converted to orthogonal circularly polarized lights with equal amplitude. Thus it will get split into two beams with equal amplitude by the Wollaston prism, resulting in a zero signal in the differential detection scheme. When the cavity is not on resonance, it gives a non-zero error signal. By applying feedback to the Ti:Sa cavity mirror piezo with a properly designed servo lockbox, we can tightly injection lock Ti:Sa2 in this way. The key to stably injection lock the Ti:Sa laser is to have enough injection power, which in our case is more than about 200mW.

After such a high power, narrow linewidth, accurate frequency source is prepared, we use AOM14 to generate pulses in different shapes we want, i.e square pulses for Raman transition, Gaussian pulses for Bragg diffraction, square pulses with ramp on and ramp off

for Bloch oscillations. When it's in idle we dump all its power to the zeroth order of AOM14. Though it's extremely powerful, the duty cycle is rather low so it doesn't damage the fiber or cause any other thermal effect. We pick up a fraction of power after the fiber coupling to detect the real pulse shape so as to compare with the intended pulse shape programmed with function generators and feedback to AOM14. It is to be noted that the feedback speed is limited by the sound speed of AOM14. It takes a few microseconds for the generated sound wave to reach the laser beam. The only way is to move the crystal closer to the actuator but it also increase the risk to burn the AOM under high power operation. For this reason, we can clearly see distortion of a Bragg pulse from a pure Gaussian pulse at around 10us time scale (see Figure 5.7). This might potentially contribute to our systematic error. We will cover it in Section 5.5.

After the pulse is ready, we need to prepare frequencies to match the resonance condition for Raman, Bragg and Bloch processes as we discussed earlier. We use AOM15 (running at 180 MHz) to generate beam 2 (called counter-propagating beam) shown in Figure 3.19. In single frequency mode (VS and single frequency Bragg), we only use 180 MHz synthesized by Phase Lock Loop (PLL) through 10 MHz reference with proper amplification. In dual frequency mode, AOM15 generates a beating signal, leaving inverted intensity modulation in the zeroth beam as well. So we use AOM16 running at the same beat frequency as AOM15 in quadrature to compensate that residual amplitude modulation in dual frequency mode. It is achieved by rerouting 180 MHz with RF switches to mix with the modulation frequency  $f_m = \omega_m/2\pi \sim 8(n+N)\omega_r/2\pi$  in phase and in quadrature for AOM15 and AOM16 respectively. More details can be found in these references [61, 62].

The zeroth order beam after AOM15 passes through AOM16 and AOM17. During single frequency mode, AOM16 is also running to cut some power from the beam in order to match the Rabi frequency of the Bragg diffraction in dual frequency mode. AOM17 is running in double pass scheme to generate the gravity ramp in beam 1 (called double pass beam) shown in Figure 3.19. A double pass scheme is chosen in order to have larger bandwidth to cover all pulses in the experiment. It switches between two ramps with the same ramp rate but slightly different offset frequency for Raman and Bragg respectively due to different resonance conditions. The ramp for Raman starts at  $t=1.033$  s, ramping roughly from 93.66 MHz to 82.16 MHz at a rate of -11.4978 MHz/s to match the required Doppler frequency ramp rate given by  $2kg$  where  $g$  is the gravitational acceleration. The ramp for Bragg starts at the same time, but ramping roughly from 95.68 MHz to 84.18 MHz. These ramps are generated by two channels of a Direct Digital Synthesizer (DDS) AD9954. In order to precisely control the ramp rate, we use an externally referenced function generator running at 15.7135 MHz to serve as the external reference for the DDS so that two units of the ramp rate control bits gives exactly the same ramp rate we want. And we use a Raspberry Pi to generate SPI control serial signal to control the absolute frequency of the DDS for Raman and Bragg modes as we need to optimize these frequency from time to time to match the fountain velocity to ensure the best VS and Bragg efficiency. After the double pass, this beam go through EOM2 running at about 9.19263 GHz for SS and 9.18863 GHz for VS. This microwave frequency is generated by the same circuit we use to generate the microwave

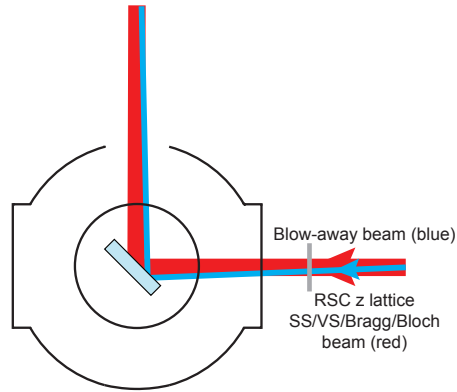


Figure 3.21: Bragg and blow-away beams setup

frequency for Adiabatic Rapid Passage (ARP), namely a Dielectric Resonator Oscillator (DRO) locked at the mixing frequency of the 51st comb line of a microwave comb with repetition frequency 180 MHz and a offset frequency from a function generator. So we can simply use frequency shift keying of this function generator to shift the frequency between SS and VS. We only turn on EOM2 for Raman transitions. After EOM2, the double pass beam will be combined with the counter-propagating beam in orthogonal linear polarization with a PBS and send to the vacuum chamber with a polarization maintaining fiber. We also inserted another beam through AOM18 as AC Stark compensation beam, which is generated by an independent diode running at a frequency with opposite single photon detuning to reduce decoherence effect due to AC Stark effect in Bloch oscillations. More details about AC Stark compensation would be discussed in Section 4.1.

After the Raman/Bragg/Bloch beam is coupled to the experiment side, we put a quarter wave plate to convert orthogonal linear polarizations into orthogonal circular polarizations to form  $\sigma^{\pm} - \sigma^{\pm}$  configuration as we discussed earlier. We also insert the Raman Sideband Cooling z-lattice beam to the first order output of AOM15 (when it's turned off) and conveniently send it to the vacuum through the same Bragg beam fiber port. Both 3-state and 4-state blow-away beams are coupled separately to a different fiber such that it has significant overlap with the Bragg beam at the region for state preparation as shown in Figure 3.21. We also add a lens to make it divergent so that it would be easier to overlap with atoms.

The timing of state preparation and atom interferometry is basically configured as shown in Figure 3.22 and 3.23. After ARP, most atoms are prepared to  $|F = 4, m_F = 0\rangle$ , while some still remain in the wrong state. So the purpose of SS is to keep atoms in the right states and get rid of the rest. Firstly, we turn on the gravity ramp at  $t=1.033$  s. Then at  $t=1.17$  s we apply a 3-state blow-away beam for 2 ms to clear all  $F = 3$  atoms. At  $t=1.19$  s, we turn on EOM and get ready for SS. The basic building blocks of a pulse consists a pulse trigger, turning on the pulse shaping AOM (AOM14), In order to generate a pulse, we normally need to turn on the pulse shaping AOM (AOM14), the intensity servo, the counter-propagating

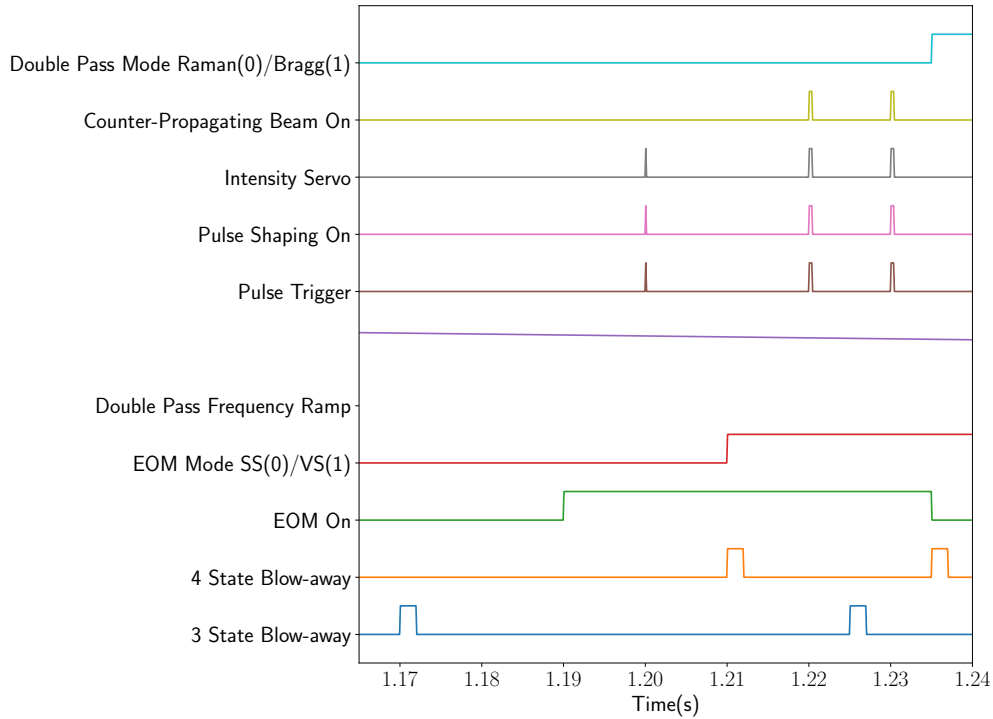


Figure 3.22: State Preparation Timing

beam AOM (AOM15) sometimes. After turning on these devices, we trigger it by either sending the reference pulse directly to the intensity servo (for square pulses like SS and VS) or sending the trigger to function generators to generate a pulse waveform stored in it (for Bragg and Bloch). The intensity servo would feedback the pulse shaping AOM to generate the waveform that matches the reference waveform. After the pulse, we turn off all these devices in order to avoid any bit light leaking through the AOM or spikes due to transient effects of the intensity servo.

So at  $t=1.20$  s, we generate such a square pulse for SS. During SS, the counter-propagating beam is off as it is unnecessary. SS pulse is a square pulse with a pulse length fixed to  $70\mu\text{s}$ . But we can still fine tune the pulse intensity to control where we want to drive to on Bloch sphere. Ideally  $\pi$  pulse would give maximum transfer efficiency, but in reality since the beam intensity is not uniform we tend to over drive it a little bit to maximize the number of atoms transferred to the new state. Subsequently we apply a 4-state blow-away at  $t=1.21$  s to clean up the remaining atoms at  $F = 4$ . After SS, almost all atoms would be in the right state ( $|F = 3, m_F = 3\rangle$ ) ready for VS. VS requires a different EOM frequency so we use FSK to switch it to VS mode at  $t=1.21$  s. In practice, we use two VS pulses at  $t = 1.22\text{s}, 1.23\text{s}$  respectively to ensure a small velocity spreads. Though the selectivity of each VS pulse is the same, if the atom velocity spreads at the input is already small, an additional VS could make it even smaller. We turn on the same triggers plus the counter-propagating beam AOM

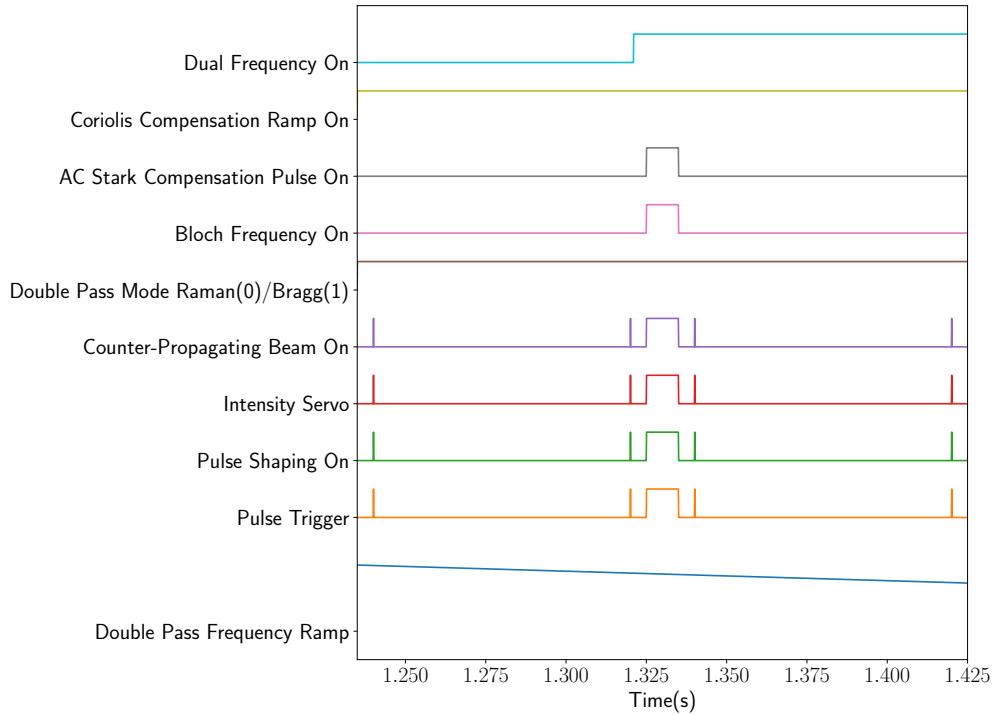


Figure 3.23: Atom Interferometry Timing

for each VS pulse. The pulse is a square pulse of  $400 \mu s$ . Based on the formula we had, the velocity FWHM for its transition probability is about  $0.24v_r$ , much smaller than the width we had after Raman Sideband cooling. After each VS pulse, we also apply appropriate blow-away beam to clean those non-selected atoms. Because the input atom velocity width is already quite small, after two VS pulses, we expect an even smaller width than this theoretical value  $0.24v_r$ . At the end of state preparation, we turn off EOM and switch the double pass frequency to Bragg mode, ready for atom interferometry sequence.

We start the atom interferometer sequence at  $t=1.24$  s. Since it's very critical in timing accuracy, we use SRS DG535 and DG645 to generate the relative timing sequence. The only absolute timing is defined by the computer timing trigger at  $t = 1.239$  s, triggering the whole interferometer timing system. One delay generator is used to trigger Bragg pulse groups. The first group contains the first two Bragg pulses running in single frequency mode. The second group contains the last two Bragg pulses running in dual frequency mode. The delay generator generates a trigger for each pulse group to trigger a second pulse generator to prepare pulse triggers for each individual pulse within the pulse group. The advantage of this configuration is that the timing for the second pulse group is the exact copy of the timing for the first pulse group, eliminating potential systematics coupled through asymmetries in timing between two groups. For each Bragg pulse, we use the same control switches as those used for VS pulses. The difference is that we trigger a function generator to generate a Gaussian reference pulse for the intensity servo. Realistically the Gaussian pulse has to be

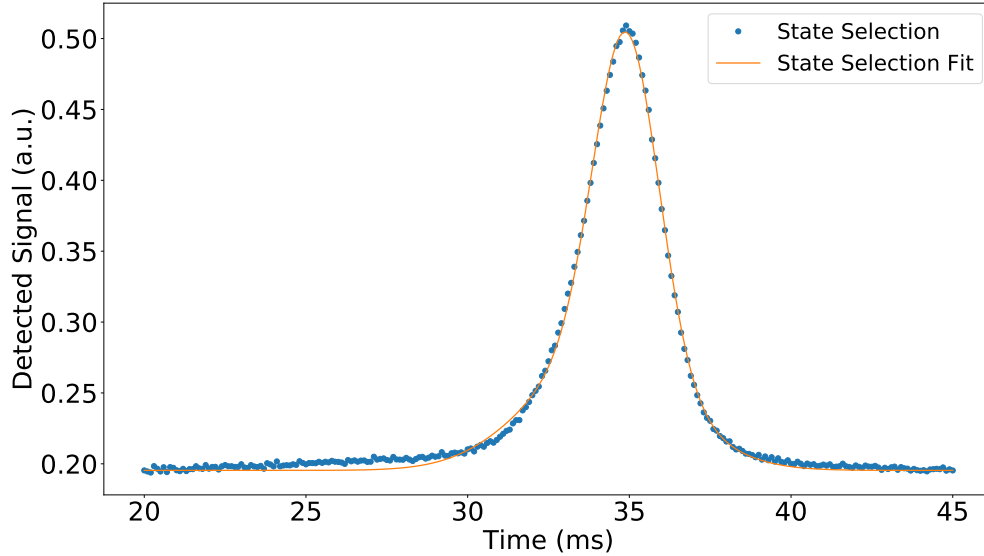


Figure 3.24: State Selection signal and its double Gaussian fit

truncated in time. So we only drive it from  $-3\sigma$  to  $3\sigma$  with  $\sigma \approx 18$  ms. After the first group of Bragg pulses are done, we switch on dual frequency mode for Bloch oscillations and the last two Bragg pulses. Normally 5 ms after the second pulse, we turn on Bloch oscillations. Bloch oscillations pulse is a square pulse that lasts for  $\tau = NT_B$  with  $100 \mu s$  ramp on and  $100 \mu s$  ramp off, where  $T_B$  is the Bloch period defined in Equation 2.120 and here is controlled by Bloch ramp rate (normally set to be 250 MHz/s). Bloch frequency ramp is generated by another DDS other than the one for gravity ramp. During Bloch oscillations, we also switch on an RF switch to disconnect the Bragg  $f_m$  and connect the Bloch frequency ramp to the RF switch yard to mix with 180 MHz for AOM15. We also turn on a shutter as well as AOM18 to get AC Stark compensation beam mixed in to compensate AC Stark shift generated by Bloch oscillations so as to restore coherence to some extent. Another trick to improve atom coherence as shown here is Coriolis compensation. Basically during the whole period of atom interferometry, we ramp the top retro-reflect mirror simultaneously with specially chosen ramp rate to cancel Coriolis effect due to the Earth's rotation. More of these tricks will be discussed in Section 4.1.

## Performance

In the actual experiment, we use a  $70 \mu s$  long square pulse to drive a Raman pulse for State Selection (SS). The CCD image after SS is quite weak so it won't give us useful information about atom cloud spatial distribution. But we can still use the SS signal from photodetector to estimate the cloud temperature. SS signal can also be fitted with a double Gaussian of width  $\sigma_z = 5.68$  mm as shown in Figure 3.24. If we holds the assumption that Raman Sideband Cooling (RSC), Adiabatic Rapid Passage (ARP) and SS won't change the



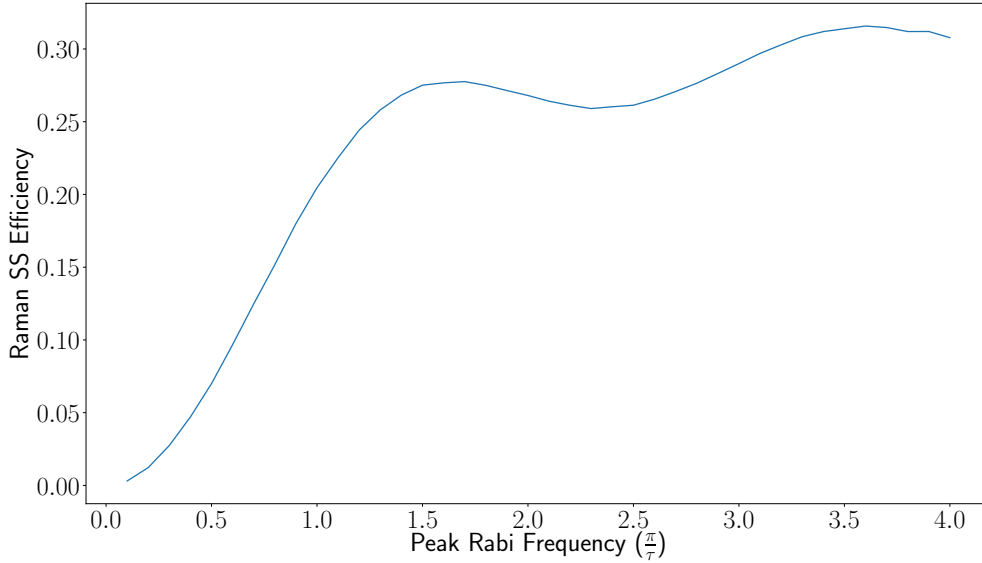


Figure 3.25: State Selection pulse efficiency vs. peak two-photon Rabi frequency given by a Monte Carlo simulation

effective atom distribution along  $z$  direction at the first passing of the detection, we can get longitudinal temperature  $T_z = 76$  nK. The efficiency of SS won't be perfect 100% because the intensity of the actual Gaussian-like beam won't be uniform. So the Raman pulse efficiency varies depending on the transverse location of the atom relative to the beam center. If the pulse is  $\pi$  pulse at the peak intensity, it might not be as efficient. Here with Monte Carlo simulation we can estimate the Raman SS efficiency as a function of the peak Rabi frequency of the beam as shown in Figure 3.25. This efficiency here is defined as the ratio between the number of Raman selected atoms and the number of all atoms in the correct Zeeman states. The Raman beam used in the simulation is assumed to be a pure Gaussian beam with waist  $w = 3.37$  mm measured by a beam profiler. The atoms before SS are assumed to follow Gaussian distribution with  $\sigma_x = \sigma_y = 4.4$  mm from CCD measurement. And we vary the peak intensity of the beam in the unit of its theoretic  $\pi$  pulse Rabi frequency  $\Omega_\pi = \pi/\tau$  where the pulse length  $\tau = 70$   $\mu$ s. In the experiment we typically optimize the efficiency of SS around the first peak in this plot, where the peak Rabi frequency is about  $1.6\Omega_\pi$ . It means we overdrive the center atoms past  $\pi$  pulse so the SS efficiency at the center would be lower than the side. It is as expected in the simulated transverse distribution after SS shown in Figure 3.26.

After SS we apply two 400  $\mu$ s long Raman square pulses to drive Raman  $\pi$  pulse for Velocity Selection (VS). Based on equation, the VS selectivity is about  $\Delta v = 0.24v_r$ . Atom clouds are completely invisible by CCD camera after this stage. But we can still detect it with the photodetector as shown in Figure 3.27. Since the hot atom class would be filtered out, VS signal can typically be well fitted to a single Gaussian. Here  $\sigma_z$  in the plot is estimated to be

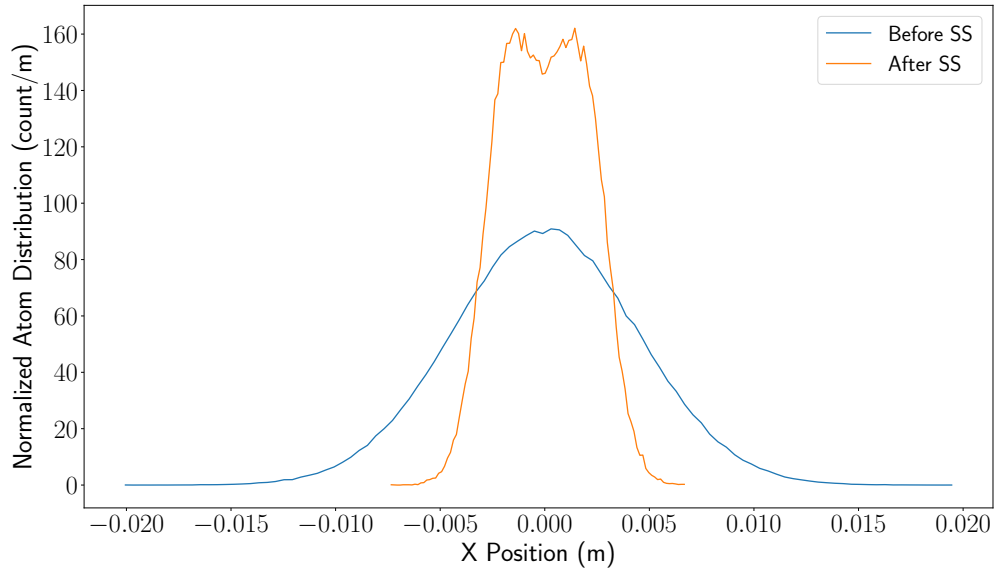


Figure 3.26: Simulated atom distribution along x axis before and after SS

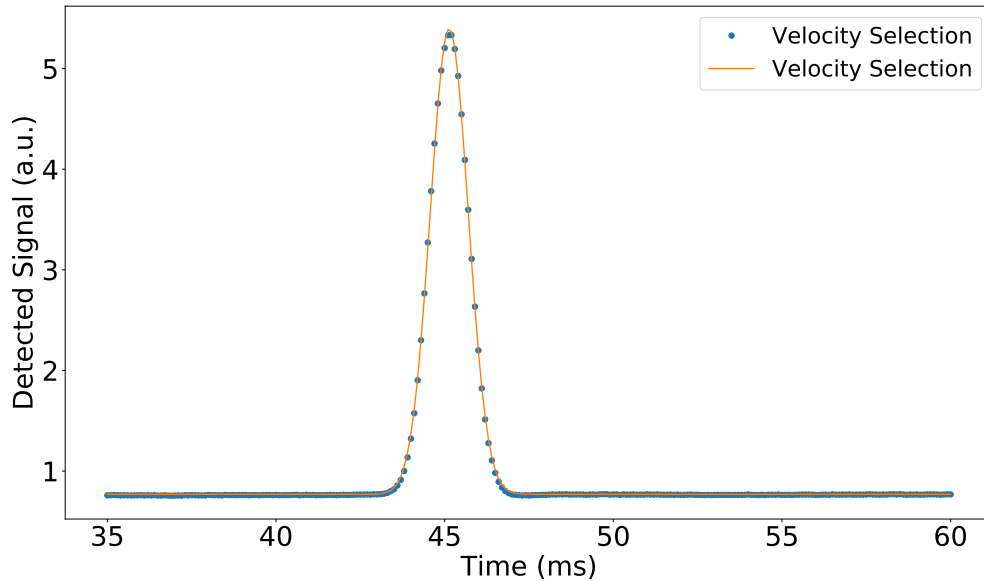


Figure 3.27: Velocity Selection signal and its Gaussian fit

about 3.18 mm. It's actually even smaller than the width of the first fountain, so we cannot use ToF to estimate the temperature. But we can still input the atom spatial and velocity distribution after SS into the Monte Carlo to estimate the efficiency of VS and atom phase space distribution after VS. Again we use the same Gaussian beam profile for VS Raman pulse. VS efficiency as a function of peak Rabi frequency is plotted here in Figure 3.28. We also typically optimize the efficiency around the first peak where the peak Rabi frequency

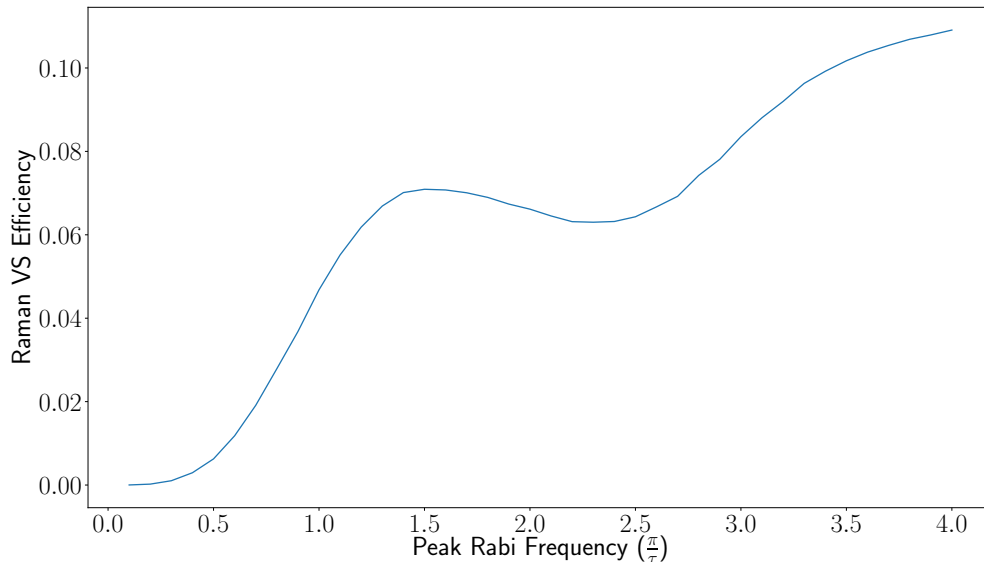


Figure 3.28: Velocity Selection pulse efficiency vs. peak two-photon Rabi frequency given by a Monte Carlo simulation

is about  $1.4\Omega_\pi$ . The donut-like spatial distribution is even more obvious after VS as shown in Figure 3.29. The longitudinal velocity distribution could also be obtained as shown in Figure 3.30. The main peak can be fitted by Gaussian with  $\sigma_v = 0.074v_r$ , which corresponds to about 1.1nK. We can also see small "sidebands" on both sides of the main peak in the velocity distribution due to the Fourier spectrum of the VS square pulse. The signal size after SS, according to the photodetector, is about 1/5-1/2 of RSC signal size. The efficiency here is different from the one defined in Figure 3.25, since not all atoms selected by SS would eventually be detected, nor does we take atom distribution of all Zeeman states into consideration in the simulation. Other things like how RSC is performed would significantly affect the detected SS signal size. VS signal is about 1/20 of SS signal, which is pretty close to the simulated efficiency. That is because what VS mostly does is selection in velocity space, which can be quite accurately reflected in the detected signal ratio. Based on these relative ratios, we can roughly estimate the number of atoms detected after each of these steps applied as shown in Table 3.5.

After all state preparation, we start the atom interferometry stage. All Bragg diffraction beam splitters used are Gaussian-shaped pulses with  $\sigma = 18.2 \mu\text{s}$  in time domain. The pulse width is chosen to minimize parasitic interferometer effect as will be discussed in Section 5.5. A single Bragg diffraction pulse would transfer  $2n\hbar k$  momentum to deflected atoms, resulting in spatial separation after certain time of free evolution as shown in Figure 3.31. It is what a  $\pi/2$  pulse would normally look like. Due to beam intensity variation across the beam cross section, atoms in certain areas would experience Bragg pulses closer to  $\pi/2$  pulses than others. Effectively the ratio of the deflected peak to the original peak would

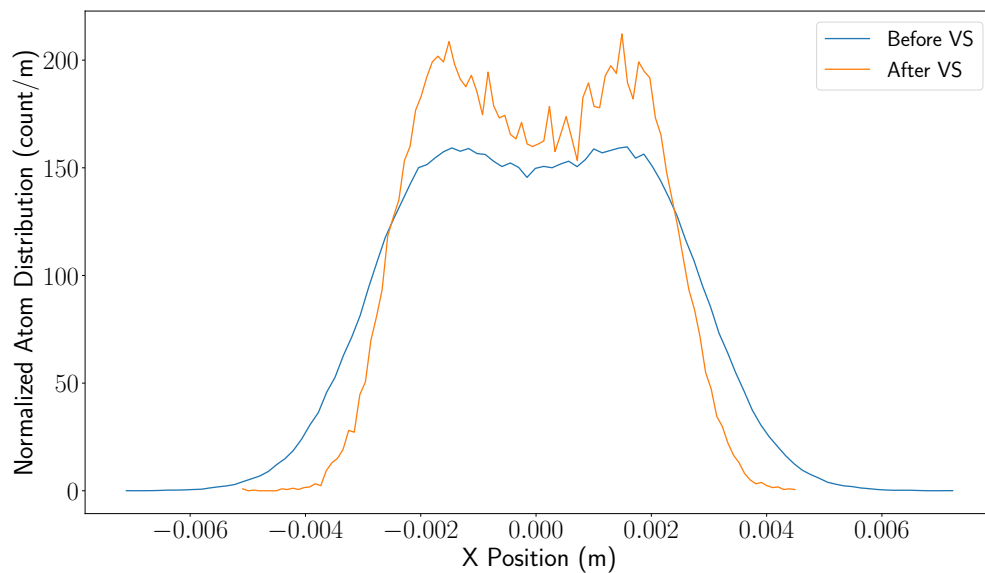


Figure 3.29: Simulated atom distribution along x axis before and after VS

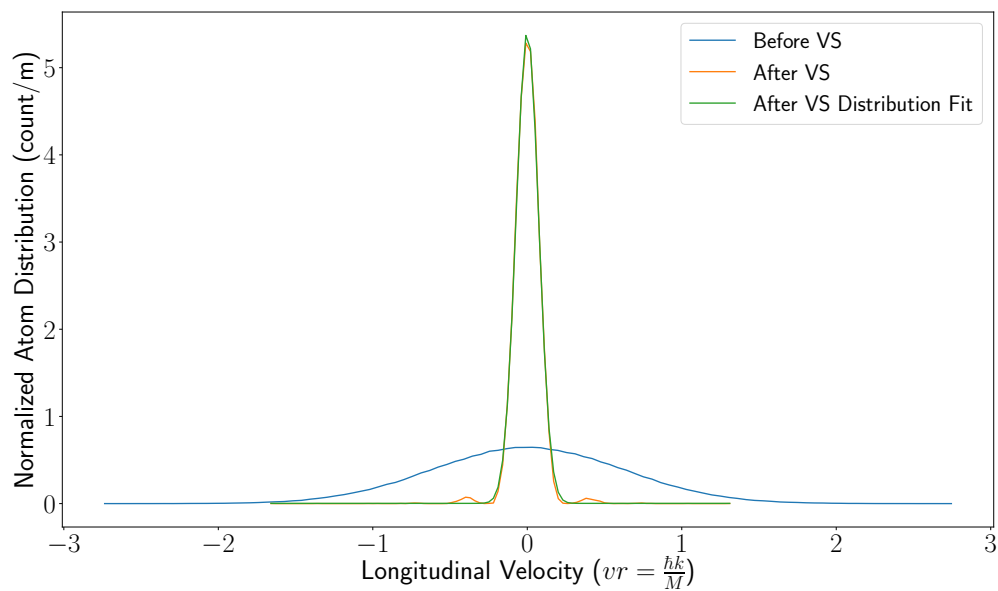


Figure 3.30: Simulated atom velocity distribution along z axis before and after VS

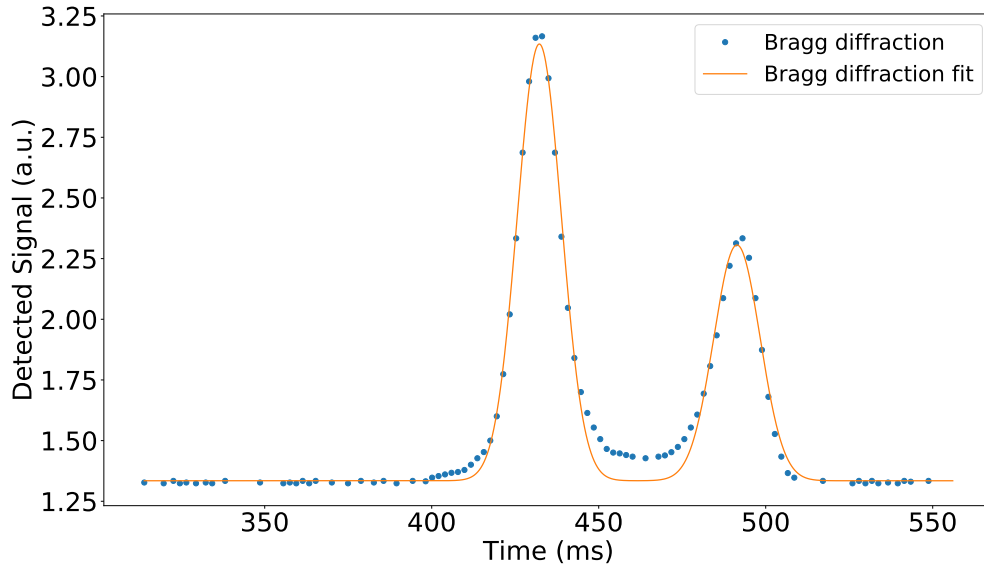


Figure 3.31: Bragg diffraction signal and its Gaussian fit

Signal Type	Estimated Atom Number
The First Fountain	$3.6 \times 10^8$
The Second Fountain (with PGC)	$3 \times 10^7$
The Second Fountain (with PGC, RSC and ARP)	$3.6 \times 10^7$
The Second Fountain (with PGC, RSC and SS)	$1.2 \times 10^7$
The Second Fountain (with PGC, RSC, SS and VS)	$6 \times 10^5$

Table 3.5: Rough estimation of atom number detected by the photodetector with each procedure applied

be less than 1:1. In the experiment, the frequency and intensity of Bragg diffraction are determined by phase and contrast measurement through atom interferometers respectively, which will be discussed Section 3.6.

Between the second and the third Bragg beam splitter in the Ramsey Bordé interferometer, we sometimes insert Bloch oscillations. It has a square pulse shape with  $100 \mu\text{s}$  ramp on and  $100 \mu\text{s}$  ramp off. Typically the ramp rate is chosen to be about  $250 \text{ MHz/s}$ , which means a  $N = 125$  Bloch pulse lasts about  $8.27 \text{ ms}$ . Bloch oscillations ramp start and stop frequencies are determined by the measured recoil frequency. It won't make a difference if it's differ by a fraction of recoil frequency. But the ramp rate as well as Bloch intensity affects both Bloch efficiency (how much fraction of atoms would be transferred) and atom interferometer contrasts. They would be optimized based on both metrics, which will be further explained in Section 4.1.

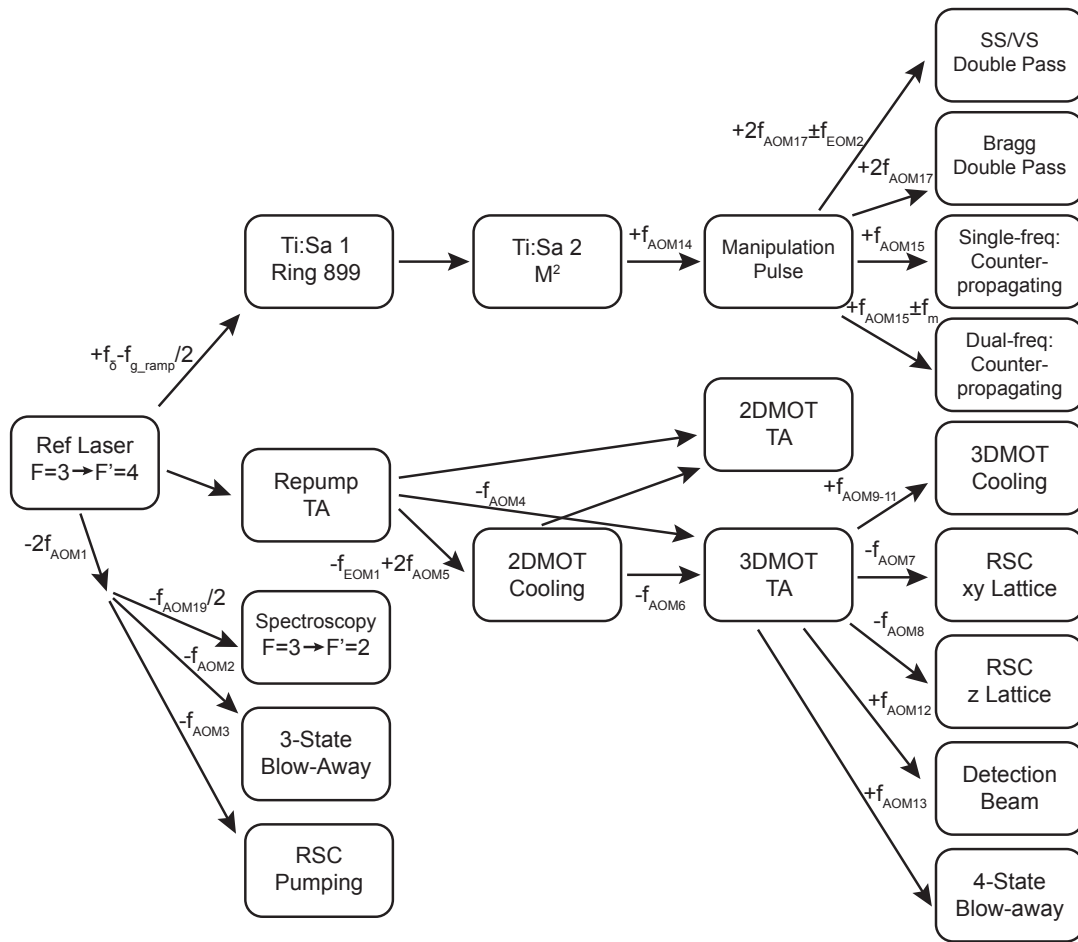


Figure 3.32: Frequency generation diagram

### 3.5 Summary

We have covered basic technical details of the whole experiment in this chapter. One difficulty of the experiment is the complicated frequency generation scheme. Here we summarize the whole scheme to make it clear for readers. Starting from the reference laser frequency, the block diagram in Figure 3.32 shows how each frequency we used in the experiment is generated and how it is referenced to other frequencies. Note that the AOM, EOM frequencies labeled here could take different values depending on different mode of operation. More details about the frequencies can be found in Table 3.6.

Notation	Component	Frequency
$f_{\text{Diode1}}$	Reference Laser	$f(F = 3 \rightarrow F' = 4)$
$f_{\text{Diode2}}$	2DMOT Slave	$f(F = 4 \rightarrow F' = 5) - 7.5 \text{ MHz}$
$f_{\text{Diode3}}$	3DMOT Slave	$f(F = 4 \rightarrow F' = 5) - 14.5 \text{ MHz (MOT) or } -43.3 \text{ MHz (PGC/RSC)}$
$f_{\text{Ti:Sa1-2}}$	Ti:Sa 1-2	$f(F = 3 \rightarrow F' = 4) + f_\delta - f_{g,\text{ramp}}/2$
$f_{\text{Diode4}}$	AC Stark Compensation Laser	$f(F = 3 \rightarrow F' = 4) - f_\Delta (\sim 50 \text{ GHz})$
$f_{\text{AOM1}}$	Reference Laser Double Pass AOM	141 MHz
$f_{\text{AOM2}}$	3-state blow-away AOM	66 MHz
$f_{\text{AOM3}}$	RSC Pumping AOM	65 MHz
$f_{\text{AOM4}}$	3DMOT Repump Shift AOM	80 MHz
$f_{\text{AOM5}}$	Trapping Frequency Double Pass AOM	130.4 MHz (MOT) or 116 MHz (PGC/RSC)
$f_{\text{AOM6}}$	2D-3DMOT Relative Shift AOM	88 MHz
$f_{\text{AOM7}}$	RSC xy Lattice AOM	120.4 MHz
$f_{\text{AOM8}}$	RSC z Lattice AOM	115.8 MHz
$f_{\text{AOM9}}$	3DMOT bottom beam AOM	80 MHz
$f_{\text{AOM10}}$	3DMOT top beam AOM	80 MHz
$f_{\text{AOM11}}$	3DMOT side beam AOM	80 MHz
$f_{\text{AOM12}}$	Detection beam AOM	93.6 MHz
$f_{\text{AOM13}}$	4-state blow-away AOM	93.6 MHz
$f_{\text{AOM14}}$	Pulse Shaping AOM	80 MHz
$f_{\text{AOM15}}$	Counter-propagating AOM	180 MHz (single f) or $180 \text{ MHz} \pm f_m$ (dual f)
$f_{\text{AOM16}}$	Intensity Compensation AOM	180 MHz (single f) or $180 \text{ MHz} \pm f_m$ (dual f)
$f_{\text{AOM17}} = f_{g,\text{ramp}}/2$	Gravity Ramp Double Pass AOM (Raman mode)	93.66 MHz $\rightarrow$ 82.16 MHz, with Ramp Rate -11.4978 MHz/s
$f_{\text{AOM17}} = f_{g,\text{ramp}}/2$	Gravity Ramp Double Pass AOM (Bragg mode)	95.68 MHz $\rightarrow$ 84.18 MHz, with Ramp Rate -11.4978 MHz/s
$f_{\text{AOM18}}$	AC Stark Compensation AOM Switch	40 MHz
$f_{\text{EOM1}}$	Repump to Trap Frequency Shift EOM	9.21 GHz
$f_{\text{EOM2}}$	Raman EOM	9.1926 GHz (SS) or 9.1886 GHz (VS)

Table 3.6: List of frequencies of main lasers and modulators. The components are labeled according to Figure 3.1.

## 3.6 Atom Interferometer

As each part of the experiment is put together, here we are ready to present the experimental procedure of the entire atom interferometry. We use two computers to control the system. One is for timing sequence control. It programs the National Instrument digital/analog control cards to generate a set of control signal every 2.4 s as a cycle. Normally the timing sequence is fixed and we don't change it while running the experiment [70, 71]. At the same time we use a separate computer to control those experiment parameters that we want to change from cycle to cycle and also to read data from the photodetector as well. While the timing sequence is continuously on, this computer can update experiment parameters during dead time by controlling slave devices via General Purpose Interface Bus (GPIB) [97] and Local Area Network (LAN). Eventually how we set these parameters depends on how we want to group the experiment running processes.

The experiment is typically grouped like this. The largest unit the program can handle at one time is a dataset. A dataset consists of multiple instruction entries. Using instruction entries we can scan parameters to discover potential correlation between a certain parameter and the measured recoil frequency. The program can go through instruction entry list once or repetitively. Each instruction entry is the smallest unit to control experiment parameters. The parameters we typically control include the modulation frequency  $f_m = \omega_m/2\pi$ , pulse

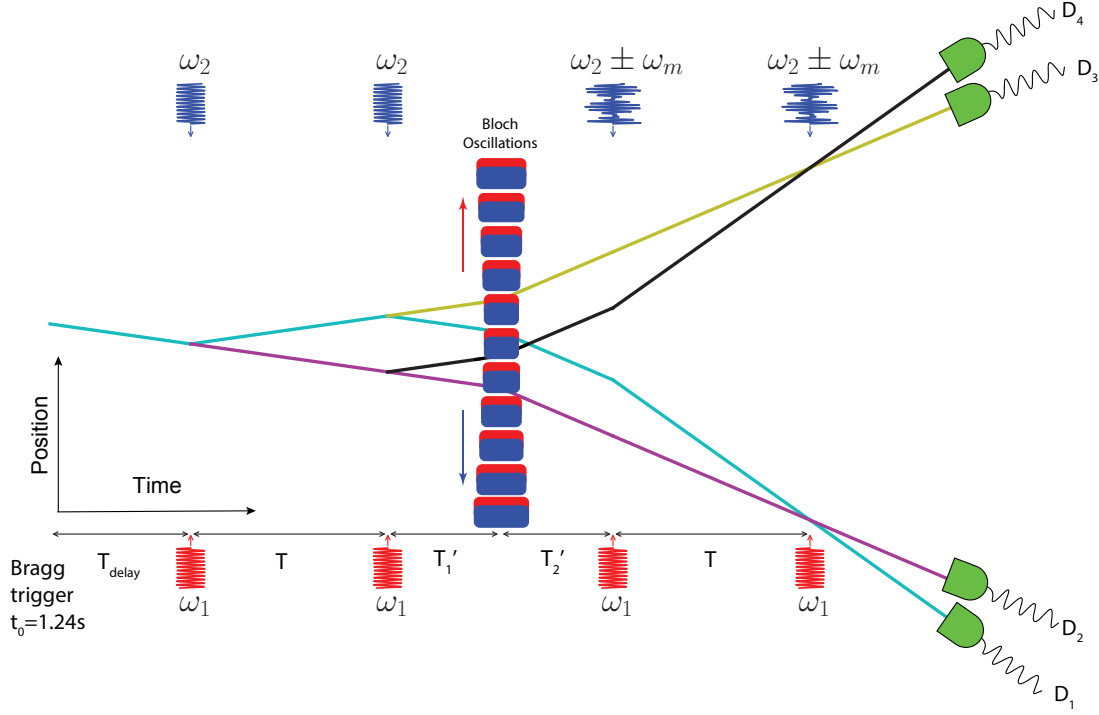


Figure 3.33: Ramsey Bordé Interferometer Scheme with Bloch Oscillations

separation time  $T, T', T_1', T_{\text{delay}}$  as shown in the figure, Velocity Selection (VS) frequency and intensity, Bragg diffraction frequency and intensity. Within each instruction entry, there are a few repeats of data bins. A data bin is the smallest unit to give one measured value of recoil frequency. The program will average the measured recoil frequencies from each data bin to calculate the expectation value and the error bar. As we mentioned earlier, we use ellipse fitting to extract the differential phase to get the recoil frequency. A caveat for ellipse fitting is that when the ellipse phase significantly deviates from  $90^\circ$ , it generates an ellipse fitting systematic error. In an extreme case when the phase is close to  $0$  the ellipse becomes like a line and the ellipse fitting algorithm would fail to get an accurate phase. To solve this problem, we introduce another small frequency modulation on top of large  $f_m$  such that it keeps the ellipse angle roughly  $\pm 90^\circ$ . We label the new frequency  $f_{m\pm} = f_m \pm \delta_m$  where an additional phase  $\pm 2n(2\pi\delta_m)T = \pm\pi/2$  is added into the ellipse readout phase. A data bin consists two separated ellipses running at  $f_{m\pm}$ . Each ellipse consists a number of data points. The number of data points for each ellipse is defined as the bin size. During the data run we alternate between  $f_{m+}$  and  $f_{m-}$  to eliminate possible systematic error due to drifting phase within one data bin. After finishing a data bin, the program would automatically fit each ellipse to get the differential phase of each data bin. Based on the phase formula of Ramsey Bordé interferometer, we have

$$\Phi_{d\pm} = 2nT(\omega_m \pm 2\pi\delta_m) - 16n(n + N)\omega_r T + \Phi_{\text{extra}} \quad (3.42)$$



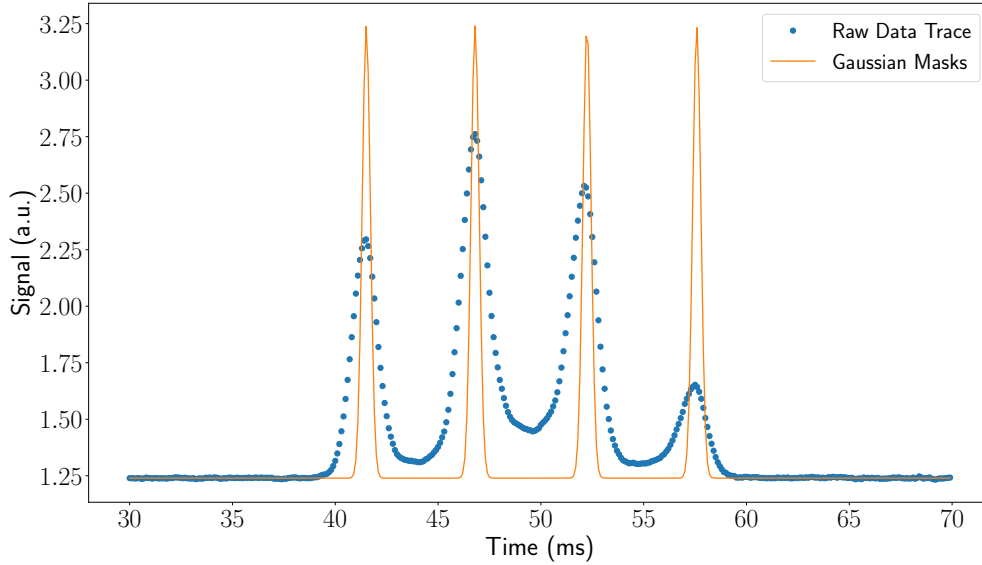


Figure 3.34: Raw data trace of a Ramsey Bordé interferometer without Bloch oscillations

If we solve this equation, we can get the recoil frequency term

$$8(n + N)\omega_r = \omega_m - \frac{\Phi_{d+} + \Phi_{d-}}{4nT} + \frac{\Phi_{\text{extra}}}{2nT} \quad (3.43)$$

Note that when we actually take the average of  $\Phi_{d\pm}$ , we would put another minus sign before  $\Phi_{d-}$  as the ellipse fitting algorithm cannot tell the difference between a positive phase and a negative phase.

For each data run, the program updates  $f_m$  to  $f_{m\pm}$  during the MOT loading time based on the sign of the current run. If it is the first run of a data bin, all other parameters will also be updated. Pulse separating timing  $T, T', T_{\text{delay}}$  would be updated through delay generators DG535. VS and Bragg frequencies would be updated as the absolute frequency of gravity ramp through DDS. VS intensity would be updated through a precision programmable voltage reference. Bragg intensity would be updated through Gaussian waveform generating function generator. After this step, the experiment would proceed until it's ready to record data. Then a trigger signal would be generated from the timing sequence to trigger an analog input card NI-PCI-4474 to record data. NI-PCI-4474 is a high-resolution (24bits) analog to digital data acquisition card [98]. The amplified signal at the photodetector as photocurrent-time trace would be low-pass filtered and analog-to-digital converted by the analog card. The cutoff frequency is typically between 2 kHz-10 kHz as the details of each atom peak below 500  $\mu\text{s}$  (compared to 1.5 ms FWHM of each peak) won't be as important. In this way we can further filter out high frequency noise. The signal would typically contains a few peaks as different output ports of the interferometer as shown in Figure 3.34.

Given each data trace, it's not as easy to extract the signal we want for each output port as many non-coherent atoms are also buried inside. If we read all atoms in one peak, contrast

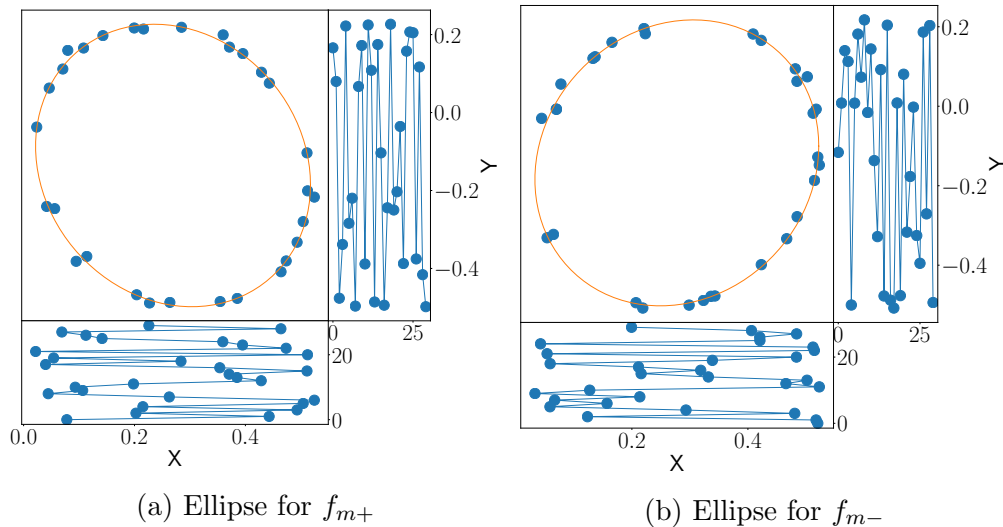


Figure 3.35: Ellipse data and fit

would be too small to be measured. And the signal would be buried in the background noise. So we use Gaussian masks at each interfering peak to evaluate an overlap integral with the signal trace to extract the signal at this output port as shown in Figure 3.34. The position of the four Gaussian masks are not arbitrarily chosen. We fit the original non-deflected peak (or peak of original VS) to get the absolute positions of four Gaussians and use theoretic calculation of atom trajectory to get relative peak positions. In order to get an accurate theoretic trajectory calculation, we also need accurate information of atom velocity and gravitational acceleration. Gravitational acceleration has been accurately measured with onsite interferometer to be  $9.798 \text{ m/s}^2$  [35], which was used to set gravity ramp rate. The absolute velocity could also be obtained by Bragg diffraction frequency and its resonance condition (see Section 5.6 for details). The width (Gaussian  $\sigma$ ) is typically set to  $0.2 \text{ ms}$  as a trade-off between contrast and signal size. After atom population at four output ports are extracted, we can follow the same procedure described in the last chapter to get X-Y coordinates of the ellipse. Thus following these procedures we can get fitted ellipse for phase measurement as shown in Figure 3.35.

As we mentioned earlier, we typically use actual atom interferometer phase and contrast measurements to determine Bragg frequency and intensity. As we scan the Bragg frequency to measure phase difference at certain  $T$ , we can get a parabola-like curve as shown in Figure 3.36. It well agrees with the theory of diffraction phase we developed in Section 2.7. So by fitting the data by a parabola, we can find the resonant Bragg frequency at the center of the parabola.

For Bragg intensity, it is determined by contrast measurements. As we scan Bragg intensity, the measured X and Y contrast shows a peak at different intensities, as shown in Figure 3.36. Though the peak doesn't give us exactly a  $\pi/2$  pulse, it's a good calibration to evaluate the actual Bragg two-photon Rabi frequency so that it would be consistent

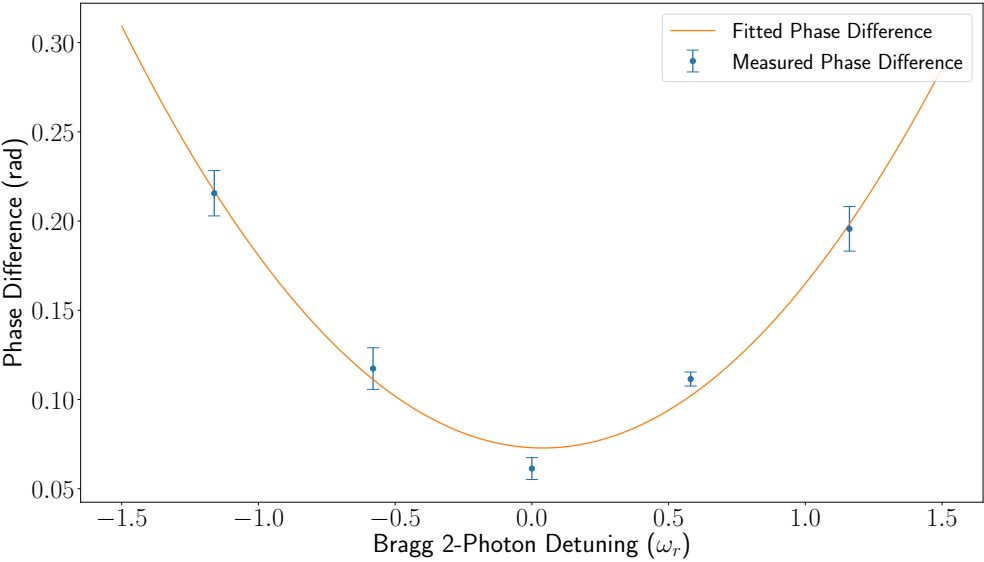


Figure 3.36: Measured phase difference between conjugated interferometers vs. Bragg 2-photon detuning. Data were taken at Bragg order  $n = 5$ , Bloch order  $N = 0$ , pulse separation time  $T = 10$  ms.

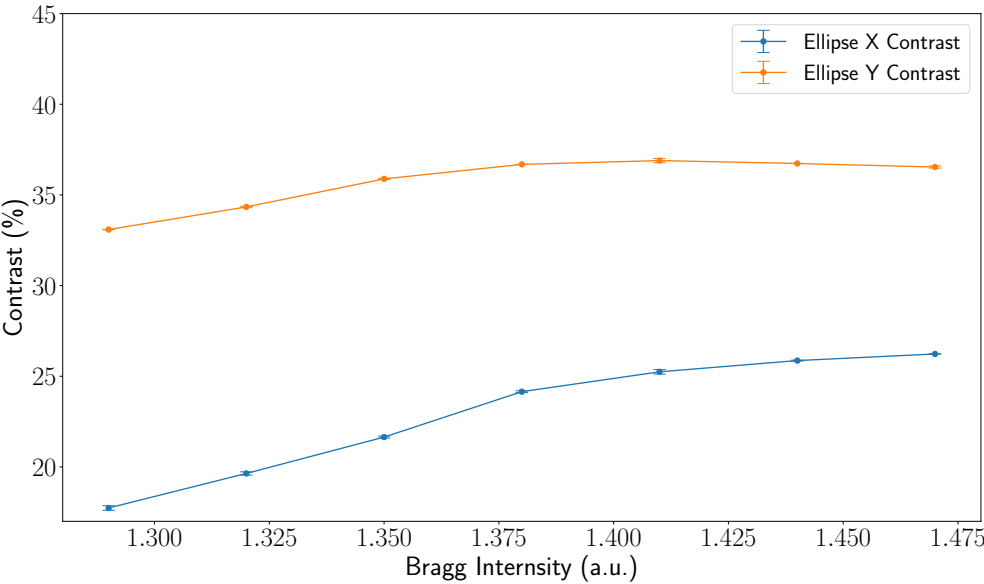


Figure 3.37: Measured ellipse contrasts vs. Bragg intensity. Data were taken at Bragg order  $n = 5$ , Bloch order  $N = 0$ , pulse separation time  $T = 10$  ms.

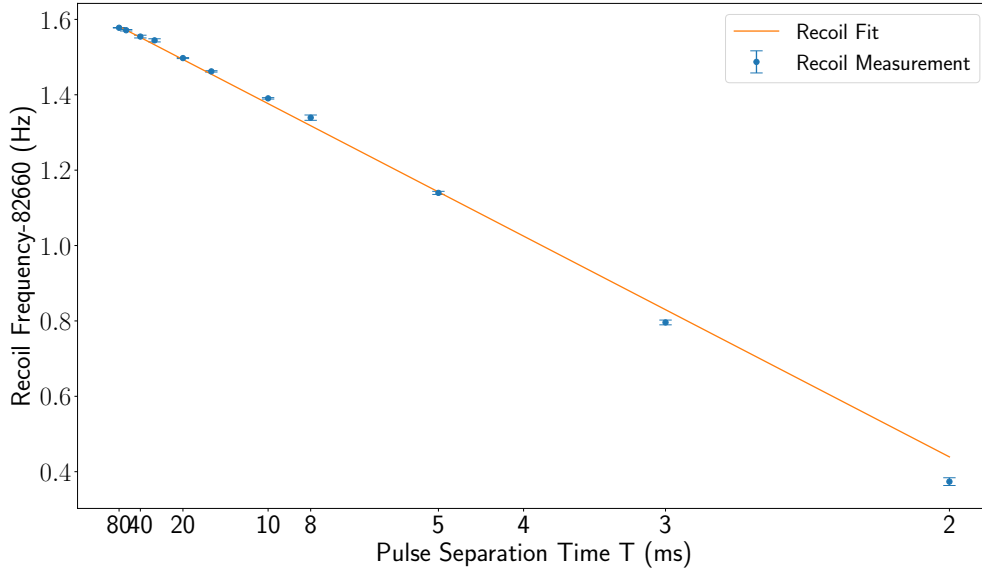


Figure 3.38: Measured recoil frequency vs. pulse separation time  $T$

throughout the entire data taking.

After we find an optimized set of Bragg parameters, we can measure the recoil frequency at different pulse separation time  $T$ . In theory, the measured recoil frequency should be independent of pulse separation time  $T$ . But we noticed a clear evidence that the measured recoil frequencies are inversely proportional to  $T$ , as shown in Figure 3.38. It can be explained by a phase constant in the formula,

$$\frac{\Phi_d}{T} = -2n\omega_m + 16n(n + N)\omega_r + \frac{\phi_0}{T} \quad (3.44)$$

where  $\phi_0$  is the phase constant. We now know that it is caused by diffraction phase that we discussed in Section 2.7. The diffraction phase could be directly measured by the slope of recoil frequency vs.  $1/T$  curve, while the recoil frequency could be extracted as y-interception when  $T \rightarrow \infty$ .

## Chapter 4

# Alpha Measurement - Statistical Uncertainty

### 4.1 On the Road to Better Sensitivity

Precision measurement always contains both challenges of experimentation, namely precision and accuracy. Precision is related to the sensitivity of the experiment. If the experiment is sensitive enough, we can average down the statistical uncertainty below what we desire in a reasonable time. This reasonable time is determined by how much time we can allocate our resources for the experiment and also how fast the measurement may drift due to environment parameters change. The other aspect of precision measurement is accuracy, which relates to systematic uncertainties of the experiment. We will be focusing on that in Chapter 5. For this chapter we will discuss some technical improvement over the years that help us improve the sensitivity to reach the level for our sub-ppb measurement.

When the experiment was just constructed in Berkeley, it was barely able to extract phase from Ramsey Bordé interferometer with Bragg order  $n = 5$  and pulse separation time  $T = 90$  ms. Bloch oscillations were not included at that time. But contrast significantly dropped when we tried to further increase  $T$ . Since then a few new techniques have been developed and now we are able to extract phase from Ramsey Bordé atom interferometer with Bragg order  $n = 5$  and Bloch order  $N = 200$  and pulse separation time  $T = 60$  ms, which sets a new record on the largest measurable phase achieved in Ramsey Bordé atom interferometer to be 12 Mrad. Over the past 7 years the sensitivity has been increased by more than 20 folds. We will give brief discussions about some important developments we made.

### Coriolis Compensation

Coriolis compensation was applied to eliminate decoherence due to the Earth's rotation. We realized that during atom interferometry, Bragg lattice set by the beam keeps changing its direction following the Earth's rotation, while atoms are only experiencing the gravity without any influence of the Earth's rotation. Or in the rotating Earth reference frame, atoms

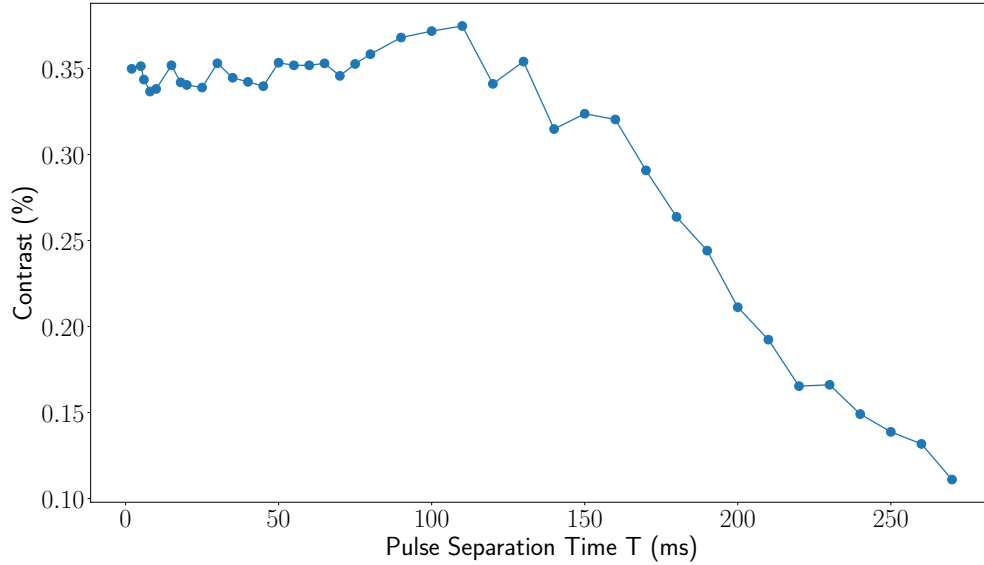


Figure 4.1: Contrast vs. pulse separation time  $T$  of a Ramsey Bordé atom interferometer without Bloch oscillations

would experience Coriolis force as an inertial force. As a result, atom interferometer couldn't close at the last pulse. The Earth's rotation will shift one atom interferometer arm slightly away from the other, making a small displacement  $\vec{\delta}$  at the last pulse. Whether atoms are still coherent, or in other words how large contrast we can get, depends on Gaussian overlap integral of two atom wave functions displaced by such an amount. For a short pulse separation time  $T$ , this displacement is not large enough to produce visible change in contrast. But it limits the largest pulse separation time  $T$  we can operate this atom interferometer. In the literature [57], we reported a new technique to ramp the retro-reflect mirror in its orientation to compensate this effect due to the Earth's rotation. We used two Thorlabs AE0505D16F piezoelectric actuators to rotate the retro-reflect mirror. These two piezoelectric actuators are able to rotate the mirror in two different axis. (The two axes form an angle of  $82^\circ$ , very close to be orthogonal so that they are almost independent [57, 61].) We use two independent function generators to generate two voltage ramps with independent tunable ramp rate to feed into Thorlabs high voltage PZT driving circuit. By optimizing the ramp rate, we were able to extract ellipse phase at pulse separation time  $T$  up to 270 ms. The contrast as a function of pulse separation time  $T$  with Coriolis compensation is shown here in Figure 4.1. We can still see contrast drop as we increase  $T$  in the region where  $T > 100$  ms. This decay is limited by transverse thermal expansion of atoms at current cooling temperature. This have been experimentally verified as we observed significant improvement in contrast when we implemented Raman Sideband Cooling.

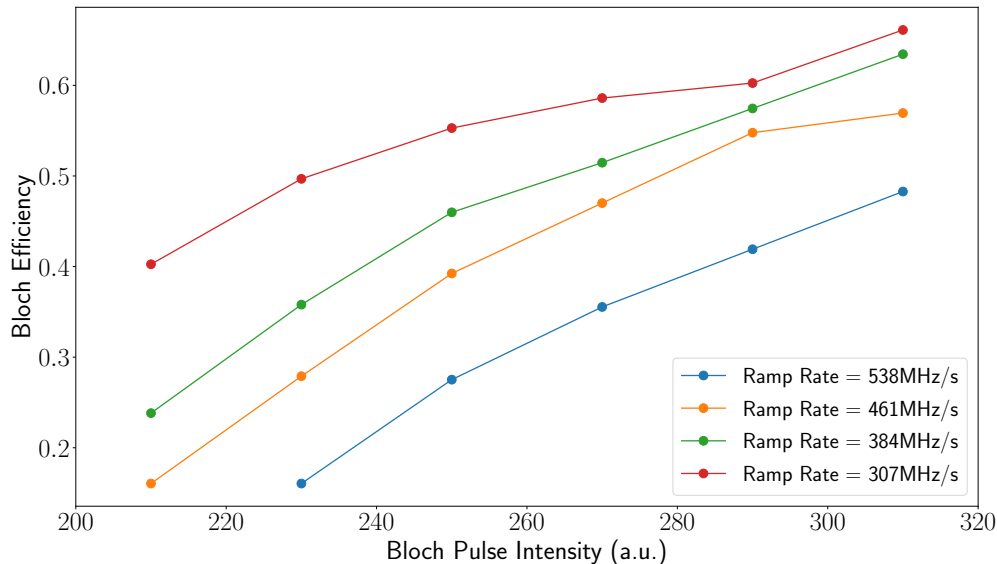


Figure 4.2: Bloch oscillations efficiency vs. Bloch intensity and Bloch ramp rate at Bragg order  $n=4$  and Bloch order  $N=50$ . Bloch efficiency here is defined as the ratio between the number of atoms arrived within the Gaussian masks of the four interferometer output ports and the total number of atoms detected in the entire data trace.

## Bloch Oscillations Optimization

Another trick we did is to add Bloch oscillations between the middle two pulses as we described in Chapter 2-3. The reason to add Bloch oscillations is to increase the overall phase linearly and to suppress relative systematic uncertainties that does not scale with Bloch order  $N$  [51, 11]. It turns out that though the overall phase in Ramsey Bordé interferometer ( $16n(n + N)\omega_r T$ ) gained by Bloch oscillations goes linearly with Bloch order  $N$  and the phase gained by Bragg diffraction goes quadratically with Bragg order  $n$ , it's a lot easier to keep the atom interferometer coherent with large  $N$  Bloch oscillations rather than a large  $n$  Bragg diffraction. A large order Bragg diffraction is not only technically limited by laser power, but also limited by decoherence. So we found the most ideal  $n$  is about 5 as we optimize Bragg parameters. But for Bloch oscillations, the contrast decays a lot slower as we increase  $N$ . More than  $N = 100$  Bloch oscillations have been demonstrated in Ramsey Bordé interferometers with Raman beam splitters [51, 11]. So also  $N > 100$  Bloch oscillations works well in the same kind of atom interferometer with Bragg beam splitters as well [8].

Here we use a quasi-square pulse with  $100 \mu\text{s}$  ramp on and  $100 \mu\text{s}$  ramp off to drive Bloch oscillations. The free parameters available to optimize Bloch oscillations are Bloch ramp rate and Bloch intensity (Rabi frequency). We found that a slower ramp rate and a higher Bloch intensity are always helpful to get higher Bloch efficiency within the parameters space we are operating our experiment as shown in Figure 4.2, which exactly agrees with the numerical result in Section 2.5. But we also noticed that as we slow down the ramp rate or turn up

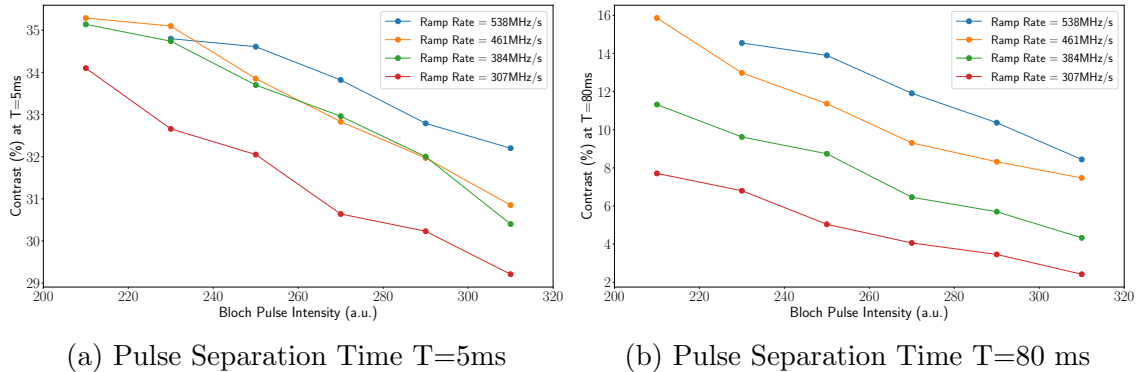


Figure 4.3: Atom interferometer Y-contrast vs. Bloch intensity and Bloch ramp rate at Bragg order  $n=4$  and Bloch order  $N=50$

Bloch intensity, the atom interferometer contrast goes in the opposite direction as shown in Figure 4.3. Part of that could be due to single photon scattering as the scattering rate is proportional to the intensity at large detuning limit. But it cannot explain most part of that because single photon scattering rate should be independent of the pulse separation time  $T$ . But we noticed a significant decay in contrast as we increase the pulse separation time  $T$  with Bloch oscillations applied. Based on our limited knowledge at that time, we simply optimized the useful "signal", i.e. the product of Bloch efficiency and atom interferometer contrast. Since the contrast at 80 ms is the bottleneck of the experiment, we use that contrast to optimize as shown in Figure 4.4. Following this general procedure, the maximum sensitivity we were able to get was at Bragg order  $n = 4$  and Bloch order  $N = 50$  and pulse separation time  $T = 80$  ms, yielding 3 Mrad total phase.

Based on the data, we have also noticed that when we apply Bloch oscillations, the contrast drops a lot faster as we increase pulse separation time  $T$  than that in the absence of Bloch oscillations. We believe it was not caused by single-photon scattering since decoherence due to that should be  $T$  independent. There are additional decoherence mechanisms involved. These will be topics of discussion in the subsequent sections.

## AC Stark Shift Compensation

One idea was brought to our attention in the literature [99] that AC Stark shift variation on beam due to wavefront intensity variation may cause decoherence. It can be tested experimentally in a quite straightforward way. We prepare another laser beam called AC Stark shift compensation beam with the opposite detuning and get it coupled into the same fiber port with the normal Bragg/Bloch beam. Since intensity variation of AC Stark shift compensation beam follows the same pattern as normal Bragg/Bloch beam does, by choosing appropriate single-photon detuning as well as intensity, we can cancel AC Stark shift atoms see at the leading order. Experimentally we use a Distributed FeedBack (DFB) diode laser (Diode4) as a frequency source to feed into another Tapered Amplifier (TA5) to generate



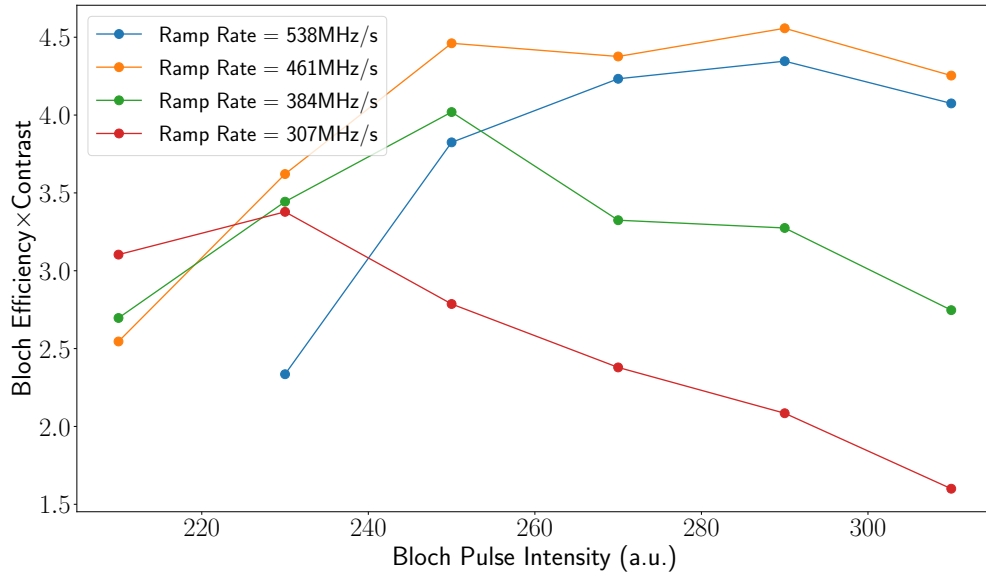


Figure 4.4: Bloch oscillations efficiency  $\times$  atom interferometer Y-contrast vs. Bloch intensity and Bloch ramp rate at Bragg order  $n=4$ , Bloch order  $N=50$  and pulse separation time  $T=80$  ms

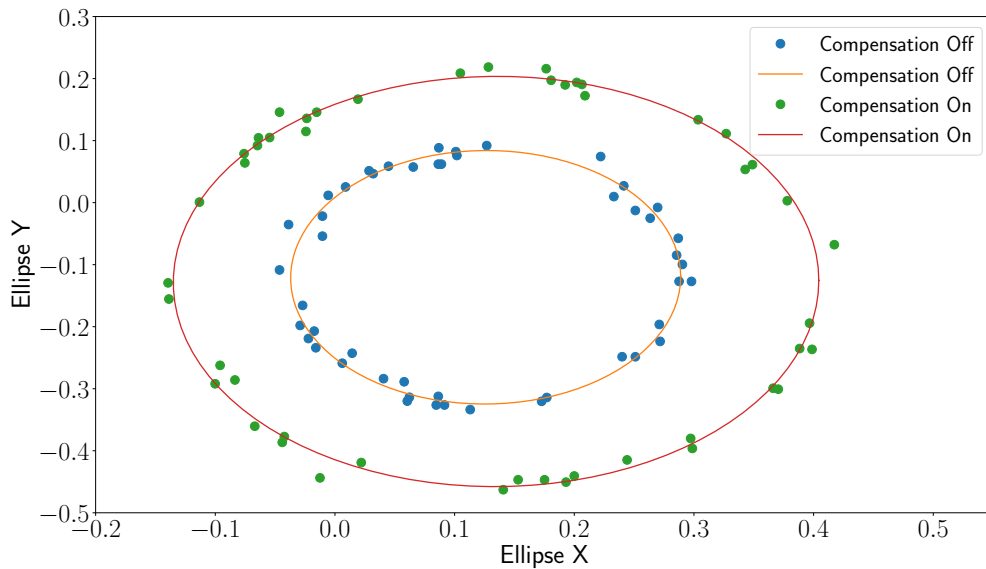


Figure 4.5: Ellipses directly from data with and without AC Stark shift compensation at Bragg order  $n=5$ , Bloch order  $N=25$

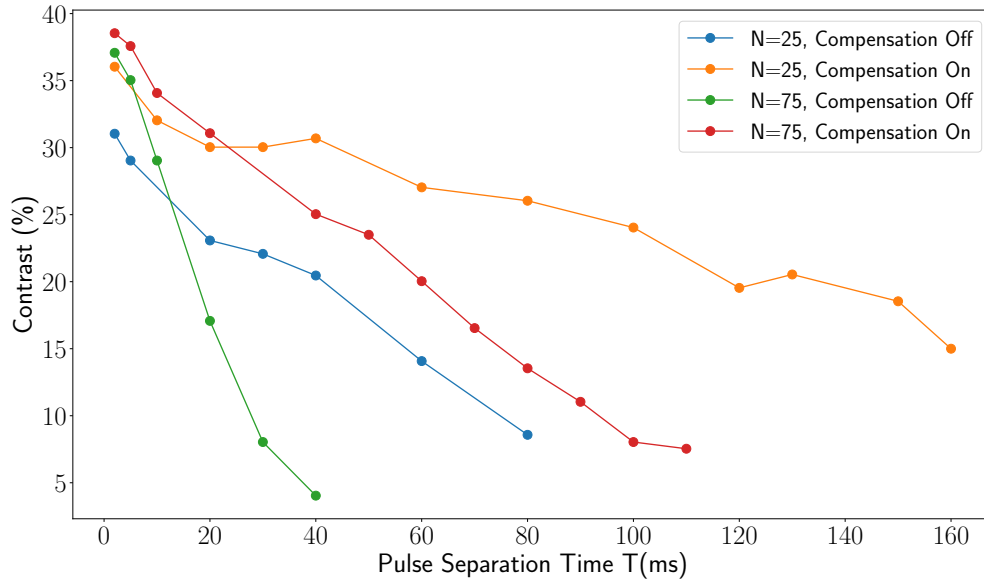


Figure 4.6: Atom interferometer contrast as a function of pulse separation time  $T$  with and without AC Stark shift compensation. Data taken with  $n=5$ ,  $N=75$ ,  $T=80$  ms

enough power for the compensation beam as shown in Figure 3.20. This beam is coupled into the Bragg fiber through the first order input port of an Acoustic Optical Modulator (AOM18). The pulse timing and shape are controlled by TA current, a mechanical shutter, and the AOM switch. With this compensation beam, we observed recovery of atom coherence as increase of contrast visually shown in Figure 4.5. This compensation effect applies to both Bragg diffraction and Bloch oscillations. But in the presence of Bloch oscillations, decoherence is dominated by Bloch oscillations. So compensating Bragg diffraction in this case won't bring visible improvement in contrast. For this reason, we only apply compensation to Bloch oscillations in practice. It also turns out that this compensation effect is not so sensitive to compensation beam detuning, intensity, pulse shape, pulse timing and so on. It makes experiment a lot easier as there is no need to lock the frequency and stabilize the intensity of the compensation beam. The compensation pulse is roughly a square pulse overlapping with Bloch oscillations pulse in time. In order to reduce single photon scattering, we further increased the single photon detuning as well as intensity as long as it's technically allowed. In the end we reach about three times as large detuning in magnitude as the Bloch beam detuning (14GHz blue detuned) as well as about three times as large intensity as Bloch beam intensity for compensation. The improved contrast vs. pulse separation time is shown in Figure 4.6, which enabled us to further increase overall measurable phase of our system to 6.6 Mrad at Bragg order  $n = 5$ , Bloch order  $N = 75$  and pulse separation time  $T = 80$  ms. The data also suggests that AC Stark shift isn't the only decoherence mechanism. There are more decoherence mechanisms at play.

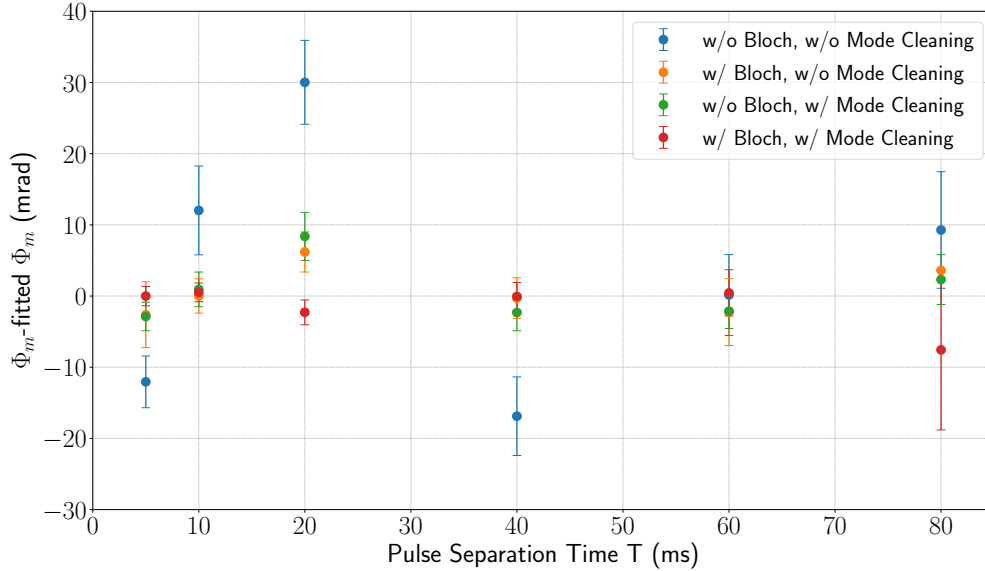


Figure 4.7: Residual phase vs pulse separation time  $T$  under various conditions. Residual phase is defined as the difference of measured phase and the fitted phase based on a constant diffraction phase model.

## 4.2 Preliminary Measurement

After implementing AC Stark shift compensation, the system has already reached the sensitivity required for  $\alpha$  measurement better than 0.25 ppb. It took about a day to reach 0.25 ppb in  $\alpha$  for at a single pulse separation time. Ideally if the diffraction phase is a constant independent of  $T$ , we only need to measure the recoil frequency at two different  $T$ s to get the recoil frequency, following the procedure discussed in Section 3.6. Unfortunately we noticed that there is a pulse separation time  $T$  dependent phase at about 10 mrad level (about 1/10 of the diffraction phase), shown as blue data points in Figure 4.7, which prevented us from proceeding toward precision measurement as it posed an parts-per-billion level uncertainty. Part of it is from diffraction phase, and another part is related to the speckle pattern of the beam. The details of these two sources will be further discussed in Chapter 5. There might be more sources unknown so we call it anomalous phase.

Since we cannot well calculate or measure this anomalous phase to the precision we need, our strategy is to suppress it until its relative uncertainty is no longer important at the accuracy we want. Bloch oscillations are one of the key solutions. As we have simulated in Section 2.7, Bloch oscillations will further increase velocity separation of two interferometers during the dual-frequency Bragg diffraction at the last two pulses, thus suppressing crosstalk from non-resonant frequencies. It is also experimentally verified to be effective shown as the orange points in Figure 4.7. Bloch oscillations at the same time also significantly boost the overall phase we measure. So the relative uncertainty of the anomalous phase is further suppressed.

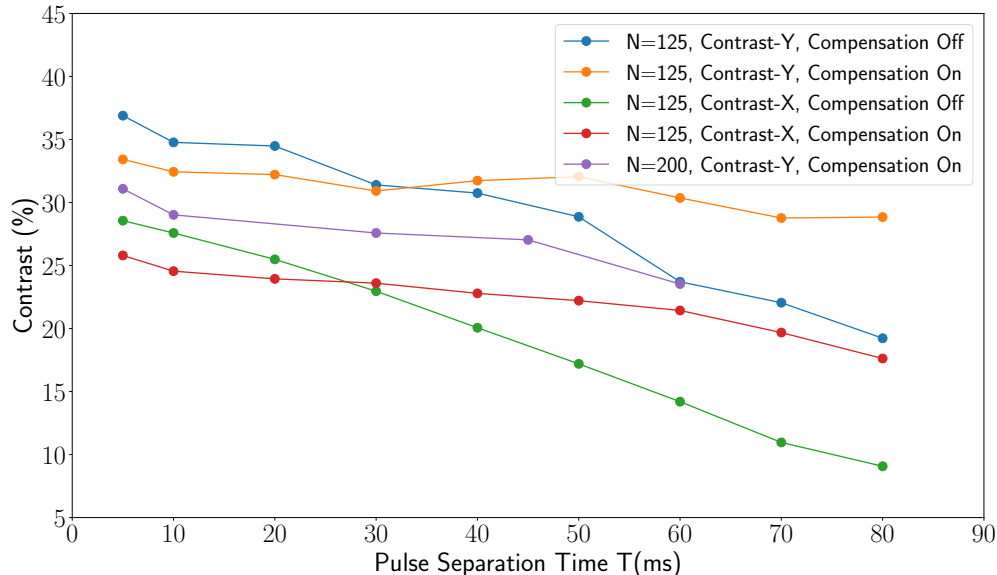


Figure 4.8: Ramsey Bordé atom interferometer contrast vs. pulse separation time  $T$ . Mode cleaning techniques have been applied. Other conditions are indicated in the legend.

Another method is to clean the mode of the beam to reduce the speckle phase. Speckle phase was identified when we observed significant change in the anomalous phase vs.  $T$  pattern by changing the Bragg fiber port to a larger one. Based on that insight, we did further investigation of the beam and discovered that the beam profile is only close to Gaussian when  $r < w$ . It significantly deviates from Gaussian beyond 1 waist. One idea to clean the mode is to filter atoms transverse velocity so that only the center part of atoms will contribute to interference signals. We started it by using a separate thinner Raman beam for state preparation. And we also shrink the detection beam size as well as detector size by pinholes. In this way only atoms with small transverse velocity will be read out. Another way is to directly clean the mode of the Bragg fiber port. To this end, we used an Thorlabs Gaussian apodizing filter NDYR20A to suppress the speckle pattern. It was proved to be also very effective. Even without Bloch oscillations, it is able to suppress the anomalous phase by a factor of 5 shown as the green points in Figure 4.7. Since the apodizing filter effectively shrinks the Bragg beam from about 6 mm to 3 mm, it can be functioning well as the thin Raman beam and there is no need for a separate thin Raman beam any more. With both Bloch oscillations and the beam cleaning technique, we were able to suppress it below 3 mrad at its peak. Surprisingly we also discovered further improvement in interferometer contrast through mode cleaning. We were able to extend the Bloch order to beyond  $N=200$ . The maximum measurable phase we could achieve is realized at Bragg order  $n=5$ , Bloch order  $N=200$ , pulse separation time  $T=60$  ms, yielding a total of 12 Mrad. It allows us to further suppress the relative uncertainty of the anomalous phase below 0.04 ppb [8]. More data of contrast vs.  $T$  with mode cleaning is shown in Figure 4.8. It is to be noted that

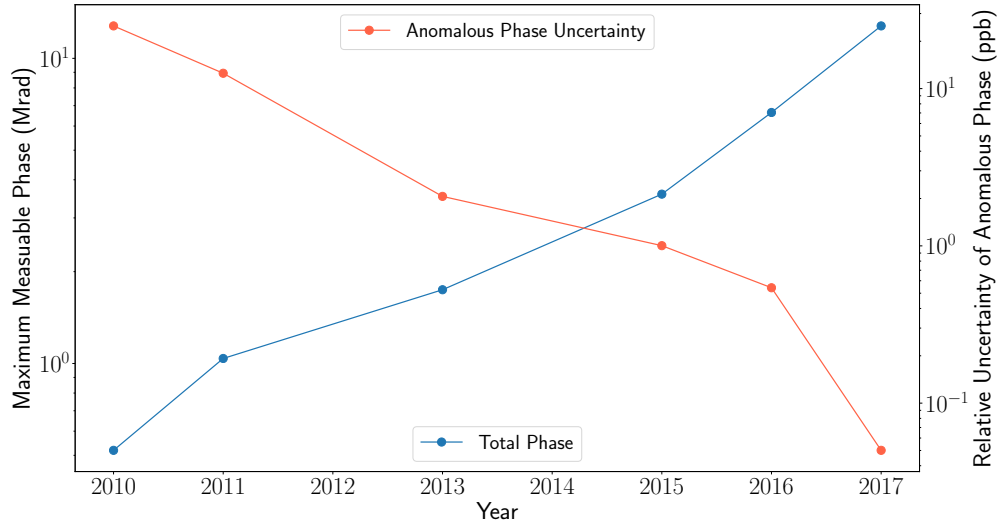


Figure 4.9: Moore's law of our atom interferometer performance

at large Bloch oscillations, the contrast of the lower interferometer (X-contrast in the plot) tends to be the bottleneck of signal to noise ratio in the measurement. So these contrasts are also included in the plot. And all other contrasts mentioned before and plotted here are exclusively the contrast of the upper interferometer (Y-contrast).

With all these innovations and progresses over the year shown as "the Moore's law" in the Figure 4.9, we eventually reach the level of precision as well as accuracy for the measurement of the fine-structure constant below 0.25 ppb.

### 4.3 The Fine-Structure-Constant Measurement

#### Data

We started data taking for  $\alpha$  measurement since Dec 2016 when our system reaches sensitivity and control of systematic errors required. The data taking lasts for a span of 7 months. All the data taken has Bloch oscillations with order ranging from 125 to 200 in order to control anomalous phase. Here to visualize how the detected data looks like, we plot a few data traces with different Bloch orders shown in Figure 4.10 (A). In the presence of Bloch oscillations, atoms participating in interferometer move further and further away on both side. There is up to  $800\hbar k$  momentum difference between the two interferometer, resulting in up to 1.7m difference at the time of detection. There are in total 28 datasets included in the measurement as shown in Figure 4.10 (C). Each dataset has roughly 1 day of data. We alternate among different pulse separation time  $T_s$  for each dataset in order to average down the anomalous phase at the same time. Most datasets have 6 different  $T_s$ ; 9 datasets have 3  $T_s$ ; 4 datasets have 4  $T_s$ . All  $T_s$  are chosen within the set  $T = \{5 \text{ ms}, 10 \text{ ms},$

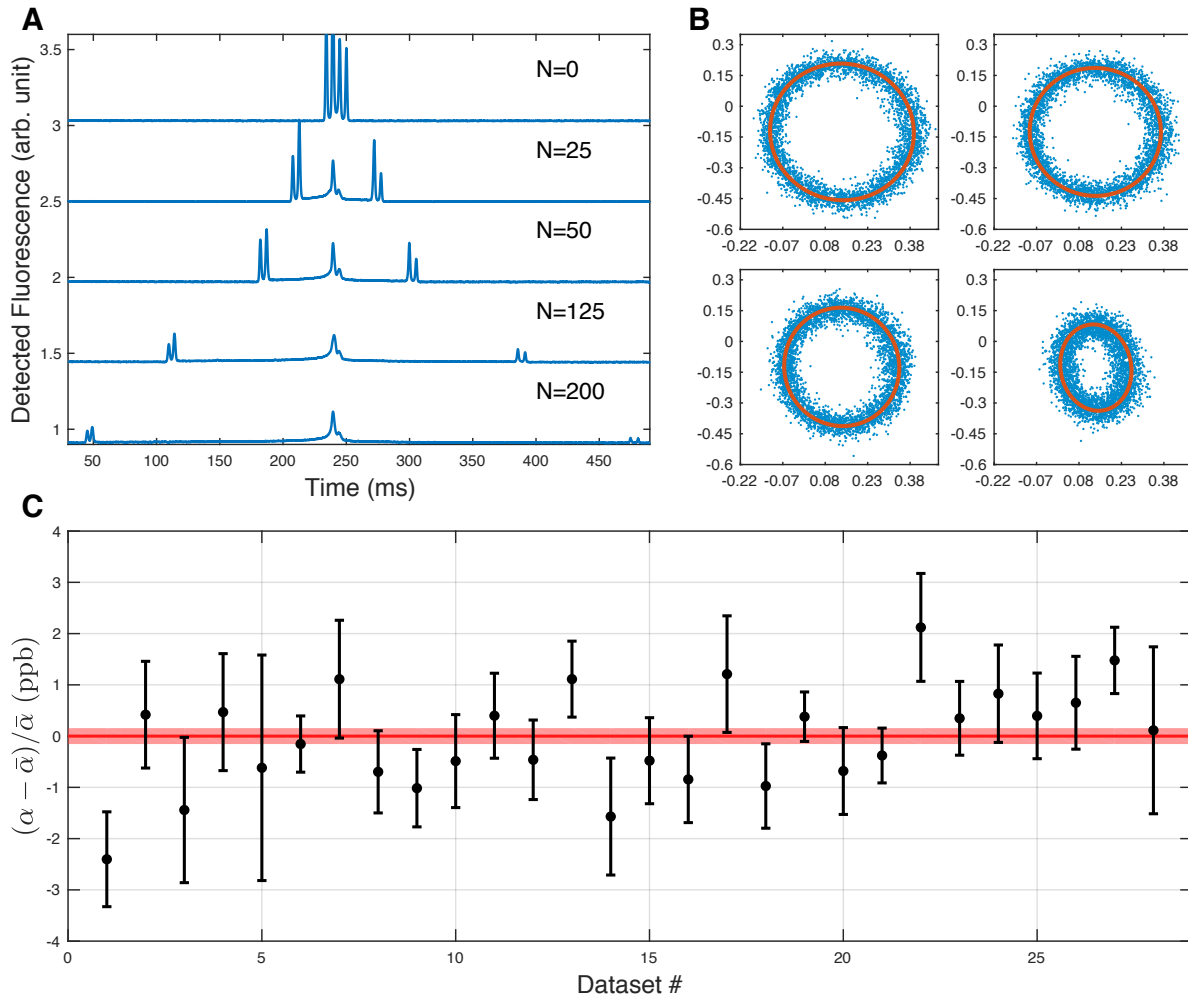


Figure 4.10: Data to characterize the system and to measure the fine-structure constant. (A) Detected fluorescence with various Bloch oscillations orders. For visibility, an arbitrary offset is applied for each trace. Data were taken at  $T=5$  ms. (B) A sample of interference ellipses used for the measurement. Data were taken at  $n=5$ ,  $N=125$ ,  $T=5, 20, 40, 80$  ms. (C) Actual  $\alpha$  measurement result. Each point shown is the measured value from each dataset. The pink band represents the overall  $\pm 1\sigma$  statistical error. These three figures are directly taken from reference [8].

20 ms, 30 ms, 40 ms, 60 ms, 70 ms, 75 ms, 80 ms}. A sample of interference ellipse data of a dataset at Bragg order  $n=5$ , Bloch order  $N=125$  and  $T=5, 20, 40, 80$  ms is shown in Figure 4.10 (B).

As described in Section 3.6, each dataset contains a list of instruction entries. Each instruction entry would change the pulse separation time  $T$ . After a cycle of entire instruction entries, it repeats itself over and over again. In order to minimize anomalous phase, we

intentionally add different  $T_{\text{delay}}$  to the sequence so all the second and the third pulses happen at the same time for all Ts. The reason to alternate among different Ts instead of taking different Ts at different times is to avoid biased result due to diffraction phase drift. Suppose the average ellipse phase  $((\Phi_{d+} + \Phi_{d-})/2)$  for the  $i^{\text{th}}$  repeat of the instruction entry with  $T = T_j$  is  $\Phi_{d,ij}$ . Based on the phase equation for Ramsey Bordé atom interferometer,

$$\Phi_{d,ij} = -2nT_j\omega_m\left(1 + \frac{v_2}{c}\right) + \frac{gnT_j(T_j + 2T'_1 + 2T'_2)\omega_m}{c} - 2n^2\frac{\hbar k_L^2}{M}T_j\frac{\omega_m}{\omega_L} \quad (4.1)$$

$$+ 8n(n + N)\frac{\hbar k_L^2}{M}T_j\left[1 + \frac{\gamma}{12}\left[\frac{n}{n + N}\left(2T_j^2 + 3T_jT'_2 + 3(T'_1 + T'_2)^2\right)\right.\right. \quad (4.2)$$

$$\left.\left. + \frac{2N}{n + N}\left(T_j^2 + 3T_j(T'_2 - \frac{NT_B}{2}) + 3T'_2(T'_2 - NT_B) + (N^2 - \frac{1}{4})T_B^2\right)\right]\right] \quad (4.3)$$

$$+ \Phi_{ij}^{\text{sys}} + \Phi_0^{\text{sys}} + \phi_i^{\text{diff}} \quad (4.4)$$

where  $v_2 = v_0 - gT$  is the velocity of non-diffracted atom at the second pulse;  $\omega_L, k_L$  are angular frequency and wave number of specified laser frequency;  $\Phi_{ij}^{\text{sys}}$  is the real-time systematic uncertainty correction term;  $\Phi_0^{\text{sys}}$  is the overall systematic uncertainty correction term;  $\phi_i^{\text{diff}}$  is the diffraction phase for the  $i^{\text{th}}$  repeat. All other parameters are defined in the same way as in Section 2.6. Due to the scheme to align the second and the third pulse,  $v_2$  is a constant within a dataset that can be calculated by Bragg frequency and gravity ramp.  $\omega_L, k_L$  are not the real laser frequency and wavenumber. They are a close estimation as an unperturbed number put into the model. Real laser frequency and wave number correction will be added into systematic correction terms. Suppose if we have  $n$  repeats and  $m$  Ts, there would be in total  $n \times m$  equations. All parameters in the equation could be determined as a input measurement parameter or separate systematic measurement, except  $n + 1$  undetermined variables, i.e.  $h/M$  and all diffraction phase terms  $\phi_i^{\text{diff}}$ . In this overdetermined system, we use Levenberg-Marquardt method to find out the mean value and error of each of them. The reason why we make  $n$  different diffraction phase is to take into account possible drift in it, which is more realistic in the real experiment. In practice we use FMINUIT developed by CERN [100] to carry out this optimization to obtain the mean and statistical uncertainty of  $h/M$  for each dataset.

It is to be noted that some systematic uncertainties are measured in the real time with monitors. Typically those systematic uncertainty would drift significantly beyond the uncertainty we want throughout the experiment. Since we cannot control them that accurately, we have to keep monitoring and apply correction in real time. Those corrections will be included in the term  $\Phi_{ij}^{\text{sys}}$ . Systematics like laser frequency, beam alignment are being monitored in real time to provide information to calculate  $\Phi_{ij}^{\text{sys}}$ . Other systematics that won't drift will be subtracted in the overall systematic phase  $\Phi_0^{\text{sys}}$ . How to calculate the systematic correction and uncertainties would be the topic to discuss in Chapter 5.

With this algorithm we got 28 measurements of  $\alpha$  with specified errorbars shown in Figure 4.10 (C). The mean value of measured  $\alpha$  is obtained by weighted average of all 28 measurements. The overall  $\pm 1\sigma$  is shown as the pink band in Figure 4.10 (C). The

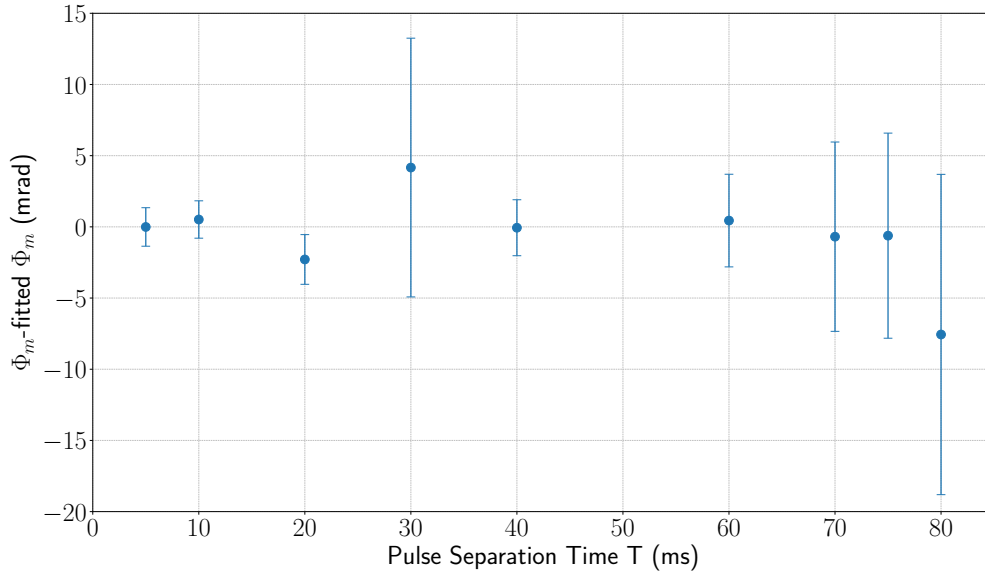


Figure 4.11: Residual phase from  $\alpha$  measurement data vs. pulse separation time  $T$ . It is adapted from reference [8]. It is used to estimate speckle phase systematic uncertainty in Section 5.2

reduced  $\chi^2$  for the combined data is 1.2, with a p-value of 0.2.  $h/M$  is measured to be  $3.0023694721(12) \times 10^{-9} \text{ m}^2/\text{s}$ , with a relative statistical uncertainty of 0.16 ppb. Note that this value of  $h/M$  has corrected all systematic effects as this is part of the procedure of Levenberg-Marquardt method mentioned above. We also plot the overall residual at each  $T$  in Figure 4.11 to test if there is still persisting anomalous phase. We see that the anomalous phase is unresolved under the statistical uncertainty, which enters into the error budget with only 0.04 ppb uncertainty. More details will be discussed in Section 5.2.

## Blind Analysis

One of the caveat for precision measurement is that measurement in the past could bias experimenters when they analyze data and systematic uncertainty in the way trying to make it “consistent” with previous measurement. Specifically even if people are totally honest, they could be subjectively biased to decide which dataset to use and which not to use and which systematic effect to include or not. What typically happens is that people stop looking for more systematic effects when the result is “close” enough to the previous one. The general treatment here is blind analysis. Typically people add a “random” number that is blind to all experimenters somewhere in the experiment so that no one is able to determine the measured value unless this number is given. We asked Prof. Rana Adhikari from Caltech to add a random frequency uniformly distributed in the range from -1 MHz to +1 MHz to the laser frequency vs. spectroscopy monitor power calibration function which we use to determine laser frequency systematic uncertainty and add correction to the measurement



(more details will be covered in Section 5.3). And he obfuscated this blinded calibration into a Matlab p-code to prevent experimenters from deciphering the random number. But the experimenters are allowed to calculate the measured value to test if there is any mistake in the experiment procedure. But there is an uncertain error of  $\pm 3$  ppb added to the result. So in this way we cannot bias the result at sub-ppb level.

In order to reduce the chances of human error, two independent data analysis codes, with different fitting algorithms were used. These two codes gave the same result for the fine-structure-constant given the same raw data. After all data were taken and analyzed, we “unblind” it with the random offset provided by Prof. Adhikari. The result was then submitted for publication without further modification, other than the correction of a typo in the phase calculation and the addition of an analysis of a new systematic effect reported recently [101]. This effect will be reported in Section 5.4.

## Chapter 5

# Alpha Measurement - Systematic Uncertainties

### 5.1 Overview of Systematic Uncertainties

We have reported our  $\alpha$  measurement with 0.16 ppb statistical uncertainty in Chapter 4. It's not enough for an accurate determination of  $\alpha$  yet. It's as important to analyze all relevant systematic effects to correct our measurement value and assign systematic uncertainties. There are already a few well known systematic effects common in Ramsey Bordé atom interferometers as in the LKB Rubidium  $h/M$  measurement, such as laser frequency, gravity gradient, Gouy phase, Zeeman effect, AC Stark light shift and so on. Some of them like Zeeman effect and AC Stark light shift are highly suppressed in our systems of Simultaneously Conjugated Interferometer (SCI) with Bragg diffraction as beam splitters. But a few new systematic effects such as the diffraction phase arise in our specific experiment. Though major component of the diffraction phase can be eliminated by fitting recoil frequency vs.  $T^{-1}$  ( $T$  is pulse separation time) data at multiple different  $T$ s, there are  $T$ -dependent components called anomalous phase in the previous chapter in need to be properly addressed. Some of these systematic effects will drift over the course of the experiment. In this case we set monitors in real time to monitor those values and correct them in the phase term  $\Phi_{ij}^{\text{sys}}$ . Some of them won't drift so we assign an overall correction in the phase terms  $\Phi_0^{\text{sys}}$ . Some of them are quite small and it's not necessary to evaluate the exact correction so we only assign a conservative uncertainty. Here are all the relevant systematic effects as well as the measurement listed in the error budget below. With measurements of electron mass, Cesium mass and Rydberg constant from other groups we have demonstrated a measurement of the fine-structure constant to 0.20 ppb overall uncertainty.

In the rest of the chapter, we will discuss each systematic uncertainties in their categories such as systematic effects due to spatial fields gradient, due to correction in the effective laser wavenumber, or due to the diffraction phase. Some small yet important systematic effects will be lumped together into Miscellaneous systematic effects.

Effect	Direct Measured Value	$\delta\alpha/\alpha(\text{ppb})$
Laser frequency (Section 5.3)	real time monitoring	$-0.24 \pm 0.03$
Acceleration gradient (Section 5.2)	$\gamma = (2256 \pm 14) \text{ E}$	$-1.79 \pm 0.02$
Gouy phase (Section 5.4)	N/A	$-2.60 \pm 0.03$
Beam alignment (Section 5.3)	real time monitoring	$0.05 \pm 0.03$
Bloch oscillations light shift (Section 5.6)	N/A	$0.000 \pm 0.002$
Density shift (Section 5.6)	N/A	$0.000 \pm 0.003$
Index of refraction (Section 5.3)	N/A	$0.00 \pm 0.03$
Speckle phase shift (Section 5.2)	N/A	$0.00 \pm 0.04$
Sagnac effect (Section 5.6)	N/A	$0.000 \pm 0.001$
Modulation frequency wavenumber (Section 5.6)	N/A	$0.000 \pm 0.001$
Thermal motion of atoms (Section 5.5)	N/A	$0.00 \pm 0.08$
Non-Gaussian waveform (Section 5.5)	N/A	$0.00 \pm 0.03$
Parasitic interferometers (Section 5.5)	N/A	$0.00 \pm 0.03$
Total systematic uncertainty	N/A	$-4.58 \pm 0.12$
Statistical uncentainty (Section 5.3)	$h/M = 3.0023694721 \times 10^{-9} \text{ m}^2/\text{s}$	$\pm 0.16$
Electron mass [1, 15]	$m_e = 5.4857990907 \times 10^{-4} \text{ u}$	$\pm 0.020$
Cesium mass [16]	$m_{Cs} = 132.9054519615 \text{ u}$	$\pm 0.030$
Rydberg constant [1]	$R_\infty = 1.0973731568508 \times 10^7 \text{ m}^{-1}$	$\pm 0.003$
Total uncertainty in $\alpha$	$\alpha^{-1} = 137.035999046$	$\pm 0.020$

Table 5.1: Error budget of the fine-structure-constant measurement. Related measurements are listed in the second column. And relative systematic corrections and uncertainties in  $\alpha$  are listed in the third column.  $1 \text{ E} = 10^{-9} \text{ s}^{-2}$ .  $\text{u}$  is atomic mass unit.

## 5.2 Spatially Dependent Potentials

Spatially varying potentials may cause phase shift in Ramsey-Bordé atom interferometer, significantly contributing to the systematic uncertainty of our fine-structure constant measurement. There are potentials well known to us such as gravity gradient and magnetic fields. There are also sources not well known and studied, which results in anomalous phase as a function of pulse separation time  $T$  as we mentioned earlier. Speckle phase is one of this type. We will discuss each type in a little bit more details.

### Gravity Gradient

As we have shown in the earlier chapter, though phase from gravity would be cancelled in the Ramsey Bordé Simultaneously Conjugated Interferometer (RB-SCI) in the differential mode phase, gravity gradient remains in the phase formula (Equation 2.146). It results in a phase shift of more than 10 mrad or a few ppb in  $\alpha$ . So it is an important phase we need to measure and understand well. Based on the definition of the matter wave Lagrangian, the

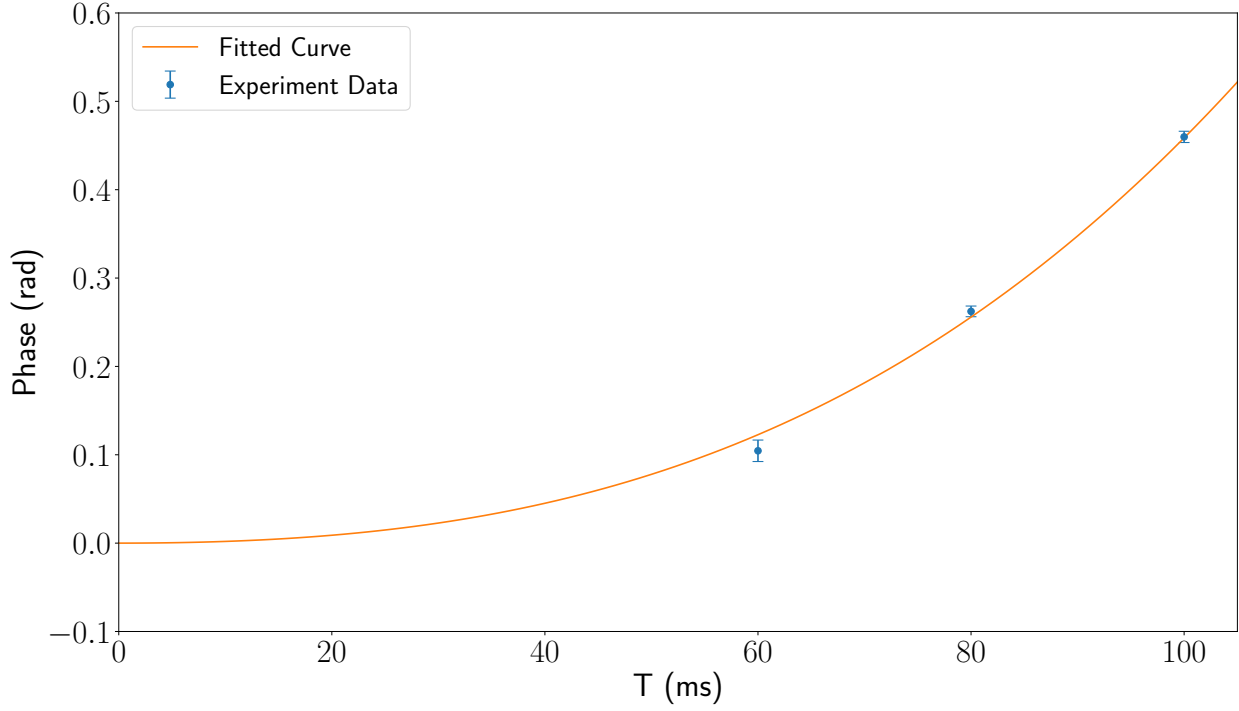


Figure 5.1: Dual Mach Zehnder atom interferometer phase vs. pulse separation time  $T$  measurement from one dataset. Data were taken at  $n = 5$ ,  $N = 125$ ,  $T'_1=5$  ms,  $T'_2=45$  ms.

gravity gradient can be related to  $\gamma$  as

$$\gamma = -\frac{dg}{dz} \quad (5.1)$$

where  $g$  is the magnitude of the gravitational acceleration. Gravity gradient can be directly measured by setting up a dual Mach-Zehnder atom interferometer as shown in Figure 2.19. The dual Mach-Zehnder atom interferometer consists of five pulses. There are three  $\pi/2$  pulses for Mach-Zehnder interferometer itself. A Bragg and a Bloch pulses are used to split the initial atom cloud into two and further accelerate them apart from each other so that they are sufficiently spatially separated before the interferometer sequence. After the interferometer, we use the same ellipse fitting technique to get the differential phase between the two interferometers. The differential phase could be calculated theoretically (Equation 2.137) as

$$\Phi_d = -2nT^2r_m + \frac{8gn(n+2N)T^2\omega_r}{c} + 8nT^2\gamma\omega_r(n(T+T'_1+T'_2) + N(2T - NT_B + 2T'_2)) \quad (5.2)$$

where pulse timing  $T$ ,  $T'_1$ ,  $T'_2$  are defined in Figure 2.19;  $T_B$  is one Bloch oscillation period;  $N$  is the Bloch order;  $n$  is the Bragg order;  $r_m$  is the additional ramp rate added to make ellipse phase closer to  $90^\circ$ . We alternate  $r_m$  between  $r_{m\pm} = \pm\frac{\pi}{4nT^2}$  in the same way as we

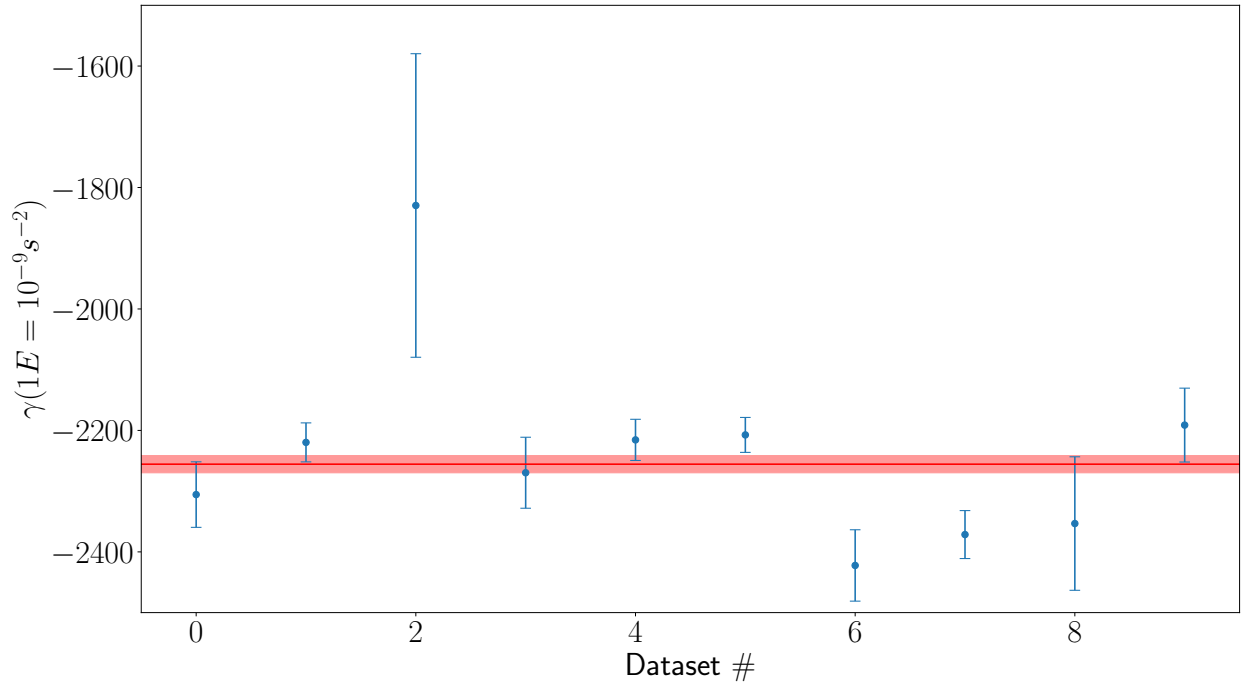


Figure 5.2: Overall gravity gradient measurements. The red band indicates the mean value and  $\pm 1\sigma$ .

modulate  $\omega_m$  in the Ramsey Bordé interferometer. Since there is a minus sign before the ramp rate term, when we get the average  $(\Phi_{d+} + \Phi_{d-})/2$  from the program, we need to add an additional minus sign such that we won't get a  $\gamma$  with the wrong sign. ( $\gamma$  should be positive based on Newtonian gravity theory.) We took 10 datasets in January 2017 and April 2017, interspersed within the entire fine-structure constant data taking period. Data were taken at  $N = 125$ ,  $T'_1 + T'_2 = 50$  ms, with pulse separation time varying from 60 to 100 ms. We chose a few Ts for each dataset to fit  $\gamma$ . One such dataset is shown in Figure 5.1. And we calculated the weighted average of all 10 datasets shown in Figure 5.2 and get  $\gamma = (2256 \pm 14)E$  where  $1E = 10^{-9} s^{-2}$ .

## Magnetic Fields and Zeeman Effect

Similarly, magnetic fields could cause phase shift by a spatially varying force gradient. More specifically, magnetic fields are coupled into the system through Zeeman effect. Considering the hyperfine interaction Hamiltonian  $H_{\text{hfs}}$  and magnetic fields coupling Hamiltonian

$H_B$  [42],

$$H_{\text{hfs}} = A_{\text{hfs}} \mathbf{I} \cdot \mathbf{J} + B_{\text{hfs}} \frac{3(\mathbf{I} \cdot \mathbf{J})^2 + \frac{3}{2} \mathbf{I} \cdot \mathbf{J} - I(I+1)J(J+1)}{2I(2I-1)J(2J-1)} \quad (5.3)$$

$$H_B = \frac{\mu_B}{\hbar} (g_J \mathbf{J} + g_I \mathbf{I}) \cdot \mathbf{B} \quad (5.4)$$

Only in small fields approximation can we use the magnitude and z-component of  $\mathbf{F} = \mathbf{J} + \mathbf{I}$  as a good quantum number. In general we need to diagonalize the total Hamiltonian numerically. But in the case where  $J = 1/2$ , there is a analytical formula called Breit-Rabi formula [102, 42], which well applies to the hyperfine ground states of alkali D transition.

$$E_{|J=\frac{1}{2} \ m_J \ I \ m_I\rangle} = -\frac{\Delta E_{\text{hfs}}}{2(2I+1)} + g_I \mu_B m_B \pm \frac{\Delta E_{\text{hfs}}}{2} \left(1 + \frac{4m x}{2I+1} + x^2\right)^{\frac{1}{2}} \quad (5.5)$$

where the hyperfine splitting  $\Delta E_{\text{hfs}} = A_{\text{hfs}}(I + 1/2)$ ,  $m = m_I \pm m_J = m_I \pm 1/2$ , and

$$x = \frac{(g_J - g_I) \mu_B B}{\Delta E_{\text{hfs}}} \quad (5.6)$$

Specifically we select  $m_F = 0$  Zeeman states to avoid linear Zeeman effect. But there is non-zero second-order Zeeman effect, i.e.

$$E_{|F \ m_F=0\rangle} = -\frac{\Delta E_{\text{hfs}}}{2(2I+1)} \pm \frac{\Delta E_{\text{hfs}}}{2} \left(1 + \frac{1}{2} x^2\right) \quad (5.7)$$

The plus sign is for  $|F = 4\rangle$  and the minus sign for  $|F = 3\rangle$ . Applying it to the state  $|F = 3, m_F = 0\rangle$  we use for our interferometer, we get

$$E_{|F=3, m_F=0\rangle}(\text{2nd-order Zeeman}) = -\frac{(g_J - g_I)^2 \mu_B^2}{4 \Delta E_{\text{hfs}}} B^2 \quad (5.8)$$

If we Taylor expand magnetic field squared as a function of vertical location  $z$ , we get

$$B^2 = B^2 \Big|_{z=0} + 2B \frac{\partial B}{\partial z} \Big|_{z=0} z + \left( \left( \frac{\partial B}{\partial z} \right)^2 + B \frac{\partial^2 B}{\partial z^2} \right) \Big|_{z=0} z^2 + O(z^3) \quad (5.9)$$

So the overall energy is

$$E = E_0 - \frac{1}{4} \frac{g_J^2 \mu_B^2}{\Delta E_{\text{hfs}}} \left( 2B \frac{\partial B}{\partial z} \Big|_{z=0} z + \left( \left( \frac{\partial B}{\partial z} \right)^2 + B \frac{\partial^2 B}{\partial z^2} \right) \Big|_{z=0} z^2 \right) \quad (5.10)$$

The Lagrangian of Zeeman effect can be mapped to that of gravity gradient defined in section with

$$g \rightarrow -\frac{1}{2m} \frac{g_J^2 \mu_B^2}{\Delta E_{\text{hfs}}} B \frac{\partial B}{\partial z} \Big|_{z=0} \quad (5.11)$$

$$\gamma \rightarrow \frac{1}{2m} \frac{g_J^2 \mu_B^2}{\Delta E_{\text{hfs}}} \left( \left( \frac{\partial B}{\partial z} \right)^2 + B \frac{\partial^2 B}{\partial z^2} \right) \Big|_{z=0} \quad (5.12)$$

where  $m$  is the mass of the Cesium atom. In fact, we used 3 layers of magnetic field shields to minimize residual magnetic fields inside the tube where we perform atom interferometer (see Figure 3.3). The remaining magnetic field inside is mostly from the solenoid we used to define the quantization axis, which is about 0.3 G. Even if there is any residual left, our Simultaneous Conjugated configuration helps eliminate the linear gradient components. Eventually only the second-order gradient or gradient squared will enter into the final phase. But it will be taken care of by gravity gradient measurement.

As an independent verification, we also took data with solenoid bias B-fields of 0.38 G and 3.7 G. The measured recoil frequencies are within  $1\sigma$  (1.4 ppb). This puts an upper-bound on any systematic due to the bias magnetic fields at 0.014 ppb. (We don't separately report this part as it has been included in the gravity gradient measurement.)

## Speckle Phase and Others

As we mentioned earlier, we observed pulse separation time  $T$  dependent anomalous phase in the phase residuals as shown in Figure 4.11. Speckle phase, diffraction phase and gradient of gravity gradient and so on could be the source of it. We don't have full knowledge of this type of systematic uncertainty. But thanks to Bloch oscillations and beam cleaning techniques, we were able to suppress it below resolution of statistical uncertainty. Though there is no clear evidence that a statistically resolved residual remains, to be more conservative, we implement a stochastic model following the residual distribution to estimate the potential shift it causes in  $\alpha$ . It causes a shift less than 0.04 ppb of  $\alpha$  at  $\pm 1\sigma$  confidence level.

## 5.3 Effective Wavenumber Correction

Another type of systematic effects affects our measurement through shifting the effective wavenumber  $k$  used in the recoil frequency definition.

$$\omega_r = \frac{\hbar k^2}{2M} \quad (5.13)$$

This type includes systematic effects due to laser frequency, beam alignment, index of refraction and Gouy phase. Since the discussion of Gouy phase is quite lengthy, we put it into a separate section.

### Laser Frequency

Laser frequency directly determines what wavenumber  $k$  we should use to extract  $h/M$ . In theory the effective laser frequency to determine the effective wavenumber  $k = (k_1 + k_2)/2$  is

$$f = \frac{kc}{2\pi} = f_{\text{Diode1}} + f_\delta + f_{\text{AOM14}} + f_{\text{AOM15}}/2 \quad (5.14)$$

where  $k_1, k_2$  are wavenumbers of Bragg beams going up and down respectively. All other definitions can be found in Table 3.6. We typically lock the reference laser to Cesium  $D_2$   $F = 3 \rightarrow F' = 4$  transition line. Frequencies of AOM14 and AOM15 are chosen to be 80 MHz and 180 MHz respectively. The single photon detuning for our fine-structure constant measurement is chosen to be 14 GHz. So putting those data in, the theoretical laser frequency could be determined as

$$f_{\text{th}} = 351.7309021 \text{ THz} + 14.17 \text{ GHz} \quad (5.15)$$

But in reality, there is always an offset frequency added on

$$f_{\text{exp}} = f_{\text{th}} + f_{\text{offset}} \quad (5.16)$$

We need to control its drifting and measure it accurately below 0.1 ppb level. In order to suppress its drift, all RF and microwave frequencies used in this experiment is phase locked to a 10 MHz reference signal. The 10 MHz reference signal is locked to a Rubidium atom clock SRS FS725 [73]. The Rubidium clock in the long term is corrected by Global Positioning System (GPS) clocks as well. Based on references [73, 103], it's able to provide short-term precision better than  $2 \times 10^{-11}$  in a second and long-term stability better than  $10^{-12}$  in a day, which is sufficient for our experiment. However, drift at 0.1 ppb level still remains due to reference laser (Diode1) spectroscopy. In order to control it below 0.1 ppb accuracy, we need to have a way to monitor the laser frequency in real-time. Since RF and microwave frequencies are ultra-stable, we can measure  $f_{\delta}, f_{\text{AOM14}}, f_{\text{AOM15}}$  occasionally with a counter. They can be measured with accuracy better than 1mHz accuracy. For  $f_{\text{Diode1}}$ , we send part of the repump power after TA1 to beat with a Titanium Sapphire based frequency comb (Menlo System FC8004 [104]). The frequency comb generates comb lines at frequencies [105, 106]

$$f_{n^{\text{th}} \text{ comb line}} = n f_{\text{rep}} + f_{\text{comb offset}} \quad (5.17)$$

The Ti:Sa laser is mode-locked at a repetition rate of 200 MHz. Then it is sent to a photonic crystal fiber to broaden the spectrum so that it covers a whole octave of frequency range. Part of it is doubled by a crystal to beat with the original so that the beat frequency is

$$f_{\text{offset beat}} = (2m f_{n^{\text{th}} \text{ comb line}} + 2f_{\text{comb offset}}) - n f_{\text{rep}} - f_{\text{comb offset}} \quad (5.18)$$

After proper low-pass filtering, it gives exactly the comb offset frequency. Knowing both repetition frequency and offset frequency, it becomes a powerful tool to measure any laser frequency within its spectrum. So we beat the repump frequency with the comb to measure the reference laser frequency as

$$f_{\text{Diode1}} = n f_{\text{rep}} + f_{\text{comb offset}} + \Delta f \quad (5.19)$$

Ideally we could use the comb to monitor the laser frequency in real time. But it doesn't work as reliably as we want. However, we noticed a correlation between the signal of a spectroscopy



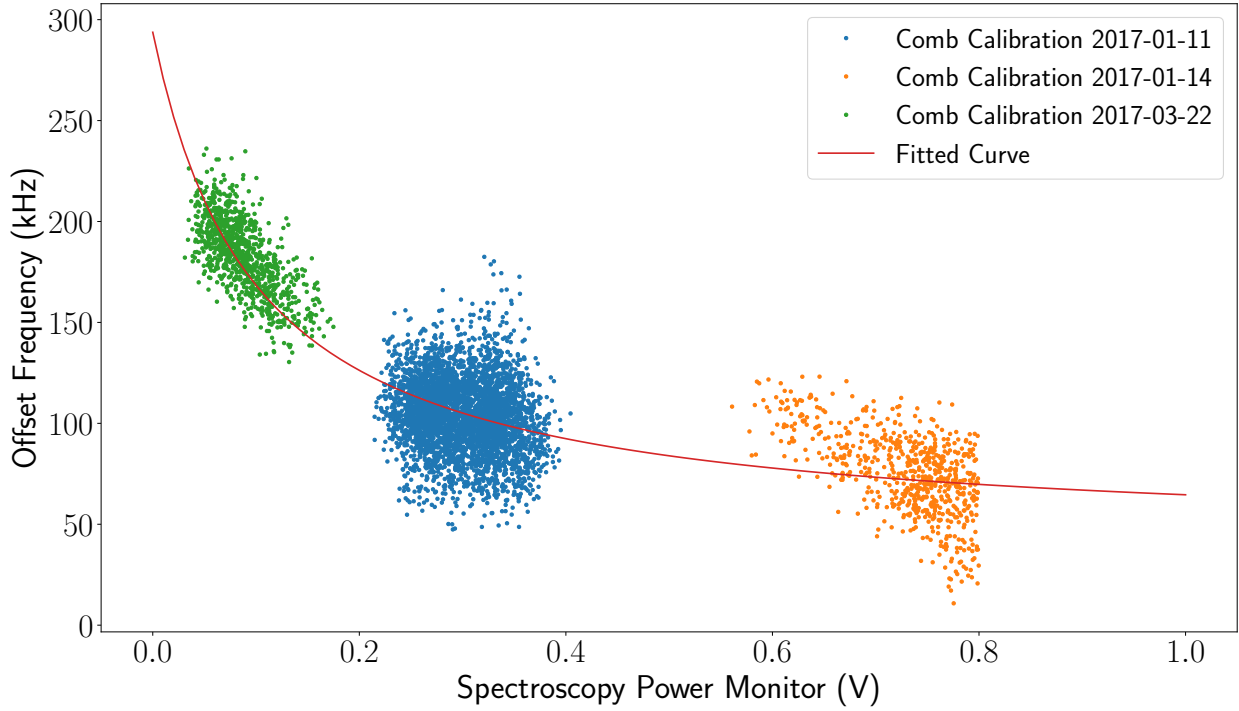


Figure 5.3: Comb calibration raw data from three measurements and the fitted calibration model

power monitor and the locked laser frequency. We use it to establish a calibration shown in Figure 5.3 as

$$f_{\text{offset}} = \frac{1019 \text{ kHz}}{39.9 \times \left(\frac{P_{\text{spectroscopy}}}{1\text{V}}\right) + 4.04} + 41.4 \text{ kHz} + f_X \quad (5.20)$$

where  $f_X$  is the blind parameter we asked Prof. Adhikari to generate for us for blind analysis. After full unblinding,  $f_X = 0$ . In this way by real-time monitoring the spectroscopy signal, we can get a real-time information of laser frequency to apply a dynamic correction to the atom interferometer phase. More specifically, in Equation 4.1 for data analysis, we set  $k_L$  to be  $2\pi f_{\text{th}}/c$ . And the frequency offset can be added into the dynamic correction term  $\Phi_{ij}^{\text{sys}}$  as

$$\Phi_{ij}^{\text{sys, laser freq}} = 32\pi n(n+N) \frac{\hbar k_L}{Mc} T_j f_{\text{offset}} \quad (5.21)$$

where  $f_{\text{offset}}$  is given above by Equation 5.20. The uncertainty of this approach could be evaluated by evaluating the standard deviation of the comb calibration residual, which is found to be better than 10 kHz (or equivalently 0.03 ppb in  $\alpha$ ). As a result, we assigned the systematic uncertainty from laser frequency to be  $-0.24 \pm 0.03$  in  $\delta\alpha/\alpha$ .

## Beam Alignment

Misalignment of the retro-reflected Bragg beam could cause effective wavenumber to change. If there is a small angle  $\theta$  between the input and reflected Bragg beam, the effective wavenumber would be shifted by

$$\delta k = \frac{1}{2} \sqrt{(\vec{k}_1 + \vec{k}_2)^2} - \frac{1}{2}(k_1 + k_2) = -\frac{1}{2} \frac{k_1 k_2}{k_1 + k_2} (1 - \cos \theta) \approx -\frac{1}{8} k \theta^2 \quad (5.22)$$

We set a photodetector to pick up the back-coupling light of the retro-reflected beam after the original Bragg fiber. Then we can use a piezoelectric transducer installed on the retro-reflection mirror to calibrate the tilt angle as a function of the relative back-coupling efficiency  $\eta = P_{\text{back coupling}}/P_{\text{back coupling, max}}$ , which is given as [62]

$$|\theta| = \sqrt{-\ln \eta} \cdot 50.4 \mu\text{rad} \quad (5.23)$$

Thus by monitoring the back-coupling efficiency in real time, we can apply a dynamic correction to the measurement by

$$\Phi_{ij}^{\text{sys, beam alignment}} = -2n(n + N) \frac{\hbar k_L^2}{M} T_j \theta^2 \quad (5.24)$$

The systematic uncertainty of this one is assigned by the standard error of the monitored back-coupling efficiency in the time span of a data bin, which is 0.03 ppb in  $\alpha$ . Retro-reflect mirror ramp for Coriolis compensation will also contribute to this systematic effect. But since it makes a reduction of the relative efficiency by less than 50%, using this formula we can get another bound of 0.01 ppb. Adding them in quadrature, we assign this systematic uncertainty to be  $0.05 \pm 0.03$  ppb in  $\delta\alpha/\alpha$ .

## Index of Refraction

The vacuum in our chamber is not pure vacuum. Due to the presence of background Cesium atoms, the index of refraction is not exactly 1. An effective index of refraction will shift the effective wavenumber by

$$\frac{\delta k}{k} = n - 1 \quad (5.25)$$

The index of refraction near resonance can be solved by Maxwell-Bloch equations. It's the semiclassical treatment of classical electromagnetic fields and quantum atomic transitions. Based on Maxwell equations in dielectrics, the index of refraction can be calculated by [64]

$$n = \frac{c}{v} = \sqrt{\frac{\epsilon\mu}{\epsilon_0\mu_0}} \approx \sqrt{\epsilon_r} = \sqrt{1 + \chi} \quad (5.26)$$

where  $\chi$  is electric susceptibility defined by the relation between electric field and polarization.

$$\mathbf{P} = \epsilon_0 \chi \mathbf{E} \quad (5.27)$$

In the microscopic view, polarization comes from induced dipole moments of particles under electric field, i.e.

$$\mathbf{P} = \frac{1}{V} \sum_i \mathbf{d}_i = \rho \langle \mathbf{d} \rangle \quad (5.28)$$

where  $\rho$  is the particle density. In our context, the dipole moment comes from atoms, which can be calculated by optical Bloch equations. Optical Bloch equations are "Schrödinger" equation of density matrix for a two-level system. It's not exactly identical since density matrix can be used to describe both pure and mixed quantum states, while Schrödinger equation can only be applied to pure quantum states. Using the same rotating frame defined in Section 2.2,

$$|\tilde{\Psi}\rangle = e^{-i\frac{\sigma_z}{2}\omega t} |\Psi\rangle \quad (5.29)$$

where  $\sigma_z$  is the z-component of Pauli matrix. We can get optical Bloch equations for the dynamics of density matrix  $\tilde{\rho} = |\tilde{\Psi}\rangle \langle \tilde{\Psi}|$  with spontaneous decay channels added in [40].

$$\dot{\rho}_{gg} = \frac{i\Omega}{2}(\tilde{\rho}_{ge} - \tilde{\rho}_{eg}) + \Gamma\rho_{ee} \quad (5.30)$$

$$\dot{\rho}_{ee} = -\frac{i\Omega}{2}(\tilde{\rho}_{ge} - \tilde{\rho}_{eg}) - \Gamma\rho_{ee} \quad (5.31)$$

$$\dot{\rho}_{ge} = -\left(\frac{\Gamma}{2} + i\Delta\right)\tilde{\rho}_{ge} - \frac{i\Omega}{2}(\rho_{ee} - \rho_{gg}) \quad (5.32)$$

The steady-state solution for  $\dot{\rho} = 0$  at  $t \rightarrow \infty$  gives

$$\tilde{\rho}_{eg} = -\frac{i\Omega}{\Gamma} \frac{1 + \frac{i2\Delta}{\Gamma}}{1 + \frac{4\Delta^2}{\Gamma^2} + 2\frac{\Omega^2}{\Gamma^2}} \quad (5.33)$$

$$\tilde{\rho}_{ge} = \tilde{\rho}_{eg}^* \quad (5.34)$$

$$(5.35)$$

For a single atom, the expectation value of the dipole moment is

$$\langle \mathbf{d} \rangle = \text{tr}(\rho \mathbf{d}) = \rho_{eg} \langle g | \mathbf{d} | e \rangle + \rho_{ge} \langle e | \mathbf{d} | g \rangle \quad (5.36)$$

Based on the definition of the Rabi frequency  $\Omega = \frac{1}{\hbar} \langle g | \mathbf{d} | e \rangle \cdot \mathbf{E}$  and the relation  $\rho_{eg} = \tilde{\rho}_{eg} \exp(-i\omega t)$ , we have the following relation between the induced dipole moment and electric field

$$\langle d_i \rangle = -\frac{i}{\hbar\Gamma} \frac{1 + \frac{i2\Delta}{\Gamma}}{1 + 4\frac{\Delta^2}{\Gamma^2} + 2\frac{\Omega^2}{\Gamma^2}} \langle e | d_j | g \rangle \langle g | d_i | e \rangle E^j e^{i\omega t} + \frac{i}{\hbar\Gamma} \frac{1 - \frac{i2\Delta}{\Gamma}}{1 + 4\frac{\Delta^2}{\Gamma^2} + 2\frac{\Omega^2}{\Gamma^2}} \langle g | d_j | e \rangle \langle e | d_i | g \rangle E^j e^{-i\omega t} \quad (5.37)$$

where index  $j$  follows the summation rule. In general, as we see, the polarizability constant  $\alpha$  is a tensor (defined by  $\langle \mathbf{d} \rangle = \alpha \mathbf{E}$ ). But for isotropic media like atomic gas considered here, non-diagonal elements are all zero and three diagonal elements are the same, i.e.

$$\langle e | d_j | g \rangle \langle g | d_i | e \rangle = \frac{1}{3} \delta_{ij} |\langle g | d_i | e \rangle|^2 \quad (5.38)$$

Now we can come back to the macroscopic polarization and separate positive frequency component  $E^+ = Ee^{-i\omega t}$  from the negative frequency component  $E^- = Ee^{i\omega t}$ , and it yields

$$\mathbf{P} = \frac{1}{2}(\mathbf{P}^+ + \mathbf{P}^-) = \epsilon_0(\chi\mathbf{E}^+ + \chi^*\mathbf{E}^-) \quad (5.39)$$

where the complex susceptibility is given as

$$\chi = 2\rho \frac{i|\langle g|\mathbf{d}|e\rangle|^2}{3\epsilon_0\hbar\Gamma} \frac{1 - \frac{i2\Delta}{\Gamma}}{1 + 4\frac{\Delta^2}{\Gamma^2} + 2\frac{\Omega^2}{\Gamma^2}} \quad (5.40)$$

So the index of refraction for  $\mathbf{E}^+ = \mathbf{E}_0 \exp(i(kx - \omega t))$  is

$$n = \sqrt{1 + \chi} \approx 1 + \rho \frac{|\langle g|\mathbf{d}|e\rangle|^2}{3\epsilon_0\hbar\Gamma^2} \frac{2\Delta}{1 + 4\frac{\Delta^2}{\Gamma^2} + 2\frac{\Omega^2}{\Gamma^2}} + \rho \frac{|\langle g|\mathbf{d}|e\rangle|^2}{3\epsilon_0\hbar\Gamma} \frac{i}{1 + 4\frac{\Delta^2}{\Gamma^2} + 2\frac{\Omega^2}{\Gamma^2}} = n_R + in_I \quad (5.41)$$

Applying the index of refraction to the original electric field, we can get the dispersion and absorption expression of the electric field in the media,

$$\mathbf{E}^+ = \mathbf{E}_0 e^{-kn_I z + i(kn_R z - \omega t)} \quad (5.42)$$

In the case of our experiment, our laser frequency is far detuned from single photon resonance. The formula could be further simplified as

$$\frac{\delta k}{k} = n_R - 1 = \rho \frac{|\langle g|\mathbf{d}|e\rangle|^2}{6\epsilon_0\hbar\Delta} = \frac{\rho\sigma_0\Gamma}{4k\Delta} = \frac{\rho\lambda_{D2}^3}{16\pi^2} \frac{2J' + 1}{2J + 1} \frac{\Gamma}{\Delta} \quad (5.43)$$

where we have used the relation between the natural linewidth and dipole moment matrix elements [42]

$$\Gamma = \frac{2J + 1}{2J' + 1} \frac{\omega_0^3}{3\pi\epsilon_0\hbar c^3} |\langle g|\mathbf{d}|e\rangle|^2 \quad (5.44)$$

and the definition of the on-resonance cross section  $\sigma_0$ ,

$$\sigma_0 = \frac{\hbar\omega_0\Gamma}{2I_{\text{sat}}} \quad (5.45)$$

$$I_{\text{sat}} = \frac{c\epsilon_0\Gamma^2\hbar^2}{4|\hat{\epsilon} \cdot \mathbf{d}|^2} \quad (5.46)$$

For Cesium  $D_2$  line, the natural linewidth  $\Gamma = 2\pi \cdot 5.2227$  MHz, and in the experiment we set the single photon detuning  $\Delta = 2\pi \cdot 14$  GHz for the Bragg beam. An estimate of  $10^6$  atoms/cm<sup>3</sup> can be made as an upper density bound for cold Cesium atoms, which gives  $n - 1 = 0.003$  ppb. For background atoms, a very conservative bound was made to be  $10^7$  atoms/cm<sup>3</sup> [8], which can set a bound of 0.03 ppb in  $\alpha$ . Adding these two in quadrature, we can bound of this systematic uncertainty conservatively to 0.03 ppb.

## 5.4 Gouy Phase

The name Gouy phase comes from a term in the Gaussian beam phase factor. The electric field of a Gaussian beam can be written as [107]

$$\mathbf{E}(\mathbf{r}, t) = \mathbf{E}_0 \frac{w_0}{w(z)} \exp\left(-\frac{r^2}{w(z)^2}\right) \exp\left(i\left(kz + k\frac{r^2}{2R(z)} + \psi(z)\right)\right) \quad (5.47)$$

where the radius of the beam  $w(z)$  can be related to beam waist  $w_0$  by

$$w(z) = w_0 \sqrt{1 + \left(\frac{z}{z_R}\right)^2}; \quad (5.48)$$

the Rayleigh range  $z_R$  is given as

$$z_R = \frac{\pi w_0^2}{\lambda}; \quad (5.49)$$

the radius of curvature which characterize the spherical wavefront is

$$R(z) = z \left[1 + \left(\frac{z_R}{z}\right)^2\right]; \quad (5.50)$$

and the last term  $\psi(z)$  is the so-called Gouy phase given as

$$\psi(z) = \arctan\left(\frac{z}{z_R}\right). \quad (5.51)$$

This Gouy phase comes from on-axis ( $r = 0$ ) effective  $k$  change due to wavefront curvature. Another phase term called curvature phase,

$$k \frac{r^2}{2R(z)} \quad (5.52)$$

would also enter into the systematic uncertainty when atoms are off-axis ( $r > 0$ ). These terms could potentially contribute to a few ppbs of systematic uncertainties so we need to measure and characterize the beam well.

## Beam Characterization

In the past, the beam coming out from an optical fiber was assumed to be a well-defined Gaussian, so basic razor blade measurements would be sufficient to determine the waist. Recently we noticed that the real beam is significant deviated from the Gaussian beam by Thorlabs scanning-slit beam profiler BP209-VIS and CCD beam profiler BC106N-VIS. So Gaussian model won't be sufficient to characterize beam profiles. We try to use a more generalized model, a Hermite-Gaussian model to fit the scanning-slit data as shown in Figure 5.4. The electric field of Hermite-Gaussian mode can be written as [107]

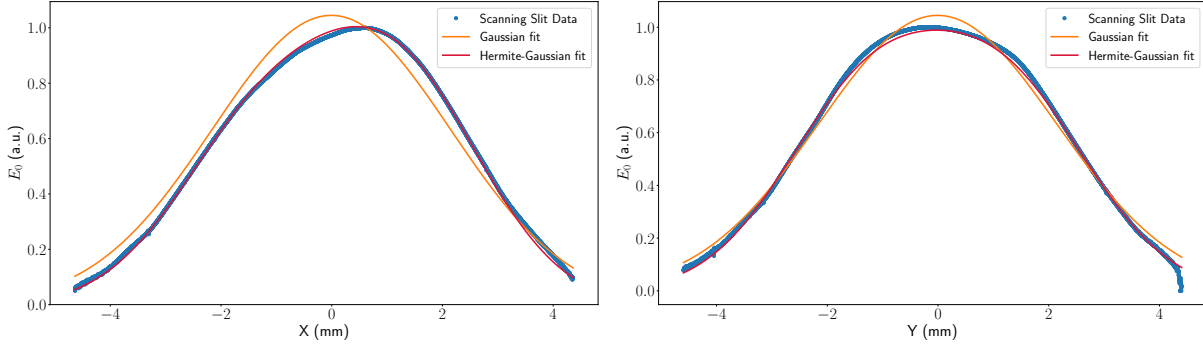


Figure 5.4: Beam profile measured by scanning-slit device. Data were taken at 4 inches out of the fiber port. The Hermite-Gaussian model is obtained by fitting all the data with consistent parameters up to the 2nd order.

$$E_{l,m}(x, y, z) = E_0 \frac{w_0}{w(z)} H_l\left(\frac{\sqrt{2}x}{w(z)}\right) H_m\left(\frac{\sqrt{2}y}{w(z)}\right) \exp\left(-\frac{x^2 + y^2}{w(z)^2}\right) \exp\left(i\left(kz + \frac{kr^2}{2R(z)} + \psi_{l,m}(z)\right)\right) \quad (5.53)$$

where new Gouy phase term  $\psi_{l,m} = (l + m + 1) \arctan\left(\frac{z}{z_R}\right)$  and  $H_l(x)$  is the  $l^{\text{th}}$  order Hermite polynomial. We have used the beam profile from scanning slit data to fit a 2D Hermite Gaussian function up to 2nd order. Since the scanning-slit data gives independent x-scan, and y-scan beam profile, we can fit them independently while restricting the overall parameters like  $w(z)$ ,  $R(z)$  to be the same. So the fitting model can be written as

$$E(x) = c_{0x}E_0(x) + c_{1x}E_1(x) + c_2E_{2x}(x) \quad (5.54)$$

$$E(y) = c_{0y}E_0(y) + c_{1y}E_1(y) + c_2E_{2y}(y) \quad (5.55)$$

where

$$E_m(x) = E_{x0} \left(\frac{w_0}{w(z)}\right)^2 H_m\left(\frac{\sqrt{2}x}{w(z)}\right) \exp\left(-\frac{x^2}{w(z)^2}\right) \quad (5.56)$$

$$E_m(y) = E_{y0} \left(\frac{w_0}{w(z)}\right)^2 H_m\left(\frac{\sqrt{2}y}{w(z)}\right) \exp\left(-\frac{y^2}{w(z)^2}\right) \quad (5.57)$$

We have measured the beam profile at 4", 30", 60", 148", 184", 217" from the fiber port and a sample of them along with its fitting curve is shown in Figure 5.4. The overall fitting results gives  $w_0 = 2.29$  mm,  $z_0 = 1.59$  m,  $z_R = 19.33$  m.

Though it fits well to the overall shape of the beam, it's not accurate enough yet for real Gouy phase calculation for atom interferometer. In a more generalized Gouy phase theory below, we will see not only the overall structure but also small-scale structure matters.

## Generalized Gouy Phase

Based on our beam profile measurement from scanning slit and CCD, we know that our Bragg beam is not quite Gaussian. In this case, how can we evaluate Gouy phase systematic uncertainty? In general for an electromagnetic wave, it satisfies the wave equation,

$$\nabla^2 U - \frac{1}{c^2} \frac{\partial^2 U}{\partial t^2} = 0 \quad (5.58)$$

where  $U$  could be any component of electric fields or magnetic fields. If we put the phase factor in such that  $U = A(\mathbf{r})e^{i(kz - \omega t)}$ , assuming the laser beam satisfies paraxial condition where

$$\frac{\partial A}{\partial z} \ll kA \quad (5.59)$$

$$\frac{\partial^2 A}{\partial z^2} \ll k^2 A \quad (5.60)$$

then we can get the paraxial wave equation [107]

$$\nabla_T^2 A + 2ik \frac{\partial A}{\partial z} = 0 \quad (5.61)$$

where  $\nabla_T^2 = \frac{\partial^2}{\partial x^2} + \frac{\partial^2}{\partial y^2}$ . Based on this equation we can try to calculate the correction it makes to the effective  $k$  due to Gouy phase and wavefront curvature. Suppose  $A(\mathbf{r}) = A_0 \exp(i\phi)$ , then the correction made to the wavenumber  $k$  can be calculated as [101]

$$\begin{aligned} \delta k &= \frac{\partial \phi}{\partial z} \quad (5.62) \\ &= \text{Im} \left( \frac{\partial}{\partial z} (\ln(A_0 e^{i\phi})) \right) \\ &= \text{Im} \left( \frac{1}{A} \frac{\partial A}{\partial z} \right) \\ &= \frac{1}{2k} \text{Re} \left( \frac{\nabla_T^2 A}{A} \right) \quad (5.63) \end{aligned}$$

This correction has included Gouy phase, curvature phase, as it can be shown in the case of the Gaussian beam. If we plug in the Gaussian beam field amplitude  $A = A_0 \exp(-\frac{r^2}{w^2}) \exp(i(kz + k\frac{r^2}{2R} + \psi(z)))$ , this formula gives

$$\delta k = \frac{1}{2k} \left( -\frac{4}{w(z)^2} + \frac{4r^2}{w(z)^4} - \frac{k^2 r^2}{R(z)^2} \right) \quad (5.64)$$

which gives exactly the same contribution from Gouy phase (the first term) and the curvature phase (the last two terms) defined in the traditional way.

## Monte Carlo Simulation

The overall phase contribution from the generalized Gouy phase of each pulse can be calculated as

$$\begin{aligned}
\delta\Phi_d = & 4n^2\omega_r T \frac{\delta k_2^\uparrow + \delta k_2^\downarrow}{k} + 2n^2\omega_r T \frac{\delta k_{3l}^\uparrow + \delta k_{3l}^\downarrow + \delta k_{3u}^\uparrow + \delta k_{3u}^\downarrow}{k} \\
& + 4nN\omega_r T \frac{\delta k_{Bl}^\uparrow + \delta k_{Bl}^\downarrow + \delta k_{Bu}^\uparrow + \delta k_{Bu}^\downarrow}{k} + 4n(n+N)\omega_r T \frac{\delta k_{4l}^\uparrow + \delta k_{4l}^\downarrow + \delta k_{4u}^\uparrow + \delta k_{4u}^\downarrow}{k} \\
& + 2n\omega_r(nT'_1 + nT'_2 + 2NT'_2) \frac{\delta k_{4l}^\uparrow + \delta k_{4l}^\downarrow + \delta k_{4u}^\uparrow + \delta k_{4u}^\downarrow - \delta k_{3l}^\uparrow - \delta k_{3l}^\downarrow - \delta k_{3u}^\uparrow - \delta k_{3u}^\downarrow}{k} \\
& + 8nN\omega_r T'_1 \frac{\delta k_2^\uparrow + \delta k_2^\downarrow - \delta k_1^\downarrow - \delta k_1^\uparrow}{k}
\end{aligned} \tag{5.65}$$

where  $\delta k_{ij}^{\uparrow/\downarrow}$  represents the generalized Gouy phase effective  $k$  shift due to the  $i^{\text{th}}$  pulse acting on the  $j = \{\text{upper (u) or lower (l)}\}$  interferometer by the upgoing ( $\uparrow$ ) or downgoing beam ( $\downarrow$ ). Note that both upper and lower interferometers overlap during the first or the second pulse so no specific  $j$  is labelled.

Here we have used the CCD beam profiler to measure both upgoing and downgoing beam profiles at the specific locations where Bragg and Bloch pulses are applied so that we can map out intensity as well as generalized Gouy phase  $\delta k$  correction locally as a function atom transverse location for each individual pulse based on 5.63. And we apply this intensity and phase map to a Monte Carlo simulation to calculate Gouy phase of each individual atom generated from a specified spatial and velocity distribution. After adding Gouy phase for about 1 million atoms, we can get one point on the ellipse as we defined in Section 3.6. After averaging many data points and ellipses, it gives us an estimate of overall generalized Gouy phase at  $-2.60 \pm 0.03$  ppb in  $\alpha$ . Note that additional noise from the CCD image could be eliminated by proper low pass filter as we try to fit the simulated contrast with the experimental value. The error bar is set by averaging with multiple CCD images as well as varying experiment parameters.

## Theoretical Verification

In the literature [101], it is reported potential ppb level phase shift due to small-scale beam wavefront distortion, which is described as the generalized Gouy phase here. To be sure that we do not suffer from this problem, we have specifically tested it by analytical calculation as well as experimental data. Analytically following [101], we can calculate the effective  $\delta k$  by averaging this generalized Gouy phase over the beam cross section, i.e.

$$\langle \delta k \rangle = \frac{1}{2k} \frac{\langle P(I) \nabla_T^2 A/A \rangle}{\langle P(I) \rangle} \tag{5.66}$$

where  $P(I)$  is probability of Bragg or Bloch pulses (complex wavefunction absolute square) as a function of local intensity  $I$ . In [101], an overoptimistic Heaviside-shaped  $P(I) = \theta(I - I_c)$



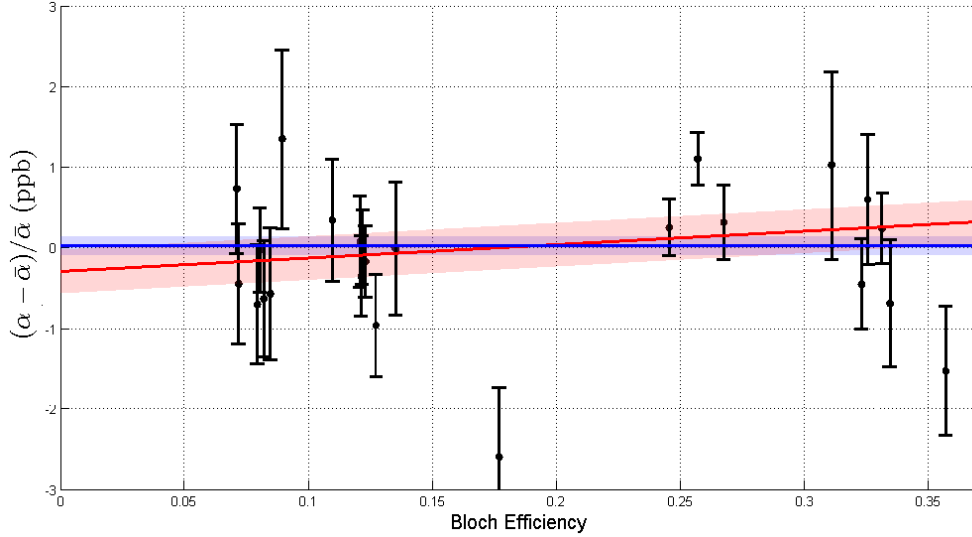


Figure 5.5: Shift in  $\alpha$  as a function of Bloch efficiency. The blue line shows the final reported value of  $\alpha$ , assuming no dependence on Bloch intensity. The red lines assumes a linear dependence. Both red and blue band represent  $\pm 1\sigma$  error bars. This figure is directly taken from supplementary materials of reference [8].

were given. Here  $I_c$  is the critical intensity where Bloch oscillations would be turned on. We instead use a Heaviside-shaped Bloch efficiency function integrated with Gaussian atom distribution to estimate this effect. The result is given as

$$\frac{\delta k}{k} = \frac{r_I^{(2)} w_0^2}{16k^2 \sigma_c^2} \left( \frac{I_c}{I_0} \right)^{w_0^2/4\sigma_c^2 - 1} \quad (5.67)$$

where  $r_I^{(2)} = \nabla_T^2 r_I(0)$  is the Laplacian of the 2-D autocorrelation function  $r_I(\mathbf{d}) = \langle I^*(\mathbf{x} + \mathbf{d}) I(\mathbf{x}) \rangle$ ;  $I_0$  the beam intensity at the center;  $\sigma_c$  atom Gaussian distribution  $\sigma$ . The autocorrelation function can be calculated from CCD intensity profile mentioned earlier, from which an estimate  $r_I^{(2)} \approx 2.44 \times 10^{-9} \mu\text{m}^{-2}$  can be obtained. With  $I_c = (0.85 \pm 0.05)I_0$  and  $\sigma_c \approx 0.6$  mm, the magnitude of this effect is found to be  $-0.030 \pm 0.019$  ppb.

## Experimental Evidences

This has also been further verified experimentally. We directly measured the shift in  $\alpha$  as we scan the Bloch intensity. The measured data and fitting result are shown in Figure 5.5. We did not observe any statistically resolved dependence, which further confirmed our analytical calculation as well as Monte Carlo simulation. We have also included some previous  $\alpha$  measurement data in a plot shown in Figure 5.6, which was taken without the

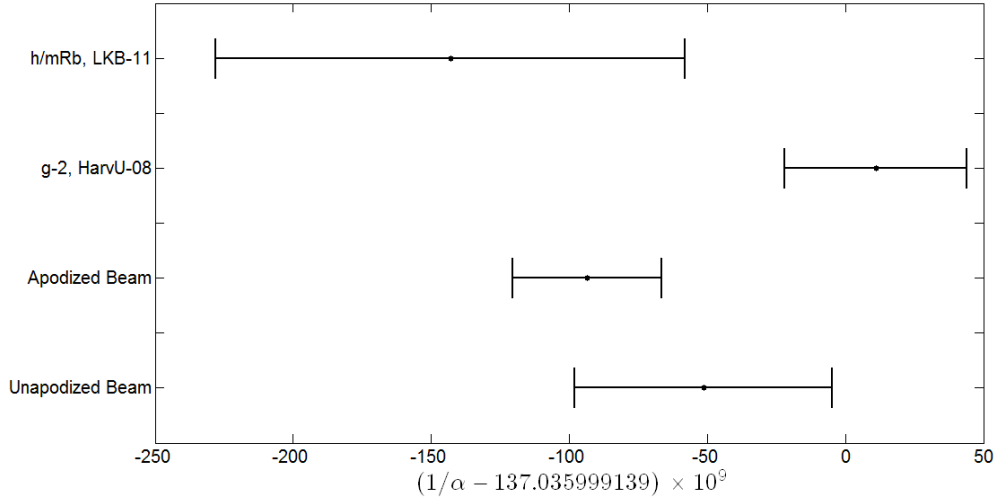


Figure 5.6: The fine-structure-constant measurement with unapodized beam compared with other measurements. This figure is directly taken from supplementary materials of reference [8].

apodizing filter. The original beam without the apodizing filter gives a 5.7 mm beam waist. The  $\alpha$  value between measurement with unapodized and apodized beams are within  $1\sigma$ .

## 5.5 Diffraction Phase Correction

### Thermal motion of atoms

As we mentioned earlier, there is a pulse separation time  $T$  independent phase produced by Bragg diffraction at the leading order. Based on the phase equation,

$$\Phi_d = -2n\omega_m T + 16n(n + N)\omega_r T + \Phi_0 + \Phi_{\text{others}} \quad (5.68)$$

it can be subtracted when we vary the pulse separation time  $T$  and fit  $\Phi_d/T$  vs.  $1/T$  line to find the interception. But at higher order when we take both thermal expansion of atoms and diffraction phase into account, a new term  $\frac{\partial\Phi_0}{\partial T}T$  arises, which would directly shift the recoil frequency measurement.

To calculate  $\partial\Phi_0/\partial T$ , a 3D Monte Carlo mentioned earlier was used. In this Monte Carlo program, we assume atom density and velocity follow 3D Gaussian distribution. We also model the beam as a Gaussian beam. As atom expand, we would take the Bragg diffraction phase interpolated from a precomputed table based on atom detuning and local beam intensity. After the simulation, we use the same ellipse fitting technique to extract this additional phase due to atom thermal expansion. All parameter were chosen from experiment parameters and we added  $\pm 1\sigma$  variation to take into account experimental parameters fluctuation during the experiment run. The simulation was run enough times so that the numerical

Effect	Value	$\delta\alpha/\alpha(\text{ppb})$
Cloud radius (mm)	$2.2 \pm 1.0$	$\pm 0.026$
Vertical velocity width ( $v_r$ )	$1.50 \pm 0.25$	$\pm 0.031$
Ensemble horizontal velocity ( $v_r$ )	$0.0 \pm 0.5$	$\pm 0.032$
Initial horizontal position (mm)	$0 \pm 1$	$\pm 0.034$
Intensity( $I_{\pi/2}$ )	$1.02 \pm 0.02$	$\pm 0.028$
Last pulse intensity ratio	$1.00 \pm 0.02$	$\pm 0.034$
In total		$\pm 0.08$

Table 5.2: Systematic shift due to thermal motion of atoms. Certain estimated experimental parameters are listed in the second column with the systematic effect it produces in the third column.

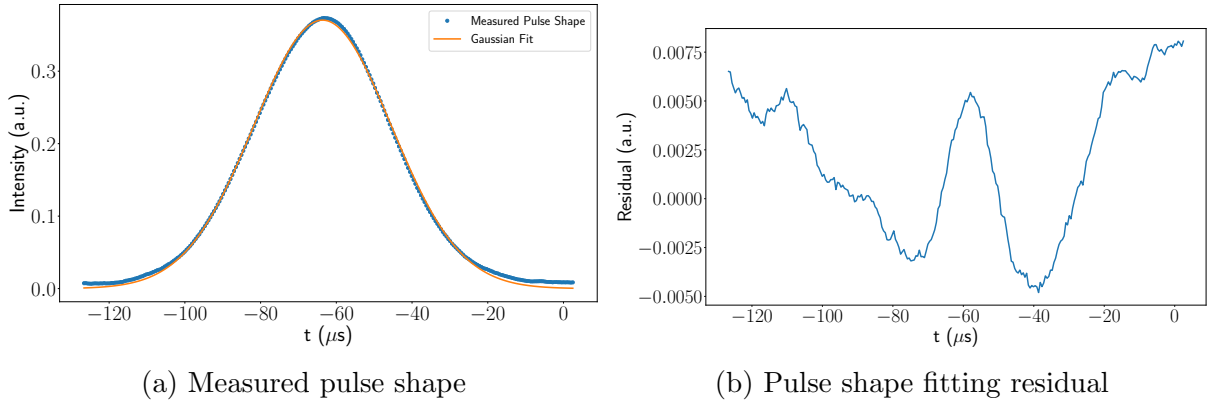


Figure 5.7: Real optimized pulse shape compared with an ideal Gaussian

statistical uncertainty would be below the level of the systematic uncertainty it produces. The simulated result is shown in Table 5.2. In total it produces an overall systematic shift of 0.08 ppb in  $\alpha$ .

## Non-Gaussian waveform

The T-dependent diffraction phase  $\frac{\partial\Phi_0}{\partial T}T$  could potentially be amplified by Bragg beam temporal pulse shape [108]. In reality, the Bragg pulse temporal waveform is slightly lagged behind a real Gaussian due to limited feedback speed as shown in Figure 5.7. We optimized the pulse shape through the servo lock box and put the measured pulse shape into the same Monte Carlo simulation described above, we were able to get a systematic bound below 0.03 ppb.

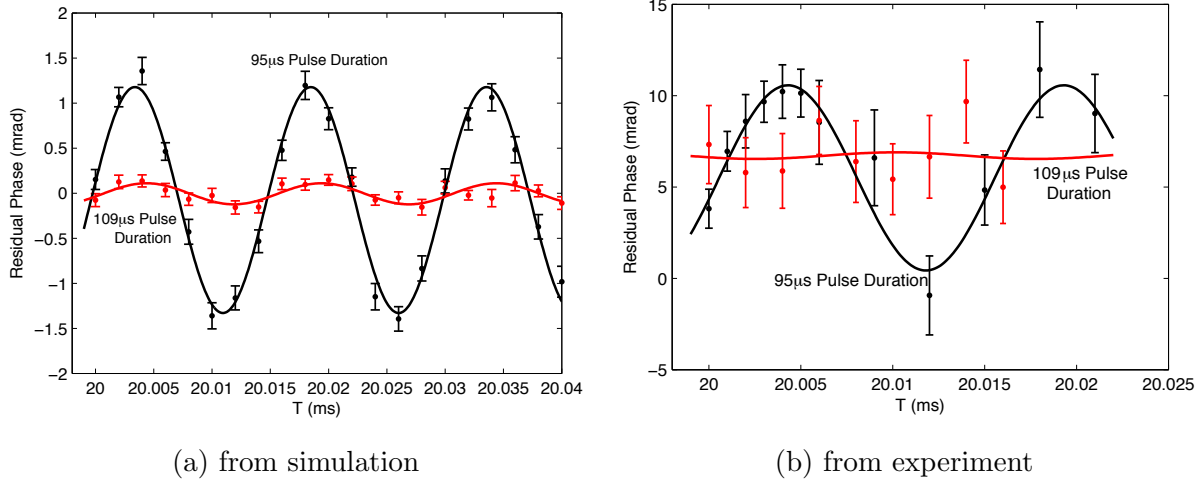


Figure 5.8: Residual phase from both a Monte Carlo simulation and the experiment. These two figures are directly taken from reference [108].

## Parasitic interferometers

The multi-port nature of Bragg diffraction allows atoms to be transferred to unwanted momentum states and some of these may even close at the last pulse and form unwanted parasitic interferometers. We first noticed it in experimental residual phase after diffraction phase extracted, that there was a small modulation as we vary the pulse separation time  $T$  as shown in Figure 5.8 (b) in black. And then we performed a Monte Carlo simulation and confirmed that the period is in good agreement with what a parasitic interferometer from  $n_p = 1$  and  $n_p = n - 1$  would produce, which shows in Figure 5.8 (a) in black.

For this type of parasitic interferometer, some residual atoms are driven to  $|n_p\rangle$  and  $|n - n_p\rangle$  as shown in Figure 5.9. Then they could close at the last pulse and form parasitic interferometers shown in black dash lines. At the detection region, since these parasitic interfering atoms are very close to some of the main interferometer output ports, parasitic interference would be mixed into the main signals as such modulation in residual phase. Though it doesn't affect interferometer performance, any such residual phase would cause significant systematic effect on our measurement. So we used the same Monte Carlo simulation to find a region where this type of parasitic interferometer would be suppressed. We found that there is a "magic" Bragg pulse duration at  $109 \mu\text{s}$  where this kind of parasitic interferometer would be suppressed as shown in Figure 5.10.

We further confirmed it with simulation and experiment at this pulse duration as shown in Figure 5.8 (a) (b) in red. We can see from experiment data that there is no statistically resolved modulation at this pulse duration. And the residual phase is fitted to be less than 2.6 mrad based on a model including such parasitic modulation. Therefore we can set this systematic uncertainty to be below 0.03 ppb in  $\alpha$ .

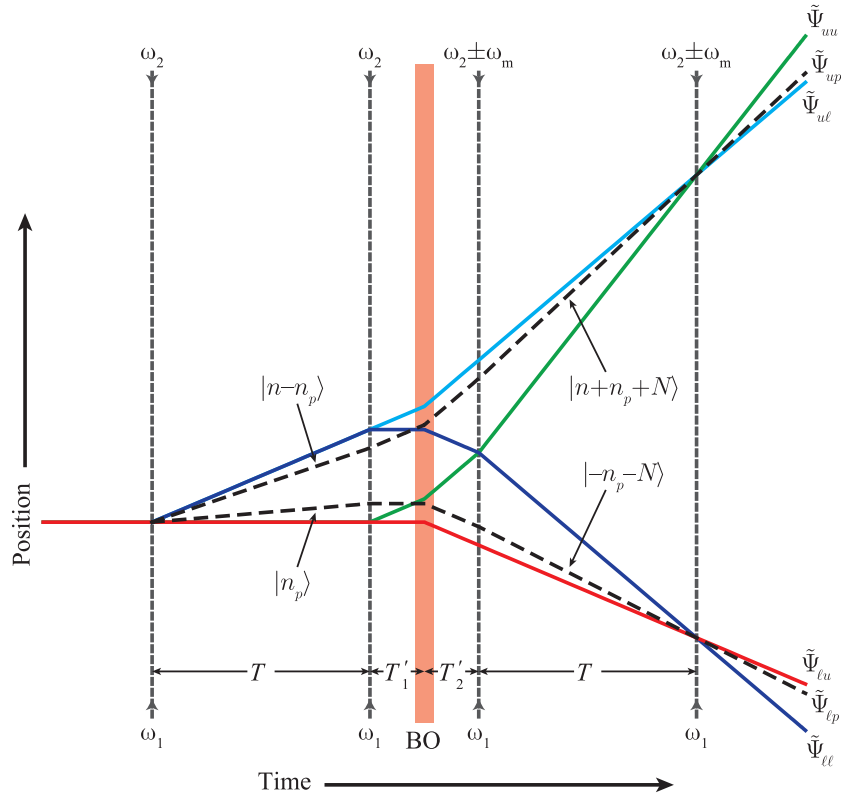


Figure 5.9: Atom interferometer configuration with parasitic interferometer plotted in dash lines. This figure is directly taken from reference [108].

## 5.6 Miscellaneous

### Additional phase shift due to modulation frequency

As we calculated in the previous section, since we added a modulation frequency  $f_m$  in the third and the fourth pulse, the effective photon momentum transferred to atoms would differ by  $\pm\hbar\omega_m/c$ . This would result in an additional phase term called splitting/ Doppler phase term mentioned in Section 2.6. Its mathematical form is given as

$$\Delta\Phi_{\text{splitting/Doppler}} = -2nT\omega_m \frac{v_0}{c} + \frac{gnT(3T + 2T'_1 + 2T'_2)\omega_m}{c} - 4n^2\omega_r T \frac{\omega_m}{\omega_L} \quad (5.69)$$

$$= -2nT\omega_m \frac{v_2}{c} + \frac{gnT(T + 2T'_1 + 2T'_2)\omega_m}{c} - 4n^2\omega_r T \frac{\omega_m}{\omega_L} \quad (5.70)$$

where  $v_2$  is the atom velocity of the non-deflected atom cloud at the time we drive the second Bragg pulse. Since we fixed the timing of the second and third Bragg pulses as we vary  $T$ ,  $v_2$  would be a constant within a dataset. The term with  $g$  contributes 0.98 ppb in

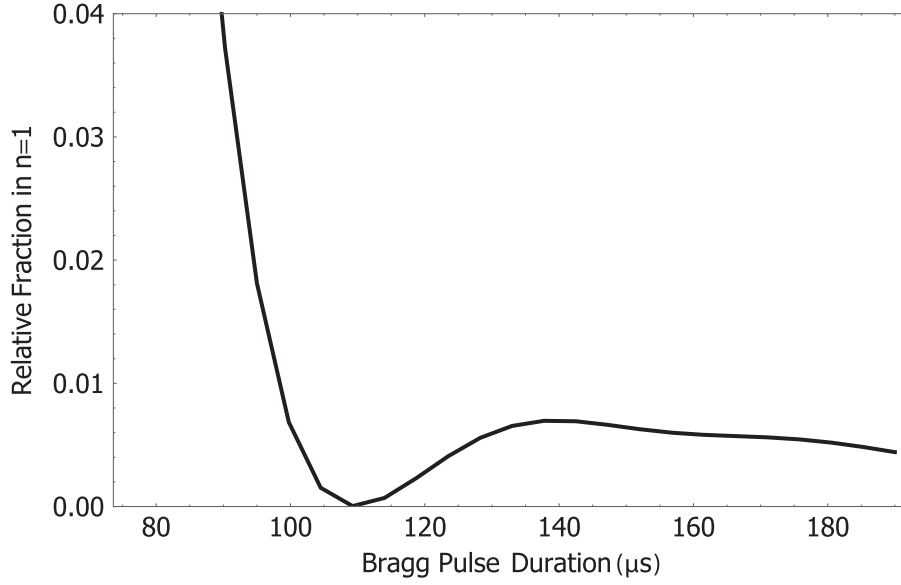


Figure 5.10: Fraction of atoms in the parasitic interferometer  $|n_p = 1\rangle$  as a function of Bragg pulse duration. Here the pulse duration is defined as  $6\sigma$  of Bragg Gaussian pulse. This figure is directly taken from reference [108].

$\alpha$  with our general configuration and  $T$  taken to be 80 ms. The uncertainty comes from the deviation between the real  $g$  and the value we use. The real  $g$  is the projection of gravitational acceleration onto Bragg beam wave vector  $\mathbf{k}$ ,

$$g = \frac{\mathbf{g} \cdot \mathbf{k}}{|\mathbf{k}|} \quad (5.71)$$

The  $g$  value we use is from our onsite measurement given with parts-per-million (ppm) level accuracy [35]. The average velocity of the entire atom interferometer is about 2 m/s. During 180 ms period of atom interferometer, atom misalignment relative to Bragg beam is estimated less than beam waist 3 mm otherwise it would produce significant effect. So it gives an upper bound of misalignment of 10 mrad. Put it into the formula, it gives an uncertainty below 0.001 ppb.

Atom velocity  $v_2$  can be accurately estimated with Bragg diffraction resonance condition. For historical reason, the gravity ramp double pass frequency for Bragg diffraction we sent to AOM17 (see Table 3.6) is given as

$$f_{\text{AOM17}} = f_{\text{g.ramp}}/2 = 59.47689 \text{ MHz} + 2f_{\text{Bragg}} - 11.49783 \text{ MHz/s} \times (t - t_0) \quad (5.72)$$

where  $f_{\text{Bragg}}$  is the parameter we type in the program and  $t_0 = 1.033$  s the launch time when we start gravity ramp. Resonance condition at  $t = t_2$  requires

$$2\pi(2f_{\text{AOM17}} - f_{\text{AOM18}}) = 2k(v_2 + n\frac{\hbar k}{M}) \quad (5.73)$$

Plugging  $f_{\text{AOM18}} = 180$  MHz into this equation, we have

$$v_2 = \frac{-206.99634 \text{ MHz} + 4\pi f_{\text{Bragg}} - 72.243 \text{ MHz/s} \times T_2}{k} \quad (5.74)$$

where  $T_2$  is the time delay from the Bragg system trigger at  $t = 1.24$  s to the time we actually trigger the second Bragg pulse, which is typically taken to be 80 ms. Given a typical  $f_{\text{Bragg}} = 18.111$  MHz used for data taking, it gives  $v_2 = 2.009$  m/s.

For Bloch order  $N = 125$  and pulse separation time  $T = 80$  ms, the term with  $v_2$  contributes about -3.35 ppb in  $\alpha$ . Since Bragg frequency uncertainty is less than 1 kHz, we can bound the uncertainty of this term to 0.0002 ppb, which is negligible. Corrections due to these terms has been applied directly into our data analysis programs. So here we only assign a systematic uncertainty of 0.001 ppb for this item in the error budget.

## Light Shift

Typically light shift comes from AC Stark shift of atomic energy level by light. AC Stark shift is a general property of atoms in the presence of oscillating electric fields. Based on the perturbation theory, second-order virtual processes would cause energy level to shift. AC Stark shift is exactly this case and the energy shift in general is given as [109]

$$\delta E_{\text{AC Stark}} = \sum_i \frac{|\langle e_i | \mathbf{E} \cdot \mathbf{d} | g \rangle|^2}{4\hbar\Delta_i} \quad (5.75)$$

where  $\Delta_i$  is the single photon detuning relative to the state  $|e_i\rangle$ . In our experiment, we only need to consider it for Bloch oscillations as its duration  $\times$  intensity is about an order of magnitude larger than that of Bragg diffraction. Applying it to dual-Bloch oscillations, we have

$$\Phi_{\text{AC Stark}} = \int dt \frac{|\langle e | \sum_i \mathbf{E}_i(t) \cdot \mathbf{d} | g \rangle|^2}{4\hbar^2\Delta} \quad (5.76)$$

The electric field here consists of three fields from the input upgoing beam  $E_1$ ,  $E_{2+}$ ,  $E_{2-}$ , and another three fields from the retro-reflected downgoing beam  $E'_1$ ,  $E'_{2+}$ ,  $E'_{2-}$ , where the naming convention follows Figure 3.19 (d). After we transform to the laser rotating frame through which we define the detuning  $\Delta = \omega_{\text{laser}} - \omega_{\text{atom}}$ , there would be a small oscillating phase factor remained in some of the electric fields due to relative frequency difference as well as Doppler shifts. So the square of dipole interaction matrix elements would produce six direct square terms with no interference factor and 15 cross terms with various interference factors depending on time and the spatial location. Only one out of 15 terms is resonant, i.e. the term is more or less constant throughout the whole pulse. For all other terms, they are oscillating way faster than the duration of the pulse, so if we integrate over the entire pulse duration, their net contribution is negligible compared with other terms. Here we can just drop them for simplicity. The resonant term for the lower interferometer would be  $\langle e | \mathbf{E}_1 \cdot \mathbf{d} | g \rangle \langle e | \mathbf{E}'_{2+} \cdot \mathbf{d} | g \rangle$  and that for the upper interferometer would be the

$\langle e|\mathbf{E}_1 \cdot \mathbf{d}|g\rangle \langle e|\mathbf{E}'_{2-} \cdot \mathbf{d}|g\rangle$ . For a blue detuned Bloch lattice where atom would be trapped at the intensity minimal, this cross term makes destructive interference between the two fields so that in total their contribution to the AC Stark shift will only be  $|\langle e|(\mathbf{E}_1 - \mathbf{E}'_{2+}) \cdot \mathbf{d}|g\rangle|^2$  for the lower interferometer and  $|\langle e|(\mathbf{E}_1 - \mathbf{E}'_{2-}) \cdot \mathbf{d}|g\rangle|^2$  for the upper interferometer. We design the experiment such that  $E_1 \approx E_{2\pm}$  so these terms would be negligible compared with other remaining terms.

After applying the definition of the Rabi frequency, we have

$$\Phi_{\text{AC Stark}}^{\text{upper}} = \int dt \frac{\Omega_{2+}^2 + \Omega_{2-}^2 + \Omega_1'^2 + \Omega_{2+}'^2}{4\Delta} \quad (5.77)$$

$$\Phi_{\text{AC Stark}}^{\text{lower}} = \int dt \frac{\Omega_{2+}^2 + \Omega_{2-}^2 + \Omega_1'^2 + \Omega_{2-}'^2}{4\Delta} \quad (5.78)$$

Our choice of Bloch oscillations as the common mode accelerator make our system immune to differential AC Stark shift at the leading order since atoms remain in the same electronic state ( $|F = 3\rangle$ ) all the time. But as the beam we use is more like a Gaussian beam instead of an infinitely large plane wave, intensity gradient along the vertical direction would cause differential phase. If we use the a simple Gaussian beam model obtained by the original razor blade measurement, we can define the intensity profile for the upgoing beam as

$$I^\uparrow(x, y, z) = I_0^\uparrow F^\uparrow(x, y, z) \quad (5.79)$$

and for retro-reflected downgoing beam as

$$I^\downarrow(x, y, z) = I_0^\downarrow F^\downarrow(x, y, z) \quad (5.80)$$

where the profile factor functions are defined as

$$F^{\uparrow\downarrow}(x, y, z) = \left( \frac{w_0}{w^{\uparrow\downarrow}(z)} \right)^2 \exp \left( - \frac{2(x^2 + y^2)}{w^{\uparrow\downarrow}(z)^2} \right) \quad (5.81)$$

$$w^\uparrow(z) = w_0 \sqrt{\frac{z - z_0}{z_R}} \quad (5.82)$$

$$w^\downarrow(z) = w_0 \sqrt{\frac{z + z_0}{z_R}} \quad (5.83)$$

Note that z coordinate here is defined in the way that z is equal to 0 at the retro mirror to satisfy the boundary condition. So we can get the differential AC Stark phase shift for an



atom interferometer at locations  $(x, y, z)$  and  $(x, y, z + \delta z)$  during Bloch oscillations as

$$\begin{aligned} \Delta\Phi_{\text{AC Stark}}^{\text{upper}} &= \int dt \left( \frac{\Omega_{2+}^2 + \Omega_{2-}^2}{4\Delta} \Big|_{\text{peak}} (F^\uparrow(x, y, z) - F^\uparrow(x, y, z + \delta z)) \right. \\ &\quad \left. + \frac{\Omega_1'^2 + \Omega_{2+}'^2}{4\Delta} \Big|_{\text{peak}} (F^\downarrow(x, y, z) - F^\downarrow(x, y, z + \delta z)) \right) \end{aligned} \quad (5.84)$$

$$= - \left( \frac{\Omega_{2+}^2 + \Omega_{2-}^2}{4\Delta} \Big|_{\text{peak}} \frac{\partial F^\uparrow}{\partial z} + \frac{\Omega_1'^2 + \Omega_{2+}'^2}{4\Delta} \Big|_{\text{peak}} \frac{\partial F^\downarrow}{\partial z} \right) \tau \delta z \quad (5.85)$$

where  $\delta z$  is vertical location difference between two arms of an interferometer, and  $\tau$  is the pulse duration of Bloch oscillations. Similarly we can get the formula for the lower interferometer.

$$\Delta\Phi_{\text{AC Stark}}^{\text{lower}} = - \left( \frac{\Omega_{2+}^2 + \Omega_{2-}^2}{4\Delta} \Big|_{\text{peak}} \frac{\partial F^\uparrow}{\partial z} + \frac{\Omega_1'^2 + \Omega_{2-}'^2}{4\Delta} \Big|_{\text{peak}} \frac{\partial F^\downarrow}{\partial z} \right) \tau \delta z \quad (5.86)$$

In order to estimate the effect for all atoms participating in the atom interferometer, we need to integrate it over an effective atom distribution including only atoms that would be detected. But we found that such integral would make the differential effect smaller. So here for simplicity we just use the peak value (assuming  $x = 0, y = 0$ ) to assign a conservative bound. The retro-mirror is at about 110 inches away from the fiber port. Using that as the  $z = 0$  reference, here we list important parameters for the beam and Bloch oscillation locations:

$$\begin{cases} z_0 &= 0.10 \text{ m} \\ z_R &= 35.0 \text{ m} \\ z_{\text{Bloch}} &= -1.40 \text{ m} \\ \delta z &= \frac{2n\hbar k T}{M} \\ \Delta z &= \frac{1}{T_B} \int_0^{T_B} dt a_B t^2 = \frac{1}{3} a_B T_B^2 \end{cases} \quad (5.87)$$

where  $z_{\text{Bloch}}$  is the location where Bloch oscillations happen;  $\Delta z$  is the vertical location difference between the upper interferometer and the lower interferometer. Putting the parameters we normally use in the experiment:  $n = 5, N = 125, T = 80 \text{ ms}, \Omega_1' = \Omega_{2\pm} = \Omega_{2\pm}'$ , we get AC Stark shift for each individual interferometer about 8 mrad.

Thanks to the simultaneously-conjugated-interferometer configuration we used, when we take the difference  $\Delta\Phi_{\text{AC Stark}}^{\text{upper}} - \Delta\Phi_{\text{AC Stark}}^{\text{lower}}$ , it gives a much smaller phase difference that enter into our error budget. Such phase difference can be calculated as follows,

$$\Delta\Phi_{\text{AC Stark}}^{\text{upper}} - \Delta\Phi_{\text{AC Stark}}^{\text{lower}} = \frac{\Omega_{2-}'^2 - \Omega_{2+}'^2}{4\Delta} \frac{\partial F^\downarrow}{\partial z} \Big|_{\text{peak}} \tau \delta z + \left( \frac{\bar{\Omega}^2}{2\Delta} \frac{\partial^2 F^\uparrow}{\partial z^2} + \frac{\bar{\Omega}^2}{2\Delta} \frac{\partial^2 F^\downarrow}{\partial z^2} \right) \Big|_{\text{peak}} \tau \delta z \Delta z \quad (5.88)$$

where  $\bar{\Omega}^2/2\Delta$  is the average ‘‘Rabi frequency’’ of Bloch oscillations, given to be  $0.2\Omega_{\text{Bragg}\pi/2} \approx 6\omega_r$  (see Section 2.5). Suppose the difference between  $\Omega_{2+}'^2$  and  $\Omega_{2-}'^2$  is only 2%, then the first

term would contribute about  $43 \mu\text{rad}$ , and the second term would contribute  $13 \mu\text{rad}$ . If we add them in quadrature, we can get a bound of  $0.002 \text{ ppb}$  in  $\alpha$ .

Note that we have AC Stark shift compensation as another safeguard, to further suppress this systematic uncertainty, which could potentially suppress this systematic effect by another order of magnitude.

## Density Shift

There is another systematic phase shift caused by the density of atom cloud. As atom density is getting higher, atom-atom interaction due to s-channel scattering would cause a phase shift. This is well described by Gross-Pitaevskii equation as follows [110, 111, 112]

$$i\hbar \frac{\partial}{\partial t} \Psi(\mathbf{r}, t) = \left[ -\frac{\hbar^2}{2M} \nabla^2 + V(\mathbf{r}) + \frac{4\pi\hbar^2 a_s}{M} |\Psi(\mathbf{r}, t)|^2 \right] \Psi(\mathbf{r}, t) \quad (5.89)$$

where  $a_s$  is the scattering length of Cesium atom given as  $a_s = 280(10)a_0$  [113] for  $F = 3$  state and  $a_0$  is the Bohr radius. For non-degenerate Bose gas like what we are using, mean-field approximation is sufficient enough.  $|\Psi(\mathbf{r}, t)|^2$  can be replaced by atom number density  $\rho$ . Effectively it becomes a Schrödinger equation with effective energy shift

$$E_{\text{density}} = \rho \frac{4\pi\hbar^2 a_s}{M} \quad (5.90)$$

For an exaggerated case where the density ratio between the upper interferometer and the lower interferometer is 3:1, and assume cold atom number density  $\rho = 10^6 \text{ atoms/cm}^3$ . An upper bound of phase shift can be estimated as

$$\Delta\Phi = \frac{\Delta E_{\text{density}}}{\hbar} (2T + T') = \left( \frac{3\rho}{4} - \frac{\rho}{4} \right) \frac{4\pi\hbar a_s}{M} (2T + T') \quad (5.91)$$

For typical parameters of  $T = 80 \text{ ms}$  and  $T' = 20 \text{ ms}$ , it gives a phase shift of  $8 \mu\text{rad}$ , which corresponds to a negligible uncertainty of  $0.003 \text{ ppb}$  in  $\alpha$ .

## Sagnac Effect

The lab reference frame where we perform atom interferometer experiment and where we calculate interferometer phase is actually a rotating frame due to the Earth's spin. When we switch back to the non-rotating frame, there is an additional phase term called Sagnac phase we need to take into account [114].

Suppose the Lagrangian of the lab frame (the rotating frame) is  $L'(\mathbf{r}', t)$  while the Lagrangian of the non-rotating inertial frame is  $L(\mathbf{r}, t)$ . The transformation between these two frames are given as

$$\begin{cases} \mathbf{r} = \mathbf{r}' \\ \mathbf{v} = \mathbf{v}' + \boldsymbol{\Omega} \times \mathbf{r}' \end{cases} \quad (5.92)$$

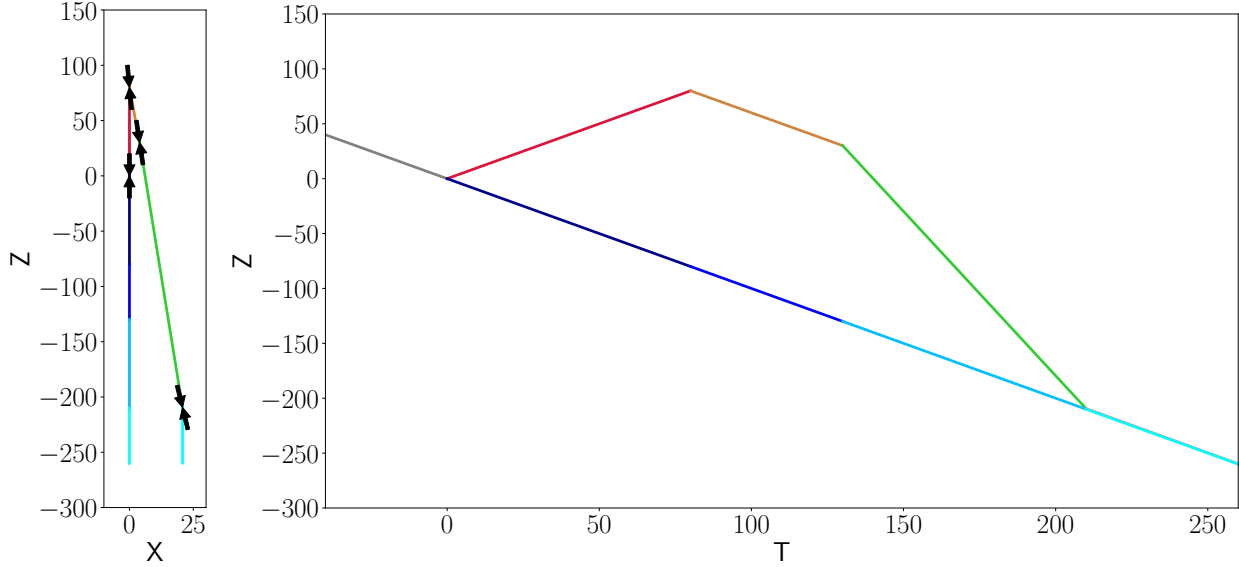


Figure 5.11: Effect of the Earth's rotation on Ramsey Bordé interferometer. The subplot on the left show atom movement in 2D as Bragg beam is rotation along with the earth. The direction of each beam splitter's wave vector is shown by arrows. The subplot on the right is the typical spatial-temporal diagram as a reference to understand the plot on the left. The same color corresponds to the same stage of the inteferometer.

So the Lagrangian in the non-rotating frame can be evaluated as [41]

$$L(\mathbf{r}, t) = \frac{1}{2} m \mathbf{v}^2 - V \quad (5.93)$$

$$= \frac{1}{2} m (\mathbf{v}' + \boldsymbol{\Omega} \times \mathbf{r}')^2 - V \quad (5.94)$$

$$= L'(\mathbf{r}', t) + m \boldsymbol{\Omega} \cdot (\mathbf{r}' \times \mathbf{v}') \quad (5.95)$$

where the higher order term  $O(\Omega^2)$  has been neglected. And this additional term, when it is integrated over the entire path loop of an interferometer, gives rise to the Sagnac phase,

$$\Phi_{\text{Sagnac}} = \frac{1}{\hbar} \int dt m \boldsymbol{\Omega} \cdot (\mathbf{r}' \times \mathbf{v}') \quad (5.96)$$

$$= \frac{1}{\hbar} \oint m \boldsymbol{\Omega} \cdot (\mathbf{r}' \times d\mathbf{r}') \quad (5.97)$$

$$= \frac{2m}{\hbar} \boldsymbol{\Omega} \cdot \mathbf{A} \quad (5.98)$$

where  $\mathbf{A}$  is the area vector enclosed by the interferometer path. In theory, our interferometer is along vertical direction so the enclosed area should be zero. But due to the Earth's rotation, though atom still try to move straight under gravity, the direction of Bragg and Bloch wave

vector keeps changing following the Earth's rotation. So in the end, atom interferometer would move transversely and open a small area as shown in Figure 5.11 Z-X plot. It is a schematic of Ramsey Bordé interferometer with each beam splitter's wave vector following the Earth's rotation labelled by arrows. Each colored section corresponds to the same section in the normal Z-T diagram shown in the right. At the same time, we also noticed that due to the Earth's rotation, the atom interferometer doesn't close at the last pulse. As long as the separation is larger than the coherence length of the matter wave, interference would disappear. That's the whole reason why we apply Coriolis compensation at the first place. If the compensation is working perfectly well, there will no Sagnac effect left.

We can calculate the enclosed area as follows [62]

$$A_i = \int x_{iu}(t) \frac{d}{dt} z_{iu}(t) dt - \int x_{il}(t) \frac{d}{dt} z_{il}(t) dt \quad (5.99)$$

where  $i$  indicate whether it's upper or lower interferometer and the second index in the subscript indicates whether it's the upper or lower path. Based on an approximated calculation given in [62] and the general experimental parameters we are using:  $n = 5$ ,  $N = 125$ ,  $T = 80$  ms,  $T'_1 = 5$  ms,  $T'_2 = 15$  ms, we can set a conservative bound of 0.001 ppb assuming the rotation angular velocity is compensated below 10% of the Earth spin angular momentum by Coriolis compensation [8].

A more careful study is performed using a 2+1D configuration as shown in Figure 5.11 to theoretically calculate the differential phase of simultaneously conjugated Ramsey Bordé interferometers with rotating wave vector. Assuming the wave vector is rotating with angular velocity  $\Omega$ , it follows

$$\mathbf{k} = k(-\sin(\Omega t)\hat{\mathbf{x}} + \cos(\Omega t)\hat{\mathbf{y}}) \quad (5.100)$$

Here we only consider the correction made to the free evolution phase due to rotating wave vectors. It has negligible effect on the laser phase itself. Since the interferometer won't close at the last pulse due to Sagnac effect, we also add an additional splitting phase as we discussed earlier. Keeping only the leading order term, we have a formula for Sagnac effect on the differential phase between two interferometers,

$$\Phi_{d, \text{Sagnac}} = 4n\omega_r T \left( N \left( 2TT'_1 + 4T_1'^2 - \gamma T^4 \right) + n \left( 2T(T'_1 + T'_2) + 2(T'_1 + T'_2)^2 - \gamma T^4 \right) \right) \Omega^2 \quad (5.101)$$

Using the same parameters we use for data taking:  $n = 5$ ,  $N = 125$ ,  $T = 80$  ms,  $T'_1 = 5$  ms,  $T'_2 = 15$  ms, setting  $\Omega$  to be the Earth spin angular momentum  $2\pi/1$  day or  $7.27 \times 10^{-5}$  rad/s, this phase difference is estimated to be only  $14.5 \mu\text{rad}$ , bounding this systematic uncertainty below 0.001 ppb even without applying Coriolis compensation.

## Finite Pulse Length

By far when we calculated the phase of atom interferometers, we assume that atom beam splitters and mirrors cost no extra time so we let atom accumulate the free evolution phase

for the entire pulse separation time  $T$ . But in reality, any pulse takes a finite time  $\tau$ . The actual time of free evolution is only  $T - \tau$ . Does it add extra phase shift into our system.

Suppose initially an atom is at state  $|\psi^S(t = t_0)\rangle$ , where the state is labelled "S" to make it clear that it is in Schrödinger picture. Our question is what the state would be like after a beam splitter pulse for  $\tau$  and free evolution for  $T - \tau$ . It can be simply written as

$$\begin{aligned} |\psi^S(t = t_0 + T)\rangle &= U_f^S(t_0 + T; t_0 + \tau) U_{\text{BS}}^S(t_0 + \tau; t_0) |\psi^S(t = t_0)\rangle \\ &= e^{-i\frac{H_f(T-\tau)}{\hbar}} e^{i\frac{H_f(\tau+t_0)}{\hbar}} U_{\text{BS}}^I(t_0 + \tau; t_0) e^{-i\frac{H_f t_0}{\hbar}} |\psi^S(t = t_0)\rangle \\ &= e^{-i\frac{H_f T}{\hbar}} e^{i\frac{H_f t_0}{\hbar}} U_{\text{BS}}^I(t_0 + \tau; t_0) e^{-i\frac{H_f t_0}{\hbar}} |\psi^S(t = t_0)\rangle \end{aligned} \quad (5.102)$$

where  $H_f$  is the Hamiltonian under free evolution. Note that we are using Hamiltonian to calculate free evolution phase here, which is equivalent to the Lagrangian picture for a closed interferometer, i.e.

$$\oint dt L(q, \dot{q}, t) = \oint dt (p\dot{q} - H(p, q, t) dt) = p \oint dq - \oint dt H = - \oint dt H \quad (5.103)$$

where we have also used conservation of momentum for the entire system.

Therefore, it's fine to calculate the free evolution phase under the assumption of instant beam splitting as long as we treat the beam splitter phase in the interaction picture as shown in eq. Or in other words, any finite pulse effect could be treated as part of the beam splitter phase.

For our specific case Ramsey Bordé atom interferometer with Bragg diffraction beam splitters, it would be part of the diffraction phase that we have experimentally measured as well as extensively studied, so there is no need to add an additional systematic uncertainty into our system.

# Chapter 6

## Conclusion and Future Prospects

### 6.1 Conclusions

Up to this chapter, we have reported and discussed our recent measurement of the fine-structure constant at 0.20 ppb overall uncertainty, as shown with some other recent measurements in Figure 6.1. It's slightly better than previous indirect determination through electron anomalous magnetic moment  $g_e - 2$  measurement at 0.24 ppb uncertainty, enabling us to test Quantum ElectroDynamics (QED) and some other branches of the Standard Model

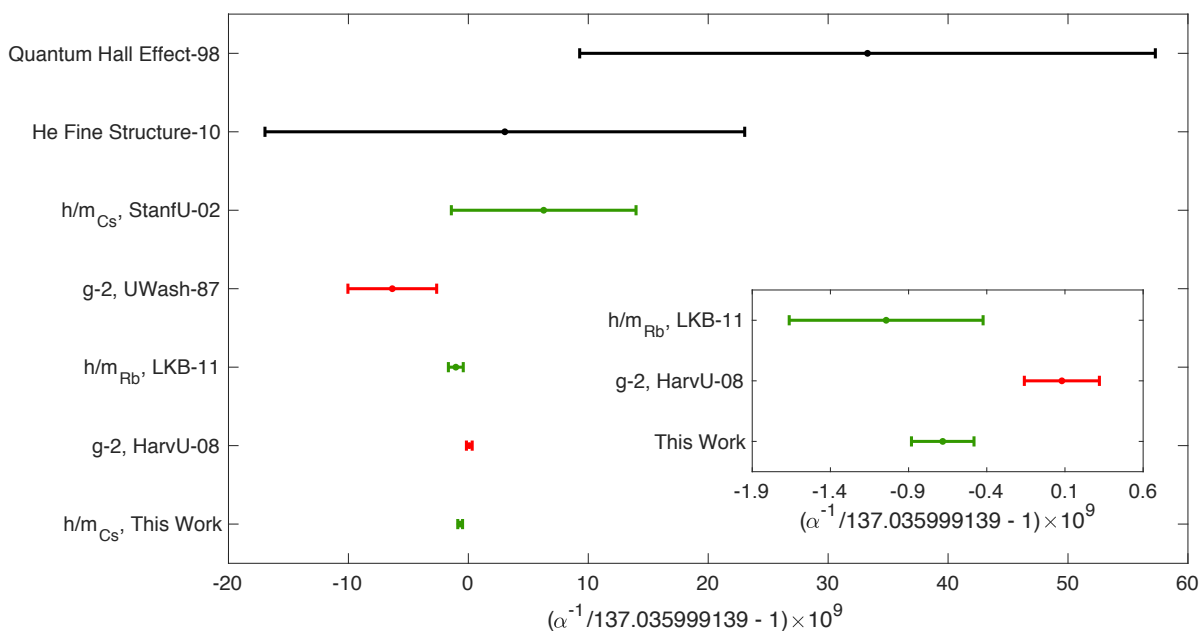


Figure 6.1: Some recent precision determination of the fine-structure constant. This figure is directly taken from reference [8]

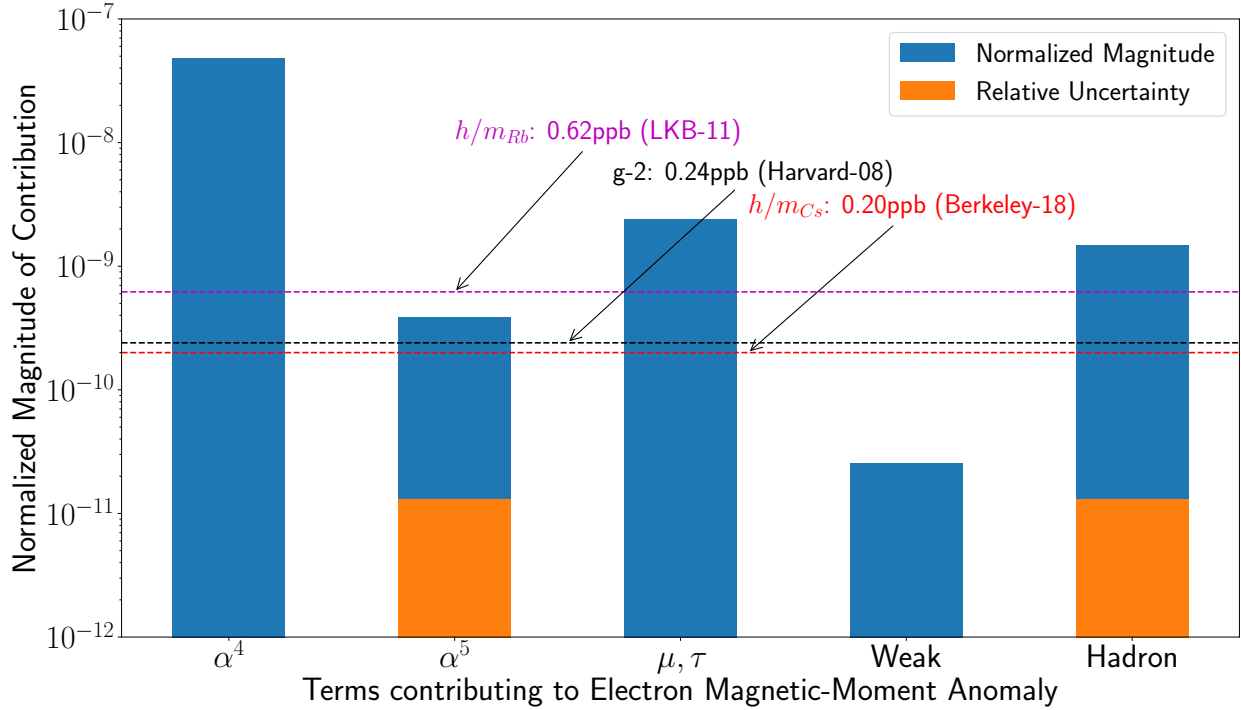


Figure 6.2: Normalized magnitude of contribution of some theoretical terms to electron magnetic-moment anomaly.  $\alpha^4$ ,  $\alpha^5$  represent 4th and 5th order QED loop correction terms.  $\mu$ ,  $\tau$  represent QED terms related to masses of  $\mu$  and  $\tau$ . Weak represents correction from weak interaction. Hadron represents correction from hadronic physics.

as shown in Figure 6.2. It is a zoomed-in histogram with terms contributing less than  $10^{-7}$  of the electron magnetic moment anomaly. We see that it is the first time that such a test is able to reach accuracy below the fifth order QED loop correction contribution. Putting our measured  $\alpha$  value to the theory as defined in Chapter 1, we got electron anomalous magnetic moment

$$a(\alpha) = \frac{g_e - 2}{2} = 0.00115965218161(23) \quad (6.1)$$

Comparing with previous measurement of  $g_e - 2$  we discovered a  $2.5\sigma$  tension between the theoretic electron magnetic anomaly from our measured  $\alpha$  and the experiment electron magnetic anomaly [2]

$$\delta a = a_{\text{meas}} - a(\alpha) = -0.88(0.36) \times 10^{-12} \quad (6.2)$$

where a combined uncertainty  $\sigma$  is given by  $\sqrt{\sigma_{g-2}^2 + \sigma_\alpha^2}$ . Based on frequentist statistics, the conclusion we can draw here is that the Standard Model by itself is incompatible with our determination of the fine-structure constant as well as the electron  $g_e - 2$  measurement at 99.27% confidence level. It's not large enough to claim we have discovered new physics

beyond the Standard Model. But it suggests that something interesting is going on that warrants further investigation.

## 6.2 Implications on Testing New Physics

### Dark Sector

Any new physics that may cause a shift in electron magnetic-moment anomaly could be tested based on our results. One such physics is testing hypothetical particles in dark sectors. We know that dark matter constitutes about 22% of all energy-matter budget [115]. Dark matter does not interact with normal matter in the Standard Model via electromagnetic interaction but via gravitational interaction. One type of particle called dark photon is proposed to explain some observation like muon  $g_\mu - 2$  discrepancy and so on [116]. It is a hypothetical gauge boson from a broken dark  $U(1)$  symmetry. It could interact with the Standard Model (SM) through kinetic mixing in the Lagrangian,

$$\mathcal{L}_{\text{gauge}} = -\frac{1}{4}B_{\mu\nu}B^{\mu\nu} + \frac{1}{2}\frac{\epsilon}{\cos\theta_W}B_{\mu\nu}D^{\mu\nu} - \frac{1}{4}D_{\mu\nu}D^{\mu\nu} \quad (6.3)$$

where  $B_{\mu\nu} = \partial_\mu B_\nu - \partial_\nu B_\mu$  is the field of the Standard Model gauge boson,  $D_{\mu\nu} = \partial_\mu A'_\nu - \partial_\nu A'_\mu$  the field of the dark photon,  $\theta_W$  the weak mixing angle, and  $\epsilon$  the mixing parameter. After some redefinition and dropping the boundary terms for the case of electromagnetic fields, the Lagrangian could be reduced to

$$\mathcal{L}_{\text{gauge}} = -\frac{1}{4}F_{\mu\nu}F^{\mu\nu} - \frac{m_{A'}^2}{2}A'_\mu A'^\mu - \epsilon e J_{em}^\mu A'_\mu \quad (6.4)$$

where  $F_{\mu\nu}$  is electromagnetic field,  $m_{A'}$  the mass of dark photon,  $J_{em}$  electromagnetic current, which is given as

$$J_{em}^\mu = Q_f \bar{f} \gamma^\mu f + \dots \quad (6.5)$$

Here  $f$  could be any four-component SM fermions,  $Q_f$  the corresponding fermionic charge. This theory could be extended to include axial coupling as well, in which the full Lagrangian is written as [117]

$$\mathcal{L}_{\text{gauge}} = -\frac{1}{4}F_{\mu\nu}F^{\mu\nu} - \frac{m_{A'}^2}{2}A'_\mu A'^\mu + A'_\mu \sum_f \bar{f} (c_V^f \gamma^\mu + c_A^f \gamma^\mu \gamma^5) f \quad (6.6)$$

where  $c_V^f = -e\epsilon$  is the vector coupling constant,  $c_A^f$  the axial coupling constant. Based on QED theory, this hypothetical dark photon will shift lepton  $l$  magnetic-moment anomaly  $a_l$  by

$$\delta a_l = \frac{(c_V^l)^2}{4\pi^2} \int_0^1 \frac{x^2(1-x)}{x^2 + \frac{m_{A'}^2}{m_l^2}(1-x)} dx - \frac{(c_A^l)^2}{4\pi^2} \frac{m_l^2}{m_{A'}^2} \int_0^1 \frac{2x^3 + (x-x^2)(4-x)\frac{m_{A'}^2}{m_l^2}}{x^2 + \frac{m_{A'}^2}{m_l^2}(1-x)} dx \quad (6.7)$$



Based on the theory, we can interpret our measurement in the following ways. From a frequentists' interpretation, since vector coupling dark photon shifts the magnetic moment anomaly positively, we can claim that our result is not consistent with the Standard Model plus only dark photon theory with vector coupling to 99.27% confidence level. However, it does not explicitly claim whether we can exclude dark photon theory or not. In high energy physics, an interpretation of exclusion is in practice based on Bayesian-like statistics. The basic question raised in the high energy community is how we can make sure a new discovery is not simply from background fluctuation. In high energy physics, statistics like  $CL_s$  or Power Constraint Limit (PCL) were developed to deal with such situations [118, 119].

Suppose there is a dark photon theory predicts electron magnetic-moment anomaly  $\mu = \delta a_0$  and we observe another value  $\hat{\mu} = \delta a_{\text{obs}}$  in the experiment (here suppose  $\delta a_{\text{obs}} < \delta a_0$ ). Then based on the experiment observation we can set a p-value  $p_\mu$  to evaluate how likely the theory would produce such an experiment result.

$$p_\mu = P(\hat{\mu} < \delta a_{\text{obs}} | \mu = \delta a_0) = \frac{1}{\sqrt{2\pi\sigma^2}} \int_{-\infty}^{\delta a_{\text{obs}}} d\hat{\mu} e^{-\frac{(\hat{\mu}-\mu)^2}{2\sigma^2}} \quad (6.8)$$

where we assume measurement error follows normal distribution. If  $p_\mu$  is less than a given number  $\alpha$  then we can claim the theory  $\mu = \delta a_0$  is not consistent with the observation  $\hat{\mu} = \delta a_{\text{obs}}$  at a confidence level  $CL = 1 - \alpha$  in a frequentist's view.

But in high energy, people want to answer the question whether the observed signal is due to background fluctuation or not. They hope in some way we can "subtract" the background from signal+background.  $CL_s$  was adopted based on this measure. A probability ratio called  $CL_s$  is defined as

$$CL_s = \frac{CL_{s+b}}{CL_b} = \frac{P(\hat{\mu} < \delta a_{\text{obs}} | \mu = \delta a_0)}{P(\hat{\mu} < \delta a_{\text{obs}} | \mu = 0)} = \frac{\Phi\left(\frac{\delta a_{\text{obs}} - \delta a_0}{\sigma}\right)}{\Phi\left(\frac{\delta a_{\text{obs}}}{\sigma}\right)} \quad (6.9)$$

where  $\mu = 0$  is what the Standard Model predicts (background).  $\Phi(x)$  here is the cumulative distribution function of standard normal distribution, i.e.

$$\Phi(x) = \frac{1}{\sqrt{2\pi}} \int_{-\infty}^x dx' e^{-x'^2/2} \quad (6.10)$$

If this ratio  $CL_s < \alpha$ , we claim to rule out theory  $\mu = \delta a_0$  at this confidence level  $1 - \alpha$ . This statistics in the specific case of dark photon is equivalent to Bayesian's statistics. Using Bayesian's language, given the information we have from data, we want to ask what's the probability that a theory with  $\mu > \delta a_{\text{min}}$  is possible so as to determine if we can rule out the theory. This can be solved based on Bayes' theorem

$$P(\mu > \delta a_{\text{min}} | \hat{\mu} = \delta a_{\text{obs}}) = \frac{P(\hat{\mu} = \delta a_{\text{obs}} | \mu > \delta a_{\text{min}})P(\mu > \delta a_{\text{min}})}{\sum_{\text{any } \delta a \geq 0} P(\hat{\mu} = \delta a_{\text{obs}} | \mu = \delta a)P(\mu = \delta a)} \quad (6.11)$$

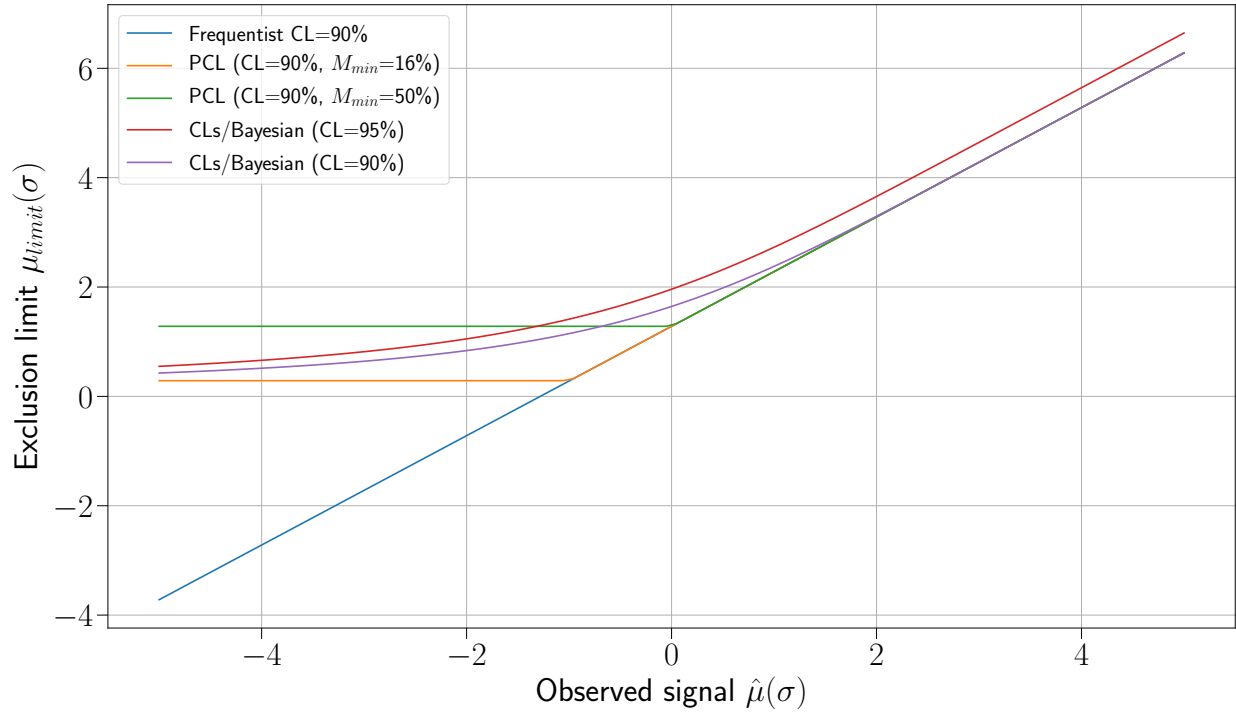


Figure 6.3: Exclusion limits under various statistical methods

If the prior distribution for dark photon  $\delta a$  is uniform for all  $\delta a > 0$ , then this can be simplified to

$$P(\mu > \delta a_{\min} | \hat{\mu} = \delta a_{\text{obs}}) = \frac{\Phi\left(\frac{\delta a_{\text{obs}} - \delta a_{\min}}{\sigma}\right)}{\Phi\left(\frac{\delta a_{\text{obs}}}{\sigma}\right)} \quad (6.12)$$

which is equivalent to  $\text{CL}_s$  mathematically. In the same way we can define the confidence level of Bayesian's statistics.

PCL (Power-Constrained Limits) is another way to set conservative limit to avoid background fluctuation. In PCL, there is a function to quantify the power of the test with respect to an alternative hypothesis  $\mu'$  defined as

$$M_{\mu'}(\mu) = P(p_{\mu} < \alpha | \mu') \quad (6.13)$$

Normally the alternative hypothesis is the background (or here the Standard Model) where  $\mu' = \delta a = 0$ . The test power function calculates the probability of observing a signal in the null hypothesis  $\mu$  critical region under the alternative theory  $\mu' = 0$ . If such a signal is also very unlikely in the alternative hypothesis, then we cannot quite tell the difference between the null hypothesis and the alternative hypothesis. We specifically set a threshold  $M_{\min}$  by convention such that if the testing power is less than  $M_{\min}$ , we cannot claim the theory is excluded according to frequentists' statistics. In this case we can only use the minimum value of  $\delta a_{\text{obs}}$  that satisfies  $M_0(\mu) = P(\hat{\mu} < \delta a_{\text{obs}} | \mu = 0) > M_{\min}$  to set exclusion limit for

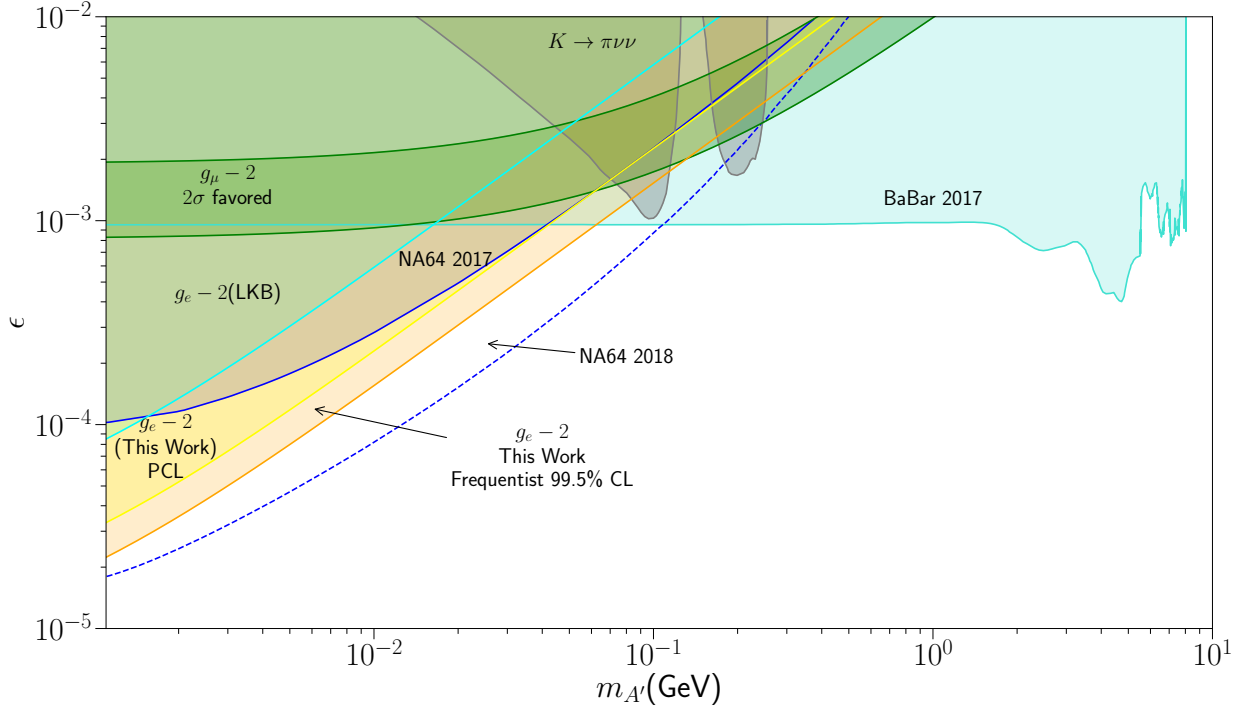


Figure 6.4: Dark photon with vector coupling exclusion plot. Constraints from BaBar were based on Bayesian limit/ frequentist profile likelihood statistics at 90% C.L. [120]. Constraints from kaon decay were obtained from BNL E787+E949 experiments at 95% C.L. [121, 122]. Constraints from NA64 2017 were based on  $CL_s$  statistics at 90% C.L. [123]. Muon  $g_\mu - 2$  data was from CODATA2014 [1]. Its favored region was obtained from its  $\pm 2\sigma$  area based on frequentist's statistics. Both electron  $g_e - 2$  for LKB and this work were analyzed under frequentists' statistics with 99.5% confidence level [1, 2, 11, 8]. We have also analyzed this work under PCL ( $M_{\min} = 16\%$ ) with 90% C.L. Note that NA64 2018 [124] came out after our result was accepted for publication. But for references, here we have also included excluded region from NA64 2018 as shown in dash line.

the theory. But if the testing power is larger than the threshold, we can draw conclusions from the frequentist' statistics. In this way the exclusion limit  $\mu_{\text{limit}}$  could be obtained as

$$\mu_{\text{limit}} = \begin{cases} \sigma(\Phi^{-1}(M_{\min}) + \Phi^{-1}(1 - \alpha)), & \text{if } \hat{\mu} < \sigma\Phi^{-1}(M_{\min}) \\ \hat{\mu} + \sigma\Phi^{-1}(1 - \alpha), & \text{otherwise.} \end{cases} \quad (6.14)$$

where the null hypothesis with  $\mu > \mu_{\text{limit}}$  would be excluded at a confidence level of  $1 - \alpha$ . Figure 6.3 is plotted showing similarities and differences among various statistical methods.

Our measurement gives a  $-2.44\sigma$  result, which constrains the dark photon  $\delta a < 0.287\sigma$  under PCL ( $M_{\min} = 16\%$ ) with 90% confidence level. It can be plotted together with other accelerator limits as shown in Figure 6.4. Both  $g_e - 2$  and  $g_\mu - 2$  are plotted based on the

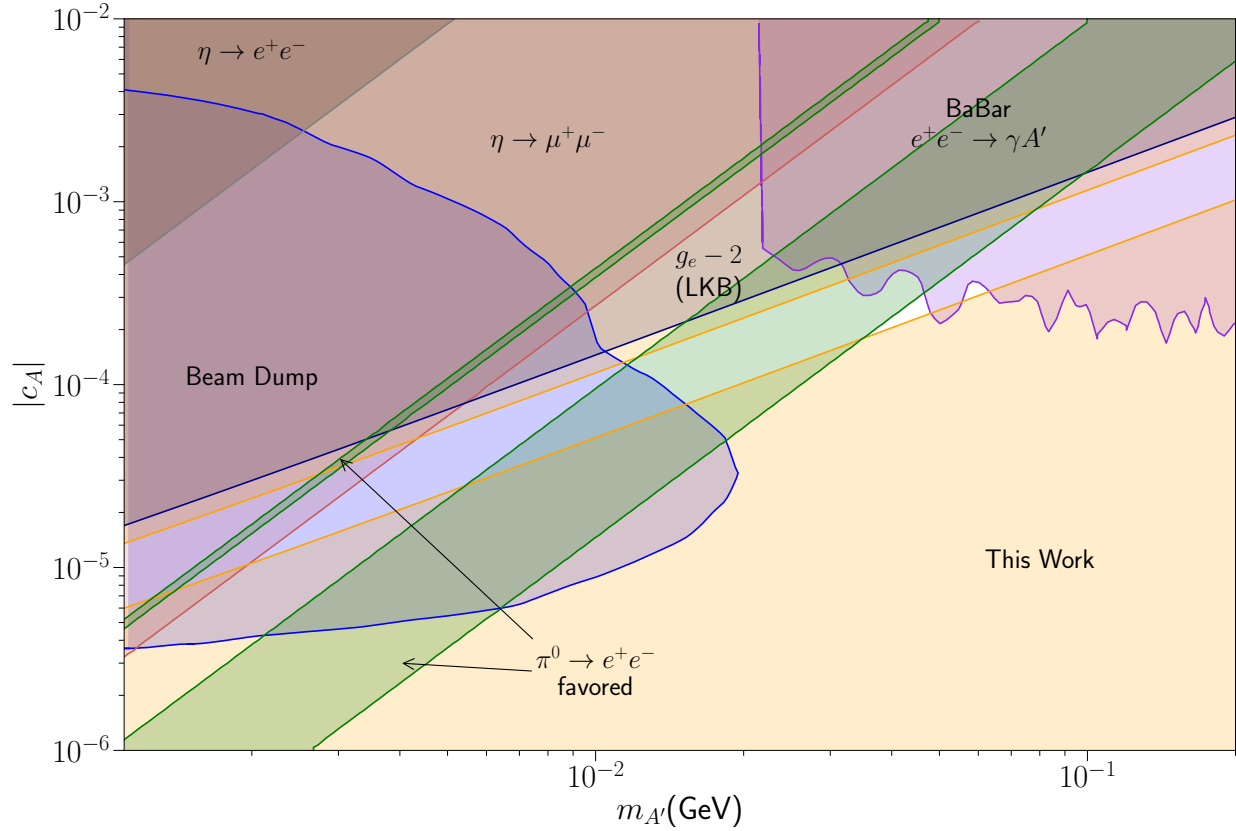


Figure 6.5: Dark photon with axial vector coupling exclusion plot. The plot is given with assumptions  $c_A^u = 10^{-3}$ ,  $c_A^d = 10^{-4}$ , and  $c_A^\mu = c_V^l = 0$ . This work is analyzed under frequentist's statistics at 90% C.L. [117].

most recent CODATA updates, so they are a bit different from plots in the most of other literatures [120, 123]. Though our result is not as impressive in dark photon search using statistics like PCL or  $CL_s$ , it does not undermine the importance of the  $2.5\sigma$  tension with the Standard Model we observed.

Our result could also be used to put constraints on axial coupling of dark photons. Assuming the coupling constants for the first-generation quarks as well as leptons satisfy  $c_A^u = 10^{-3}$ ,  $c_A^d = 10^{-4}$ , and  $c_A^\mu = c_V^l = 0$ , we can plot the exclusion plot as shown in Figure 6.5. We extended the exclusion region to the lower part of the parameter space where the old electron  $g_e - 2$  cannot put constraints.

More types of particles that would produce a shift in  $\delta a$  would be sensitive by our measurement, such as B-L vector bosons, axial vector coupled bosons, and scalar and pseudoscalar bosons and so on. It is an ongoing promising test of new physics beyond the Standard Model in which a bit more progress in precision and accuracy would result in rich understanding of fundamental physics.

## Electron Substructure

Electron substructure is another theory that can be tested by our measurement [2, 125]. An electron whose constituents have mass  $m^* \gg m_e$  would shift  $\delta a$  by  $\Delta(\delta a) \sim (m_e/m^*)$ . In a chirally invariant model, the shift would scale quadratically, i.e.  $\Delta(\delta a) \sim (m_e/m^*)^2$ . If we assume for a simple theory,

$$\delta a = \frac{m_e}{m^*} = (0.88 \pm 0.36) \times 10^{-12} \text{ (our measurement)} \quad (6.15)$$

Based on our result, we can set  $|\delta a| < 1.242 \times 10^{-12}$ , which places a limit to the substructure at a scale of  $m^* > 411,000 \text{ TeV}/c^2$ . In the same way, we can set the limit to the substructure in the chirally invariant model at a scale of  $m^* > 460 \text{ GeV}/c^2$ . These limits improve over the previous limits of  $m^* > 240,000 \text{ TeV}/c^2$  for the simple model and  $m^* > 350 \text{ GeV}/c^2$  for the chirally invariant model by an  $O(1)$  factor respectively.

## 6.3 Future Prospects

As we observe a growing tension between what the Standard Model predicts and the experiment  $g_e - 2$  results, there is no doubt that something interesting and important about the Standard Model and even new physics may come out as we further improve our precision and accuracy. At this point, the testing of the Standard Model is not limited by the fine-structure-constant measurement. But a new measurement of  $g_e - 2$  with potentially an order of magnitude accuracy and precision improvement is on the way. So there is still much more reasons to improve our measurement for the next generation fine-structure-constant measurement.

The question is whether our apparatus is able to reach higher precision and accuracy. Currently we are limited by sensitivity and a few systematics as shown in the error budget in Chapter 5.

In order to improve sensitivity, we are looking forward to even larger order Bloch oscillations inserted in the interferometer. Current we are still limited by decoherence due to beam quality. Better beam cleaning techniques will have great potential to help us improve our sensitivity.

At the same time we are also limited by systematics like gravity gradient, Gouy phase, and diffraction phase. We are going to test a new scheme where gravity gradient would be exactly cancelled. For Gouy phase as we improve the mode of the beam and develop better beam characterization techniques, it will be improved as well. For diffraction phase, the leading order is eliminated. But the higher order due to thermal expansion is still a limiting factor for us. Better transverse cooling, smaller atomic cloud size and larger beam cross section will for sure help to constrain this systematic effect.

The most significant technical challenge here is laser power, which can be addressed by a powerful 532 nm pulse laser scheme developed by D. DeMille. And this we can help us deliver strong 852 nm pulse by certain amplification techniques. We are expected to get

a few hundreds of mJs of power for each pulse, which is more than 3 orders of magnitude improvement in laser intensity. Definitely there would be more challenges as no one has ever done so. But all technologies required seem to be available so it's very promising to improve the fine-structure-constant measurement by an order of magnitude or even better.

# Bibliography

- [1] Peter J. Mohr, David B. Newell, and Barry N. Taylor. “CODATA recommended values of the fundamental physical constants: 2014”. In: *Rev. Mod. Phys.* 88 (3 Sept. 2016), p. 035009.
- [2] D. Hanneke, S. Fogwell, and G. Gabrielse. “New Measurement of the Electron Magnetic Moment and the Fine Structure Constant”. In: *Phys. Rev. Lett.* 100 (12 Mar. 2008), p. 120801.
- [3] P. A. M. Dirac. “The quantum theory of the electron”. In: *Proceedings of the Royal Society of London A: Mathematical, Physical and Engineering Sciences* 117.778 (1928), pp. 610–624. ISSN: 0950-1207.
- [4] ARTHUR RICH and JOHN C. WESLEY. “The Current Status of the Lepton  $g$  Factors”. In: *Rev. Mod. Phys.* 44 (2 Apr. 1972), pp. 250–283.
- [5] Tatsumi Aoyama et al. “Tenth-Order QED Contribution to the Electron  $g-2$  and an Improved Value of the Fine Structure Constant”. In: *Phys. Rev. Lett.* 109 (11 Sept. 2012), p. 111807.
- [6] Tatsumi Aoyama et al. “Tenth-order electron anomalous magnetic moment: Contribution of diagrams without closed lepton loops”. In: *Phys. Rev. D* 91 (3 Feb. 2015), p. 033006.
- [7] Tatsumi Aoyama et al. “Erratum: Tenth-order electron anomalous magnetic moment: Contribution of diagrams without closed lepton loops [Phys. Rev. D 91, 033006 (2015)]”. In: *Phys. Rev. D* 96 (1 July 2017), p. 019901.
- [8] Richard H. Parker et al. “Measurement of the fine-structure constant as a test of the Standard Model”. In: *Science* 360.6385 (2018), pp. 191–195.
- [9] E. R. Williams et al. “A low field determination of the proton gyromagnetic ratio in water”. In: *IEEE Transactions on Instrumentation and Measurement* 38.2 (Apr. 1989), pp. 233–237.
- [10] A. M. Jeffery et al. “NIST comparison of the quantized Hall resistance and the realization of the SI OHM through the calculable capacitor”. In: *IEEE Transactions on Instrumentation and Measurement* 46.2 (Apr. 1997), pp. 264–268.
- [11] Rym Bouchendira et al. “New Determination of the Fine Structure Constant and Test of the Quantum Electrodynamics”. In: *Phys. Rev. Lett.* 106 (8 Feb. 2011), p. 080801.

- [12] Andreas Wicht et al. “A Preliminary Measurement of the Fine Structure Constant Based on Atom Interferometry”. In: *Physica Scripta* 2002.T102 (2002), p. 82.
- [13] E Krüger, W Nistler, and W Weirauch. “Determination of the fine-structure constant by a precise measurement of  $h/m_n$  : the final result”. In: *Metrologia* 35.3 (1998), p. 203.
- [14] Axel Beyer et al. “The Rydberg constant and proton size from atomic hydrogen”. In: *Science* 358.6359 (2017), pp. 79–85.
- [15] S. Sturm et al. “High-precision measurement of the atomic mass of the electron”. In: *Nature* 506 (Feb. 2014), p. 467.
- [16] G. Audi et al. “The Nubase2012 evaluation of nuclear properties”. In: *Chinese Physics C* 36.12 (2012), p. 1157.
- [17] Michael P. Bradley et al. “Penning Trap Measurements of the Masses of  $^{133}\text{Cs}$ ,  $^{87,85}\text{Rb}$ , and  $^{23}\text{Na}$  with Uncertainties  $\leq 0.2$  ppb”. In: *Phys. Rev. Lett.* 83 (22 Nov. 1999), pp. 4510–4513.
- [18] Brianna J. Mount, Matthew Redshaw, and Edmund G. Myers. “Atomic masses of  $^6\text{Li}$ ,  $^{23}\text{Na}$ ,  $^{39,41}\text{K}$ ,  $^{85,87}\text{Rb}$ , and  $^{133}\text{Cs}$ ”. In: *Phys. Rev. A* 82 (4 Oct. 2010), p. 042513.
- [19] A Peters, K Y Chung, and S Chu. “High-precision gravity measurements using atom interferometry”. In: *Metrologia* 38.1 (2001), p. 25.
- [20] Mark Kasevich and Steven Chu. “Atomic interferometry using stimulated Raman transitions”. In: *Phys. Rev. Lett.* 67 (2 July 1991), pp. 181–184.
- [21] M. J. Snadden et al. “Measurement of the Earth’s Gravity Gradient with an Atom Interferometer-Based Gravity Gradiometer”. In: *Phys. Rev. Lett.* 81 (5 Aug. 1998), pp. 971–974.
- [22] G. D’Amico et al. “Bragg interferometer for gravity gradient measurements”. In: *Phys. Rev. A* 93 (6 June 2016), p. 063628.
- [23] G. Rosi et al. “Measurement of the Gravity-Field Curvature by Atom Interferometry”. In: *Phys. Rev. Lett.* 114 (1 Jan. 2015), p. 013001.
- [24] Peter Asenbaum et al. “Phase Shift in an Atom Interferometer due to Spacetime Curvature across its Wave Function”. In: *Phys. Rev. Lett.* 118 (18 May 2017), p. 183602.
- [25] Susannah M. Dickerson et al. “Multiaxis Inertial Sensing with Long-Time Point Source Atom Interferometry”. In: *Phys. Rev. Lett.* 111 (8 Aug. 2013), p. 083001.
- [26] Xuejian Wu et al. “Multiaxis atom interferometry with a single-diode laser and a pyramidal magneto-optical trap”. In: *Optica* 4.12 (Dec. 2017), pp. 1545–1551.
- [27] Kayleigh Cassella et al. “Recoil-Sensitive Lithium Interferometer without a Subrecoil Sample”. In: *Phys. Rev. Lett.* 118 (23 June 2017), p. 233201.
- [28] J. B. Fixler et al. “Atom Interferometer Measurement of the Newtonian Constant of Gravity”. In: *Science* 315.5808 (2007), pp. 74–77.



- [29] G. Rosi et al. “Precision measurement of the Newtonian gravitational constant using cold atoms”. In: *Nature* 510 (June 2014), p. 518.
- [30] Shau-Yu Lan et al. “A Clock Directly Linking Time to a Particle’s Mass”. In: *Science* 339.6119 (2013), pp. 554–557.
- [31] Michael A. Hohensee et al. “Equivalence Principle and Gravitational Redshift”. In: *Phys. Rev. Lett.* 106 (15 Apr. 2011), p. 151102.
- [32] Holger Müller et al. “Atom-Interferometry Tests of the Isotropy of Post-Newtonian Gravity”. In: *Phys. Rev. Lett.* 100 (3 Jan. 2008), p. 031101.
- [33] Holger Müller, Achim Peters, and Steven Chu. “A precision measurement of the gravitational redshift by the interference of matter waves”. In: *Nature* 463 (Feb. 2010), p. 926.
- [34] Savvas Dimopoulos et al. “Testing General Relativity with Atom Interferometry”. In: *Phys. Rev. Lett.* 98 (11 Mar. 2007), p. 111102.
- [35] P. Hamilton et al. “Atom-interferometry constraints on dark energy”. In: *Science* 349.6250 (2015), pp. 849–851.
- [36] Matt Jaffe et al. “Testing sub-gravitational forces on atoms from a miniature in-vacuum source mass”. In: *Nature Physics* 13 (July 2017), p. 938.
- [37] Robert B. Leighton Richard P. Feynman and Matthew Sands. *The Feynman Lectures on Physics, Volume III: Quantum mechanics*. Addison-Wesley, 1964.
- [38] Jim J. Napolitano J. J. Sakurai. *Modern Quantum Mechanics*. Pearson, 2010.
- [39] Alexander D. Cronin, Jörg Schmiedmayer, and David E. Pritchard. “Optics and interferometry with atoms and molecules”. In: *Rev. Mod. Phys.* 81 (3 July 2009), pp. 1051–1129.
- [40] Daniel A. Steck. *Quantum and Atom Optics*. 2007. URL: <http://atomoptics-nas.uoregon.edu/~dsteck/teaching/quantum-optics/quantum-optics-notes.pdf>.
- [41] Claude Cohen-Tannoudji and David Guéry-Odelin. *Advances in Atomic Physics An Overview*. World Scientific, 2011.
- [42] Daniel A. Steck. *Cesium D Line Data*. Jan. 1998. URL: <http://steck.us/alkalidata/cesiumnumbers.1.6.pdf>.
- [43] Liang Hu et al. “Atom Interferometry with the Sr Optical Clock Transition”. In: *Phys. Rev. Lett.* 119 (26 Dec. 2017), p. 263601.
- [44] Sheng-wei Chiow. “A precision measurement of the photon recoil using large area atom interferometry”. PhD thesis. Stanford University, 2008.
- [45] Achim Peters. “High precision gravity measurements using atom interferometry”. PhD thesis. Stanford University, 1998.

- [46] Holger Müller, Sheng-wei Chiow, and Steven Chu. “Atom-wave diffraction between the Raman-Nath and the Bragg regime: Effective Rabi frequency, losses, and phase shifts”. In: *Phys. Rev. A* 77 (2 Feb. 2008), p. 023609.
- [47] Holger Müller et al. “Atom Interferometry with up to 24-Photon-Momentum-Transfer Beam Splitters”. In: *Phys. Rev. Lett.* 100 (18 May 2008), p. 180405.
- [48] Michael T. Heath. *Scientific Computing*. 2ed. The McGraw-Hill Companies, Inc., 2002.
- [49] Maxime Ben Dahan et al. “Bloch Oscillations of Atoms in an Optical Potential”. In: *Phys. Rev. Lett.* 76 (24 June 1996), pp. 4508–4511.
- [50] Ekkehard Peik et al. “Bloch oscillations of atoms, adiabatic rapid passage, and monokinetic atomic beams”. In: *Phys. Rev. A* 55 (4 Apr. 1997), pp. 2989–3001.
- [51] Malo Cadoret et al. “Combination of Bloch Oscillations with a Ramsey-Bordé Interferometer: New Determination of the Fine Structure Constant”. In: *Phys. Rev. Lett.* 101 (23 Dec. 2008), p. 230801.
- [52] W. V. Houston. “Acceleration of Electrons in a Crystal Lattice”. In: *Phys. Rev.* 57 (3 Feb. 1940), pp. 184–186.
- [53] Gregory H. Wannier. “Wave Functions and Effective Hamiltonian for Bloch Electrons in an Electric Field”. In: *Phys. Rev.* 117 (2 Jan. 1960), pp. 432–439.
- [54] ANDREY R. KOLOVSKY and HANS JÜRGEN KORSCH. “BLOCH OSCILLATIONS OF COLD ATOMS IN OPTICAL LATTICES”. In: *International Journal of Modern Physics B* 18.09 (2004), pp. 1235–1260.
- [55] “Non-adiabatic crossing of energy levels”. In: *Proceedings of the Royal Society of London A: Mathematical, Physical and Engineering Sciences* 137.833 (1932), pp. 696–702.
- [56] Claude Cohen-Tannoudji Pippa Storey. “The Feynman path integral approach to atomic interferometry. A tutorial”. In: *J. Phys. II France* 4.11 (1994), pp. 1999–2027.
- [57] Shau-Yu Lan et al. “Influence of the Coriolis Force in Atom Interferometry”. In: *Phys. Rev. Lett.* 108 (9 Feb. 2012), p. 090402.
- [58] G. T. Foster et al. “Method of phase extraction between coupled atom interferometers using ellipse-specific fitting”. In: *Opt. Lett.* 27.11 (June 2002), pp. 951–953.
- [59] Andrew Fitzgibbon, Maurizio Pilu, and Robert B. Fisher. “Direct Least Square Fitting of Ellipses”. In: *IEEE Trans. Pattern Anal. Mach. Intell.* 21.5 (May 1999), pp. 476–480.
- [60] John K. Stockton, Xinan Wu, and Mark A. Kasevich. “Bayesian estimation of differential interferometer phase”. In: *Phys. Rev. A* 76 (3 Sept. 2007), p. 033613.
- [61] Pei-Chen Kuan. “Compton clock and recoil frequency measurements using a large momentum transfer atom interferometer”. PhD thesis. University of California at Berkeley, 2013.

- [62] Brian Vincent Estey. “Precision Measurement in Atom Interferometry Using Bragg Diffraction”. PhD thesis. University of California, Berkeley, 2016.
- [63] Sheng-wei Chiow et al. “Noise-Immune Conjugate Large-Area Atom Interferometers”. In: *Phys. Rev. Lett.* 103 (5 July 2009), p. 050402.
- [64] Eugene Hecht. *Optics*. 5ed. Pearson, 2016.
- [65] A. A. Michelson and E. W. Morley. “On the relative motion of the Earth and the luminiferous ether”. In: *American Journal of Science Series 3 Vol. 34*. 203 (1887), pp. 333–345.
- [66] Steven Chu et al. “Three-dimensional viscous confinement and cooling of atoms by resonance radiation pressure”. In: *Phys. Rev. Lett.* 55 (1 July 1985), pp. 48–51.
- [67] E. L. Raab et al. “Trapping of Neutral Sodium Atoms with Radiation Pressure”. In: *Phys. Rev. Lett.* 59 (23 Dec. 1987), pp. 2631–2634.
- [68] Paul D. Lett et al. “Observation of Atoms Laser Cooled below the Doppler Limit”. In: *Phys. Rev. Lett.* 61 (2 July 1988), pp. 169–172.
- [69] Wolfgang Ketterle and N.J. Van Druten. “Evaporative Cooling of Trapped Atoms”. In: ed. by Benjamin Bederson and Herbert Walther. Vol. 37. *Advances In Atomic, Molecular, and Optical Physics*. Academic Press, 1996, pp. 181–236.
- [70] National Instruments Corporation. *NI 6533/6534 Specifications*. Nov. 2005. URL: <http://www.ni.com/pdf/manuals/374163a.pdf>.
- [71] National Instruments Corporation. *NI 6321 Specifications*. Sept. 2015. URL: <http://www.ni.com/pdf/manuals/374461b.pdf>.
- [72] Analog Devices. *AD9954 Data Sheet*. URL: <http://www.analog.com/media/en/technical-documentation/data-sheets/AD9954.pdf>.
- [73] Stanford Research Systems. *FS725 - Benchtop rubidium frequency standard*. URL: <http://www.thinksrs.com/downloads/pdfs/catalog/FS725c.pdf>.
- [74] Stanford Research Systems. *DG535 - Digital delay and pulse generator (4-channel)*. URL: <http://www.thinksrs.com/downloads/pdfs/catalog/FS725c.pdf>.
- [75] New Focus. *TLB-6900 Vortex II Tunable Lasers*. URL: [http://assets.newport.com/webDocuments-EN/images/TLB-6900\\_Vortex\\_Brochure.PDF](http://assets.newport.com/webDocuments-EN/images/TLB-6900_Vortex_Brochure.PDF).
- [76] Gary C. Bjorklund. “Frequency-modulation spectroscopy: a new method for measuring weak absorptions and dispersions”. In: *Opt. Lett.* 5.1 (Jan. 1980), pp. 15–17.
- [77] G. Camy, Ch.J. Bordé, and M. Ducloy. “Heterodyne saturation spectroscopy through frequency modulation of the saturating beam”. In: *Optics Communications* 41.5 (1982), pp. 325–330.
- [78] Jon H. Shirley. “Modulation transfer processes in optical heterodyne saturation spectroscopy”. In: *Opt. Lett.* 7.11 (Nov. 1982), pp. 537–539.

- [79] Fei Zi et al. “Laser frequency stabilization by combining modulation transfer and frequency modulation spectroscopy”. In: *Appl. Opt.* 56.10 (Apr. 2017), pp. 2649–2652.
- [80] William D. Phillips and Harold Metcalf. “Laser Deceleration of an Atomic Beam”. In: *Phys. Rev. Lett.* 48 (9 Mar. 1982), pp. 596–599.
- [81] J. Schoser et al. “Intense source of cold Rb atoms from a pure two-dimensional magneto-optical trap”. In: *Phys. Rev. A* 66 (2 Aug. 2002), p. 023410.
- [82] Vladan Vuletić et al. “Degenerate Raman Sideband Cooling of Trapped Cesium Atoms at Very High Atomic Densities”. In: *Phys. Rev. Lett.* 81 (26 Dec. 1998), pp. 5768–5771.
- [83] Mark Kasevich et al. “Atomic velocity selection using stimulated Raman transitions”. In: *Phys. Rev. Lett.* 66 (18 May 1991), pp. 2297–2300.
- [84] Erling Riis et al. “Atom funnel for the production of a slow, high-density atomic beam”. In: *Phys. Rev. Lett.* 64 (14 Apr. 1990), pp. 1658–1661.
- [85] Philipp Treutlein, Keng Yeow Chung, and Steven Chu. “High-brightness atom source for atomic fountains”. In: *Phys. Rev. A* 63 (5 Apr. 2001), p. 051401.
- [86] P. D. Lett et al. “Optical molasses”. In: *J. Opt. Soc. Am. B* 6.11 (Nov. 1989), pp. 2084–2107.
- [87] J. Dalibard and C. Cohen-Tannoudji. “Laser cooling below the Doppler limit by polarization gradients: simple theoretical models”. In: *J. Opt. Soc. Am. B* 6.11 (Nov. 1989), pp. 2023–2045.
- [88] Y. Castin and J. Dalibard. “Quantization of Atomic Motion in Optical Molasses”. In: *EPL (Europhysics Letters)* 14.8 (1991), p. 761.
- [89] Andrew J. Kerman. “Raman sideband cooling and cold atomic collisions in optical lattices”. PhD thesis. Stanford University, 2002.
- [90] A. Clairon et al. “Ramsey Resonance in a Zacharias Fountain”. In: *EPL (Europhysics Letters)* 16.2 (1991), p. 165.
- [91] Tomasz M Brzozowski et al. “Time-of-flight measurement of the temperature of cold atoms for short trap-probe beam distances”. In: *Journal of Optics B: Quantum and Semiclassical Optics* 4.1 (2002), p. 62.
- [92] Peter van der Straten Harold J. Metcalf. *Laser Cooling and Trapping*. Springer Science+Business Media New York, 1999.
- [93] A. R. Edmonds. *Angular Momentum in Quantum Mechanics*. Princeton University Press, Princeton, 1957.
- [94] Inc M Squared Lasers. *ULTRA NARROW LINEWIDTH CW TI: SAPPHIRE LASER*. URL: [http://www.m2lasers.com/images/SolsTiS\\_Datasheet.pdf](http://www.m2lasers.com/images/SolsTiS_Datasheet.pdf).

- [95] Sheng-wey Chiow et al. “6W, 1kHz linewidth, tunable continuous-wave near-infrared laser”. In: *Opt. Express* 17.7 (Mar. 2009), pp. 5246–5250.
- [96] T.W. Hansch and B. Couillaud. “Laser frequency stabilization by polarization spectroscopy of a reflecting reference cavity”. In: *Optics Communications* 35.3 (1980), pp. 441–444.
- [97] National Instruments Corporation. *INSTALLATION GUIDE AND SPECIFICATIONS GPIB Hardware*. 2017. URL: <http://www.ni.com/pdf/manuals/370426r.pdf>.
- [98] National Instruments Corporation. *NI 447x Specifications*. 2009. URL: <http://www.ni.com/pdf/manuals/373861d.pdf>.
- [99] Tim Kovachy. “New Techniques for Precision Atom Interferometry and Application to Fundamental Test of Gravity and of Quantum Mechanics”. PhD thesis. Stanford University, 2016.
- [100] CERN Giuseppe Allodi. *FMINUIT - A binding to Minuit for Matlab, Octave and Scilab*. May 2010. URL: [http://www.fis.unipr.it/~giuseppe.allodi/Fminuit/Fminuit\\_intro.html](http://www.fis.unipr.it/~giuseppe.allodi/Fminuit/Fminuit_intro.html).
- [101] S. Bade et al. “Photon momentum in a distorted optical field”. In: *ArXiv e-prints* (Dec. 2017). arXiv: 1712.04023 [physics.atom-ph].
- [102] G. Breit and I. I. Rabi. “Measurement of Nuclear Spin”. In: *Phys. Rev.* 38 (11 Dec. 1931), pp. 2082–2083.
- [103] Daly Peter et al. “Frequency and time stability of GPS and glonass clocks”. In: *International Journal of Satellite Communications* 9.1 (), pp. 11–22.
- [104] MenloSystems. *FC8004 Optical Frequency Comb*. 2016. URL: [http://www.menlosystems.com/assets/datasheets/MENLO\\_FC8004-D-EN\\_2016-06\\_3w.pdf](http://www.menlosystems.com/assets/datasheets/MENLO_FC8004-D-EN_2016-06_3w.pdf).
- [105] Jun Ye et al. “Accuracy Comparison of Absolute Optical Frequency Measurement between Harmonic-Generation Synthesis and a Frequency-Division Femtosecond Comb”. In: *Phys. Rev. Lett.* 85 (18 Oct. 2000), pp. 3797–3800.
- [106] Jun Ye and Steven T. Cundiff. *Femtosecond Optical Frequency Comb: Principle, Operation and Applications*. Springer, 2005.
- [107] Bahaa E. A. Saleh and Malvin Carl Teich. *Fundamentals of Photonics*. John Wiley & Sons, Inc., 2001.
- [108] Richard H. Parker et al. “Controlling the multiport nature of Bragg diffraction in atom interferometry”. In: *Phys. Rev. A* 94 (5 Nov. 2016), p. 053618.
- [109] C. J. Foot. *Atomic Physics*. Oxford University Press, 2005.
- [110] C. J. Pethick and H. Smith. *Bose-Einstein Condensation in Dilute Gases*. Cambridge University Press, 2008.
- [111] E. P. Gross. “Structure of a quantized vortex in boson systems”. In: *Il Nuovo Cimento (1955-1965)* 20.3 (May 1961), pp. 454–477.

- [112] L.P. Pitaevskii. “Vortex Lines in an Imperfect Bose Gas”. In: *JETP* 13.2 (Aug. 1961), p. 451.
- [113] Cheng Chin et al. “High Resolution Feshbach Spectroscopy of Cesium”. In: *Phys. Rev. Lett.* 85 (13 Sept. 2000), pp. 2717–2720.
- [114] F. Riehle et al. “Optical Ramsey spectroscopy in a rotating frame: Sagnac effect in a matter-wave interferometer”. In: *Phys. Rev. Lett.* 67 (2 July 1991), pp. 177–180.
- [115] Planck Collaboration et al. “Planck 2015 results - XIII. Cosmological parameters”. In: *A&A* 594 (2016), A13.
- [116] Hooman Davoudiasl, Hye-Sung Lee, and William J. Marciano. “Muon  $g-2$ , rare kaon decays, and parity violation from dark bosons”. In: *Phys. Rev. D* 89 (9 May 2014), p. 095006.
- [117] Yonatan Kahn et al. “Light weakly coupled axial forces: models, constraints, and projections”. In: *Journal of High Energy Physics* 2017.5 (May 2017), p. 2.
- [118] A L Read. “Presentation of search results: the CL s technique”. In: *Journal of Physics G: Nuclear and Particle Physics* 28.10 (2002), p. 2693.
- [119] G. Cowan et al. “Power-Constrained Limits”. In: *ArXiv e-prints* (May 2011). arXiv: 1105.3166 [physics.data-an].
- [120] J. P. Lees et al. “Search for Invisible Decays of a Dark Photon Produced in  $e^+e^-$  Collisions at BaBar”. In: *Phys. Rev. Lett.* 119 (13 Sept. 2017), p. 131804.
- [121] S. Adler et al. “Further Evidence for the Decay  $K^+ \rightarrow \pi^+\nu\bar{\nu}$ ”. In: *Phys. Rev. Lett.* 88 (4 Jan. 2002), p. 041803.
- [122] A. V. Artamonov et al. “Study of the decay  $K^+ \rightarrow \pi^+\nu\bar{\nu}$  in the momentum region  $140 < P_\pi < 199$  MeV/ $c$ ”. In: *Phys. Rev. D* 79 (9 May 2009), p. 092004.
- [123] D. Banerjee et al. “Search for Invisible Decays of Sub-GeV Dark Photons in Missing-Energy Events at the CERN SPS”. In: *Phys. Rev. Lett.* 118 (1 Jan. 2017), p. 011802.
- [124] D. Banerjee et al. “Search for vector mediator of dark matter production in invisible decay mode”. In: *Phys. Rev. D* 97 (7 Apr. 2018), p. 072002.
- [125] G. Gabrielse et al. “Fundamental Physics in Particle Traps”. In: ed. by Wolfgang Quint and Manuel Vogel. Springer Tracts in Modern Physics 256. Springer, 2014. Chap. 1, pp. 1–40.